Beyond Simple Imaging with Energetic Beams – Nanopatterning, Correlative Microscopy and Statistical Analysis of Inclusions

Michael Schmidt, Dipl.-Phys.

Presented for the Ph.D. Degree to the National University of Ireland, Cork

ucc

Coláiste na hOllscoile Corcaigh, Éire
University College Cork, Ireland

Department of Chemistry

Tyndall National Institute

University College Cork

Ireland

Head of Department:

Prof. Martyn E. Pemble

Supervisors:

Prof. Justin D. Holmes

Dr. Nikolay Petkov

May 2015

Contents

Declaration

I, Michael Schmidt, certify that this thesis is my own work and I have not obtained a degree in this university or elsewhere on the basis of this PhD thesis.

_____

Michael Schmidt

Acknowlegdements

In deep gratitude I thank all the kind souls who gave support, guidance, advice, samples and time for discussions over the last 4 years. In particular my supervisors Prof Justin D Holmes and Dr Nikolay Petkov for their constant support and the opportunity for this thesis in the first place, Dr Graeme Maxwell for giving me the time to finish this thesis, Dr Feroze Nazneen for the electropolished stainless steel samples that created such beautiful images after the FIB patterning, Dr Lynette Keeney for the multiferroic thin films followed by the question 'Are there really no inclusions in there?', Prof Roger W Whatmore for keeping this question alive for nearly two years and the patience to wait for the answer that long, Dr Gillian Collins for the Pd nanoparticles that were so nicely uniform, Dr Andreas Amann for all the late evening discussions about statistics, all the collaborators on the short projects, Dr Paul Galvin, Dr Gregoire Herzog, Dr. Damien WM Arrigan, Dr Eva McLoughlin, Dr Gerard McGlacken, Dr Colm O'Dwyer, Prof Martyn Pemble, Dr Calum Dickinson, Dr Johann P de Silva, Dr Declan Scanlan, Dr Neal O'Hara, Prof Graham LW Cross, Dr Nitin Deepak, Dr Saibal Roy, Tuhin Maity, all the friends and colleagues in Tyndall and UCC, Pat, Yordan, Anushka, Shelly, Roisin, Colm, Barbara, Ray, Shirin, JP, Isabelle, Ran, Paul, Hanno, Donagh, Ilias, Ciara, Richard, Vince, Pat, Noel, Alan, Dan, Vladimir and everybody else I forgot in this short list. A special thank goes naturally to my parents, my wife and children for their continued support along those years.

Publications that arose from this PhD research:

Absence of evidence ≠ evidence of absence: statistical analysis of inclusions in multiferroic thin films

Michael Schmidt, Andreas Amann, Lynette Keeney, Martyn E Pemble, Justin D Holmes, Nikolay Petkov, Roger Whatmore, Sci Reports, **4** (2014) 5712

FIB Patterning of Stainless Steel for the De-velopment of Nano-Structured Stent Surfaces for Cardiovascular Applications **(invited)**

Michael Schmidt, Feroze Nazneen, Paul Galvin, Nikolay Petkov, Justin D Holmes

Chapter in ‚FIB Nanopatterning', Springer book series ‚Lecture Notes on Nanoscale Science and Technology' vol. 20 (2013), 391-416

Correlative Microscopy Study of FIB Patterned Stainless Steel Surfaces as Novel Nano-Structured Stents for Cardiovascular Applications

Michael Schmidt, Feroze Nazneen, Gregoire Herzog, Damien Arrigan, Paul Galvin, Calum Dickinson, Johann P de Silva, Declan Scanlan, Neal O'Hara, Graham LW Cross, Nikolay Petkov, Justin D Holmes, MRS Proceedings **1466** (2012)

FIB Patterning of Stainless Steel for the Development of Nano-Structured Stent Surfaces for Cardiovascular Applications

M Schmidt, F Nazneen, Y Georgiev, G Herzog, P Galvin, N Petkov, Journal of Physics: Conference Series **371** (2012), 012065

Enhanced Catalytic Activity of High-Index Faceted Palladium Nanoparticles in Suzuki-Miyaura Coupling Due to Efficient Leaching Mechanism

Gillian Collins, Michael Schmidt, Colm O'Dwyer, Gerard McGlacken, Justin D Holmes, ACS Catalysis, **4** (2014) 3105-3111

The Origin of Shape Sensitivity in Palladium-Catalyzed Suzuki-Miyaura Cross Coupling Reactions

Gillian Collins, Michael Schmidt, Colm O'Dwyer, Justin D Holmes, Gerard P McGlacken, Angew Chem, **53** (2014) 4142-4145

Stability, Oxidation and Shape Retention of PVP-Capped Pd Nanocrystals

Gillian Collins, Michael Schmidt, Gerard McGlacken, Colm O'Dwyer, Justin D Holmes, J Phys Chem C, **118** (2014) 6522-6530

Impact of Surface Nano-textured Stainless Steel Prepared by Focused Ion Beam on Endothelial Cell Growth

F Nazneen, M Schmidt, E McLoughlin, N Petkov, G Herzog, DWM Arrigan, P Galvin

Journal of Nanoscience and Nanotechnology 13 (2013), 5283-5290

Magnetic Field-Induced Ferroelectric Switching in Multiferroic Aurivillius Phase Thin Films at Room Temperature **(invited)**

Lynette Keeney, Tuhin Maity, Michael Schmidt, Andreas Amann, Nitin Deepak, Nikolay Petkov, Saibal Roy, Martyn E Pemble, Roger W Whatmore

Journal of the American Ceramic Society 96 (2013), 2339-2357

Room temperature ferroelectric and magnetic investigations and detailed phase analysis of Aurivillius phase $Bi_5Ti_3Fe_{0.7}Co_{0.3}O_{15}$ thin films

Lynette Keeney, Santosh Kulkarni, Nitin Deepak, Michael Schmidt, Nikolay Petkov, Panfeng F Zhang, Stuart Cavill, Saibal Roy, Martyn E Pemble, Roger W Whatmore, Journal of Applied Physics **112** (2012), 052010-052010-10

Abstract

Electron microscopy (EM) has advanced in an exponential way since the first transmission electron microscope (TEM) was built in the 1930's. The urge to 'see' things is an essential part of human nature (talk of 'seeing is believing') and apart from scanning tunnel microscopes which give information about the surface, EM is the only imaging technology capable of really visualising atomic structures in depth down to single atoms. With the development of nanotechnology the demand to image and analyse small things has become even greater and electron microscopes have found their way from highly delicate and sophisticated research grade instruments to key-turn and even bench-top instruments for everyday use in every materials research lab on the planet. The semiconductor industry is as dependent on the use of EM as life sciences and pharmaceutical industry. With this generalisation of use for imaging, the need to deploy advanced uses of EM has become more and more apparent. The combination of several coinciding beams (electron, ion and even light) to create DualBeam or TripleBeam instruments for instance enhances the usefulness from pure imaging to manipulating on the nanoscale. And when it comes to the analytic power of EM with the many ways the highly energetic electrons and ions interact with the matter in the specimen there is a plethora of niches which evolved during the last two decades, specialising in every kind of analysis that can be thought of and combined with EM. In the course of this study the emphasis was placed on the application of these advanced analytical EM techniques in the context of multiscale and multimodal microscopy – multiscale meaning across length scales from micrometres or larger to nanometres, multimodal meaning numerous techniques applied to the same sample volume in a correlative manner.

In order to demonstrate the breadth and potential of the multiscale and multimodal concept an integration of it was attempted in two areas: I) Biocompatible materials using polycrystalline stainless steel and II) Semiconductors using thin multiferroic films.

I) The motivation to use stainless steel (316L medical grade) comes from the potential modulation of endothelial cell growth which can have a big impact on the improvement of cardio-vascular stents – which are mainly made of 316L – through nano-texturing of the stent surface by focused ion beam (FIB) lithography. Patterning with FIB has never been reported before in connection with stents and cell growth and in order to gain a better understanding of the beam-substrate interaction during patterning a correlative microscopy approach was used to illuminate the patterning process from many possible angles. Electron backscattering diffraction (EBSD) was used to analyse the crystallographic structure, FIB was used for the patterning and simultaneously visualising the crystal structure as part of the monitoring process, scanning electron microscopy (SEM) and atomic force microscopy (AFM) were employed to analyse the topography and the final step being 3D visualisation through serial FIB/SEM sectioning.

II) The motivation for the use of thin multiferroic films stems from the ever-growing demand for increased data storage at lesser and lesser energy consumption. The Aurivillius phase material used in this study has a high potential in this area. Yet it is necessary to show clearly that the film is really multiferroic and no second phase inclusions are present even at very low concentrations – ~0.1vol% could already be problematic. Thus, in this study a technique was developed to analyse ultra-low density inclusions in thin multiferroic films down to concentrations of 0.01%. The

goal achieved was a complete structural and compositional analysis of the films which required identification of second phase inclusions (through elemental analysis EDX(Energy Dispersive X-ray)), localise them (employing 72 hour EDX mapping in the SEM), isolate them for the TEM (using FIB) and give an upper confidence limit of 99.5% to the influence of the inclusions on the magnetic behaviour of the main phase (statistical analysis).

1. Material Systems Introduction

As indicated in the abstract the thesis attempts to demonstrate the breadth and potential of the multiscale and multimodal concept by its application in two areas: I) Biocompatible materials using polycrystalline stainless steel and II) Semiconductors using thin multiferroic films. This chapter will hence start with a general introduction into the materials used: **1.1** stents, their building materials and the advantage of stainless steel and **1.2** an overview of multiferroic materials, especially Aurivillius phase materials.

1.1. Stents overview: design, desired properties, materials

A stent is generally a metal mesh tube inserted into a natural passage/conduit in the body to prevent or counteract a disease-induced, localized flow constriction or to temporarily hold such a natural conduit open to allow access for surgery [1]. The mesh structure allows the stent to bend and follow the blood or hollow vessels to the point it is required. The surface of stents is geometrically complex because of its mesh structure (**Fig. 1.1**). In a first approximation one can assume the surface that is in strongest contact with the body material to be flat – like an unrolled straw. To simplify the conditions flat substrates are used in this study.

The key characteristics of stents are strength to withstand the peristaltic movements of blood vessels, flexibility and minimal size to reach the tiniest body tubes. Austenitic type 316L stainless steel can supply these desired properties, is commonly used for manufacturing medical implants [2] and so it is also commonly used as stent material. Though in recent years there also have been studies on other alloys, containing Co, Cr and Pt [3-6] for higher strength and Mg as base metal for biodegradable stents [7].

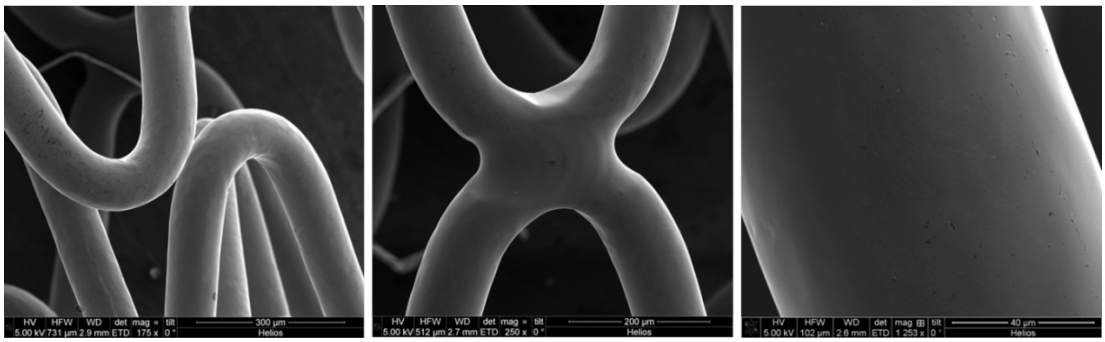

Figure 1.1: Various views on complex stent surfaces

There are various ways to improve the stent design in order to make it more effective. One way is coating the surface with organic and inorganic materials. This is not trivial with the complex geometry of the stainless steel mesh. Nevertheless this route is extensively studied given its benefit of incorporating drugs into the polymer based surface coating which can be eluted over time into the surrounding vessel material. However, there are several reasons including concerns about increased risks of late stent thrombosis when using drug-eluting stents [8, 9], why the development focus is likely to return to bare metal or polymer-free stent technologies [3].

While from the invention of stents it was aimed for a surface as smooth and polished as possible in order to minimize abrasion and inflammation of the body tubes it becomes ever more apparent that a somewhat roughened/textured surface might be a better fit for the task.

The influence of textured material surfaces on the behaviour of cells has been studied for many years by now [10-16]. On one hand, theoretical studies show that cells prefer to grow on rough surfaces in general as it imitates best naturally occurring surfaces [17]. On the other hand, in order to have a better control over and to minimise the complexity of the experimental conditions the natural urge to study regular patterns lead scientists from rough to micro- to nano-patterned surfaces. Especially in tissue engineering where the tissues involved require certain mechanical and structural properties for proper functioning, the trend from micro- to nano-structured surfaces serving as artificially-created support systems has become

evident within the last decade [18-24]. Also for drug delivery the control over biointerfacial interactions is often the key to biomedical applications [14].

In particular endothelial, smooth muscle and fibroblast cells play an important role in the healing process and maintenance of cardiovascular systems and thus are likely to be in contact with biomedical implants such as stents and grafts. During a surgical procedure involving the introduction of a stent, vascular tissues in the arteries may be damaged. Healing of vascular tissues is promoted by the formation of an endothelial cells lining on the stent substrate [25], while the presence of smooth muscle cells and fibroblasts may cause re-stenosis. Micro- and nano-textures on substrates may provide control of cell functions. Such structures could promote better vascular cell adhesion, decrease the need for systemic administration of drugs and reduce the requirement for secondary surgery after stent implantation.

Only one study reported the protein adsorption on FIB patterned glass surfaces [26]. To date, no cellular studies have been reported on FIB structured surfaces. Moreover, this and other aforementioned techniques have not been employed for patterning the key vascular stent material 316L stainless steel for vascular cell functions. Studies do not exist that determine the endothelial cell (EC) response on 316L steel with nano-pit features. Endothelial cell studies on unpatterned 316L stainless steel substrates have shown that the grain size and grain boundaries have an impact on their adhesion and morphology [27]. Chemically etched substrates with 16 µm grain size etched have demonstrated cell densities significantly higher than with grain sizes of 31, 47 and 66 µm. The authors attribute this increased cell density to greater boundary area and associated higher surface free energy [27]. Cell proliferation was also subject to another study discussing different materials. There

the grain sizes varied from 320 nm to 22 µm. Again cell proliferation was inversely proportional on the grain size [28].

Austenitic type 316L stainless steel is commonly used for manufacturing medical implants [29] and was hence selected as the substrate of choice for this study. Austenitic stainless steels have face-centered cubic (fcc) crystal structure, in which the unit cell is a cube with atoms located at the corners and middle of each side (**Fig. 1.2a**). The presence of higher concentration of Ni in austenitic stainless steels stabilises the fcc crystal structure, because Ni is a fcc crystal itself. This enhances the ductility, i.e. it can sustain large plastic deformation without fracture compared to other stainless steels (martensitic and ferritic phases).

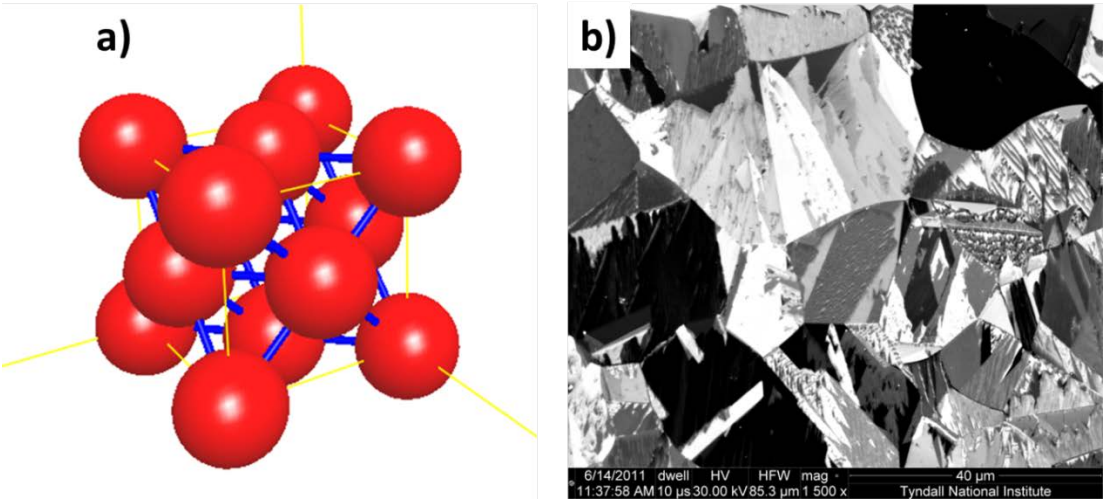

Figure 1.2: a) Schematic face-centered cubic crystal structure and b) FIB image of polycrystalline 316L used in this study

Most metallic materials are composed of many small single crystalline planes called grains. These materials are referred as polycrystalline materials (e.g. steel), in which individual grains have identical arrangement of atoms but the orientation of the atom arrangement or crystal structure is different from each adjoining grain (see **Fig. 1.2b** for visualisation). The interfaces between these grains are grain boundaries, the surface that separates the individual grains [30].

The austenitic stainless steel function can be affected by two microstructure features: grain (or crystal) size and shape. The general grain size suggested for 316L is 100 μm or less [29]. This is because smaller grains have more grain boundaries, which provide resistance to plastic deformation as they responsible for slip deformation by dislocations.

Depending on the process conditions such as annealing and cold-working, the shape of austenitic stainless steel grains vary. Annealing is a heat treatment process where a material is modified, resulting in changes in its properties for example strength and hardness. It is a method that generates conditions via heating to above the recrystallization temperature, maintaining an appropriate temperature, and subsequently cooling. This method is applied to reduce internal tensions, material softening, enhance ductility, improve the structure by creating it uniform and enrich cold-working properties. Austenite grains of the stainless steels under an annealed condition exhibit an equiaxial granular shape (i.e. the grains having axes of equal length).

Cold-working produces plastic deformation in the steels and generates a strain hardening effect, which improves both yield strength and tensile strength of steel considerably. However, in cold-worked steel, depending on the amount of cold

work, the grains are elongated (i.e. longer in the rolling direction). During large plastic deformation, textured grain structures are produced and preferentially align the grains in specific crystallographic orientations. Hence, cold-worked steel with textured structures demonstrates anisotropic mechanical properties. When employing a cold-worked steel for implant fabrication, microstructure analysis is suggested as implants can be better prepared if the loading direction is concurrent to the high strength direction in the steel [29]. Hence, it is clear that the microscopic and crystalline structure can play a strong role on the nano-structuring of the stainless steel surface.

1.2. Introduction to multiferroics

With the continued rapid expanse of computer usage there comes an increasing need for data storage technologies with higher densities, non-volatility and lower power consumption.[31] Single-phase, room temperature multiferroic materials are of considerable interest for such applications[32-38]. However, materials that are magnetoelectric at room temperature are very unusual[39]. The perovskite ferroelectric $BiFeO_3$ exhibits antiferromagnetic ordering at ambient temperature[40]. Although its electric polarisation has been used to control ferromagnetism[41], its ferroelectric polarisation cannot be switched by a magnetic field. There has, therefore, been an intense search for room temperature magnetoelectric multiferroics within which the coupling of ferroelectric and ferromagnetic polarisations might be demonstrated.

The ferroelectric Aurivillius layer-structures[42], described by general formula $Bi_2O_2(A_{m-1}B_mO_{3m+1})$, are naturally 2-dimensionally nanostructured with large *c*-axis parameters. The number of ABO_3 perovskite units (*m*) per half-cell can be changed within the range 2 to 9, depending on composition, and a wide variety of *B*-site cations with +3 to +5 oxidation states accommodated[43-46]. The system offers the potential for including substantial amounts of magnetic cations within a strongly ferroelectric system, and is therefore an exciting candidate for potential use in multiferroic, magnetoelectric logic devices.

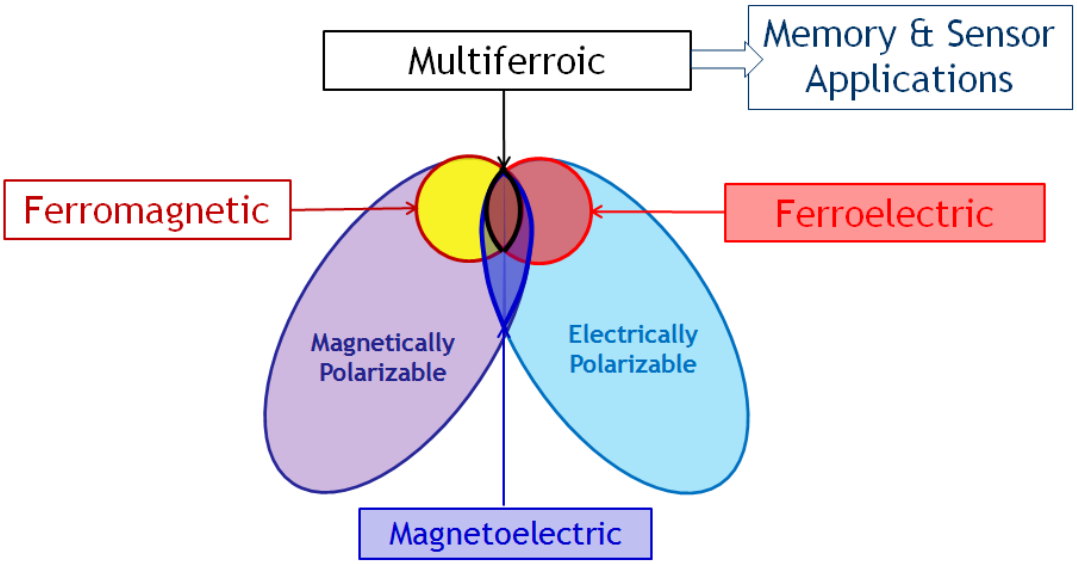

Figure 1.3. The relationship between multiferroic and magnetoelectric materials. (Redrawn from [47]).

Ferroelectric materials form a subset of the polar electrically polarizable materials for which the electrical dipole moments within their structure can be switched between at least two stable states (e.g. up and down) by an external electric field. Ferromagnets form a subset of the magnetically polarizable materials. Materials which demonstrate both ferroelectric and ferromagnetic properties within the same phase are known as multiferroic materials (**Fig. 1.3)**. Magnetoelectric coupling refers to the induction of magnetization by an electric field, or vice versa, and may arise through direct coupling between magnetic and electric polarisations in a single material.

Aurivillius[42] bismuth-based compounds, sometimes referred to as the layered perovskites and described by the general formula $Bi_2O_2(A_{m-1}B_mO_{3m+1})$, represent an important class of ferroelectric compounds. The materials are members of an homologous series of Bi-layered oxides, where the structure is a naturally-layered nano-composite. The 2-dimensional nano-structures have large *c*-axis lattice

parameters, in the nanometer range, and consist of fluorite-structured $(Bi_2O_2)^{2+}$ layers of thickness *f* (typically ~0.4nm) lying in the (001) plane alternating with $mABO_3$ perovskite units in a sandwich type arrangement. The average thickness of the perovskite-type block, *h*, depends on the number of octahedral perovskite units (*m*) in the block: $h = pm$ where *p* is the average thickness of the perovskite-like units (also typically ~0.4 nm).[48] (Note that this is only an approximation, as octahedral tilting, and choice of A & B cations will change the average height of each perovskite unit.[49-51]) The value of *m* can be integer or fractional.[52] Fractional values of *m* usually occur with "mixtures" between a pure Aurivillius phase compound and a perovskite end member and are formed by recurrent intergrowth of the perovskite blocks of two Aurivillius end-members, eg. $BaBi_8Ti_7O_{27}$ ($m = 3.5$) is formed from $(Bi_4Ti_3O_{12})_{0.75}$-$(BaTiO_3)_{0.25}$.[53, 54] The values of *f* and *h* are related to the c cell parameter by $f + h = c/2$.

The layered-structured Aurivillius phase materials are a particularly attractive class of oxides as their structure allows the design and synthesis of new materials in thin film form with interesting electrical and magnetic properties. Between the bismuth oxide layers, the number of octahedral layers can be increased and a homologous series of compounds with the general formula $Bi_{m+1}Fe_{m-3}Ti_3O_{3m+3}$ (m = 4 to 9) has been realised by inserting bismuth ferrite units, $BiFeO_3$, into 3-layered bismuth titanate, $Bi_4Ti_3O_{12}$.

References

1. Dugdale, D.C., *Stent*, in *MedicinePlus*2012. p. http://www.nlm.nih.gov/medlineplus/ency/article/002303.htm.
2. Balamurugan, A., S. Rajeswari, G. Balossier, A.H.S. Rebelo, and J.M.F. Ferreira, *Corrosion aspects of metallic implants — An overview.* Materials and Corrosion, 2008. **59**(11): p. 855-869.
3. O'Brien, B. and W. Carroll, *The evolution of cardiovascular stent materials and surfaces in response to clinical drivers: A review.* Acta Biomaterialia, 2009. **5**(4): p. 945-958.
4. Clerc, C.O., M.R. Jedwab, D.W. Mayer, P.J. Thompson, and J.S. Stinson, *Assessment of wrought ASTM F1058 cobalt alloy properties for permanent surgical implants.* Journal of biomedical materials research, 1997. **38**(3): p. 229-234.
5. Craig, C., C. Friend, M. Edwards, L. Cornish, and N. Gokcen, *Mechanical properties and microstructure of platinum enhanced radiopaque stainless steel (PERSS) alloys.* Journal of Alloys and Compounds, 2003. **361**(1): p. 187-199.
6. Craig, C., C. Friend, M. Edwards, and N. Gokcen. *Tailoring Radiopacity of Austenitic Stainless Steel for Coronary Stents*. in *Medical Device Materials: Proceedings from the Materials & Processes for Medical Devices Conference 2003, 8-10 September 2003, Anaheim, California*. 2004. American Society for Metals.
7. Heublein, B., R. Rohde, V. Kaese, M. Niemeyer, W. Hartung, and A. Haverich, *Biocorrosion of magnesium alloys: a new principle in cardiovascular implant technology?* Heart, 2003. **89**(6): p. 651-656.

8. Lüscher, T.F., J. Steffel, F.R. Eberli, M. Joner, G. Nakazawa, F.C. Tanner, and R. Virmani, *Drug-Eluting Stent and Coronary Thrombosis Biological Mechanisms and Clinical Implications.* Circulation, 2007. **115**(8): p. 1051-1058.

9. Daemen, J., P. Wenaweser, K. Tsuchida, L. Abrecht, S. Vaina, C. Morger, N. Kukreja, P. Jüni, G. Sianos, and G. Hellige, *Early and late coronary stent thrombosis of sirolimus-eluting and paclitaxel-eluting stents in routine clinical practice: data from a large two-institutional cohort study.* The Lancet, 2007. **369**(9562): p. 667-678.

10. Chou, L., J.D. Firth, V.-J. Uitto, and D.M. Brunette, *Substratum surface topography alters cell shape and regulates fibronectin mRNA level, mRNA stability, secretion and assembly in human fibroblasts.* Journal of Cell Science, 1995. **108**(4): p. 1563-1573.

11. Boyan, B.D., T.W. Hummert, D.D. Dean, and Z. Schwartz, *Role of material surfaces in regulating bone and cartilage cell response.* Biomaterials, 1996. **17**(2): p. 137-146.

12. Craighead, H.G., C.D. James, and A.M.P. Turner, *Chemical and topographical patterning for directed cell attachment.* Current Opinion in Solid State and Materials Science, 2001. **5**(2–3): p. 177-184.

13. Curtis, A. and C. Wilkinson, *Nantotechniques and approaches in biotechnology.* Trends in Biotechnology, 2001. **19**(3): p. 97-101.

14. Koegler, P., A. Clayton, H. Thissen, G.N.C. Santos, and P. Kingshott, *The influence of nanostructured materials on biointerfacial interactions.* Advanced Drug Delivery Reviews, 2012. **64**(15): p. 1820-1839.

15. Nikkhah, M., F. Edalat, S. Manoucheri, and A. Khademhosseini, *Engineering microscale topographies to control the cell–substrate interface.* Biomaterials, 2012. **33**(21): p. 5230-5246.

16. Chen, L., D. Han, and L. Jiang, *On improving blood compatibility: From bioinspired to synthetic design and fabrication of biointerfacial topography at micro/nano scales.* Colloids and Surfaces B: Biointerfaces, 2011. **85**(1): p. 2-7.

17. Gentile, F., L. Tirinato, E. Battista, F. Causa, C. Liberale, E.M. di Fabrizio, and P. Decuzzi, *Cells preferentially grow on rough substrates.* Biomaterials, 2010. **31**(28): p. 7205-7212.

18. Kasemo, B., *Biological surface science.* Surface Science, 2002. **500**(1–3): p. 656-677.

19. Duncan, A.C., F. Weisbuch, F. Rouais, S. Lazare, and C. Baquey, *Laser microfabricated model surfaces for controlled cell growth.* Biosensors and Bioelectronics, 2002. **17**(5): p. 413-426.

20. Berry, C.C., G. Campbell, A. Spadiccino, M. Robertson, and A.S.G. Curtis, *The influence of microscale topography on fibroblast attachment and motility.* Biomaterials, 2004. **25**(26): p. 5781-5788.

21. Yim, E.K.F. and K.W. Leong, *Significance of synthetic nanostructures in dictating cellular response.* Nanomedicine: Nanotechnology, Biology and Medicine, 2005. **1**(1): p. 10-21.

22. Falconnet, D., G. Csucs, H. Michelle Grandin, and M. Textor, *Surface engineering approaches to micropattern surfaces for cell-based assays.* Biomaterials, 2006. **27**(16): p. 3044-3063.

23. Yu, L.M.Y., N.D. Leipzig, and M.S. Shoichet, *Promoting neuron adhesion and growth.* Materials Today, 2008. **11**(5): p. 36-43.

24. Roach, P., T. Parker, N. Gadegaard, and M.R. Alexander, *Surface strategies for control of neuronal cell adhesion: A review.* Surface Science Reports, 2010. **65**(6): p. 145-173.

25. Nazneen, F., G. Herzog, D.W. Arrigan, N. Caplice, P. Benvenuto, P. Galvin, and M. Thompson, *Surface chemical and physical modification in stent technology for the treatment of coronary artery disease.* Journal of Biomedical Materials Research Part B: Applied Biomaterials, 2012.

26. Raffa, V., O. Vittorio, V. Pensabene, A. Menciassi, and P. Dario, *FIB-nanostructured surfaces and investigation of bio/nonbio interactions at the nanoscale.* NanoBioscience, IEEE Transactions on, 2008. **7**(1): p. 1-10.

27. Choubey, A., D. Marton, and E.A. Sprague, *Human aortic endothelial cell response to 316L stainless steel material microstructure.* Journal of Materials Science: Materials in Medicine, 2009. **20**(10): p. 2105-2116.

28. Misra, R.D.K., C. Nune, T.C. Pesacreta, M.C. Somani, and L.P. Karjalainen, *Understanding the impact of grain structure in austenitic stainless steel from a nanograined regime to a coarse-grained regime on osteoblast functions using a novel metal deformation–annealing sequence.* Acta Biomaterialia, 2013(0).

29. Russell, A. and K.L. Lee, *Structure-property relations in nonferrous metals*2005: Wiley-Interscience.

30. Shi, D., *Introduction to biomaterials*2006: World Scientific.

31. Assessment of the Potential and Maturity of Selected Emerging Research Memory Technologies Workshop & ERD (Emerging Research Devices) /ERM Working Group Meeting (April 6-7 2010), 2010.

32. Emerging Research Materials, INTERNATIONAL TECHNOLOGY ROADMAP FOR SEMICONDUCTORS, 2009 Edition, 2009.

33. Rao, C.N.R., A. Sundaresan, and R. Saha, *Multiferroic and Magnetoelectric Oxides: The Emerging Scenario.* The Journal of Physical Chemistry Letters, 2012. **3**(16): p. 2237-2246.

34. Bibes, M., *Nanoferronics is a winning combination.* Nat Mater, 2012. **11**(5): p. 354-357.

35. Wang, L., D. Wang, Q. Cao, Y. Zheng, H. Xuan, J. Gao, and Y. Du, *Electric control of magnetism at room temperature.* Sci. Rep., 2012. **2**.

36. Ramesh, R., *Magnetoelectrics: Making metallic memories.* Nat Nano, 2010. **5**(11): p. 761-762.

37. Scott, J.F., *Data storage: Multiferroic memories.* Nature Materials, 2007. **6**(4): p. 256-257.

38. Vaz, C.A.F., J. Hoffman, C.H. Ahn, and R. Ramesh, *Magnetoelectric Coupling Effects in Multiferroic Complex Oxide Composite Structures.* Advanced Materials, 2010. **22**(26-27): p. 2900-2918.

39. Hill, N.A., *Why Are There so Few Magnetic Ferroelectrics?* Journal of Physical Chemistry B, 2000. **104**(29): p. 6694-6709.

40. Catalan, G. and J.F. Scott, *Physics and Applications of Bismuth Ferrite.* Advanced Materials, 2009. **21**(24): p. 2463-2485.

41. Chu, Y.-H., L.W. Martin, M.B. Holcomb, M. Gajek, S.-J. Han, Q. He, N. Balke, C.-H. Yang, D. Lee, W. Hu, Q. Zhan, P.-L. Yang, A. Fraile-

Rodriguez, A. Scholl, S.X. Wang, and R. Ramesh, *Electric-field control of local ferromagnetism using a magnetoelectric multiferroic.* Nat Mater, 2008. **7**(6): p. 478-482.

42. Aurivillius, B., *Mixed Bismuth Oxides with Layer Lattice II. Structure of Bi4Ti3O12.* Ark. Kemi., 1949. **1**: p. 499.

43. Patri, S., R. Choudhary, and B. Samantaray, *Studies of structural, dielectric and impedance properties of Bi9Fe5Ti3O27 ceramics.* J. Electroceram., 2008. **20**(2): p. 119-126.

44. Zhang, P., N. Deepak, L. Keeney, M. Pemble, and R. Whatmore, *The structural and piezoresponse properties of c-axis-oriented Aurivillius phase Bi5Ti3FeO15 thin films deposited by atomic vapor deposition.* Applied physics letters, 2012. **101**(11): p. 112903.

45. Ahn, S.-l., Y. Noguchi, M. Miyayama, and T. Kudo, *Structural and electrical characterization of Bi5Ti3Fe1-xMnxO15 system.* Materials Research Bulletin, 2000. **35**(6): p. 825-834.

46. Keeney, L., C. Groh, S. Kulkarni, S. Roy, M.E. Pemble, and R.W. Whatmore, *Room temperature electromechanical and magnetic investigations of ferroelectric Aurivillius phase Bi5Ti3 (FexMn1− x) O15 (x= 1 and 0.7) chemical solution deposited thin films.* Journal of Applied Physics, 2012. **112**(2): p. 024101.

47. Martin, L.W., S.P. Crane, Y.H. Chu, M.B. Holcomb, M. Gajek, M. Huijben, C.H. Yang, N. Balke, and R. Ramesh, *Multiferroics and magnetoelectrics: thin films and nanostructures.* Journal of Physics-Condensed Matter, 2008. **20**: p. 434220.

48. Lomanova, N.A., M.I. Morozov, V.L. Ugolkov, and V.V. Gusarov, *Properties of aurivillius phases in the Bi4Ti3O12-BiFeO3 system.* Inorganic Materials, 2006. **42**(2): p. 189-195.

49. Suarez, D.Y., I.M. Reaney, and W.E. Lee, *Relation between tolerance factor and Tc in Aurivillius compunds.* J. Mater. Res., 2001. **16**(11): p. 3139-3149.

50. Glazer, A.M., *The Classification of Titled Octahedra in Perovskites.* Acta Cryst., 1972. **B28**: p. 3384-3392.

51. Hervoches, C.H., A. Snedden, R. Riggs, S.H. Kilcoyne, P. Manuel, and P. Lightfoot, *Structural Behavior of the Four-Layered Aurivillius-Phase Ferroelectrics SrBi4Ti4O14 and Bi5Ti3FeO15.* J. Solid State Chem., 2002. **164**: p. 280-291.

52. Lomanova, N.A., V.G. Semenov, V.V. Panchuk, and V.V. Gusarov, *Structural changes in the homologous series of the Aurivillius phases Bin+1Fen−3Ti3O3n+3.* Journal of Alloys and Compounds, 2012. **528**(0): p. 103-108.

53. Sanson, A. and R.W. Whatmore, *Properties of Bi4Ti3O12-(Na1/2Bi1/2)TiO3 Piezoelectric Ceramics.* Jpn. J. Appl. Phys. Part 1, 2002. **41**(11B): p. 7127-7130

54. Sanson, A. and R.W. Whatmore, *Phase Diagram of the Bi4Ti3O12–BaTiO3–(Na1/2Bi1/2)TiO3 System.* Journal of the American Ceramic Society, 2005. **88**(11): p. 3147-3153.

2. Methods and Techniques

This chapter aims at giving an overview of the techniques (**2.1**) and methods used: **2.2** patterning methods and the advantage of using a focused ion beam, **2.3** correlative microscopy including 3D, **2.4** a short introduction into EDX used for **2.5** the statistical approach to EDX analysis in analytical electron microscopy and **2.6** details of the microstructural analysis of the multiferroic Aurivillius phase thin films and observed inclusions.

2.1. Techniques

FIB patterning The FIB system used in the current study is the FEI Helios NanoLab 600i, which is a dual beam FIB for localized milling and deposition, transmitting a beam of Ga^+ ions combined with a high resolution SEM. In the work on stainless steel patterning, the working current was tuned between 0.28 nA (for 120 nm pits) up to 0.92 nA (180 nm) depending on size of the nano-texture. The available pit sizes and the large range of obtainable working currents could make the FIB technique an ideal device for nanomachining in the range from 10 nm to a few micrometres. Nano-structured features (pits/holes) ordered in rectangular arrays were patterned on 316L steel surfaces.

Samples for serial sectioning of stainless steel were prepared in the FEI Helios NanoLab 600i using protective carbon and Pt layers [1]. The electron beam induced (EBID) carbon deposition supplied necessary contrast difference between the protective Pt and the stainless steel surface, hence enabling accurate determination of the concave's shape and depth

EBSD technique was used to analyse the crystallographic structured surfaces of the polished stainless steel. EBSD imaging was performed in a Hitachi SEM SU-70 equipped with an Oxford Instruments EBSD attachment AztecHKL at 10kV under 70° tilt angle and step size 2µm. Initial top-down SEM imaging was used to analyse the topography of nano-textured surfaces of the polished stainless steel.

An AFM (MFP 3DTM, Asylum Research) in AC mode was used for topography mapping of the surfaces. Olympus AC160TS silicon cantilevers (Al reflex coated, ~300 kHz resonant frequency) were used for imaging. Optimal results were achieved with a medium scan rate of 1 Hz and 256 x 256 pixels image resolution.

Topography Mapping: HR-SEM images and EDX analysis spectra were obtained using a FEI Quanta 630 High Resolution Scanning Electron Microscope with attached Oxford X-Max 20 detector and Inca analysis software. A commercial atomic force microscope (MFP-3D^{TM}, Asylum Research) in AC mode, equipped with Olympus AC160TS silicon cantilevers (Al reflex coated, ~300 kHz resonant frequency), was used for topography mapping of the films. Cross-sections of the films were prepared for micro-structural analysis using a FEI DualBeam Helios NanoLab 600i Focussed Ion Beam (FIB) (final thinning at 93 pA 30 kV, final polish 2 kV 28 pA). Micro-structural analysis was performed on the B6TFMO films using HR-TEM (Jeol 2100 transmission electron microscope; 200 kV; double tilt holder) in conjunction with selected area electron diffraction (SAED). Note that normally ~10% error should be accounted for when calculating *d*-spacings from SAED due to electron optics of the instrumentation. Elemental mapping using EDX (Oxford X-Max 80 detector and Inca analysis software) over larger sample areas (3.99 μm^2 to 1 mm^2, medium spot size, x-ray generation area 10-30 nm in diameter, 200 nm thickness) was performed using the HR-SEM and STEM mode at the FEI Helios Nanolab.

Surface EDX mappings and cross section sample preparation required a thin Au coating (< 20 nm) to reduce the high surface charging of the B6TFMO films. After the Au sputter coating a 60 nm layer of amorphous carbon and 300 nm Pt layer were deposited within the DualBeam FIB by electron beam induced deposition and 2 µm thick Pt layer with ion beam induced deposition. These three layers have been grown for protection before the milling process. A 30 µm long lamella was prepared and thinned down to 40-60 nm for the TEM analysis. The thinning at 30 kV was finished by polishing at 5 kV and 2 kV to reduce the ion-beam induced damage to a less than 2 nm thin layer on both sides [2].

TEM analysis was done in a JEOL JEM-2100 operating at 200 kV in bright field condition for imaging and selected area electron diffraction (SAED) mode to record diffraction pattern of single grains. Crystal Studio was used to determine the crystal structure by comparing the simulated electron diffraction pattern with the recorded.

EDX measurements were recorded in the FEI Helios NanoLab 600i operating at 20 kV and 1.4 nA with an attached Oxford X-Max 80 detector. The spectra were analysed with the Inca software.

2.2. Correlative Microscopy including 3D imaging

The principal concept of correlative microscopy calls for analysis of one and the same volume of interest by two or more imaging techniques. Subsequently, the signals recorded by different imaging modes are merged together to obtain unique information that is difficult to acquire with a single imaging regime. Correlative light and electron microscopy has been the most widely used technique until now featuring two imaging modes in one instrument. Other emerging correlative microscopy techniques include AFM-TEM, SNOM-TEM, AFM-nanoSIMS, TEM-atom-probe microscopy which use dedicated platforms to localize one and the same volume of interest for analysis.

Historically correlative microscopy is commonly referred to as correlative light and electron microscopy (CLEM), a technique used mainly for biological materials. The oldest reference to CLEM dates back to the 1960s.[3, 4] In those beginnings the correlation was far from a simple process with hours spent to find the same region again in the light or electron microscope as the techniques were not yet incorporated in one system. Thus, it took nearly

three decades until correlative microscopy gathered momentum in the 1990s. Though samples still have to be transferred between light and electron microscopes CLEM has been established as standard method with dedicated workshops and improvements in hard- and software only within the last ten years.[5, 6]

Although many different microscopy techniques are incorporated by now, like fluorescence microscopy, (laser scanning) confocal microscopy, cryo-TEM and advanced techniques like 3D structured illumination microscopy and spinning disk laser scanning microscopy, the limitation of the term 'correlative microscopy' to biomedical research is still dominant with many review papers within the last few years written on this topic. [7-10] Even the results chapter of this thesis will start out in this area with the surface patterning of stainless steel for potential application in cardiovascular stents, yet concentrating the correlative microscopy clearly on the inorganic materials side.

An advanced characterisation protocol for analysis of the structures aiming at comprehensive evaluation **(Fig 2.1)** of the 3D shape of the patterned arrays as function of SS crystal structure using a combination of Electron Backscatter Diffraction (EBSD), FIB, Scanning Electron Microscopy (SEM), Atomic Force Microscopy (AFM), serial FIB-SEM sectioning and transmission electron microscopy (TEM) in bright field, dark field and selected area electron diffraction mode is attempted in the ***Results (3.1.3)***.

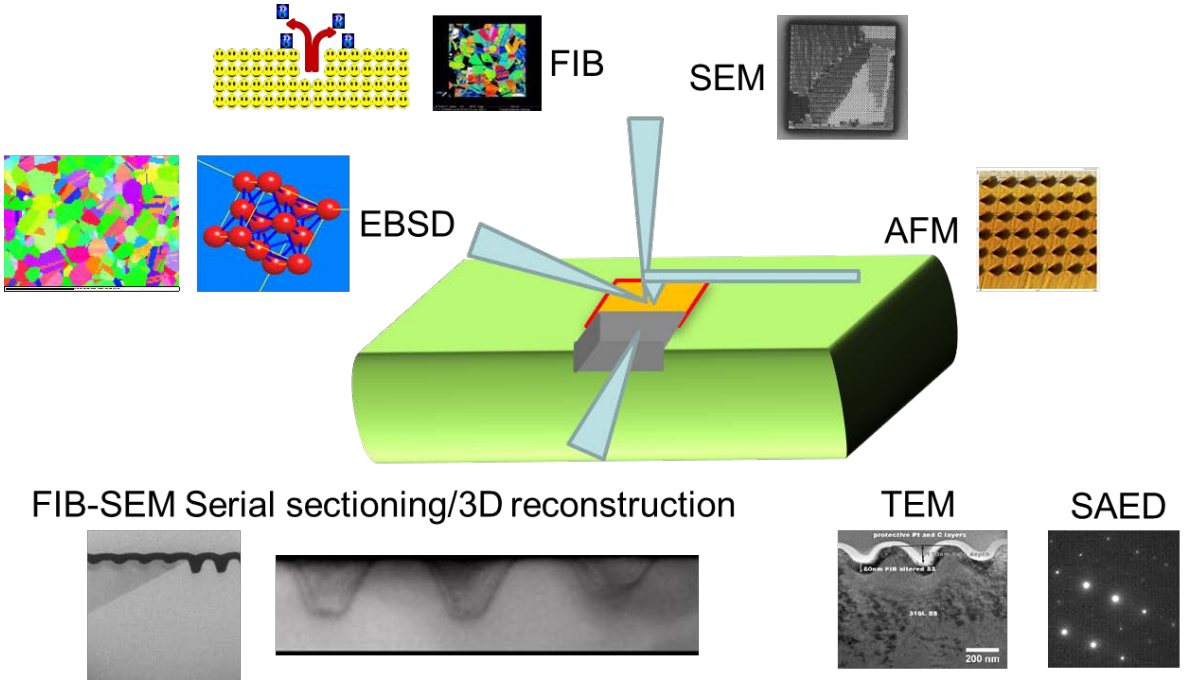

Figure 2.1. Complementary analysis techniques on the exact same sample location

In particular, EBSD is an SEM based non-destructive microstructural technique that uses Kikuchi patterns to measure individual grain orientations, local texture, point-to-point orientation correlations and phase identification and distributions on the surfaces of bulk polycrystals. It is performed using the electron beam of an SEM as beam source. The SEM gives the possibility of generating maps of the crystal orientations for polycrystalline material. EBSD patterns are generated on a phosphor screen by backscatter diffraction of a stationary beam of high energy electrons from the typically 70° tilted sample surface. Because of the high tilt angle this technique is very surface sensitive and gives information of the top 10-50 nm down into the substrate [11]. A disadvantage of this technique could be seen in the long time that it takes to collect a large map at high resolution which takes several hours.

AFM is also a non-destructive surface sensitive technique (with the information coming only from the top few atomic layers up to a few nm) that can be operated in three basic modes,

contact, tapping and non-contact-mode. The vast range of cantilevers, different attachments, modifications and extensions opens up another realm of information due to the multitude of signals that can be collected from the AFM: topography, phase, magnetic properties, surface potential to name just a few. As with EBSD the main disadvantage of this method could be seen in the long time taken for high resolution mapping, taking in some cases hours to stabilise the cantilever alone.

SEM is the third non-destructive technique mentioned above. Conductive samples like stainless steel do not need any preparation to be imaged at high resolution within minutes. And with the advent of environmental SEMs and beam deceleration even non-conductive samples can easily be imaged without further preparation, otherwise a conductive coating needs to be applied to ground the sample properly to be able to conduct the incoming electrons away.

FIB is at the edge between destructive and non-destructive. If a modification of the top 10-50 nm through the ion bombardment does not alter the main characteristics of the sample it could still be considered as non-destructive. Usually though the surface amorphisation and incorporation of Ga^+ ions are regarded as destructive which is the main disadvantage of this method. Otherwise FIB offers advantages over SEM of a higher secondary electron yield that leads to even faster imaging and contrast enhancement in polycrystalline material because of the above mentioned channelling effects.

Serial FIB-SEM sectioning, also known as slice-and-view, then is truly destructive. As the name implies the sample is destroyed by taking slice after slice off a cross section and imaging with the SEM after each slice. This is a long process stretching over several hours, yet the information gained is compared to the aforementioned techniques three dimensional rather than 2D. With software programs like ImageJ or Amira it is possible to reconstruct a

full 3D model of the examined volume. This can be further enhanced by EBSD and elemental analysis though the analysis time goes up even higher by adding these techniques. Another disadvantage is the extensive sample preparation for serial FIB-SEM, which starts by protecting the sample surface with layers of electron beam deposited Pt or similar and usually cutting a trench around the sample volume to be analysed to enhance secondary electron yield and make 3D reconstruction simpler (by defining the volume at the start).

TEM is the other destructive method described here, though technically it is only destructive for bulk materials that need extensive sample preparation to make a thin foil that is electron transparent. TEM is on the other hand very versatile giving access to much information about the material structure down to single atom resolution[12, 13]. The basic modes of operation are bright field (BF), dark field (BF) and (selected area) electron diffraction ((SA)ED). A further very common feature is the scanning TEM (STEM) which again opens another universe of analytic techniques. While in BF imaging matter appears dark and vacuum brighter, DF is complementary where the direct beam is blocked and only one or more diffracted beams allowed to pass the objective aperture to form the image. DF is very useful in combination with SAED in which the reflections for (poly)crystalline materials are shown (amorphous materials will show rings instead of defined reflection dots). Then one reflection is chosen using the objective aperture to obtain an image of the crystal region that the reflection belongs to. The pattern created by SAED are useful to gain insight into the crystalline structure of the material in question in the first place. The recorded pattern can be compared with simulated pattern created by software like Crystallographica, Crystal Studio or Crystal Maker to determine the material composition and the orientation of the sample towards the electron beam during the ED imaging.

As described above many techniques reveal overlapping information that can be used for a better cross correlation of the recorded data. The additional complementary information

gained by each individual method is promising to give a full view of the surface structure in 3D.

2.3. Surface patterning with a focus on Focused Ion Beam and medical grade stainless steel

As the name implies nano-texturing involves the creation of patterns or features with nanometre precision. In the context of this thesis the focus is laid on patterning methods that are most useful to create a flexible platform for future cell studies on stainless steel. Recent advances in micro- and nanotechnology have allowed the patterning of surfaces with the desired textures for cell scaffolding [14-17]. The choice of the texturing method depends largely on the nature of the substrate that needs to be modified and on the dimensions of the features expected. Indeed, photolithography was particularly successful for the patterning of features of microscopic dimensions on elastomers such as polydimethylsiloxane (PDMS) [18-21] and on polymers such as polystyrene (PS) [22-25]. E-beam lithography is used for many years for the patterning of sub-micron features on silicon substrates [26, 27] and on Poly(methyl methacrylate) (PMMA) [28]. Features of 350 nm were patterned on PDMS and PMMA substrates by nano-imprint lithography [29]. Metal substrates such as Ti, were also textured using micro-machining for feature dimensions in the microscopic range [30, 31]. Cell adhesion, migration, elongation, proliferation and gene expression on textured substrate can be greatly altered depending on the shape and the dimension of the features [28].

The different techniques are compared in **Tab. 2.1**. In indirect photolithography methods, patterns are formed over a large area using a mask [32]. Such lithography processes are time-consuming with many steps, and inherently inappropriate for prototype designs and

processes. Electrodeposition is a simple, fast and cost-effective method of reproducing nano-structures on many materials using templates made of polymers and metals. However, this method is applicable only for electrically conductive substrates. Imprint lithography is a high resolution direct technique for nano-patterning of large surfaces, but it requires moulds and is restricted to polymeric materials [33], but this could then be used as etch masks or filled with metal electrodeposition. E-beam lithography and lithography based on scanning tunnel microscopy (STM), atomic force microscopy (AFM) or dip pen are high-resolution mask-less procedures, but with a very low throughput and unsuitable for wide surface nano-patterning [34]. Interference lithography can be utilized to create or transfer array patterns on various metallic and polymeric surfaces, but only patterned features can be reproduced. Microtexturing of surfaces has also been reported by pulsed laser patterning [35, 36]. The feature sizes are however limited to the micron range.

Patterning by FIB milling is direct and offers several advantages for flexible prototyping practically any sufficiently conductive substrate material that is able to withstand high vacuum conditions of the microscope chamber, there is high flexibility in the obtainable shapes and geometries by modulating the ion beam current and the patterning conditions, reduced complexity of the pattering process e.g. it is a single-step process with a possibility of real-time monitoring of the milling progression. Thus for any particular type of substrate, various depths as well as lateral dimensions including the optimal feature size can be obtained with high degree of flexibility at minimum number of processing steps.

Table 2.1: Advantages and drawbacks of indirect and direct nano-structuring techniques

Mask/ molds require	Technique	Advantages	Drawbacks

Yes	Photolithography	Well controlled features High throughput	Requires photoresist, spin coaters and organic solvents Low aspect ratio Limited to set of materials
	Electrodeposition	Precise geometries and patterns Large surface area	Require templates for creating of nano-structures Limited to electrically conducting substrates
	Imprint lithography	High resolution High aspect ratio Large surface	Requires molds Applied to polymers only
No	E-beam	High resolution Precise geometry and patterns	No direct writing on substrate – etching required Multi-step process Low throughput Requires vacuum Time consuming Small surface coverage Expensive
	Interference lithography	No complex optical systems	Limited to patterned array features only Multi-step process

	STM / AFM / Dip pen	Very high resolution	Low aspect ratio Very low throughput Very small surface area
	Nanoindentation	High aspect ratio Control over features depth Less expensive than FIB or e-beam writer	Wide and shallow features Slow process
	Laser patterning	Any material High throughput with high power laser	Wide and shallow features Micron resolution
	FIB milling	High resolution High aspect ratio High etch rate Any material	Time consuming Process requires vacuum Very expensive Low throughput

Except FIB, none of the texturing techniques mentioned above were suitable to achieve features in the nanoscopic range on a hard substrate as 316L stainless steel. Nanoimprint lithography (NIL) and e-beam lithography (EBL) are able to pattern sub-micron features, which with NIL were achieved on soft substrates such as polymers and elastomers only, and with EBL is a very time consuming and expensive multi-step process. The preeminent advantage of FIB is its flexibility. In this research work, FIB milling was used to create nano-structures onto stainless steel because it is a direct writing process with simple steps, high

resolution and aspect ratios. The goal of the study was to identify optimal FIB patterning conditions for achieving reasonably high throughput (patterned rate of about 0.03 mm^2 per hour) and nano-size accuracy in dimensions and shapes of the features.

As the name implies FIB systems employ a finely focused ion beam (usually gallium ions (Ga^+)). Depending on the current used it can be operated for milling (at high beam currents) or imaging (low beam currents). Material is sputtered when the high-energy ions hit the sample surface. Primary Ga^+ atoms are also implanted into the sample surface. This is limited to 10-50 nm depending on the sample material. **Fig. 2.2** illustrates the interaction of the primary Ga^+ ion beam with the sample surface. Secondary electrons are also generated during the interaction which can be used to form images. This is especially helpful when the top surface layer can be sacrificed as the yield of secondary electrons is much higher than from incident electron beams and a 5 nm resolution can be attained. [37, 38]

Programs exist to simulate and model the interaction of ions with matter, called Stopping and Range of Ions in Matter (SRIM).[39, 40] These are widespread in the ion implantation research community due to their universality based on binary collision approximation (a Monte Carlo simulation method). Given the ion type and energy and the type of target, it can produce 3-dimensional distribution maps of ions in matter and its parameters like penetration depth, sputtering rate and concentration of vacancies to name just a few. For the case of interaction with polycrystalline stainless steel however its usefulness is severely limited as it does not take channelling effects and crystal structure into account.

Channelling effects happen in crystalline materials where the incoming ions can follow certain crystallographic directions easier than others. The atomic distances in low index oriented crystals are larger, hence the ions can travel deeper into the material before losing

their momentum. This leads to reduced sputtering along low index facets. As will be shown in the results section this is not a negligible effect with the polycrystalline stainless steel.

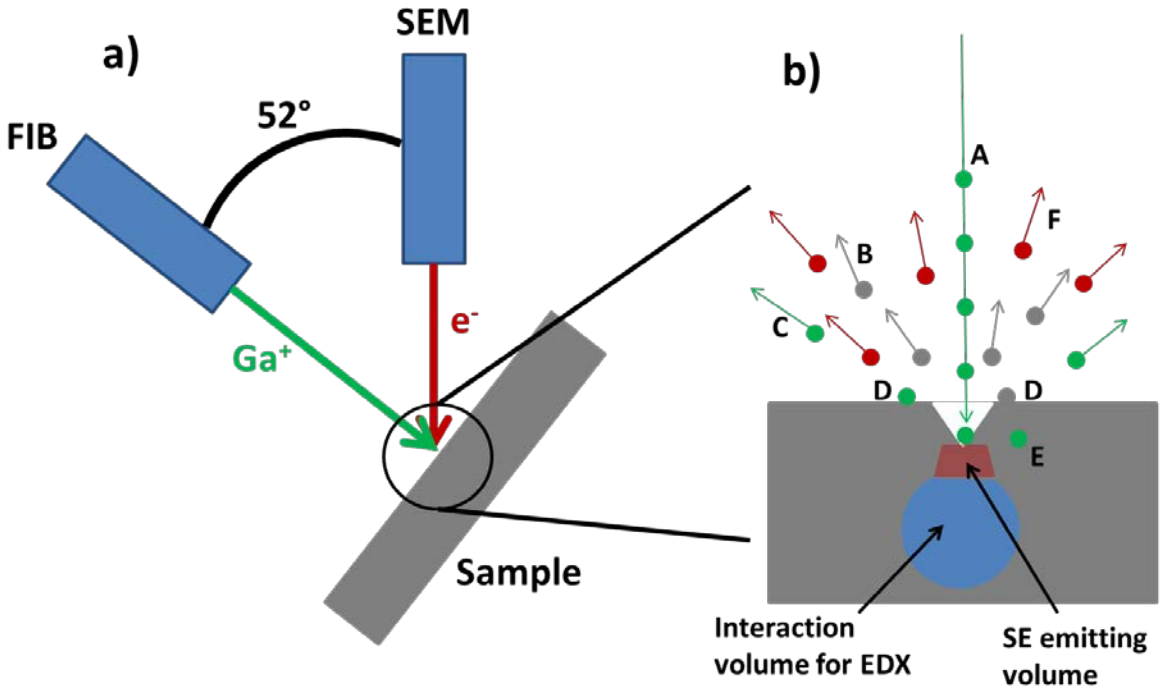

Figure 2.2: a) DualBeam FIB schematics. b) beam sample interactions: A – incident Ga+ ions, B – sputtered substrate atoms, C – scattered Ga^+ ions, D – re-deposited Ga+ ions and substrate atoms, E – in substrate trapped Ga^+ ions, and F – secondary electrons. Also depicted are the interaction volume for characteristic X-rays (EDX signal) in the sample (light blue) and the surface near volume from which the secondary electrons are emitted (light red which forms also part of the interaction volume of course).

FIB originated in the semiconductor industry and has become an important tool for a wide array of applications, ranging from circuit editing, reverse engineering, sample preparation for transmission electron microscopy (TEM), microstructural analysis and prototype nanomaching to name just a few [41]. Many modern FIB instruments supplement the FIB column with an additional SEM column so that it becomes a versatile dual-beam platform as depicted in **Fig 2.2**. In nano-patterning, FIB has been used to create nano-structures on Si

[42], silicon nitride [43, 44] and glass substrates [45] and to fabricate platinum nano-structures on peptide based soft surfaces [46].

2.4. EDX analysis

As EDX analysis plays such a vital role in this study it is explained in this subchapter separately including some raw data. EDX is an established technique used to characterise the elemental composition of samples in the EM. Opposite to X-ray machines used in medical and material imaging that use the broad Bremsstrahlung for high intensity beams, EDX exploits the fact that the X-rays that are generated when an orbiting electron is displaced by an electron of the microscope beam are at characteristic energies for each element. [47]

The Oxford Instruments EDX system used in this study makes use of a silicon drift detector (SDD) which has an energy resolution of 130-170 eV in the region 6-11 keV that was used to identify Fe, Mn and Bi. **Fig 2.3** shows a typical sum spectrum for a 72h surface scan normalised in counts per second (cps). The process time was set to a medium level 4 which produced a dead time in the range of 30% as is typical for SDDs for the e-beam current of 1.4 nA that was found optimal between signal height and spatial resolution. In this condition the lifetime of the spectrum was about 200,000 s with a total count of 5×10^9 counts over 72 hours.

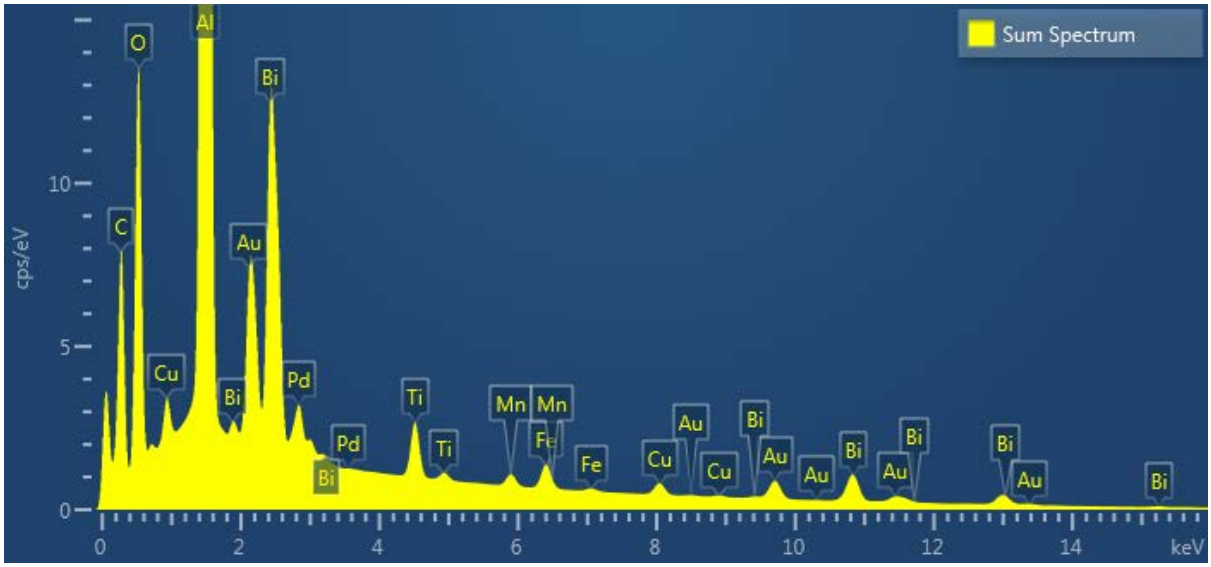

Figure 2.3. Typical sum spectrum of sample B6TFMO for a 72h surface scan normalised in counts per second (cps).

For the subtraction method described in detail in **3.2.2** the element characteristic lines shown in **Fig 2.4** have been used that showed as little overlap as reasonable. After application of the subtraction method described in **3.2.2** spot spectra of Fe rich and Fe + Mn rich could be compared in **Fig 2.5**.

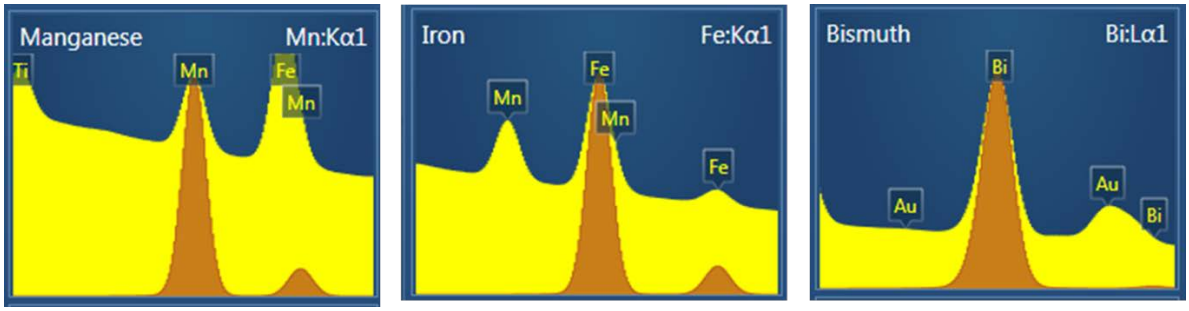

Figure 2.4. Characteristic lines for the elements used in the subtraction method, Mn Kα1 at 5.90 keV, Fe Kα1 at 6.40 keV and Bi Lα1 at 10.84 keV.

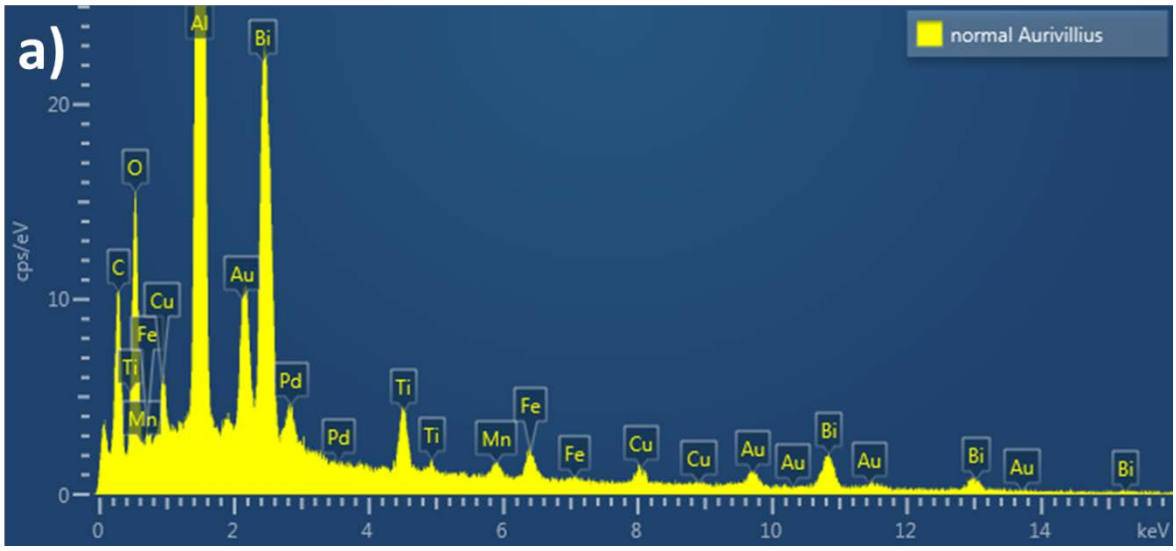
a)
normal Aurivillius
cps/eV
keV
O
C
Cu
Fe
Ti
Mn
Al
Bi
Au
Pd

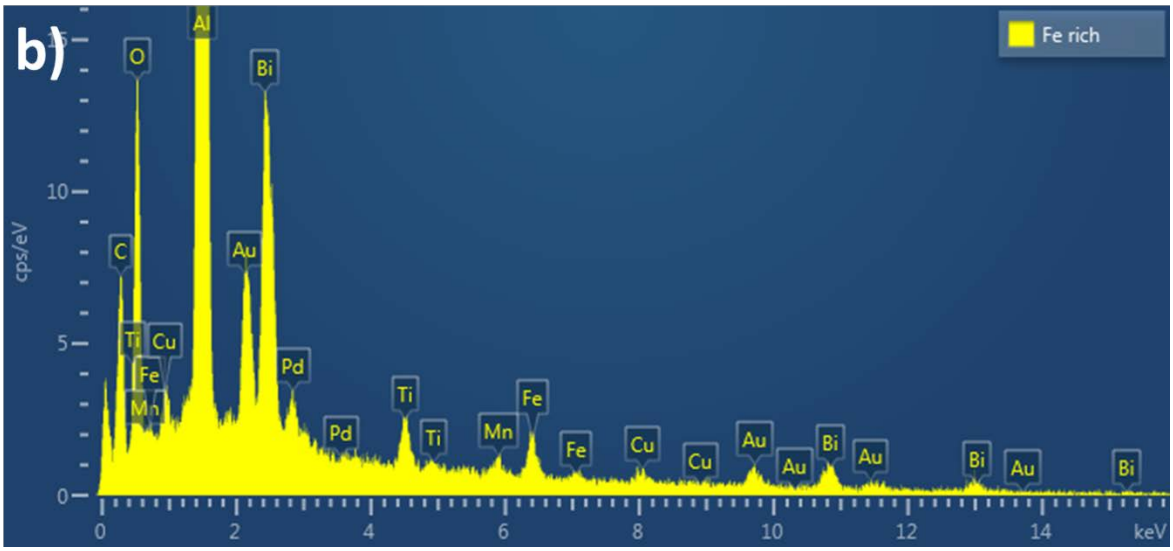
b)
Fe rich
cps/eV
keV
O
C
Ti
Cu
Fe
Mn
Al
Bi
Au
Pd

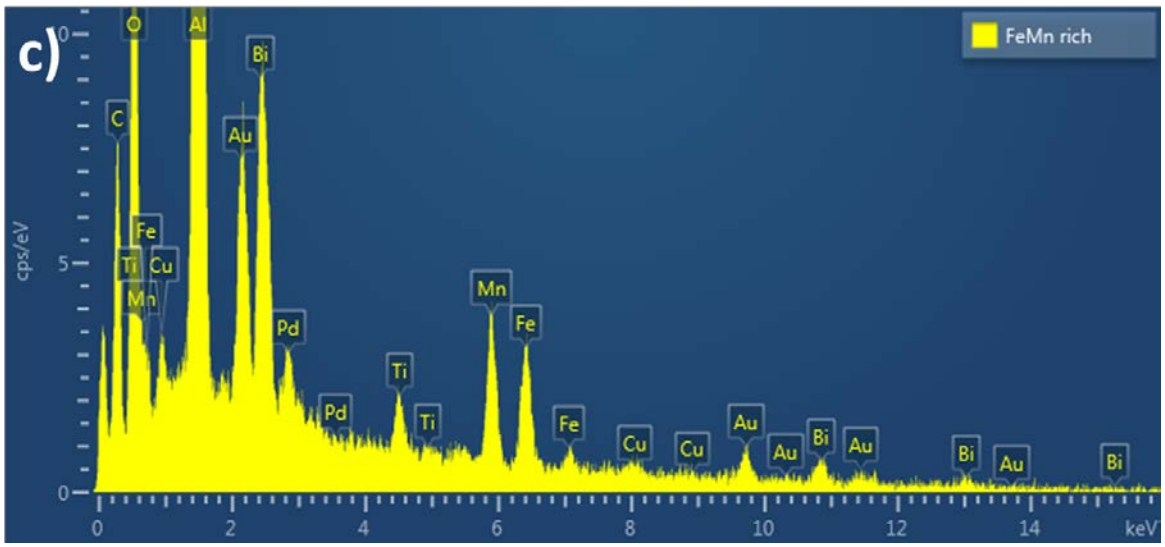
c)
FeMn rich
cps/eV
keV
O
C
Fe
Ti
Cu
Mn
Al
Bi
Au
Pd

Figure 2.5. Spot spectra of a) normal Aurivillius phase B6TFMO, b) Fe rich area and c) Fe and Mn rich area

Two points are to be considered when comparing these spot spectra: I) The large interaction volume in which characteristic X-rays are generated (for the 20 kV normally used the volume equals a pear shaped sphere with approx. 2 µm diameter in in this material) would render these spectra quite useless for localisation of nm sized inclusions. II) The low thickness of the thin B6TFMO layer of 200 nm increases the spatial resolution again. However, as the subtraction method makes use of spatial differential anti-correlation between Fe, Mn and Bi, local spot spectra have not been used in the statistical approach described in the following chapter.

2.5. Statistical approach to EDX analysis of trace inclusions

"Absence of Evidence is not Evidence of Absence" is a truism which confounds many analytical assertions. The confident statement of certainty: "There was nothing there" leads to the obvious retort: "How do you know?". In many analyses, especially those using microscopes (optical or electron), it is only possible to look at restricted volumes, and the smaller the inclusion, or defect, or the lower the level of the impurity being sought, the smaller the volume that can reasonably be examined. The absence of any evidence for second phases, defects or impurities in these volumes can lead to the erroneous conclusion (perhaps driven by wishful thinking) that there are none in the sample as a whole, when in fact all that can be asserted with certainty was that there was nothing in the volumes examined at the limit of resolution for the technique used. And yet all is not lost, because if the detection thresholds of a particular method are well understood, the volumes examined

are known and one makes some justifiable assumptions about the size distributions of second phase particles being sought, then one can apply statistical methods to determine the confidence level that surrounds such a statement. In other words, one can convert the assertion of "certainty-of-absence" to one which gives a level of probability that the density of the sought-for impurity or second phase inclusion is below a certain critical level. Conversely, it is possible to apply such methods to the design of experiments which will yield any required level of confidence. For example, it is possible to say that if one requires a confidence of 99.5 % that the density of a certain impurity or defect of known composition and/or size is below a certain critical level in a specimen, then given the sensitivities of the analytical methodologies being used, the statistical analysis can be used to determine how large a total volume needs to be examined.

If one considers different examples of materials analysis, there are different cases according to whether one is searching for impurity elements in a simple, single element material like silicon, trying to detect inclusions which are widely different in composition/structure from the parent matrix or looking for second phases that are similar in composition and/or structure to the parent. If the material is a pure element like silicon, for instance, claims with respect to a given level of purity can be verified relatively easily by using a host of different techniques such as SIMS (secondary ion mass spectrometry), ICP-MS (inductively coupled plasma mass spectrometry), EPMA (electron probe micro analysis) or Auger Spectroscopy and the level of impurities can be determined down to the level of ppb [48-52]. On the other hand, there are scanning methods which can locate inclusions and structural defects [53, 54], but, as commonly used, these are generally limited to detecting a minimum amount of 1-2 weight% of a particular inclusion type [55]. Atom probe tomography (APT) [56] and scanning transmission electron microscopy (STEM) coupled with energy dispersive X-ray spectroscopy (EDS/EDX) [57] and/or electron energy loss spectroscopy (EELS) [58, 59]

provide techniques which can resolve single atoms spatially and elementally, but are limited to very small sample volumes (areas of a few nm^2 within a single atomic layer such as graphene film for example). Hence they cannot deal with a statistical distribution of small numbers of such entities dispersed over tens of μm^3. There is a significant probability that the examination of a small volume of material at the high detail needed to see such very small inclusions may easily miss them, simply because they are not present in the particular volume of material examined. In such a case it is prejudicial to say that such defects or inclusions are not present in the sample - one can only put a probability upon them for their density being below a certain critical level.

On the other hand, an aggressive search for new materials is in progress and the development of single-phase multiferroic (simultaneously ferromagnetic and ferroelectric) oxides is a good example of this. These materials are of considerable interest for future memory and sensing applications [60-66]. Here, the assertion that a new material is a single-phase, room-temperature multiferroic may be confounded by the presence of second-phase ferromagnetic inclusions that may have formed during the sample preparation. This is the single most critical factor in the analysis of such materials because the magnetic properties of the sample overall are highly susceptible to the presence of such inclusions. The difficulty in excluding second phase inclusions as being responsible for any observed ferromagnetism of a given sample is that some of the elements used to form the main phase could easily be responsible for formation of a ferromagnetic second phase. The differences between main and second phases could be in stoichiometry and/or crystal structure and both factors may have influence on the magnetic behaviour.

This thesis demonstrates an original methodology for the detection, localization and quantification of second phase inclusions in thin Aurivillius type films. Even when the

compositional differences between inclusion and main phase are rather subtle, this methodology provides a viable approach to not only identifying the inclusions but also to their localization and further in-depth structural investigation.

The goal was to develop a dedicated statistical model applied to the design of the analytical (EDX) measurements and demonstrate its application to the analysis of $Bi_6Ti_{2.8}Fe_{1.52}Mn_{0.68}O_{18}$ (B6TFMO) thin films. A detailed account of the sample preparation, transmission electron microscopy (TEM) and energy dispersive X-ray analysis (EDX) that was necessary to put a high, defined confidence level (> 99.5 %) to the statement of 'new single phase multiferroic material' is presented in the ***Results (3.2)***.

2.6. Microstructural Analysis of Multiferroic Aurivillius Phase Thin Films and Observed Inclusions

One of the samples studied during this thesis – a thin films of Aurivillius phase $Bi_6Ti_{2.8}Fe_{1.52}Mn_{0.68}O_{18}$ – gives a distinct room temperature in-plane ferromagnetic signature (M_s = 0.74emu/g, H_c = 7mT). The microstructural analysis needed to conclude that the ferromagnetism does not originate from second phase inclusions is described in this chapter.

Chemical solution deposition processes were used to make $BiFeO_3$ and $BiMn_xFe_yO_3$ doped $Bi_4Ti_3O_{12}$ Aurivillius thin films on sapphire substrates. Two sols were formulated, with the intention of producing materials with m=6 (6 perovskite units per half cell). These possessed Ti:Fe:Mn ratios of 1:1:0 and 1:0.7:0.3 respectively. Considerable (17.5 mol %) excesses of Bi were used in both cases to suppress pyrochlore formation[67]. X-ray diffraction (XRD) demonstrated that both sols produced Aurivillius phase type thin films, with the film lattice parameters being a = 5.468, b = 5.472 and c = 57.554 Å for the first sol, evidently producing

an m=6 film - $Bi_7Ti_3Fe_3O_{21}$ (B7TFO). The second gave a = 5.497, b = 5.415 and c = 49.280 Å, clear evidence for an m=5 film, from an average sol composition of $Bi_6Ti_{2.5}Fe_{1.75}Mn_{0.75}O_{18}$ (B6TFMO). (Note that as a considerable excess of Bi is included in the sol, the minor changes in excess given by producing an m=5, rather than an m=6 film are not significant.) All diffraction lines could be indexed either to the relevant Aurivillius phase patterns, substrate peaks or CuKβ lines from the strongest main phase peaks. The thin films are predominantly *c*-axis oriented with a Lotgering factors[68], *f*, of 0.977 for B7TFO and 0.997 for B6TFMO. The 5-layered structure for B6TFMO was confirmed by High Resolution Transmission Electron Microscopy (HR-TEM) and electron diffraction. There are no detectable lines from spinel (or indeed any other) minor phases visible in the XRD patterns of the films - the strongest (311) spinel reflections would be expected at 2θ=35.4°. However, the noise level in any XRD scan places a limit on the detectability on such minor phases and the method is intrinsically unable to detect trace levels (typically 1-3 vol %) of strongly magnetic secondary phases which may affect the overall magnetization of the sample.[69] Clearly, detailed microstructural assessment is required for any sample of this type to exclude this as a possibility, and ideally to place a confidence level on that exclusion.

HR-SEM (high resolution scanning electron microscopy) images reveal the characteristic plate-like grain morphologies expected from Aurivillius phase materials. Multiple HR-SEM energy dispersive x-ray (EDX) surface scans (areas ranging from 900μm^2 to 1mm^2) showed an average film composition of $Bi_6Ti_{2.8}Fe_{1.52}Mn_{0.68}O_{18}$, which is slightly deficient in Fe and Mn relative to the sol. Neither a 2 hour HR-SEM-EDX area scan of a 26μm x22.6μm area (120μm^3 volume), nor a STEM (scanning transmission electron microscopy) EDX examination of a 30 μm long cross-section of thin film (1.2 μm^3 volume) produced any evidence of Fe-rich regions that might indicate possible evidence of low-level minor phases.

However, a 72 hour long HR-SEM-EDX data collection over a 1600μm^2 area, followed by subtraction of the Bi Lα from the Fe Kα and Mn Kα signals produced maps which showed areas of excess Fe and Mn for the B7TFO and B6TFMO films (**Figs 2.6(a),(b),(c)**). These maps showed extremely small amounts (~0.01 vol %) of FeO_x oxide inclusions in B7TFO and slightly larger amounts (~0.1 vol%) of a $Fe_xMn_yO_z$ phase in the B6TFMO with Mn:Fe ratio of 1.13:1 and a size of ~350nm. HR-STEM-EDX examination of the $Fe_xMn_yO_z$ inclusions demonstrated a composition of $Mn_{0.53}Fe_{0.47}O$. HR-TEM/SAED (selected area electron diffraction) (**Fig 2.6(e))** indicates a cubic structure with a lattice parameter of 4.4Å, that closely corresponds to that of a rock-salt-structure[70]. Magnetite (Fe_3O_4) and Jacobsite ($MnFe_2O_4$) structures can be excluded since the measured Mn:Fe ratio of 1.13:1 does not fit the compositions of these phases. Additionally, the space group Fd-3m (227) for Magnetite and Jacobsite does not fit the electron diffraction pattern obtained for the inclusions. The bixbyite phase ($Mn_{2-2x}Fe_{2x}O_3$ where x = 0.4-0.6) can also be discounted as the Ia-3 (206) spacegroup also demonstrates a different electron diffraction pattern from that obtained. Neither the angles of the reflections nor the lattice parameters of Fd-3m (227) / Ia-3 (206) fit in any direction to the electron diffraction pattern of the inclusions. A composition closely related to that of the inclusions, $Mn_{0.56}Fe_{0.44}O$ (Mangano Wüstite), has a cubic lattice with the space group Fm-3m (225)[70, 71]. It should be noted that this rock-salt composition is non-ferromagnetic, and antiferromagnetic at low temperatures with a Neel point of ~150K[71]. The electron diffraction pattern captured for the $Mn_{0.53}Fe_{0.47}O$ inclusions fits simulations of this space group along the (110) direction perfectly[72] assuming micro/nano-twinning[73, 74] causes reflections at half positions. This assumption is strengthened by the observations in TEM dark field mode (**Fig 2.7**). In this technique the unscattered or zero order beam is excluded. Only electrons diffracted on crystal planes contribute to the formed image. **Fig 2.7** shows clearly that different diffraction spots in the summary SAED (**Fig 2.7(a)**) stem from

different micro/nano-crystals. In particular three regions nearly parallel to the substrate surface are discernable in different distances. Viewed from the substrate the bottom part is most visible in **Fig 2.7(a)**, the top part in **Fig 2.7(e)** and the interface inbetween in **Fig 2.7(f)**. A second random twinning in horizontal direction is also observable within the inclusion which is illuminated by the complimentary highlighting of different crystals in **Figs 2.7(d)** and **(g)**.

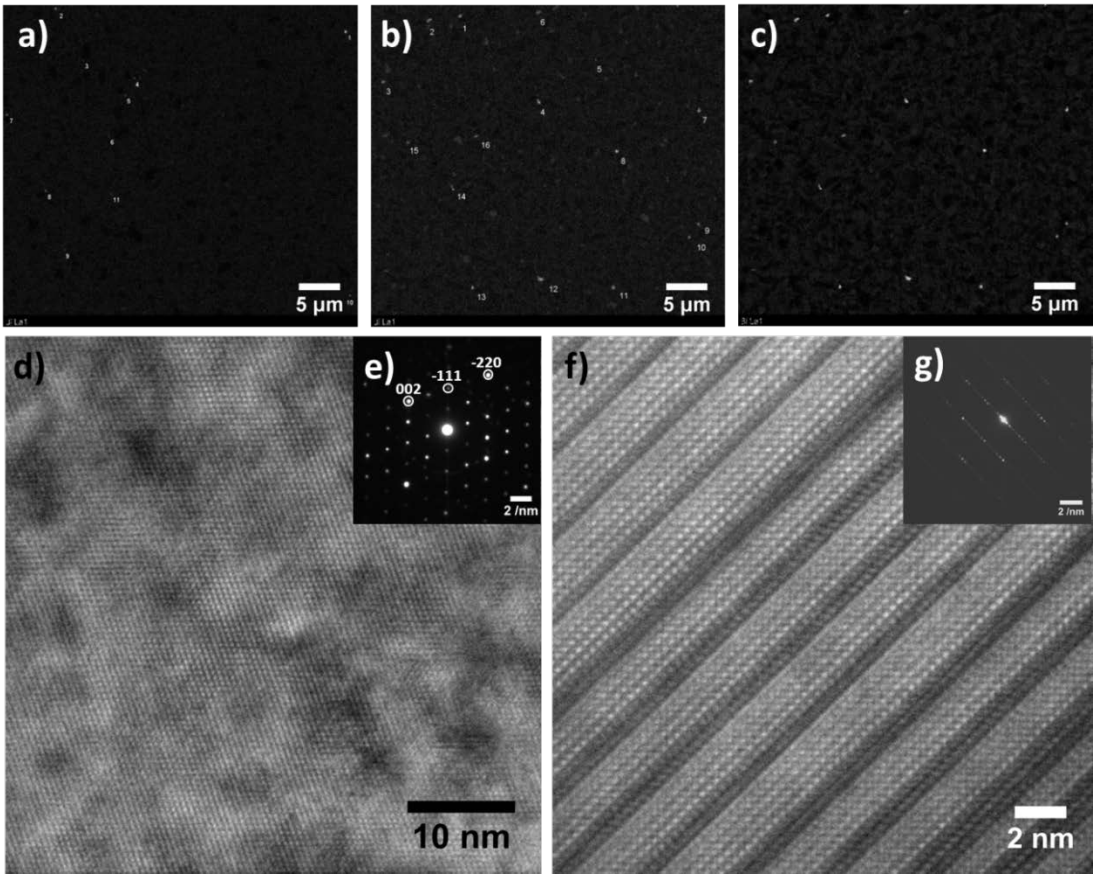

Figure 2.6. Compositional maps produced by extended period (72 hour) data collections from a 1600µm^2 sample area, followed by subtraction of the Bi Lα from the Fe Kα and Mn Kα signals. These show **a)** regions of excess Fe in B7TFO **b)** regions of excess Fe in B6TFMO and **c)** regions of excess Mn in B6TFMO. Note the one-to-one correspondence between the small, bright (numbered) regions showing Fe in **b)** and Mn excesses in **c)**. Note also the larger pale areas in **b)** corresponding to areas where the Fe content slightly exceeds

the surrounding grains. **d)** Cross-sectional HR-TEM image and **e)** diffraction pattern taken from a single $Mn_{0.53}Fe_{0.47}O$ inclusion. **f)** Cross-sectional HR-TEM image and **g)** diffraction pattern taken from a single higher-Fe content Aurivillius grain within B6TFMO.

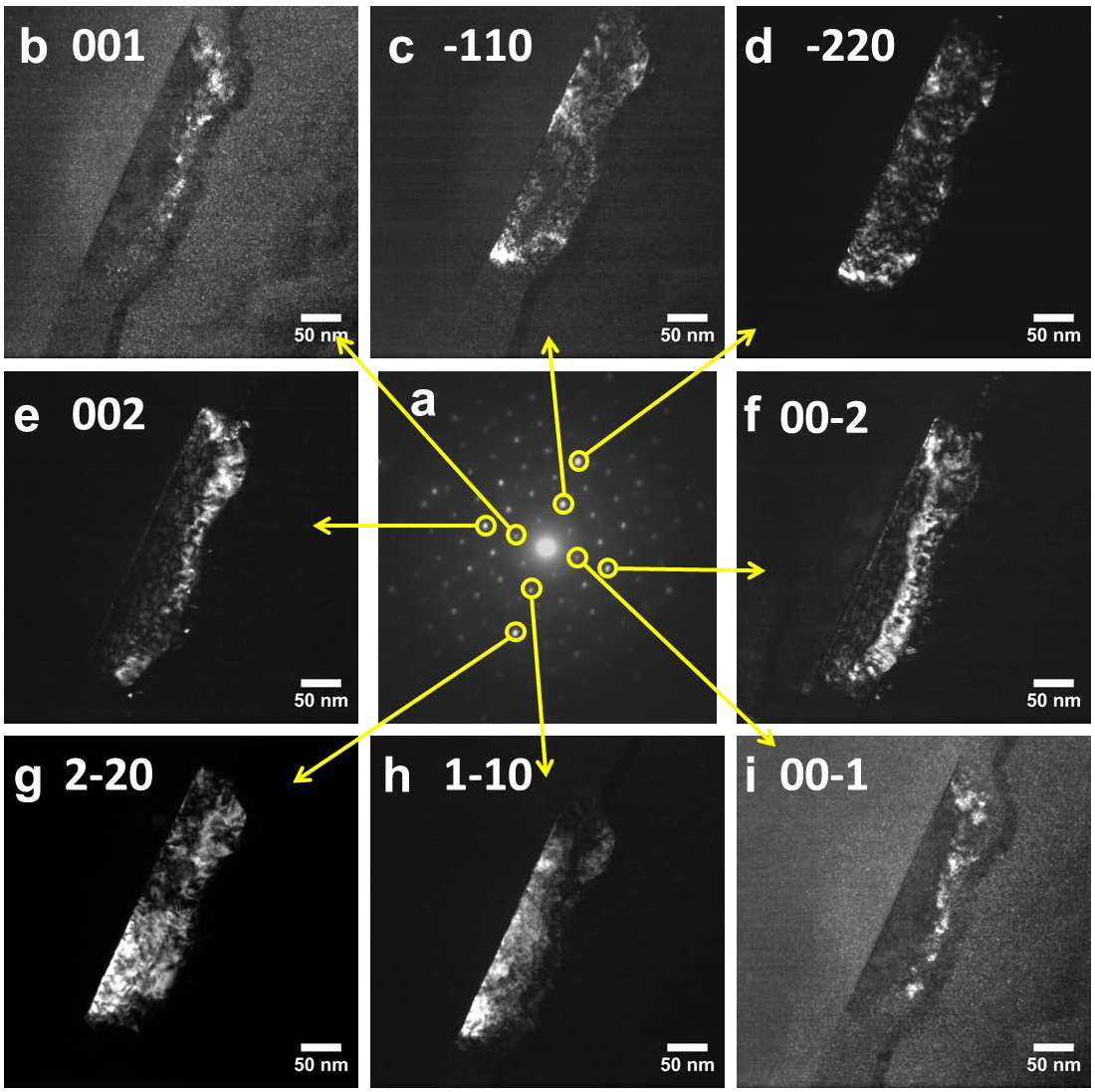

Figure 2.7. Dark field TEM analysis of a single $Mn_{0.53}Fe_{0.47}O$ inclusion. These show **a)** SAED pattern **b)** – **i)** dark field images taken from the spots indicated in a), crystal direction indicated in each image. The sapphire substrate is on the left side of the images.

Also visible in these surface HR-SEM-EDX maps were larger areas, similar in shape to the Aurivillius grains, where the Fe content slightly exceeded the surrounding grains. Detailed cross-sectional HR-TEM/SAED and HR-STEM-EDX examination of these grains (**Fig**

2.6(f),(g) and **Fig 3.19**) showed that they were *m*=5 Aurivillius-structured grains possessing a higher Fe content than the average of the film composition determined by surface area HR-SEM-EDX. A compositional survey by cross-section HR-STEM-EDX of 55 individual Aurivillius grains within the B6TFMO sample, followed by normalisation of the Ti:Fe:Mn ratios to give 5 octahedral B-site cations, showed a strong relationship between the Fe and Ti contents in these grains, with the Mn content being less strongly dependent on the Ti B-site composition (**Fig. 2.8(a)**). The range of grain compositions (ranging from Ti:Fe:Mn = 3.38:1.14:0.48 to 2.18:2.16:0.66) spans both the average compositions determined from the sol and the area EDX scan noted above. This graph helps to explain why a sol which was set-up to deliver an m=6 structure could produce an m=5 structure without large amounts of second phase appearing in the film. Mn is well-known for taking variable valency from 3-4 in perovskite oxide materials[75], and permitting non-stoichiometry to exist. As the Fe^{3+} replaces Ti^{4+}, it is suggested that Mn^{3+} is progressively oxidised to Mn^{4+}, to maintain charge balance. In this case, the proportion converted to the higher valence state is easily calculated and is plotted in **Fig 2.8(b)**. It is interesting to note that, while the Fe and Ti *B*-site compositions are strongly inter-dependent, the Mn composition within these grains does not vary systematically with either, averaging around 0.63, and the maximum Fe content of the *B*-site, at 1.77, occurs when all of the Mn^{3+} is converted to Mn^{4+}. It is believed that this has important consequences for the magnetic properties of the grains, as will be discussed below.

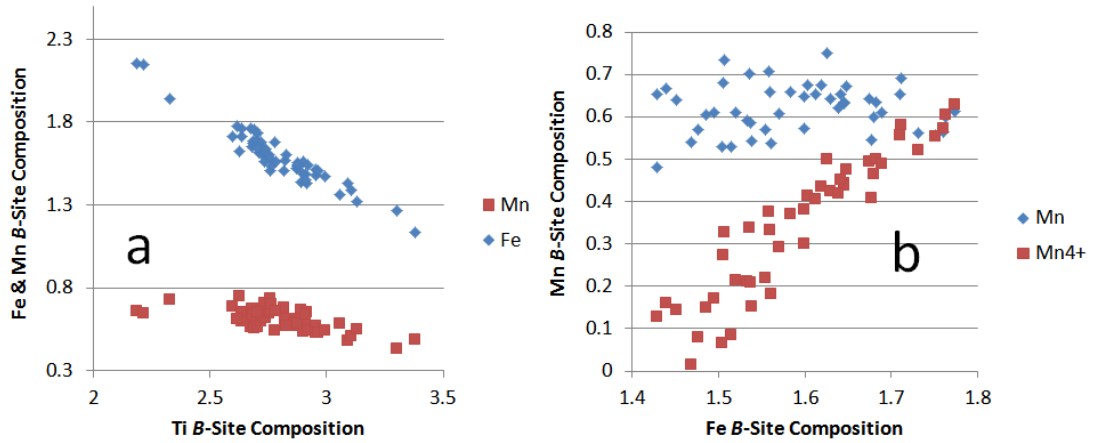

Figure 2.8. **a)** Plotting the normalised B-site composition of Fe and Mn vs that for Ti, as determined by cross-section HR-STEM-EDX from 55 Aurivillius grains within the B6TFMO sample. **b)** Plotting the total B-site Mn composition and B-site Mn^{4+} composition, calculated to maintain charge balance, vs the B-site Fe composition.

B6TFMO samples demonstrate in-plane ferromagnetic hysteresis between 2 to 300 K. A thorough microstructural phase analysis performed on the B6TFMO thin films showed no traces of ferromagnetic inclusions and a statistical analysis based on the volumes inspected placed a confidence of 99.5% that the observed ferromagnetism was not coming from unobserved ferromagnetic grains of spinel. Direct evidence for magnetic-field-induced ferroelectric domain switching at the nanoscale in a single phase magnetoelectric has been presented. The body of evidence reported here suggests that the higher Fe/Mn content grains with a composition of around $Bi_6Ti_{2.6}Fe_{1.77}Mn_{0.63}O_{18}$ are single phase room temperature magnetoelectric multiferroics. An explanation for the effect has been given based upon the Goodenough-Kanamori rule for super-exchange and the Mn largely being present as Mn^{4+}. These materials could find application to a wide range of new or improved devices and potentially meet future industry requirements in high density memory applications. Clearly, further work is now required which will include the direct measurement of the compositions

of the multi-ferroically switchable grains and x-ray photoelectron spectroscopy to determine Mn oxidation states (which failed so far), as well as the development of synthetic techniques to develop thin films in which all grains possess a composition around $Bi_6Ti_{2.6}Fe_{1.77}Mn_{0.63}O_{18}$, for which it is expected that higher remanent magnetizations will be achieved. Also the growth on other substrates that give better alignment of the thin films gives room for further studies, as well as studying the long-term stability of the films themselves as there are hints of sensitivity to prolonged exposure to light.

References

1. Giannuzzi, L. and F. Stevie, *A review of focused ion beam milling techniques for TEM specimen preparation.* Micron, 1999. **30**(3): p. 197-204.
2. Giannuzzi, L.A., R. Geurts, and J. Ringnalda, *2 keV Ga+ FIB milling for reducing amorphous damage in silicon.* Microscopy and Microanalysis, 2005. **11**(S02): p. 828-829.
3. Tamarin, A. and L.M. Sreebny, *The rat submaxillary salivary gland. A correlative study by light and electron microscopy.* Journal of morphology, 1965. **117**(3): p. 295-352.
4. Watari, N. and L. Herman. *Correlative light and electron microscopy of bat islets of Langerhans in hibernating and nonhibernating states*. in *American Zoologist*. 1965. AMER SOC ZOOLOGISTS 1041 NEW HAMPSHIRE ST, LAWRENCE, KS 66044.
5. Hayat, M., *Correlative microscopy in biology: instrumentation and methods*2012: Elsevier.
6. Müller-Reichert, T. and P. Verkade, *Correlative light and electron microscopy*. Vol. 111. 2012: Academic Press.
7. Sartori, A., R. Gatz, F. Beck, A. Rigort, W. Baumeister, and J.M. Plitzko, *Correlative microscopy: bridging the gap between fluorescence light microscopy and cryo-electron tomography.* Journal of structural biology, 2007. **160**(2): p. 135-145.
8. Su, Y., M. Nykanen, K.A. Jahn, R. Whan, L. Cantrill, L.L. Soon, K.R. Ratinac, and F. Braet, *Multi-dimensional correlative imaging of subcellular events: combining the strengths of light and electron microscopy.* Biophysical Reviews, 2010. **2**(3): p. 121-135.

9. Jahn, K.A., D.A. Barton, K. Kobayashi, K.R. Ratinac, R.L. Overall, and F. Braet, *Correlative microscopy: Providing new understanding in the biomedical and plant sciences.* Micron, 2012. **43**(5): p. 565-582.

10. Jin, S.E., J.W. Bae, and S. Hong, *Multiscale observation of biological interactions of nanocarriers: From nano to macro.* Microscopy research and technique, 2010. **73**(9): p. 813-823.

11. Schwartz, A.J., M. Kumar, B.L. Adams, and D.P. Field, *Electron backscatter diffraction in materials science*2009: Springer.

12. Suenaga, K., M. Tencé, C. Mory, C. Colliex, H. Kato, T. Okazaki, H. Shinohara, K. Hirahara, S. Bandow, and S. Iijima, *Element-Selective Single Atom Imaging.* Science, 2000. **290**(5500): p. 2280-2282.

13. Meyer, J.C., C.O. Girit, M. Crommie, and A. Zettl, *Imaging and dynamics of light atoms and molecules on graphene.* Nature, 2008. **454**(7202): p. 319-322.

14. Norman, J.J. and T.A. Desai, *Methods for fabrication of nanoscale topography for tissue engineering scaffolds.* Annals of biomedical engineering, 2006. **34**(1): p. 89-101.

15. Buzea, C., G. Beydaghyan, C. Elliott, and K. Robbie, *Control of power law scaling in the growth of silicon nanocolumn pseudo-regular arrays deposited by glancing angle deposition.* Nanotechnology, 2005. **16**(10): p. 1986.

16. Dolatshahi-Pirouz, A., M.B. Hovgaard, K. Rechendorff, J. Chevallier, M. Foss, and F. Besenbacher, *Scaling behavior of the surface roughness of platinum films grown by oblique angle deposition.* Physical Review B, 2008. **77**(11): p. 115427.

17. Tseng, A.A. and A. Notargiacomo, *Nanoscale Fabrication by Nonconventional Approaches.* Journal of Nanoscience and Nanotechnology. **5**(5): p. 683-702.

18. Sarkar, S., M. Dadhania, P. Rourke, T.A. Desai, and J.Y. Wong, *Vascular tissue engineering: microtextured scaffold templates to control organization of vascular smooth muscle cells and extracellular matrix.* Acta Biomaterialia, 2005. **1**(1): p. 93-100.

19. Houtchens, G.R., M.D. Foster, T.A. Desai, E.F. Morgan, and J.Y. Wong, *Combined effects of microtopography and cyclic strain on vascular smooth muscle cell orientation.* Journal of Biomechanics, 2008. **41**(4): p. 762-769.

20. Biela, S.A., Y. Su, J.P. Spatz, and R. Kemkemer, *Different sensitivity of human endothelial cells, smooth muscle cells and fibroblasts to topography in the nano–micro range.* Acta Biomaterialia, 2009. **5**(7): p. 2460-2466.

21. Green, A.M., J.A. Jansen, J.P.C.M. Van der Waerden, and A.F. Von Recum, *Fibroblast response to microtextured silicone surfaces: Texture orientation into or out of the surface.* Journal of biomedical materials research, 1994. **28**(5): p. 647-653.

22. Walboomers, X., H. Croes, L. Ginsel, and J. Jansen, *Contact guidance of rat fibroblasts on various implant materials.* Journal of biomedical materials research, 1999. **47**(2): p. 204-212.

23. Walboomers, X., H. Croes, L. Ginsel, and J. Jansen, *Growth behavior of fibroblasts on microgrooved polystyrene.* Biomaterials, 1998. **19**(20): p. 1861-1868.

24. Walboomers, X., L. Ginsel, and J. Jansen, *Early spreading events of fibroblasts on microgrooved substrates.* Journal of biomedical materials research, 2000. **51**(3): p. 529-534.

25. Walboomers, X., W. Monaghan, A. Curtis, and J. Jansen, *Attachment of fibroblasts on smooth and microgrooved polystyrene.* Journal of biomedical materials research, 1999. **46**(2): p. 212-220.

26. Loesberg, W.A., J. te Riet, F.C.M.J.M. van Delft, P. Schön, C.G. Figdor, S. Speller, J.J.W.A. van Loon, X.F. Walboomers, and J.A. Jansen, *The threshold at which substrate nanogroove dimensions may influence fibroblast alignment and adhesion.* Biomaterials, 2007. **28**(27): p. 3944-3951.

27. Dalby, M.J., N. Gadegaard, M.O. Riehle, C.D.W. Wilkinson, and A.S.G. Curtis, *Investigating filopodia sensing using arrays of defined nano-pits down to 35 nm diameter in size.* The International Journal of Biochemistry & Cell Biology, 2004. **36**(10): p. 2005-2015.

28. Dalby, M.J., N. Gadegaard, and C.D. Wilkinson, *The response of fibroblasts to hexagonal nanotopography fabricated by electron beam lithography.* Journal of Biomedical Materials Research Part A, 2008. **84**(4): p. 973-979.

29. Yim, E.K.F., R.M. Reano, S.W. Pang, A.F. Yee, C.S. Chen, and K.W. Leong, *Nanopattern-induced changes in morphology and motility of smooth muscle cells.* Biomaterials, 2005. **26**(26): p. 5405-5413.

30. Lee, S.W., S.Y. Kim, I.C. Rhyu, W.Y. Chung, R. Leesungbok, and K.W. Lee, *Influence of microgroove dimension on cell behavior of human gingival fibroblasts cultured on titanium substrata.* Clinical oral implants research, 2009. **20**(1): p. 56-66.

31. Chou, L., J.D. Firth, V.-J. Uitto, and D.M. Brunette, *Substratum surface topography alters cell shape and regulates fibronectin mRNA level, mRNA stability, secretion and assembly in human fibroblasts.* Journal of Cell Science, 1995. **108**(4): p. 1563-1573.

32. Ito, T. and S. Okazaki, *Pushing the limits of lithography.* Nature, 2000. **406**(6799): p. 1027-1031.

33. Chou, S.Y., P.R. Krauss, and P.J. Renstrom, *Imprint of sub-25 nm vias and trenches in polymers.* Applied physics letters, 1995. **67**(21): p. 3114-3116.

34. Raffa, V., P. Castrataro, A. Menciassi, and P. Dario, *Focused ion beam as a scanning probe: Methods and applications.* Applied Scanning Probe Methods II, 2006: p. 361-412.

35. Iordanova, I., V. Antonov, and S. Gurkovsky, *Changes of microstructure and mechanical properties of cold-rolled low carbon steel due to its surface treatment by Nd:glass pulsed laser.* Surface and Coatings Technology, 2002. **153**(2–3): p. 267-275.

36. Duncan, A.C., F. Rouais, S. Lazare, L. Bordenave, and C. Baquey, *Effect of laser modified surface microtopochemistry on endothelial cell growth.* Colloids and Surfaces B: Biointerfaces, 2007. **54**(2): p. 150-159.

37. Castaldo, V., C.W. Hagen, B. Rieger, and P. Kruit, *Sputtering limits versus signal-to-noise limits in the observation of Sn balls in a Ga+ microscope.* Journal of Vacuum Science & Technology B, 2008. **26**(6): p. 2107-2115.

38. Orloff, J., L. Swanson, and M. Utlaut, *Fundamental limits to imaging resolution for focused ion beams.* Journal of Vacuum Science & Technology B, 1996. **14**(6): p. 3759-3763.

39. Ziegler, J.F., J. Biersack, and U. Littmark, *The stopping and range of ions in solids*. Vol. 1. 1985: New York.

40. Ziegler, J.F., J.P. Biersack, and M.D. Ziegler, *SRIM, the stopping and range of ions in matter*2008: Lulu. com.

41. Volkert, C. and A. Minor, *Focused ion beam microscopy and micromachining.* Mrs Bull, 2007. **32**(5): p. 389-395.

42. Lanyon, Y.H., G. De Marzi, Y.E. Watson, A.J. Quinn, J.P. Gleeson, G. Redmond, and D.W. Arrigan, *Fabrication of nanopore array electrodes by focused ion beam milling.* Analytical chemistry, 2007. **79**(8): p. 3048-3055.

43. Kalantar-Zadeh, K. and B. Fry, *Nanotechnology enabled sensors*2007: Springer, US.

44. Choi, C.H., S. Heydarkhan-Hagvall, B.M. Wu, J.C. Dunn, R.E. Beygui, and C.J. Kim, *Cell growth as a sheet on three-dimensional sharp-tip nanostructures.* Journal of Biomedical Materials Research Part A, 2009. **89**(3): p. 804-817.

45. Raffa, V., O. Vittorio, V. Pensabene, A. Menciassi, and P. Dario, *FIB-nanostructured surfaces and investigation of bio/nonbio interactions at the nanoscale.* NanoBioscience, IEEE Transactions on, 2008. **7**(1): p. 1-10.

46. Joshi, K., P. Singh, and S. Verma, *Fabrication of platinum nanopillars on peptide-based soft structures using a focused ion beam.* Biofabrication, 2009. **1**(2): p. 025002.

47. Statham, P., *Digital pulse processing and pile up correction for accurate interpretation of high rate SDD spectrum images.* Microscopy and Microanalysis, 2007. **13**(S02): p. 1428-1429.

48. Jercinovic, M., M. Williams, J. Allaz, and J. Donovan. *Trace analysis in EPMA*. in *IOP Conference Series: Materials Science and Engineering*. 2012. IOP Publishing.

49. Watanabe, M. and D. Williams, *Atomic-level detection by X-ray microanalysis in the analytical electron microscope.* Ultramicroscopy, 1999. **78**(1): p. 89-101.

50. Carlson, T.A., *Photoelectron and auger spectroscopy.* Physics Today, 1975. **29**(8): p. 53.

51. Benninghoven, A., F. Rudenauer, and H.W. Werner, *Secondary ion mass spectrometry: basic concepts, instrumental aspects, applications and trends.* 1987.

52. Jenner, G., H. Longerich, S. Jackson, and B. Fryer, *ICP-MS—a powerful tool for high-precision trace-element analysis in earth sciences: evidence from analysis of selected USGS reference samples.* Chemical Geology, 1990. **83**(1): p. 133-148.

53. Khuri-Yakub, B., *Scanning acoustic microscopy.* Ultrasonics, 1993. **31**(5): p. 361-372.

54. Wong, Y., R. Thomas, and J. Pouch, *Subsurface structures of solids by scanning photoacoustic microscopy.* Applied physics letters, 1979. **35**: p. 368.

55. Goldstein, J., D.E. Newbury, D.C. Joy, C.E. Lyman, P. Echlin, E. Lifshin, L. Sawyer, and J.R. Michael, *Scanning electron microscopy and X-ray microanalysis*2003: Springer.

56. Kelly, T.F. and M.K. Miller, *Atom probe tomography.* Review of Scientific Instruments, 2007. **78**(3): p. 031101.

57. Williams, D.B., A.J. Papworth, and M. Watanabe, *High resolution X-ray mapping in the STEM.* Journal of Electron Microscopy, 2002. **51**(suppl 1): p. S113-S126.

58. Servanton, G., R. Pantel, M. Juhel, and F. Bertin, *Two-dimensional quantitative mapping of arsenic in nanometer-scale silicon devices using STEM EELS–EDX spectroscopy.* Micron, 2009. **40**(5): p. 543-551.

59. Muller, D., T. Sorsch, S. Moccio, F. Baumann, K. Evans-Lutterodt, and G. Timp, *The electronic structure at the atomic scale of ultrathin gate oxides.* Nature, 1999. **399**(6738): p. 758-761.

60. Vaz, C.A., J. Hoffman, C.H. Ahn, and R. Ramesh, *Magnetoelectric coupling effects in multiferroic complex oxide composite structures.* Advanced Materials, 2010. **22**(26-27): p. 2900-2918.

61. Scott, J., *Data storage: Multiferroic memories.* Nature materials, 2007. **6**(4): p. 256-257.

62. Ramesh, R., *Magnetoelectrics: Making metallic memories.* Nature Nanotechnology, 2010. **5**(11): p. 761-762.

63. Wang, L., D. Wang, Q. Cao, Y. Zheng, H. Xuan, J. Gao, and Y. Du, *Electric control of magnetism at room temperature.* Scientific reports, 2012. **2**.

64. Bibes, M., *Nanoferronics is a winning combination.* Nature materials, 2012. **11**(5): p. 354-357.

65. Rao, C., A. Sundaresan, and R. Saha, *Multiferroic and Magnetoelectric Oxides: The Emerging Scenario.* The Journal of Physical Chemistry Letters, 2012. **3**(16): p. 2237-2246.

66. Iwai, H., *Roadmap for 22nm and beyond.* Microelectronic Engineering, 2009. **86**(7): p. 1520-1528.

67. Keeney, L., C. Groh, S. Kulkarni, S. Roy, M.E. Pemble, and R.W. Whatmore, *Room temperature electromechanical and magnetic investigations of ferroelectric Aurivillius phase Bi5Ti3 (FexMn1− x) O15 (x= 1 and 0.7) chemical solution deposited thin films.* Journal of Applied Physics, 2012. **112**(2): p. 024101.

68. Lotgering, F.K., *Topotactical reactions with ferrimagnetic oxides having hexagonal crystal structures—I.* Journal of Inorganic and Nuclear Chemistry, 1959. **9**(2): p. 113-123.

69. Keeney, L., S. Kulkarni, N. Deepak, M. Schmidt, N. Petkov, P.F. Zhang, S. Cavill, S. Roy, M.E. Pemble, and R.W. Whatmore, *Room temperature ferroelectric and magnetic investigations and detailed phase analysis of Aurivillius phase $Bi_5Ti_3Fe_{0.7}Co_{0.3}O_{15}$ thin films.* Journal of Applied Physics, 2012. **112**(5): p. 052010.

70. Foster, P.K. and J.E. Welch, *METAL-OXIDE SOLID SOLUTIONS. PART l.-LATTICE-CONSTANT AND PHASE RELATIONSHIPS IN FERROUS OXIDE (WUSTITE) AND IN SOLID SOLUTIONS OF FERROUS OXIDE AND MANGANOUS OXIDE.* Trans. Faraday Soc., 1956. **52**: p. 1626.

71. Hope, D.A., A.K. Cheetham, and G.J. Long, *A Neutron Diffraction, Magnetic Susceptibility, and Mossbauer-Effect Study of the (Mn,Fel-,)yO Solid Solutions.* Inorganic Chemistry, 1982. **21**: p. 2804-2809.

72. Zaera, R., J.A. Rodríguez-Martínez, A. Casado, J. Fernández-Sáez, A. Rusinek, and R. Pesci, *A constitutive model for analyzing martensite formation in austenitic steels deforming at high strain rates.* International Journal of Plasticity, 2012. **29**(0): p. 77-101.

73. Retuerto, M., M.-R. Li, Y. Go, A. Ignatov, M. Croft, K. Ramanujachary, R. Herber, I. Nowik, J. Hodges, and W. Dachraoui, *High magnetic ordering temperature in the perovskites Sr 4− x La x Fe 3 ReO 12 (x= 0.0, 1.0, 2.0).* Journal of Solid State Chemistry, 2012. **194**: p. 48-58.

74. Reyes-Gasga, J., A. Gómez-Rodríguez, X. Gao, and M. José-Yacamán, *On the interpretation of the forbidden spots observed in the electron diffraction patterns of flat Au triangular nanoparticles.* Ultramicroscopy, 2008. **108**(9): p. 929-936.

75. Mizusaki, J., N. Mori, H. Takai, Y. Yonemura, H. Minamiue, H. Tagawa, M. Dokiya, H. Inaba, K. Naraya, T. Sasamoto, and T. Hashimoto, *Oxygen nonstoichiometry and defect equilibrium in the perovskite-type oxides La1−xSrxMnO3+d.* Solid State Ionics, 2000. **129**(1–4): p. 163-177.

3. Results and Discussion

This chapter will follow the multiscale and multimodal concept as outlined in the introduction starting with **3.1** the patterning of stainless steel including 3D correlative microscopy followed by **3.2** the statistical inclusion analysis in multiferroic thin films including extensive microstructural analysis of the multiferroic films and their inclusions.

3.1. FIB patterning and correlative microscopy analysis of stainless steel surfaces

3.1.1. FIB tests: challenges with anisotropic milling

From the literature survey, promising cell responses to nano-structured features were identified including nano-pit features [1, 2]. However, to date no endothelial cell (EC) studies have been reported on nano-pit structures. Based on this, two pit designs were patterned on three electropolished 316L stainless steel samples on areas of 400 µm × 400 µm using FIB: design A, pits of 120 nm diameter with a pitch of 240 nm and intended depth of 50-100 nm, and design B, pits of 180 nm diameter with pitch of 360 nm at the same depth[3, 4].

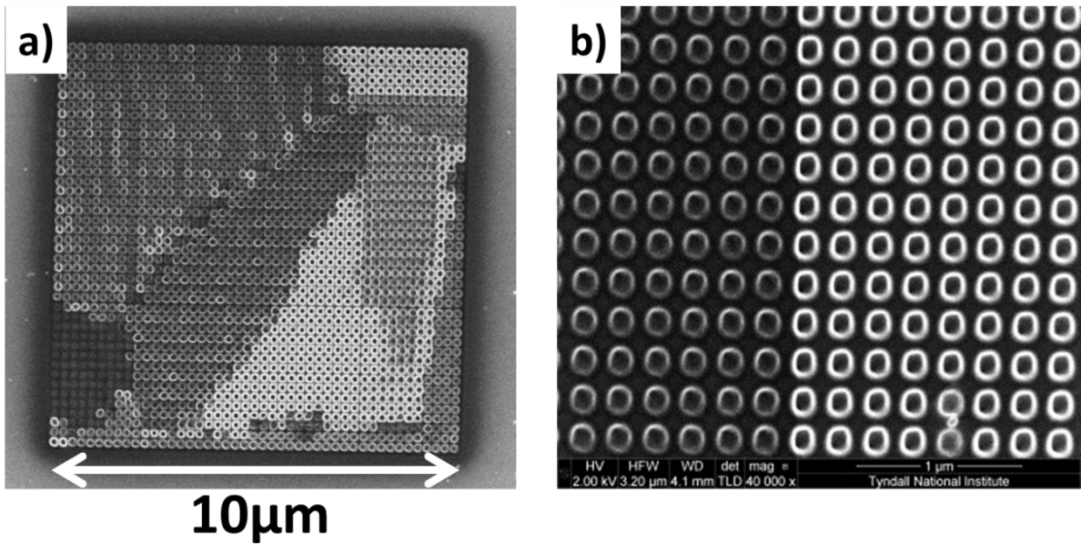

Figure 3.1. SEM images of preliminary FIB tests to determine the feasibility of the prototyping approach; a) 10 x 10 µm area pattern by FIB in preliminary tests with nominal 120 nm wide pits at 240 nm pitch; b) detail of another area exhibiting the

same pattern. Clearly visible the differences in appearance of the patterned surface depending on the polycrystallinity of stainless steel.

Before attempting prototyping on large 400 x 400 μm areas used for the biological tests optimisation tests on relatively small test patterns have been performed, one such area is shown in **Fig. 3.1a**. From the known polycrystalline nature of the 316L stent material one can assume that when subjected to ion milling or imaging it will show pronounced channelling contrast. It is well known for about a century for W, Ag or Cu which are all fcc metals that they etch and sputter faster in preferred directions [5-8], as well as Si [9, 10]. Similarly polycrystalline fcc austenitic stainless steel will show milling rates that are varying by the different orientation of grains towards the incoming beam.

Fig. 3.1 illustrates how much this anisotropic milling affects the desired outcome of uniform concaves. Shown in here are examples from the pre-tests on 10μm x 10μm areas with 120 nm diameter holes at 240 nm pitch. The structures that appear with the brightest contrast showed deeper and sharper edges than the structures that appear darker in contrast. This will be discussed in more detail in the following section describing the correlative microscopy approach. A later section will focus on the study on the patterned substrates used for actual cell adhesion tests and the preliminary FIB tests.

3.1.2. Prototyping: Samples prepared for cell adhesion tests

After the initial tests for the feasibility of the patterning was finished successfully on the batch of samples with small scale pattern, the 'real' prototyping on the 400 x 400 µm patterned areas had been started. As consensus between statistical needs for ideally a high number of samples on one hand and the slow process of patterning with the FIB on the other hand, 5 samples with each 1 area of 120 nm pits / 240 nm pitch and 1 area 180 nm pits / 360 nm pitch were manufactured.

The two pit designs, A and B were created on electropolished stainless steel samples by FIB and are presented in **Fig. 3.2**. Three things can be observed. First, the square areas that have been milled by the FIB are very different from the electropolished areas. Second, the triangular areas in the centre have higher contrast than the areas at the edges. Finally, within and outside these triangular areas, the different colour tones observed are due to the polycrystallinity of the stainless steel as described in detail in the previous section.

The triangular appearance is very intriguing here. The Ga^+ ion source has a cylindrical symmetry and the beam optics have quadrupoles and octopoles only. From discussions with the manufacturer and within the EM community it is believed that the origin of the triangular shape is correlated with beam misalignment – most likely a cut through the overlap of the two squares created by the octopoles.

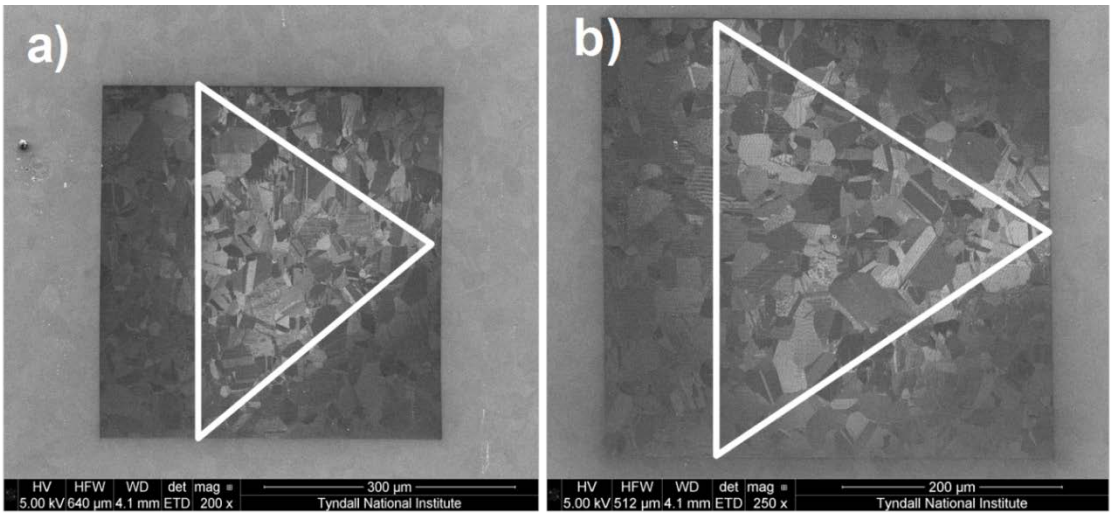

Figure 3.2. Overview of SEM images of (a) design A and (b) design B showing: (1) differences in milled (inside the square area) and electropolished surfaces (outside the square area), (2) triangular areas (triangles drawn to guide the eye) covering more than half of the 400 µm × 400 µm square are much better defined than the areas at the corners in the squares and (3) different colours tones illustrates the polycrystallinity of the stainless steel

All these variations in pit dimensions reported in stainless steel samples can be due to the: atomic arrangement or random orientation of crystallographic structures and non-uniformity in grain size, though the shape of the incident beam at the point of impact on the sample surface will have the greatest effect of all the factors, followed by the crystallographic orientation of the grain at the surface.

Endothelial cell studies will remain a subject to further examinations as initial results showed no major improvement over the unpatterned stainless steel samples. On the

positive side though the cells strived also on the patterned surfaces and did not perish.

FIB has compelling advantages for flexible prototyping compared to other traditional techniques, however the milling rates and the corresponding shape and size of the formed structures is largely affected by the grain size of the polycrystalline 316L stainless steel and stability of the ion beam quality over large areas. Moreover this method is practically limited to 120 nm resolution for the desired pit depth and uniform scan size of 200 μm x 200 μm. Nevertheless formed structures show large variation of pit depths and shapes and as such surfaces might serve as a resourceful platform for screening large variations of cell/pattern stainless steel interactions. However, the FIB nano-pits design A and B created on polycrystalline stainless steel surfaces demonstrated low EC adhesion and proliferation relative to unpolished and electropolished specimens. There was no significant difference in EC adhesion and proliferation between unpolished-electropolished samples and design A and B pits. Further morphological examination of EC response on nano-structured steel surfaces would verify the mechanism for low EC adhesion and proliferation on these surfaces. Nano-patterning the stainless steel surfaces by FIB is time-consuming and expensive, especially when patterning large areas. The precision and reproducibility of this technique is greatly affected by the polycrystallinity of stainless steel and a stable beam quality over large sample areas.

3.1.3. Towards better understanding of ion beam-substrate interactions: 3D correlative microscopy of FIB patterned stainless steel.

The principal concept of correlative microscopy calls for analysis of one and the same volume of interest by two or more imaging techniques. In this chapter the use of back-scattered electron diffraction (EBSD), AFM and 3D SEM/FIB serial sectioning, applied in a correlative microscopy approach is demonstrated, to gain comprehensive understanding of the beam-substrate interaction during FIB formation of nano-pits in stainless-steel. Using developed markers on the stainless steel surface (see **Fig 3.3** and **3.4**) one and the same volume of the surface was investigated by EBSD first and then patterned by FIB and analysed by SEM, AFM and serial sectioning. Hence direct correlation of the crystal structure of the stainless-steel to the 3D shape and size of the formed nano-pits is presented.

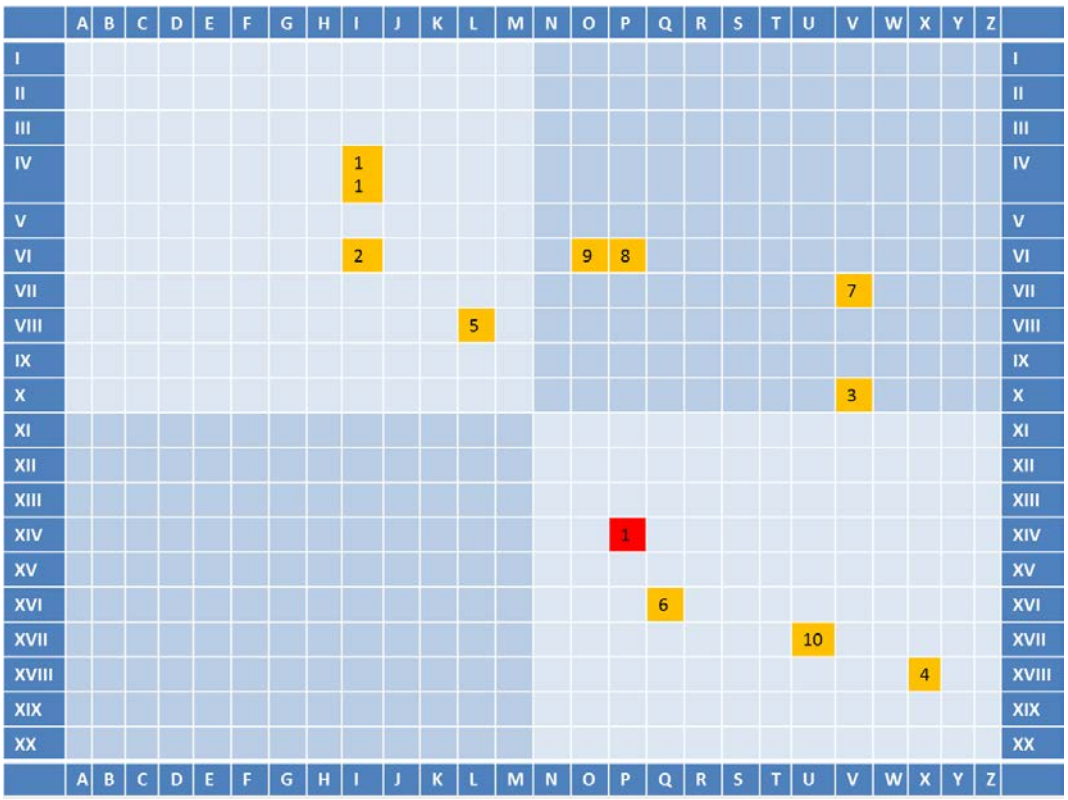

Figure 3.3. Theoretical design of the marker pattern.

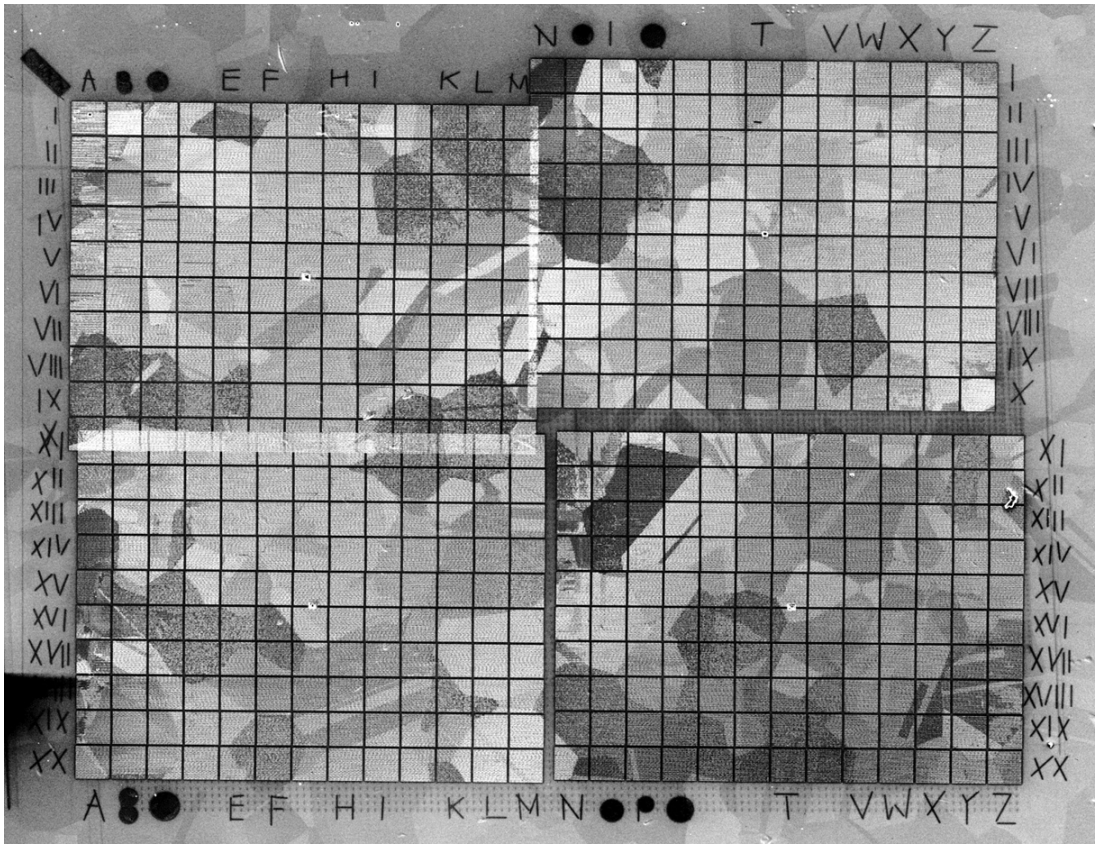

Figure 3.4. Actual resulting pattern overlaid over the region where EBSD analysis was performed. The marks from the EBSD analysis are still visible at the bottom of the image as dark dots in a 2µm x 2µm steps array. The red and orange coloured fields in a) represent the most promising areas for correlative microscopy study showing strong contrasting features in the SEM images (see ***Annex*** for detailed data).

Fig. 3.5 illustrates the detailed analysis flow of the correlative approach.

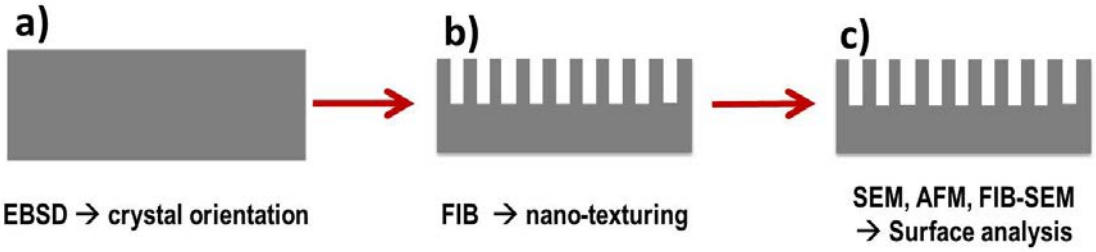

Figure 3.5: Analysis flow in the correlative microscopy approach; a) the crystallographic grain orientations are measured by EBSD before patterning; b) surface patterning using FIB, also gaining FIB SE images as part of the monitoring process; c) extensive analysis of the textured steel surface with SEM, AFM and finally destructive serial FIB-SEM sectioning.

EBSD mapping was accomplished before the area was patterned in order to determine a correlation between crystal grain orientation on one hand and shape, size and depth of the FIB milled concaves on the other hand. **Fig. 3.6** shows the random size and orientation of the crystal grains and illustrates the correlative microscopy approach of three techniques combined in the exact same sample location, EBSD, FIB and SEM. In general the intensity of the emitted SE depends on the different inclination of the sample surface towards the incoming beam and crystal orientation [11]. Thus, the grey levels in the SEM image are directly linked to the surface topography, e.g. the shape of the pits and side-wall profile and the crystal orientation of the surface material. In this way the EBSD data can be correlated to the grey levels in the SEM images. The FIB reveals not surprisingly the same contrast in the SE image as the one taken afterwards in the SEM. The correlation between SE yield and crystal orientation is independent of the type of the beam; hence the same contrast is achieved. The additional information of the SEM SE image lies in the much higher resolution. The FIB which was run as a monitoring tool only during the

patterning process produced one pixel every 360 nm in X and Y direction. The SEM on the other hand was used afterwards as an analysis tool with an image resolution of 4096 x 3775 pixels which calculates at roughly 3 nm image resolution. Using a low current of 86 pA ensured that the real resolution is not far from this theoretical limit.

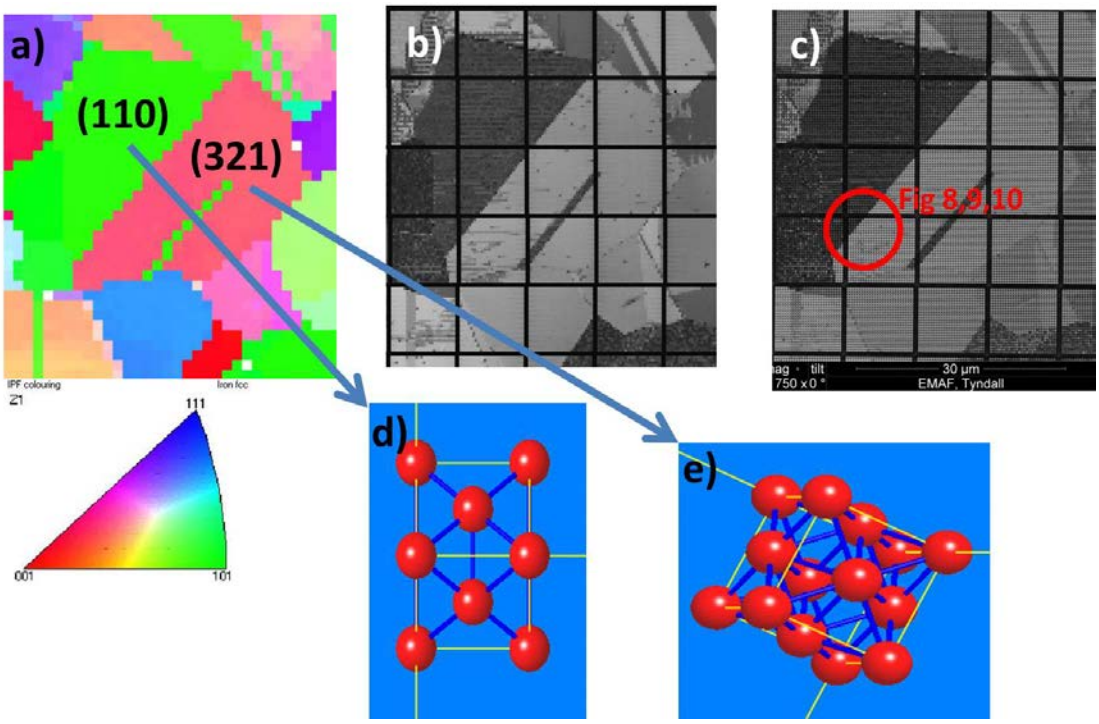

Figure 3.6. Correlative microscopy on the exact same sample location: a) Inverse pole figure (IPF) as measured by EBSD before surface texturing with (110) and (321) crystal orientation labelled and legend underneath; b) FIB SE image obtained during patterning as part of monitoring; c) SE image taken after the patterning – the red circle indicates the region used for AFM and serial sectioning (see figures 8 - 10 for details); d) graphical visualisation of (110) orientation; e) graphical visualisation of (321) orientation.

Two different grains were chosen for additional correlation with AFM and the serial FIB-SEM sectioning based on the crystallographic orientation, a low index grain with (110) orientation and a high index grain with (321) orientation. From as early as

the 1920s it is known that the sputter yield is dependent on the crystal orientation [5]. It is also known that the SE yield is dependent on the crystal orientation [11]. Based on this fact the chosen grains should display a very different behaviour when exposed to the ion beam during sputtering and also to the electron beam in the SEM study.

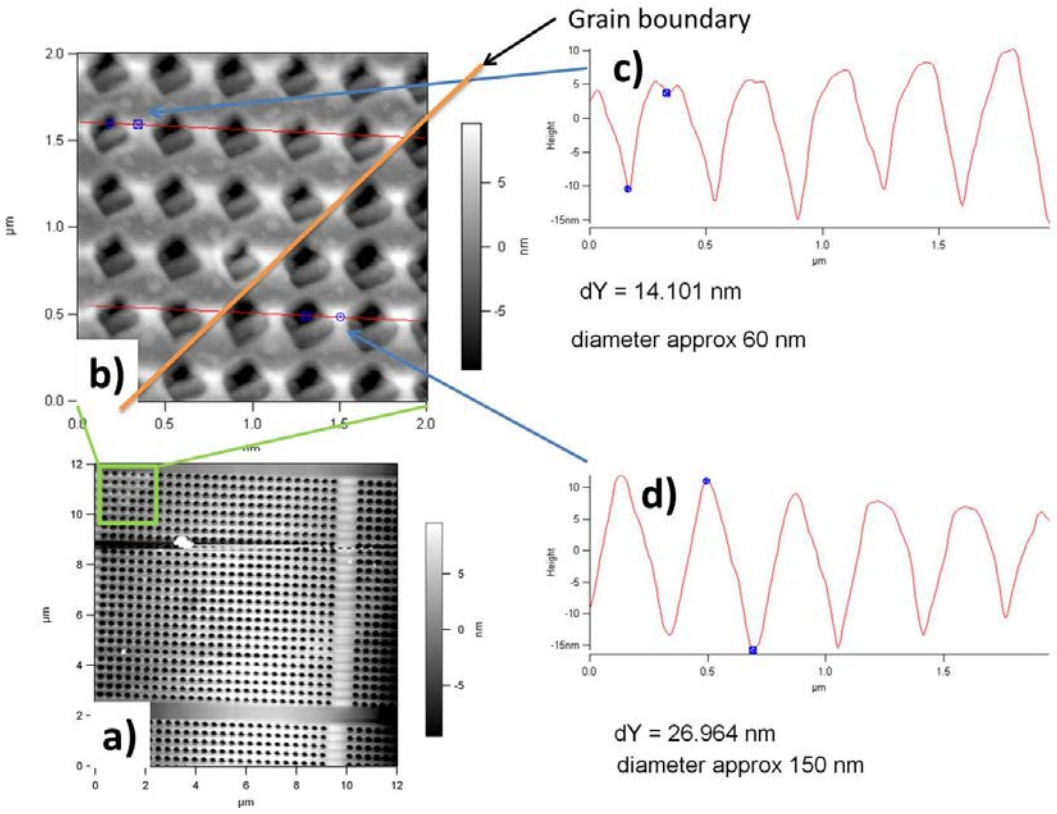

Figure 3.7. Representative AFM scans of the marked region from **Fig. 3.6**; a) overview scan over the whole 12 µm x 12 µm region; b) detailed 2 µm x 2 µm scan of the area around the crystal grain boundary; c) line profile along one row of 5 holes determining depth and diameter of the holes in the (110) oriented grain; d) same line profile determining the depth and diameter of the holes in the (321) oriented grain.

Studying the marked region from **Fig. 3.6** across the grain boundary using the AFM (see **Fig. 3.7**) it appears that there is a difference in hole depth and diameter

depending on crystallographic orientation of the patterned surface. A detailed statistical study was completed as part of Feroze Nazneen's PhD work and is presented in her thesis[12], as well as in[13]. Even the shape of the rim is evidently not circular but rather rhombohedral. Because of the high aspect ratio of the pits the standard tip could not reach down and probe the full depth of the pits, therefore the pit depth must be confirmed by the serial sectioning.

It is well known that for a crystalline target such as metal substrates the orientation of the crystal axes with respect to the target surface is relevant. When the direction of the ion-beam is parallel to a low index crystal axis, the ions can channel deeper in the material[14]. Hence surface sputtering is diminished in this case. Unfortunately until now direct correlation of the ion beam-substrate interactions to the 3D shape of the formed nano-scale pits and crystal orientation of the metal grains has not been presented.

However, when seeing the rhombohedral shape of the pits one can think of the directional dependence in which atoms are ejected when sputtering at threshold energy [6]. In this study however the energy used to create the patterned surfaces in the FIB were way beyond the threshold energy, which for Cr, Ni and Fe as main elements in 316L lies in the range of 60 - 90 eV. The directional dependence decreases with higher sputter energies and has no influence on the direction of the sputtered atoms at the 30 keV used here. It is also obvious when looking in detail at the (111) oriented grain at the bottom of the AFM overview scan that shows the same rhombohedral shaped pits as the whole area around this region instead of the expected triangular shape[6]. As can be seen below in the detailed AFM and SEM studies on the 400 μm x 400 μm patterns used for the cell adhesion studies the shape

of the holes is solely determined by the ion beam quality (focus, stigmation) at the place of impact on the sample surface.

In the SEM surface study as depicted in **Fig. 3.8a)** it appears as if the holes in both grains seem equal in diameter with only the higher SE yield obvious for the higher index grain. In order to clarify this impression the region was imaged again after depositing a carbon layer as shown in **Fig. 3.8b)**. Because secondary electrons are emitted from an area very close to the surface of the sample this amorphous carbon layer masks the crystal orientation of the sample surface and the image is more related to topographical features. Indeed, the difference in diameter of the holes becomes pronounced and it is visible that the higher index grain has apparently much larger holes than the lower index grain.

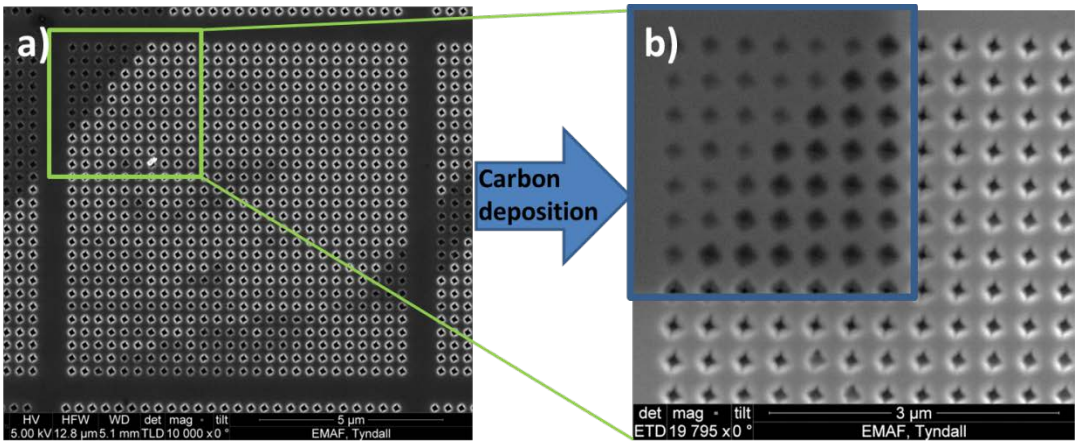

Figure 3.8: Detailed SEM images of patterned area marked by the red circle in previous picture; a) freshly patterned surface displays high SE yield for the high index grain and low yield for the low index grain, though the holes seem equal in diameter; b) detail of a) after carbon deposition, the 'true' diameter shines through as crystal orientations are hidden behind the amorphous carbon layer.

Serial sectioning of again the same region was performed composing 250 images of 8 rows by 5 holes, with one image taken every 12 nm. This detailed analysis verifies the difference not only in the diameter but even more pronounced in the depth. Though **Fig. 3.9a)** presents a 3D reconstruction of all the 250 slices, more details can be observed when looking at the individual slices of **Fig. 3.9b-l)**. The diameter of the pits in the low index (110) oriented grain are 150 ± 10 nm while the diameter in the (321) oriented grains is only slightly bigger with 170 ± 10 nm as measure at the centre of the row (**Fig. 3.9g)** and **3.10**). The depth however is much more influenced by the differences of sputter yield depending on the crystal orientation and hence the (110) grain shows only 55 ± 5 nm depth in contrast to the 200 ± 20 nm depth of the (321) grain, nearly a factor of 4 between them (see **Fig. 3.10**).

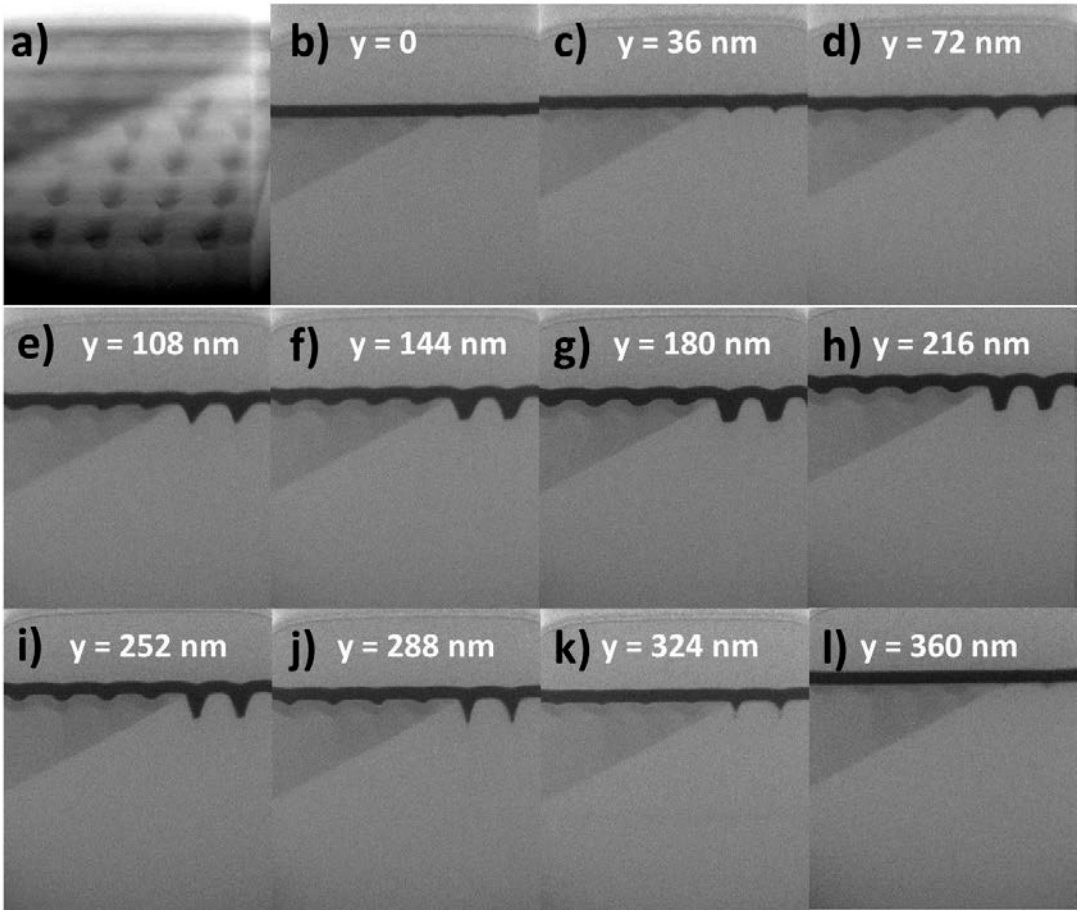

Figure 3.9. Serial sectioning as final destructive step of the correlative microscopy; a) 3D reconstruction of all the 250 slices; b-l) image series illustrating one row of 6 holes taken every 36 nm (every 3rd image). The darker left region is the low index grain (110) oriented, the brighter right hand side is the higher index (321) oriented grain.

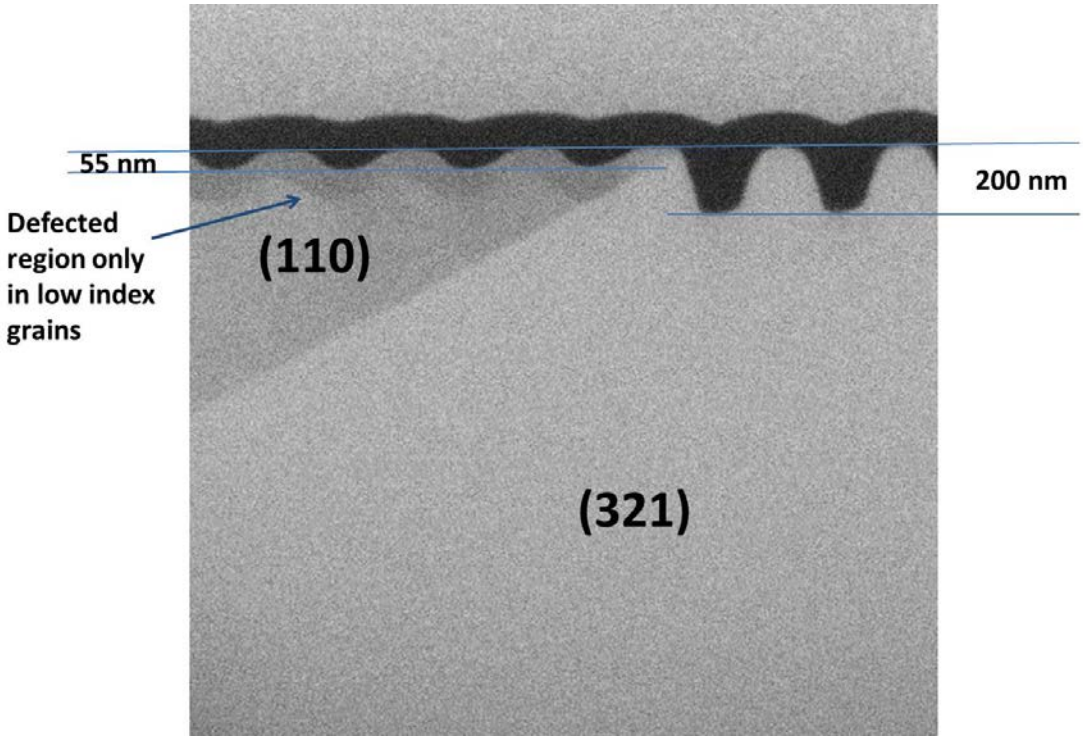

Figure 3.10. Detail from the serial section (slice **g** at the centre of the row). The darker left region is the low index grain (110) oriented, the brighter right hand side is the higher index (321) oriented grain. Obvious is the difference in depth by more than a factor of 3 between the two patterned grains.

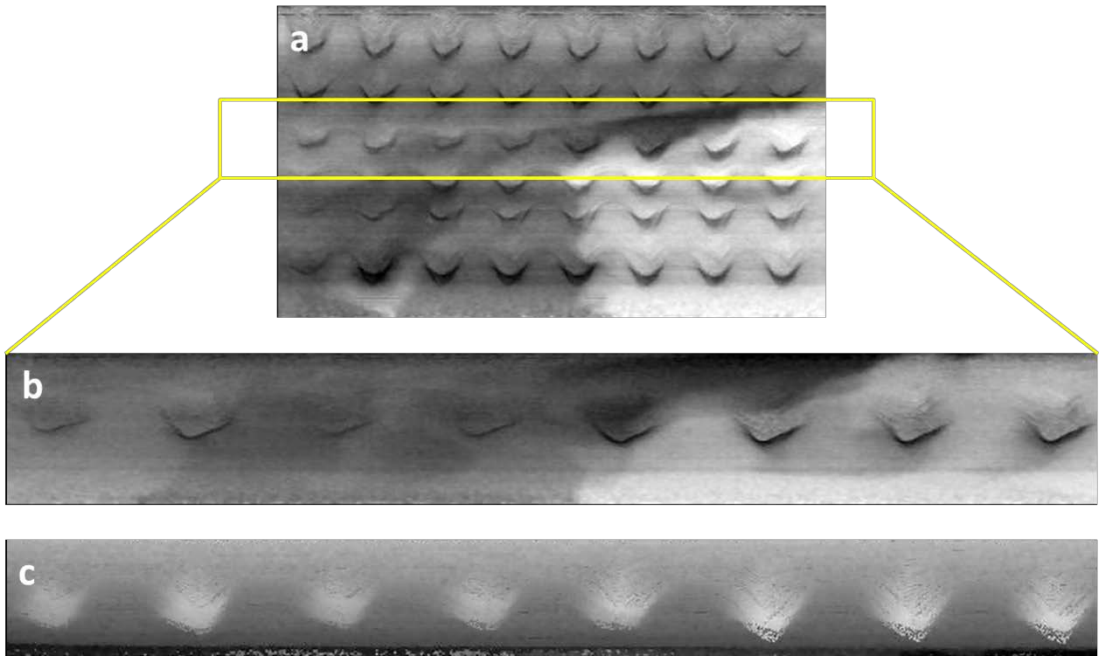

Figure 3.11. a) 3D reconstruction of serial sectioning over 5 rows. One row in detail, 3D reconstruction with b) normal contrast and c) inverted contrast. Normal contrast enhances visibility of the crystal grains. Inverted contrast shows the bottom of the pits in better detail.

Looking at the 3D construction of one row in more detail (**Fig. 3.11**) it is clearly evident that the rhombohedral shape of the pits is independent of the crystal orientation as both orientations exhibit the same shape.

Finally, TEM studies were performed at the same grain boundary between (110) and (321) oriented crystals. The results shown in **Fig 3.12** and **3.13** confirm the findings of the serial sectioning with FIB/SEM (**Fig 3.10**) exactly showing the same differences in depth and surface modification. Interestingly, the FIB modified top layers are not amorphous but crystalline, all oriented the same way as could best be observed by dark field TEM imaging (not shown here).

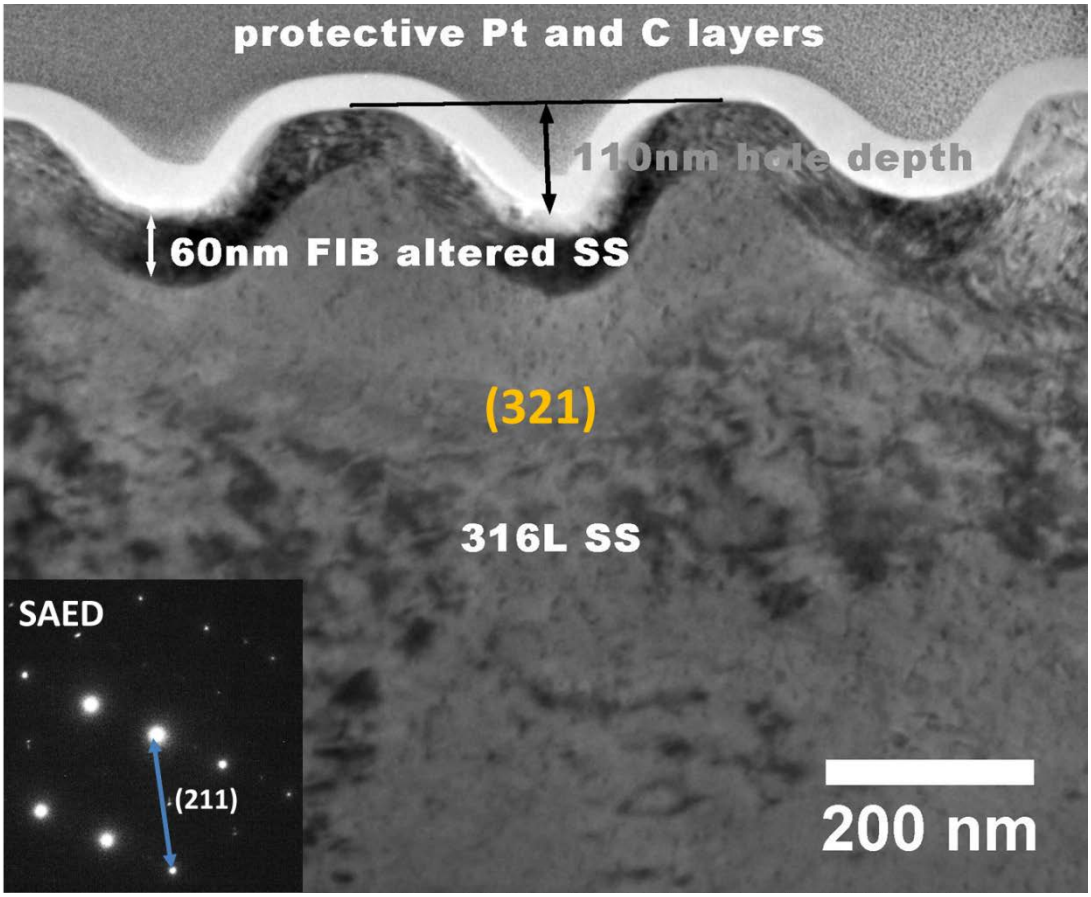

Figure 3.12. TEM bright field micrograph of high index (321) oriented cross section illustrating high depth of pits but shallow FIB altered surface. The inset shows the SAED pattern confirming the high index orientation.

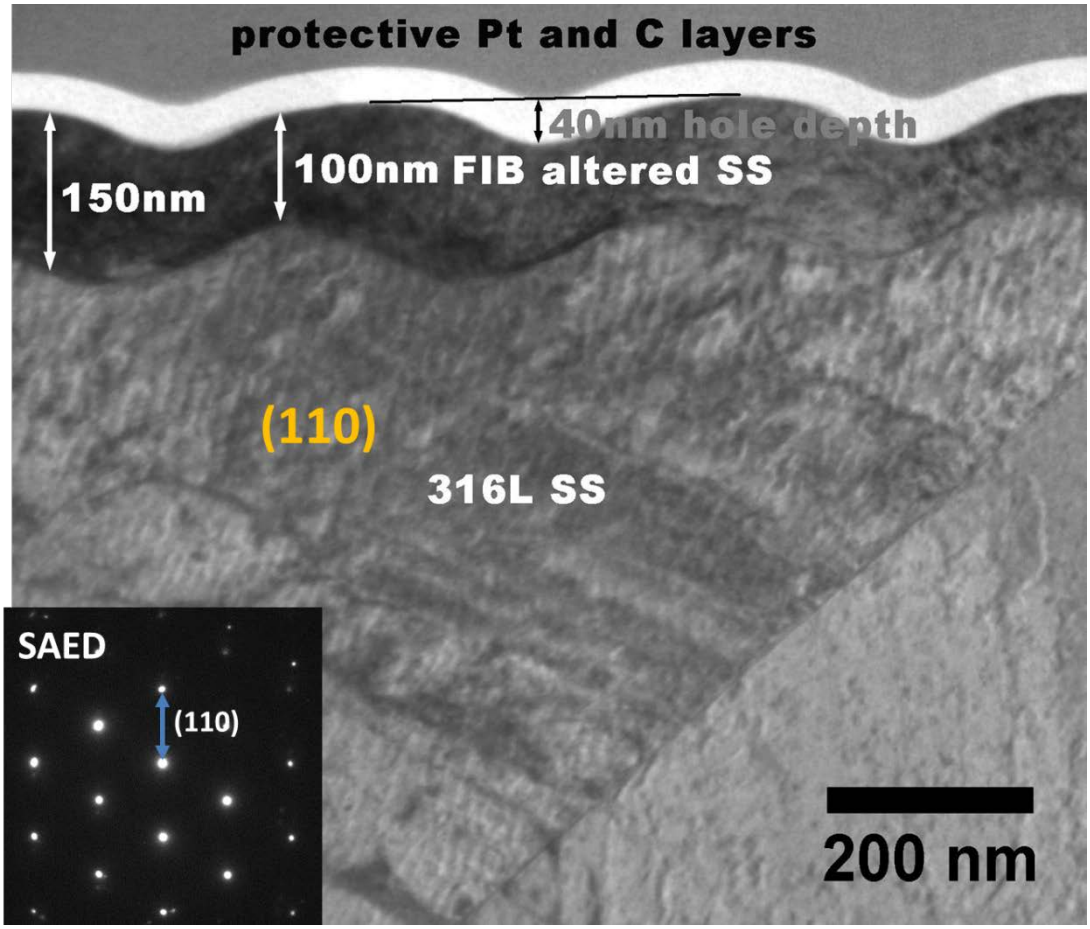

Figure 3.13. TEM bright field micrograph of low index (110) oriented cross section showing low depth of pits but deep FIB altered surface. The inset showing the SAED pattern confirming the (110) orientation.

3.2. Statistical analysis of inclusions in multiferroic Aurivillius thin films

3.2.1. Statistical Analysis

This analysis requires a number of concepts from statistics, which will be introduced now. It starts by analysing the statistical significance of a single measurement of a given sample volume and at a fixed resolution, and then proceeds to evaluate a series of measurements at varying volumes and resolutions. Finally it is shown how to conclude with a high, pre-set statistical confidence level (e.g. 99.5 %) that a physical effect (which in the case at hand is the magnetic remanence of the sample) is *not* caused by undetected inclusions or defects

3.2.1.1. Single Measurement

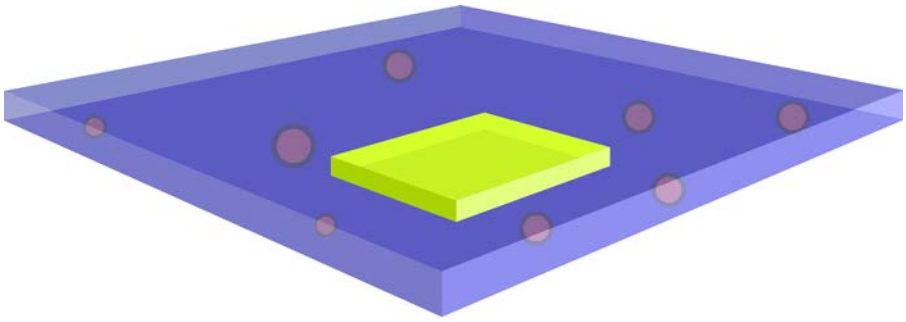

Figure 3.14. Schematic illustration of a scan of a volume V (small yellow box). What conclusions can be drawn, if no inclusions (red balls) are detected during the scan?

In general, it is impossible to prove with certainty that no inclusions exist in a given sample, unless the whole sample is scanned for inclusions. In order to nevertheless obtain statistically significant results, the method of statistical inference through the refutation of a null hypothesis can be used. In the case at hand it is assumed that the level of concentration of a particular impurity exceeds a certain level, and then shown that this assumption does not hold with a certain statistical level of confidence. More specifically, it is first assumed that a particular type of second (or impurity) phase inclusion is present in the sample at a known (volume) density ρ and it is further assumed that the individual inclusions do not interact with each other and are therefore independently distributed. The number of inclusions found in a scan of a small volume V is measured, as shown schematically in **Fig. 3.14.** This can be described as a counting process as in the spatial Poisson process. The spatial Poisson process is still used today as a reference model describing a 'normal' case, a situation without interaction. It finds application in a variety of fields, e.g. cell patterns, metal particles, plant distribution patterns, concrete, blood particles, galaxies, etc. all related to counting processes[15] and can also be applied here. Hence, the probability $P(N,\rho)$ of finding precisely N inclusions is given by the Poisson distribution

$$P(N,\rho) = \frac{(\rho V)^N}{N!} e^{-\rho V}. \qquad (1)$$

In particular, the probability that no inclusions are present in a scanned volume V(**Fig. 3.14**) is given by

$$P(0,\rho) = e^{-\rho V}. \qquad (2)$$

If now a desired confidence level γ (in this case $\gamma = 99.5\ \%$) is fixed and the value ρ_u^N implicitly defined for a given number of inclusions N and volume V via

$$\sum_{m=0}^{N} P(m, \rho_u^N) = 1 - \gamma \qquad (3)$$

then it follows from **(1)** that for any value of the impurity density ρ bigger than ρ_u^N, the probability of finding N or less inclusions within a volume V is below $1 - \gamma = 0.5\ \%$. In the special case that no inclusions were found equation **(3)** can be solved explicitly and yields

$$\rho_u^0 = \frac{-ln(1-\gamma)}{V} \approx \frac{5.3}{V}, \qquad (4)$$

If a performed scan of the volume V yields N or less inclusions, it can therefore be concluded that

$$\rho < \rho_u^N \qquad (5)$$

with a confidence of $\gamma = 99.5\ \%$. Subject to this confidence level, the ρ_u^N defined in equation **(5)** establishes an upper bound for the unknown inclusion density ρ.

3.2.1.2. The grain size distribution function

So far it has been assumed that there exists only one type of inclusion. In reality, inclusions can vary in grain size and composition. For simplicity, the case where the chemical composition of the inclusion is fixed (for example, Fe_3O_4 as worst case scenario in this case – with having the highest remanent magnetisation of the

compounds to be build from the elements of the main phase, see also inset in **Fig. 3.22**) and all inclusions are spherical is looked at first. However, no prior assumptions with regards to the inclusion grain size are made. Thus, a grain size distribution function $p_G(d)$ can be introduced, such that for small Δd the quantity $p_G(d)\Delta d$ is the density of inclusions with diameters in the range $[d, d+\Delta d]$. Now the upper bound **(5)** for the case of a size dependent distribution function can be generalised as follows: it is assumed that a scan of a certain volume V established that there are N inclusions present which are larger than a minimal detectable size d_m. Then it can be concluded that

$$\int_{d_m}^{d_0} dq p_G(q) < \rho_u^N \qquad (6)$$

with confidence level $\gamma = 99.5\ \%$.

3.2.1.3. Series of measurements

So far only one volume scan has been considered. In practice, any analysis will employ a number (K) of scans with different volume sizes V_k possessing different minimal detectable grain sizes d_k where the index $k = 1, \ldots,$ K enumerates the individual scans starting at large d_k (i.e. $d_k > d_{k+1}$) that yielded N_k or less inclusions. Furthermore it is assumed that there is a physical upper bound $d_0 > d_1$ on the grain size. For a given grain size distribution function $p_G(d)$ the density of inclusions bigger than d_k can be defined via

$$\rho_k = \int_{d_k}^{d_0} p_G(q)dq \qquad (7)$$

Then the probability of finding N_k or less inclusions in one particular scan k is given by

$$P_k(N_k) = \sum_{m=0}^{N_k} P(m, \rho_k) \qquad (8)$$

The probability of finding no more than N_k inclusions in a sequence of scans from $k = 1, \dots, K$ is given by the product of the individual probabilities

$$P = P_1(N_1)P_2(N_2)\cdots P_K(N_K) \qquad (9).$$

Now can be assumed that all individual scans establish that no inclusion was detected larger than the respective minimal grain size, d_k. This is the case for the application at hand and therefore will now be discussed in more detail. The probability for this zero outcome is given by

$$P(0) = P_1(0)P_2(0)\cdots P_K(0) \qquad (10).$$

The volume fraction φ_k of inclusions between sizes d_k and d_{k-1} can be calculated from the grain size distribution $p_G(d)$ assuming spherical inclusions

$$\varphi_k = \int_{d_k}^{d_{k-1}} dq p_G(q) \frac{4}{3}\pi(\frac{q}{2})^3 \leq \left[\int_{d_k}^{d_{k-1}} dq p_G(q)\right] \frac{\pi}{6} d_{k-1}^3 \qquad (11).$$

In this step the worst case scenario has been employed that the weight of the grain size distribution function is located at the large inclusion sizes (assuming that the remanent magnetisation of pure Fe_3O_4 grains is decreased for smaller grains and vanishes for $< 5nm$)[16, 17]. It therefore follows that there is an upper limit $\varphi_{k,u}$ on

the volume fraction φ_k of inclusions with diameter in the interval $[d_k, d_{k-1}]$ given by

$$\varphi_k < \varphi_{k,u} = \frac{-d_{k-1}^3}{\sum_{j=K}^{k} V_j} \frac{\pi}{6} ln(1-\gamma) \approx 2.8 \frac{d_{k-1}^3}{\sum_{j=K}^{k} V_j}, \qquad (12)$$

which again holds with a confidence level of $\gamma = 99.5\ \%$.

3.2.1.4. Effect of inclusions on remanent magnetisation

In the previous paragraph an upper limit of the volume fraction of inclusions in thin films was established. However, the aim is to establish an upper bound on the contribution of such inclusions on a measurable quantity. For multiferroic materials, the relevant quantity is the remanent magnetisation, which will be discussed now. Given the bound on the volume fraction, the maximal contribution to the remanence from inclusions with diameters in the interval $[d_k, d_{k-1}]$ can be defined as

$$M_{r,k,u} = \varphi_{k,u} M_{r,F}(d_{k-1}) \qquad (13)$$

Here $M_{r,F}(d)$ is the remanent magnetisation of pure Fe_3O_4 grains of diameter d. For simplicity it is assumed that $M_{r,F}(d)$ vanishes for $< 5nm$. Furthermore it is set that $M_{r,F}(d) = 10emu\ /\ g$ for $5nm < d < 20nm$ and $M_{r,F}(d) = 20emu\ /\ g$ for $d > 20nm$ which are conservative estimates.

Finally an upper bound for the total contribution from inclusions to the remanent magnetisation can be established as

$$M_{r,u} = \max_{W_1,\ldots,W_K} \{ \sum_{k=1}^{K} W_k M_{r,k,u} \} \qquad (14)$$

with a confidence level γ. Here, the weighted means $0 \leq W_1, \ldots, W_K \leq 1$ fulfill the normalisation constraint

$$\sum_{k=1}^{K} W_k = 1 \qquad (15)$$

giving all the weight to the interval with the highest calculated impact on the remanent magnetisation. Therefore it can be concluded that the contribution to the magnetization remanence from inclusions M_r has an upper bound

$$M_{r,u} = \max_{k=1\ldots K} \{ M_{r,k,u} \} \qquad (16)$$

with confidence $\gamma = 99.5\ \%$.

3.2.2. Microstructural Analysis

Guided by the statistical analysis detailed above, analysis measurements were designed taking into account the sizes of the volumes scanned and the minimum size resolution of the EDX. Monte Carlo simulations [18, 19] of the electron beam matter interactions estimated a cone shaped interaction volume within the 200 nm film thickness with a base width of less than 200 nm and the EDX signal coming from a cylinder with roughly 15 nm diameter (interaction volume ~35000 nm^3). The interaction volume is only dependent on the e-beam energy (20 kV), spot size (11.5 nm) and material (assuming that the main phase is the main contributor to calculated

interactions) which all stay constant across all measurements. Taking all these factors into account a number of EDX maps were taken from the surface varying the surface area between 36 μm^2 and 1,000,000 μm^2 (1 mm^2). As the mapping was done at a set resolution of 1024 × 886 pixels (max scanning resolution) the size of one pixel for each surface area can be determined. Hence the smallest detectable size of inclusion across all scanned areas is equal to 1 single pixel except for the smallest area where it is within 2×2 pixels.

A set of 6 samples was made that went through microstructural analysis. All samples are Aurivillius type thin oxide films and their composition is summarised in **Tab. 3.1**.

Table 3.1. Summary of 6 samples that underwent microstructural analysis.

Sample	**Nominal composition**	**Acronym**
1	$TbBi_5Ti_3Fe_2O_{18}$	TbBi5TFO
2	$Tb_{0.5}Bi_{5.5}Ti_3Fe_2O_{18}$	Tb5Bi55TFO
3	$Tb_{0.05}Bi_{5.95}Ti_3Fe_2O_{18}$	Tb5B595TFO
4	$Bi_5Ti_3Fe_{0.7}Co_{0.3}O_{15}$	BTF7C3O[20]
5	$Bi_7Ti_3Fe_3O_{21}$	B7TFO
6	$Bi_6Ti_{2.8}Fe_{1.52}Mn_{0.68}O_{18}$	B6TFMO

As described above, spinel-phase magnetite (Fe_3O_4) [16, 17] is the worst case scenario for second phase inclusions in the type of samples that were analysed, but many other oxides exist that could be built from the elements of the main phase, and thus could occur as second phase inclusions. Some of these are also ferromagnetic.

Hence it is necessary to scan for concentrations of all the magnetic elements that are present. The difficulty with these elements, however, is that they are also present in the main phase, and the ions in the main phase will produce the majority of the X-ray signal detected for a given element. **Fig. 3.15** shows a typical result from a scanned area of 1600 μm^2 in B6TFMO (sample 6). At first, the elemental maps were colour coded, added up into an RGB image and superimposed onto the SEM image, all done within the Oxford INCA software. Although an average recording of 5×10^9 counts over 72 hours improved the signal-to-noise-ratio by a factor of 71 compared to a standard scan with an average of 1×10^6 total counts, and eliminated all the noise that was inhibiting the visibility of possible inclusions in the maps achieved from shorter scans, the RGB colour coded images did not reveal inclusions instantly. The subtraction of the normalised Bi EDX signal from the normalised EDX signals coming from the Fe and Mn allows us to detect subtle variations in the latter from the average value. The resulting maps are shown in **Fig. 3.15d**) Fe Kα map minus Bi Lα map and **e**) Mn Kα map minus Bi Lα map respectively which revealed small bright spots with higher Fe and Mn content and larger (~1 μm) pale areas with higher Fe content. The subtraction of the spectral imaging data was done under the assumption that the average Fe and Mn content in the main phase stays constant over the whole sample and all that is sought to find are small changes from that average. In other words Fe and Mn are correlated to Bi in the main phase and the simple but effective subtraction method reveals the areas Fe and Mn rich that are anticorrelated to Bi which are then scrutinised under microstructural analysis. Also interesting to note is the stability of the conditions during the 72 h scan. Because of the imperfect vacuum in the SEM chamber there is an approx. 100-200 nm layer of carbon deposited over 72 h and this carbon is regularly patterned. Each of the carbon dots

represents exactly one pixel in the EDX measurement that was exposed approx. 1100 times.

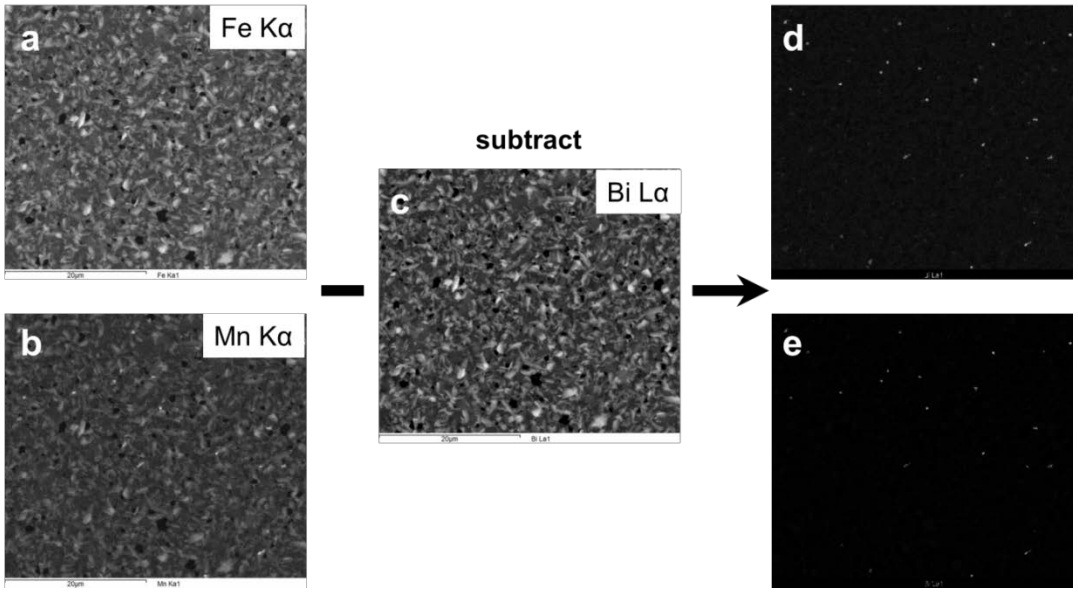

Figure 3.15. Example of EDX signal subtraction in case of B6TFMO sample: a) Fe Kα intensity map, b) Mn Kα intensity map, c) Bi Lα intensity map. The results of subtraction of main phase bound Fe and Mn are shown in d) and e) respectively.

This method of subtracting the images to eliminate the signal from the Fe in the major phase was applied to all 6 samples. Except for the B6TFMO, all other analysed samples showed potentially ferromagnetic inclusions of $Fe_xA_yO_z$ (see **Fig. 3.16**) where A is substituted by Tb for the three samples containing Tb (samples 1-3), by Co for BTF7C3O (sample 4) and without A for B7TFO (sample 5).

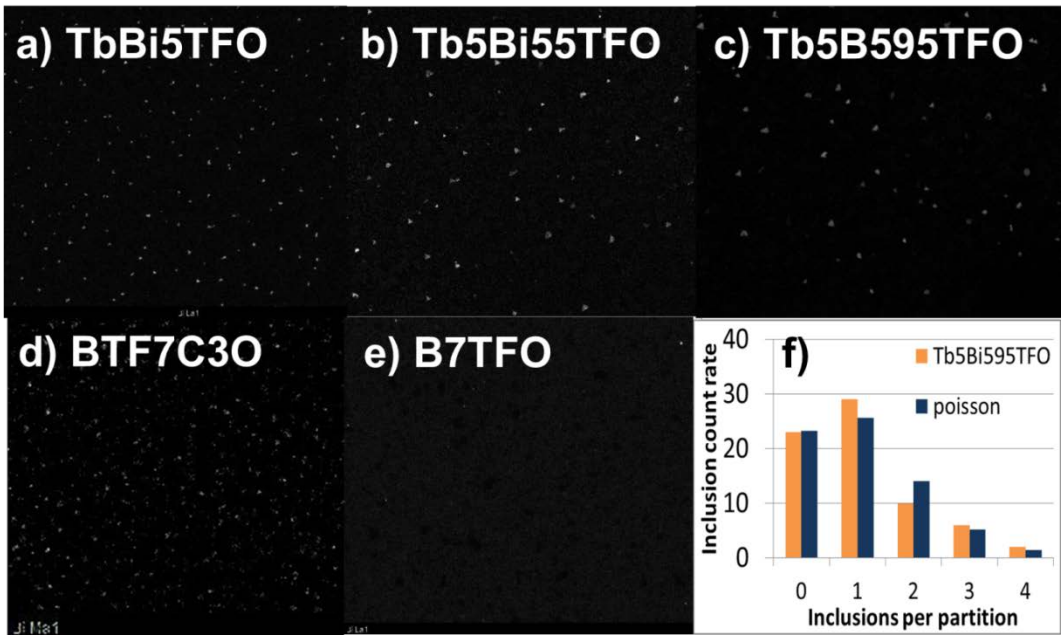

Figure 3.16. a) - e) EDX surface maps for samples 1-5 respectively. Main phase bound Fe subtracted as per **Fig 3.15**. The small bright spots visible are potentially ferromagnetic $Fe_xA_yO_z$ inclusions. f) exemplary inclusion-count-rate histogram of c) subdivided into 90 partitions, where the x-axis is the number of counts in a partition and the y-axis represents the number of partitions containing that number of counts. The theoretical poisson distribution is depicted for comparison.

It is also noted that the inclusions are independently distributed. This assumption has been tested by subdividing the images into partitions and counting the number of inclusions in each partition. The resulting count histograms, as represented by the typical example in **Fig. 3.16f)**, show the expected Poisson distribution. It therefore follows that the spatial distribution of the inclusions is random and without detectable correlations, and justifies the basic assumption in the statistical analysis.

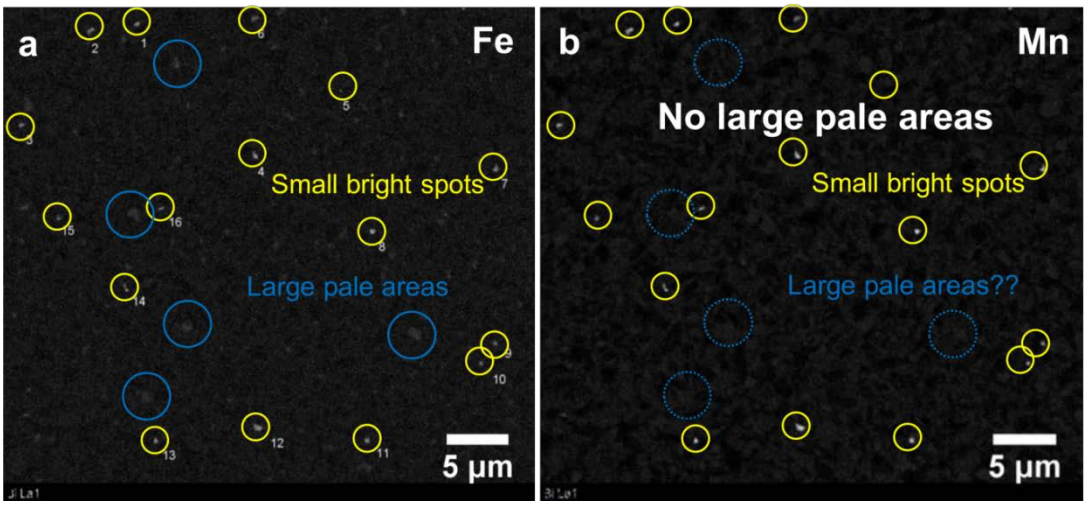

Figure 3.17. A comparison between Fe map (left) and Mn map (right) for the B6TFMO after subtraction of the Bi signal reveals the absence of the 'large pale areas' in the Mn map.

The B6TFMO (sample 6) is interesting insofar as small bright spots (100-500 nm in diameter) with higher Fe and Mn content and larger paler areas (~1µm in diameter) with higher Fe content have been found (Fig. **3.15, 3.17**). Notably when comparing the Fe and Mn maps, the 'large pale areas' appear only in the Fe map (see **Fig. 3.17**). In order to investigate the microstructure and localization of some of these inclusions across the film thickness, and to correlate this to the magnetic response observed, a site-specific sample preparation was performed using a focused ion beam (FIB) (**Fig. 3.18**). At first the locations of a 'small bright spot' (labelled in yellow) and a 'large pale area' (labelled in blue) were marked with a pillar of e-beam deposited carbon (**Fig. 3.19a**). After the cross section lamella was successfully lifted out, attached to a copper half-grid and was polished to about 300 nm thickness the pillars were confirmed to be 250 nm in diameter and hence the location of the two areas was determined to this accuracy.

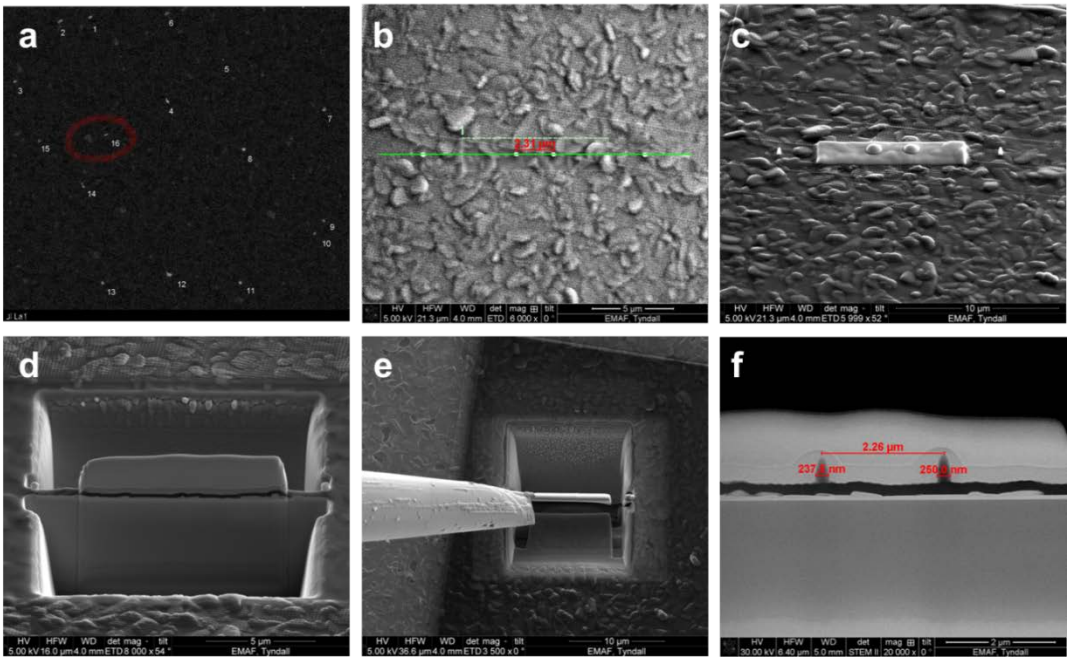

Figure 3.18. Site specific TEM cross section sample preparation on the B6TFMO. a) One ‘small bright spot’ and one ‘large pale area‘ were chosen, b) marked with carbon pillars, c) protected with platinum. d) Lamella prepared, e) lifted out, before attached to TEM half grid and f) analysed with STEM.

With the two types of areas isolated, a STEM-EDX scan was performed as shown in figure **3.19b)** and **c)**. This measurement confirmed the absence of Mn excess in the ‘large pale areas’. TEM imaging, in conjunction with selected area electron diffraction (SAED) and spot EDX measurements confirm this type of inclusion rather to be grains of the main Aurivillius phase with a 40 % increased Fe content which has been associated previously to be the most probable cause of the magnetic behaviour of the sample [21].

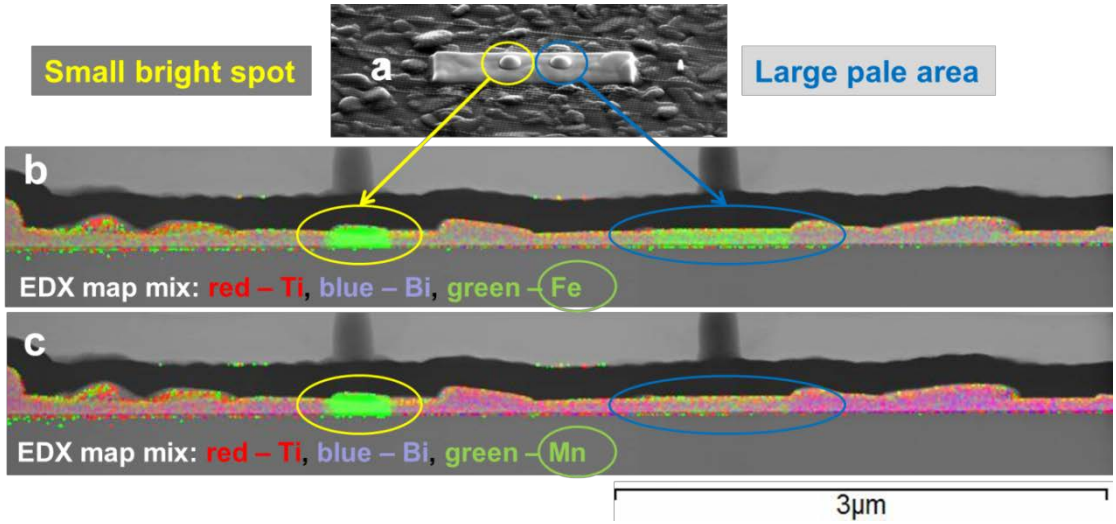

Figure 3.19. Elemental mapping of a cross section of B6TFMO prepared from the area shown in a). b) Fe is coded is green colour; c) Mn is coded in green colour.

TEM imaging, in conjunction with SAED and spot EDX[21] measurements confirm the 'small bright spots' as mangano-wüstite ($Mn_{0.56}Fe_{0.44}O$). This is reported to be non-ferromagnetic, antiferromagnetic below 150 K [22] and hence not to be responsible for the magnetic behaviour of the sample. In conclusion, the inclusions found in the B6TFMO are not ferromagnetic. Hence their impact on the main phase magnetism is zero supported by statistical analysis which is elaborated in the ***Discussion (3.2.3)***.

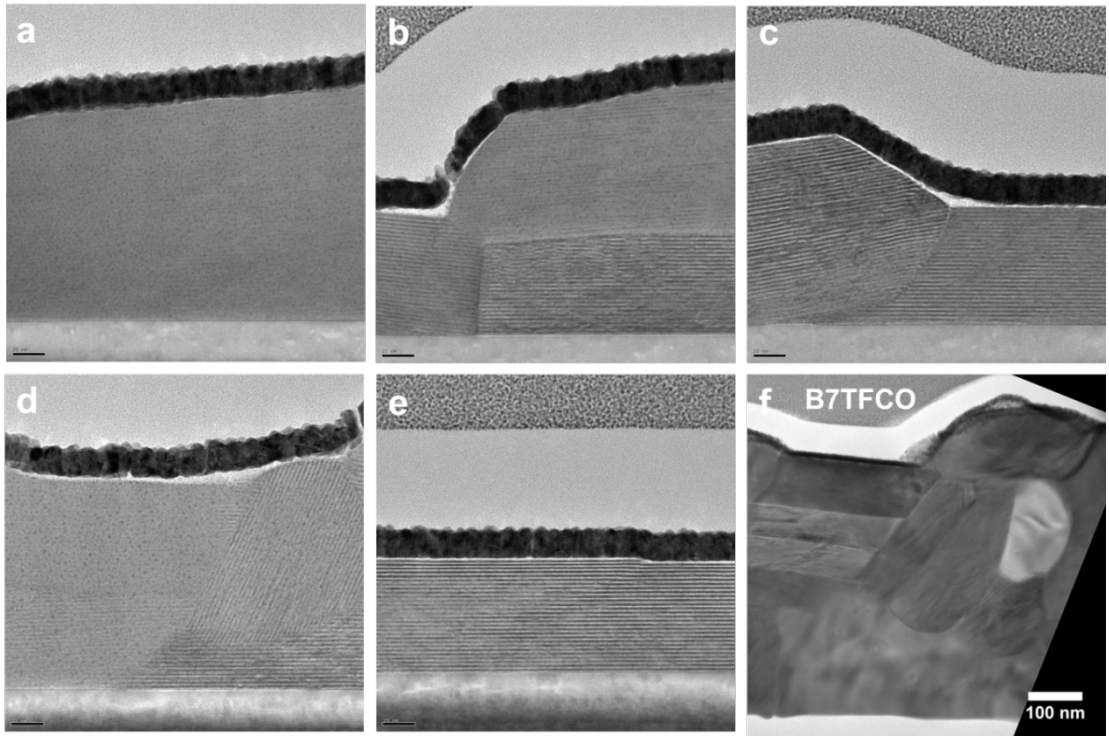

Figure 3.20. Representative TEM images of B6TFMO from the 30µm long lamella. The single crystalline grains are tightly packed without any appearing inclusions of different phases. The scale bar is 20 nm. f) Here a BTF7C3O sample is depicted for comparison to illustrate the presence of inclusions (bright grain at the middle right hand side of the image, scale bar 100 nm). [20]

The link to the smallest volume in the statistical analysis for the B6TFMO sample consists of additional (168) bright field TEM images that were taken along a 30 µm long lamella from a randomly chosen location for the structural analysis. There have been no inclusions observed in a volume of 0.32 μm^3. Every image shows smooth single crystalline Aurivillius phase material with grains touching each other smoothly and tightly (**Fig. 3.20**). In former studies at similar samples (BTF7C3O [20]) following such a "random" sampling approach, the microstructure and composition of inclusions could be identifed and imaged in detail, similar to the type of second phase material being sought here. Hence for the sample under study in this

report it can be confirmed with 99.5% confidence level that there are none. The resolution at the chosen magnification in the TEM was such that inclusions down to 2 nm would be identified, if present.

3.2.3. Discussion

The main question asked regarding the multiferroic oxide thin films is: 'Are there any ferromagnetic inclusions?'. This is the single most critical factor in the analysis of new single phase multiferroic materials because the magnetic response is particularly sensitive to the amount of such inclusions. To answer this question a comprehensive framework was developed based on linking the experimental EDX data from SEM and TEM scans with the numerical statistical analysis described above. The analytical framework that was developed is schematically described in a flow chart (**Fig. 3.21**). The first step is in finding the optimum experimental analytical technique that can obtain spatially resolved maps of elemental compositions. EDX analysis is an obvious choice as it has the spatial resolution necessary to localize the impurities, and reasonably-good detection limits to most elements ($Z \geq 10$). Moreover, EDX analysis on SEM in the case of flat substrates does not require any extensive and elaborate sample preparation. The data acquisition (productivity of detection) has increasingly been improved by the introduction of large area Si drift detectors (SSD), increasing the solid angle of detection and automation procedures. In the next step, the obtained results experimental analysis can be treated as: YES/NO in regard to second phase detected. Once the choice is made the statistics need to be developed in order to supply the

parameters that provide the input for the design of the experiment. The major steps in the development of the statistical analysis are demonstrated in detail in the section ***Statistical Analysis (3.2.2)***; starting analyses of the statistical significance of a single measurement of a given sample volume and at a fixed resolution, and then proceeded to evaluate series of measurements at varying volumes and resolutions. This finally gives the possibility to conclude, in this case with a statistical confidence level of 99.5 %, that a physical effect (e.g. the magnetic remanence of the sample) is *not* caused by undetected inclusions (NO choice feeds into the statistical analysis to calculate the upper limit of impact).

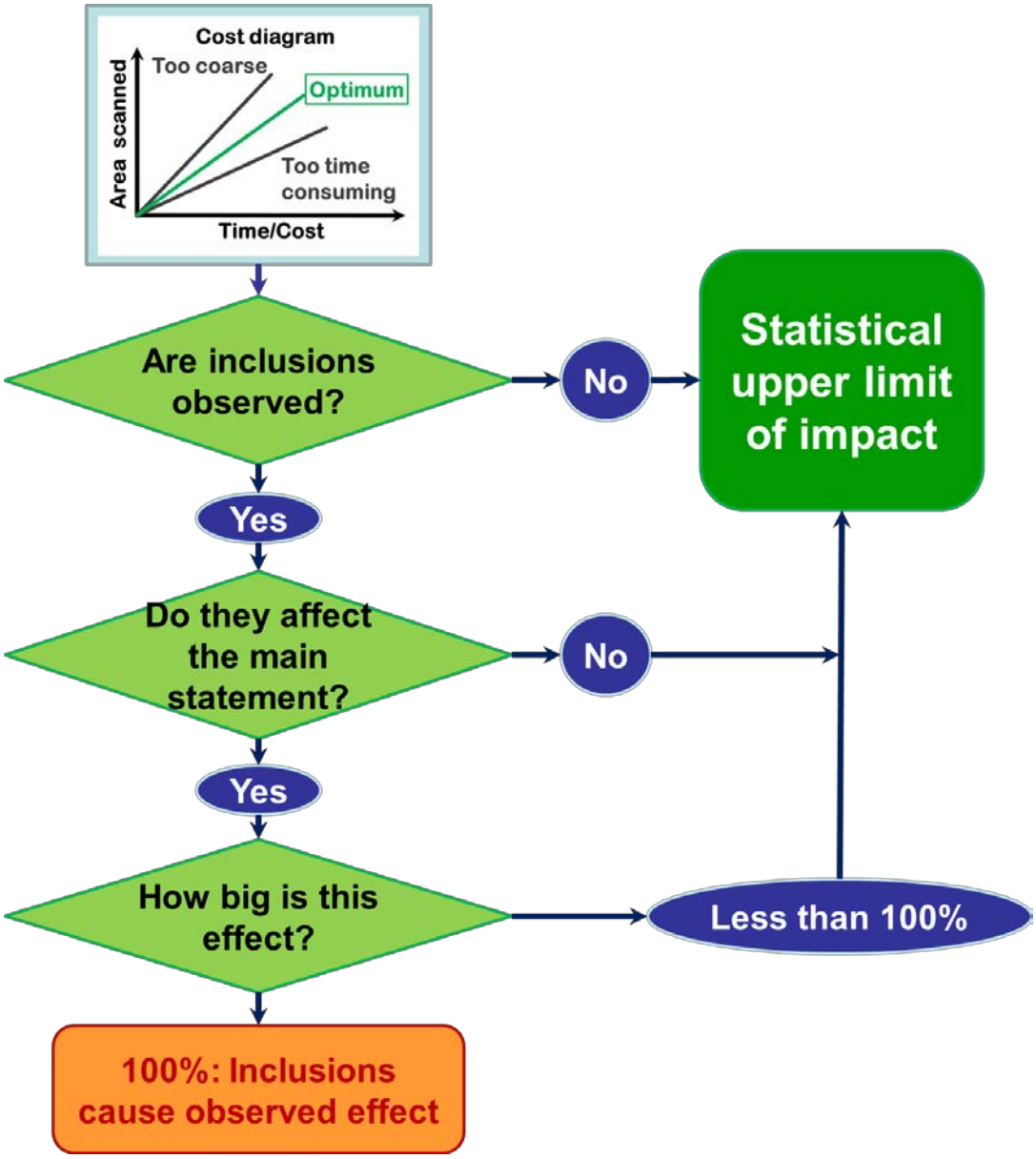

Figure 3.21. The whole process flow of the new generic methodology for localization, identification and grain size distribution of inclusions in thin films with high confidence level.

In the case of inclusions being observed (YES outcome), the nature (structural, compositional properties) of these has to be determined in order to answer the next question in the flow chart: 'Do the observed inclusions have an effect on the magnetic remanence of the main phase?' If they do, the percentage of impact needs to be calculated. For example, the presence of second phase magnetic inclusions at a

volume fraction of 3.95% accounted for all of the observed magnetization in the BTF7C3O thin films reported previously.[20] Though any trace of ferromagnetic inclusions within asserted multiferroic materials might raise concerns, the multiferroic property of a new material can still be established with a given confidence level, if the calculated impact of the inclusions seen is minor.

Table 3.2. Performed Volume Scans for sample B6TFMO.

Method	k	Volume V_k [μm^3]	smallest diameter d_k [nm]	ϕ_k	$M_{r,k}$ [$m$emu/g]
Surface EDX	1	200000	1000 (d0 = 3μm)	0.003	0.67
Surface EDX	2	18000	450	0.003	0.68
Surface EDX	3	6000	120	0.003	0.51
Surface EDX	4	450	80	0.001	0.16
Surface EDX	5	120	60	0.001	0.18
Surface EDX	6	28	40	0.002	0.34
Surface EDX	7	7.2	20	0.002	0.47
TEM	8	0.32	2	0.007	0.69

In the case of no inclusions being observed (NO case) the contribution of inclusions to the remanence can be estimated statistically. As a worked example a number of

measurements (labelled k = 1,…,8) at varying detection limits (d_k = 1 μm,… 2 nm) and scanning volumes (V_k = 200000 μm^3,… ,0.32 μm^3) have been performed on the B6TFMO sample (see **Tab 3.2**). It is not possible to scan the whole sample at the smallest resolution, and therefore the possibility for ferromagnetic inclusions cannot be excluded with certainty. However, the approach described in section ***Statistical Analysis (3.2.2)*** can be used to provide an upper bound for their contribution to the remanence of the sample with a confidence level of 99.5%. The worst case scenario in the worked example of B6TFMO would be undetected Fe_3O_4 inclusions and therefore the upper bound for this case can be calculated. It is assumed that the remanent magnetization is directly proportional to the volume fraction of the inclusions. A direct correlation between the volume fraction of magnetic impurity inclusions and the observed magnetisation was previously demonstrated for the BTF7C3O sample [20]. It is also assumed that the magnetic inclusions do not interact with the Aurivillius phase matrix. This was justified by the lack of exchange-bias interactions at 2K (± 5 T) between the 4-layered BTF7C3O sample (Aurivillius phase is antiferromagnetic at 2K) and the ferrimagnetic $CoFe_{2-x}Ti_xO_4$ impurity inclusions (present at 3.95 vol. %) [23]. The effects of long-range magnetic interactions between unseen magnetic particles (<2nm) were also excluded, since there was no evidence of a super-paramagnetic blocking temperature for B6TFMO [21].

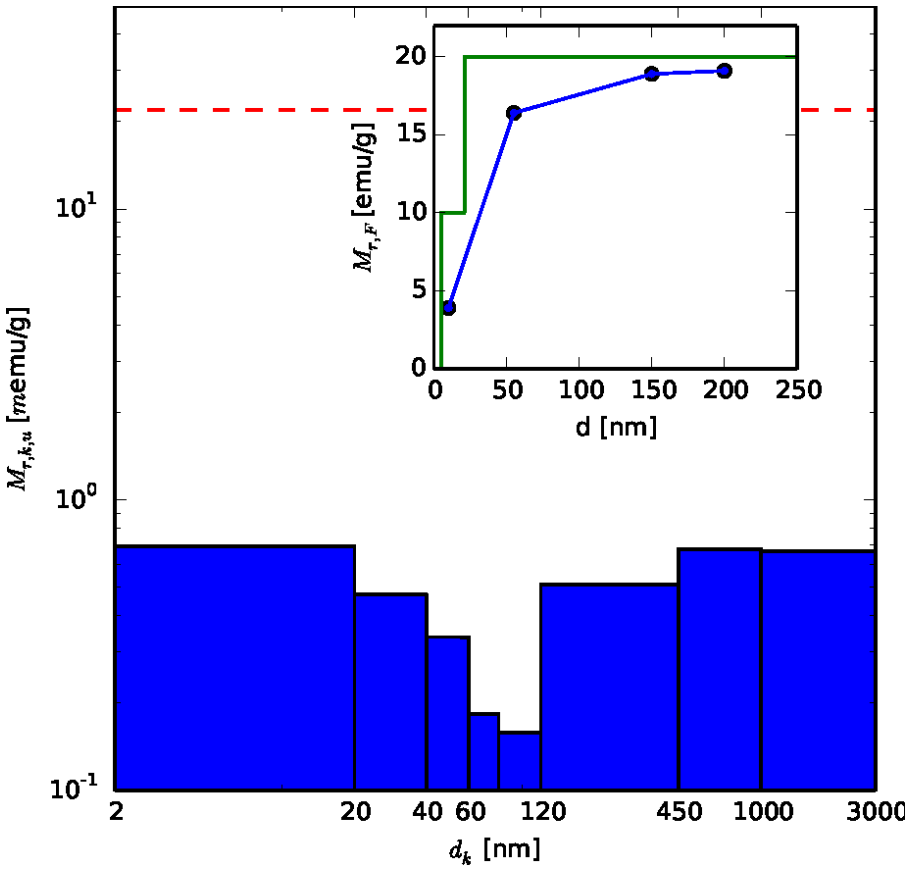

Figure 3.22. The blue bars indicate the maximal contribution $M_{r,k,u}$ to the remanent magnetization from possible unobserved inclusions with diameters in the interval $[d_k, d_{k-1}]$ as obtained from equation **(13)**. The measured remanence of 22 *m*emu/g for the B6TFMO sample is shown by the dashed red line. The inset shows the remanent magnetization $M_{r,F}$ of Fe_3O_4 as function of grain size. Here the blue line shows literature data from reference[16] and reference[17]. Because there are only a few literature values, a conveniently chosen (piecewise constant) green line was chosen which conservatively overestimates the remanent magnetization for all grain sizes d.

To simplify the calculation it is assumed that the remanent magnetization of Fe_3O_4 inclusions as a function of the grain size ($M_{r,k,u}$) is given by the green line in the inset of **Fig. 3.22**, which is chosen to be consistently above the literature values. The

values $M_{r,k,u}$ which are the upper limits for the remanence contribution for each resolution interval $[d_k,d_{k-1}]$ are then calculated according to formula (**5**). The result is shown in the main panel of **Fig. 3.22**. It is observed that all values $M_{r,k,u}$ are well below the experimentally measured remanent magnetisation of the sample (red dashed line of **Fig. 3.22**). Therefore a value of $M_{r,u}$ = 0.69 *m*emu/g is found for the upper limit of the remanence by unobserved Fe_3O_4 inclusions with a confidence level 99.5%. This $M_{r,u}$ is only 3% of the measured magnetic remanence. This compares with a value of 13% as reported in [21], for which the $M_{r,u}$ was calculated using a more restricted dataset as noted above. Following section ***Statistical Analysis (3.2.2)*** this implies that the measured remanence is not due to undetected Fe_3O_4 inclusions. This bound does not critically depend on the inclusions being spherical, for the errors made in the case of cubic, cylindric or ellipsoidal are minimal as the method of detection works with volume fractions independent of the shape of the inclusions.

In conclusion it can be said that a comprehensive and reliable method was developed to detect, localize, isolate and analyse nm- and µm-inclusions in multiferroic thin films and their impact on the properties of the main phase was calculated. More importantly this newly developed analytical methodology fills the gap between µm inclusions and atomic scale inclusions. It can be said with confidence that this method can be applied to materials where a functional property (electrical, optical etc.), might be confounded by a second phase with dimensons in the nm and µm range provided that the statistical design of the measurement is adapted to the particular problem and material system in question. Due to the fast pace of development in the hard- and software for elemental detection when using the electron beam as a probe, further development of the presented methodology can be sought by introducing necessary automation [24],[25].

References

1. Dalby, M.J., C.C. Berry, M.O. Riehle, D.S. Sutherland, H. Agheli, and A.S.G. Curtis, *Attempted endocytosis of nano-environment produced by colloidal lithography by human fibroblasts.* Experimental Cell Research, 2004. **295**(2): p. 387-394.
2. Dalby, M.J., N. Gadegaard, and C.D. Wilkinson, *The response of fibroblasts to hexagonal nanotopography fabricated by electron beam lithography.* Journal of Biomedical Materials Research Part A, 2008. **84**(4): p. 973-979.
3. Schmidt, M., F. Nazneen, Y. Georgiev, G. Herzog, P. Galvin, and N. Petkov, *FIB Patterning of Stainless Steel for the Development of Nano-Structured Stent Surfaces for Cardiovascular Applications.* Journal of Physics: Conference Series, 2012. **371**(1): p. 012065.
4. Nazneen, F., M. Schmidt, E. McLoughlin, N. Petkov, G. Herzog, D.W. Arrigan, and P. Galvin, *Impact of Surface Nano-textured Stainless Steel Prepared by Focused Ion Beam on Endothelial Cell Growth.* Journal of Nanoscience and Nanotechnology, 2013. **13**(8): p. 5283-5290.
5. Feitknecht, W., *Über den Angriff von Krystallen durch Kanalstrahlen.* Helvetica Chimica Acta, 1924. **7**(1): p. 825-842.
6. Wehner, G.K., *Controlled Sputtering of Metals by Low-Energy Hg Ions.* Physical Review, 1956. **102**(3): p. 690-704.
7. Wehner, G.K. and D. Rosenberg, *Angular Distribution of Sputtered Material.* Journal of Applied Physics, 1960. **31**(1): p. 177-179.
8. Sigmund, P., *Theory of Sputtering. I. Sputtering Yield of Amorphous and Polycrystalline Targets.* Physical Review, 1969. **184**(2): p. 383-416.

9. Bean, K.E., *Anisotropic etching of silicon.* Electron Devices, IEEE Transactions on, 1978. **25**(10): p. 1185-1193.

10. Seidel, H., L. Csepregi, A. Heuberger, and H. Baumgärtel, *Anisotropic etching of crystalline silicon in alkaline solutions I. Orientation dependence and behavior of passivation layers.* Journal of the Electrochemical Society, 1990. **137**(11): p. 3612-3626.

11. Stark, Y., R. Fromter, D. Stickler, and H.P. Oepen, *Sputter yields of single- and polycrystalline metals for application in focused ion beam technology.* Journal of Applied Physics, 2009. **105**(1): p. 013542-013542-5.

12. Nazneen, F., *Phd Thesis*, 2012.

13. Schmidt, M., F. Nazneen, P. Galvin, N. Petkov, and J.D. Holmes, *FIB patterning of stainless steel for the development of nano-structured stent surfaces for cardiovascular applications*, in *FIB Nanostructures*2013, Springer International Publishing. p. 391-416.

14. Volkert, C. and A. Minor, *Focused ion beam microscopy and micromachining.* Mrs Bull, 2007. **32**(5): p. 389-395.

15. Illian, J., A. Penttinen, H. Stoyan, and D. Stoyan, *Statistical analysis and modelling of spatial point patterns*. Vol. 70. 2008: John Wiley & Sons.

16. Guan, N., Y. Wang, D. Sun, and J. Xu, *A simple one-pot synthesis of single-crystalline magnetite hollow spheres from a single iron precursor.* Nanotechnology, 2009. **20**(10): p. 105603.

17. Goya, G., T. Berquo, F. Fonseca, and M. Morales, *Static and dynamic magnetic properties of spherical magnetite nanoparticles.* Journal of Applied Physics, 2003. **94**(5): p. 3520-3528.

18. Drouin, D., A.R. Couture, D. Joly, X. Tastet, V. Aimez, and R. Gauvin, *CASINO V2.42—A Fast and Easy-to-use Modeling Tool for Scanning Electron Microscopy and Microanalysis Users.* Scanning, 2007. **29**(3): p. 92-101.

19. Hovington, P., D. Drouin, and R. Gauvin, *CASINO: A new Monte Carlo code in C language for electron beam interaction—part I: Description of the program.* Scanning, 1997. **19**(1): p. 1-14.

20. Keeney, L., S. Kulkarni, N. Deepak, M. Schmidt, N. Petkov, P.F. Zhang, S. Cavill, S. Roy, M.E. Pemble, and R.W. Whatmore, *Room temperature ferroelectric and magnetic investigations and detailed phase analysis of Aurivillius phase $Bi_5Ti_3Fe_{0.7}Co_{0.3}O_{15}$ thin films.* Journal of Applied Physics, 2012. **112**(5): p. 052010.

21. Keeney, L., T. Maity, M. Schmidt, A. Amann, N. Deepak, N. Petkov, S. Roy, M.E. Pemble, and R.W. Whatmore, *Magnetic Field-Induced Ferroelectric Switching in Multiferroic Aurivillius Phase Thin Films at Room Temperature.* Journal of the American Ceramic Society, 2013. **96**(8): p. 2339-2357.

22. Hope, D.A., A.K. Cheetham, and G.J. Long, *A neutron diffraction, magnetic susceptibility, and Moessbauer-effect study of the (manganese iron) oxide ((MnxFe1-x) yO) solid solutions.* Inorganic Chemistry, 1982. **21**(7): p. 2804-2809.

23. Keeney, L., T. Maity, S. Roy, and R.W. Whatmore, *unpublished work.*

24. Genç, A., H. Cheng, J. Winterstein, L. Pullan, and B. Freitag, *3D Chemical Mapping using Tomography with an Enhanced XEDS System.* Microscopy and Analysis, 2012. **24**(02): p. 23-25.

25. Longo, P. and R.D. Twesten, *Fast STEM Spectrum Imaging Using Simultaneous EELS and EDS.* Microscopy Today, 2013. **21**(01): p. 28-33.

3. Summary *and Outlook*

To summarise and recap, in the course of this study the emphasis was placed on the application of advanced analytical EM techniques in the context of multiscale and multimodal microscopy – multiscale meaning across length scales from micrometres or larger to nanometres, multimodal meaning numerous techniques applied to the same sample volume in a correlative manner.

In order to demonstrate the breadth and potential of the multiscale and multimodal concept an integration of it was attempted in two areas: I) Biocompatible materials using polycrystalline stainless steel and II) Semiconductors using thin multiferroic films.

I) In this study a FIB patterning protocol for nano-structuring features (concaves) ordered in rectangular arrays on pre-polished 316L stainless steel surfaces was presented together with an investigation based on correlative microscopy approach of the size, shape and depth of the developed arrays in relation to the crystal orientation of the underlying SS domains. The correlative microscopy protocol is based on cross-correlation of top-view Scanning Electron Microscopy, Electron Backscattering Diffraction, Atomic Force Microscopy, cross-sectional (serial) sectioning and Transmission Electron Microscopy/Electron Diffraction. Various FIB tests were performed, aiming at improved productivity by preserving nano-size accuracy of the patterned

process. The optimal FIB patterning conditions for achieving reasonably high throughput (patterned rate of about 0.03 mm^2 per hour) and nano-size accuracy in dimensions and shapes of the features, were discussed as well.

FIB has compelling advantages for flexible prototyping compared to other traditional techniques, however the milling rates and the corresponding shape and size of the formed structures is largely affected by the grain size of the polycrystalline 316L stainless steel and stability of the ion beam quality over large areas. Moreover this method is practically limited to 120 nm resolution for the desired pit depth and uniform scan size of 200 µm x 200 µm at a high throughput. Nevertheless formed structures show large variation of pit depths and shapes and as such surfaces might serve as a resourceful platform for screening large variations of cell/pattern stainless steel interactions. However, the FIB nano-pits design A and B created on polycrystalline stainless steel surfaces demonstrated low EC adhesion and proliferation relative to unpolished and electropolished specimens in initial tests. There was no significant difference in EC adhesion and proliferation between unpolished-electropolished samples and design A and B pits. Nano-patterning of the stainless steel surfaces by FIB is time-consuming and expensive, especially when patterning large areas. The precision and reproducibility of this technique is greatly affected by the polycrystallinity of stainless steel and a stable beam quality over large sample areas.

Further morphological examination of EC response on nano-structured steel surfaces are needed to verify the mechanism for low EC adhesion and proliferation on these surfaces. Further optimisation of the patterning of

stainless steel by FIB is also needed in order to increase the chance of this method being viable for mass production, especially given the wavy surfaces of real stents, not just stainless steel substrates, a lot of work remains there.

Also for further studies remain AFM scans with very high aspect ratio tips which could reveal the depth profile of the patterned surface non-destructively, an undoubtful advantage over the destructive serial FIB/SEM and TEM techniques. It also should be far quicker with the AFM instruments being advanced at fast speed. The correlation of grey scales in the FIB and SEM images to the false coloured EBSD maps is unfortunately not possible due to the undulating (and hence ambigious) intensity over the crystal orientation. Yet a better correlation of this crystalline dependence of the SE yield could be achieved by ordering the data with that focus in mind. The drawback of hitherto published work is that single crystalline samples had been prepared in only one or two crystal orientation and the SE yield measured as function of the calculated crystal orientaion from the angle of the tilted sample.

II) For the statistical and microstructural analysis of inclusions in multiferroic thin films it can be said in conclusion that a comprehensive and reliable method was developed to detect, localize, isolate and analyse nm- and µm-inclusions in multiferroic thin films and their impact on the properties of the main phase was calculated. More importantly this newly developed analytical methodology fills the gap between µm inclusions and atomic scale inclusions. It can be said with confidence that this method can be applied to materials where a functional property (electrical, optical etc.), might be confounded by a second phase with dimensons in the nm and µm range provided that the statistical design of the

measurement is adapted to the particular problem and material system in question.

A thorough microstructural phase analysis performed on the B6TFMO thin films showed no traces of ferromagnetic inclusions and a statistical analysis based on the volumes inspected placed a confidence of 99.5% that the observed ferromagnetism was not coming from unobserved ferromagnetic grains of spinel. The body of evidence reported here suggests that the higher Fe/Mn content grains with a composition of around $Bi_6Ti_{2.6}Fe_{1.77}Mn_{0.63}O_{18}$ are single phase room temperature magnetoelectric multiferroics. An explanation for the effect has been given based upon the Goodenough-Kanamori rule for super-exchange and the Mn largely being present as Mn^{4+}. These materials could find application to a wide range of new or improved devices and potentially meet future industry requirements in high density memory applications.

Clearly, further work is now required which will include the direct measurement of the compositions of the multi-ferroically switchable grains and x-ray photoelectron spectroscopy to determine Mn oxidation states, as well as the development of synthetic techniques to develop thin films in which all grains possess a composition around $Bi_6Ti_{2.6}Fe_{1.77}Mn_{0.63}O_{18}$, for which it is expected that higher remanent magnetizations will be achieved. Also the growth on other substrates that give better alignment of the thin films gives room for further studies, as well as studying the long-term stability of the films themselves as there are hints of sensitivity to prolonged exposure to light.

This multiscale concept described in this thesis could also be expanded in further studies into the realm of atomic scale by an investigation of potential

oxidation at boundaries or of the presence of atomically thin inter-granular phases in these complex oxides.

This adaptation of the statistical analysis would be very interesting to see for another material/analysis technique, for instance the occurance of sponteanus glass breakage due to µm-sized inclusions in sheets of tempered glass.

Appendix

The Appendix contains

A. detailed data for further correlative microscopy studies on the patterned stainless steel,
B. further data of a microstructural analysis on BTFMO films on sapphire that was particles rich in mixed phases and
C. publications that came out of other work carried out within the PhD training, TEM investigations regarding the structure-activity-relationship between metallic nanoparticles as catalyst and reaction efficiencies in Suzuki-Miyaura-Reactions.

    C.1. Stability, Oxidation and Shape Retention of PVP-Capped Pd Nanocrystals

    C.2. The Origin of Shape Sensitivity in Palladium-Catalyzed Suzuki–Miyaura Cross Coupling Reactions

    C.3. Enhanced Catalytic Activity of High-Index Faceted Palladium Nanoparticles in Suzuki–Miyaura Coupling Due to Efficient Leaching Mechanism

A. detailed data for further correlative microscopy studies on the patterned stainless steel

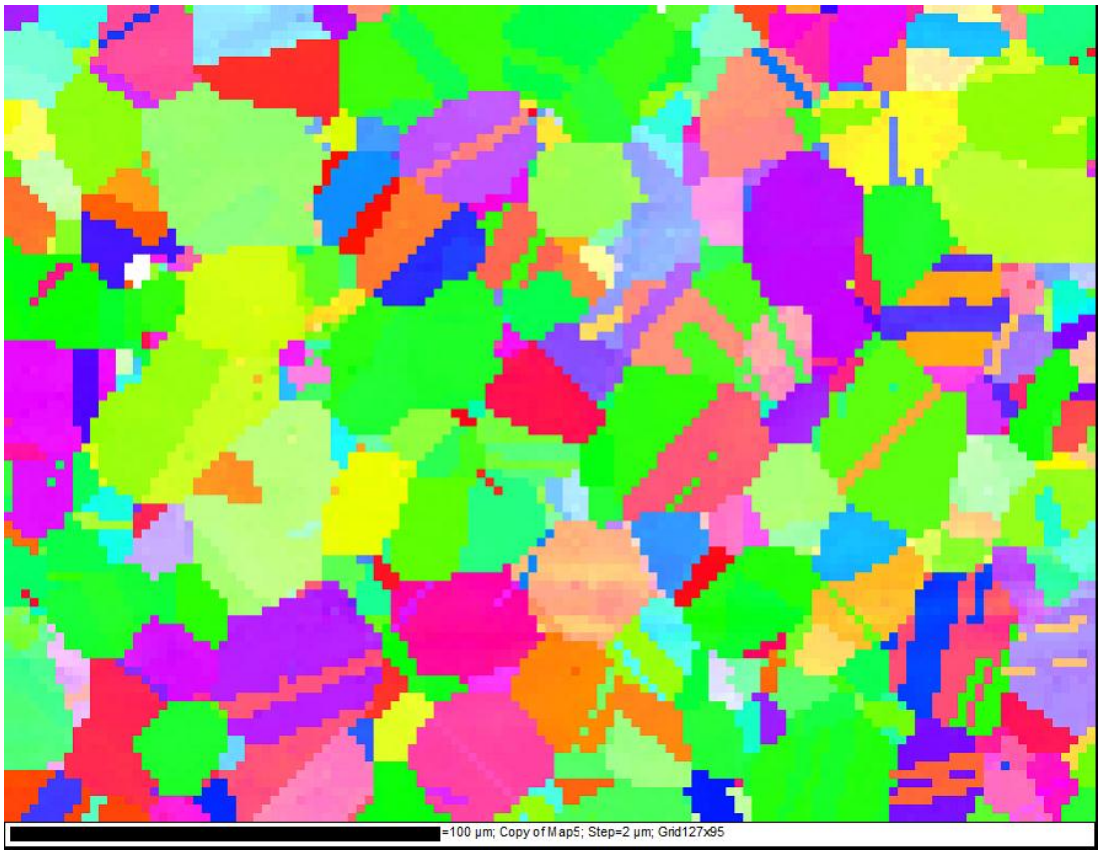

Inverse pole figure (IPF, Z-map) from the EBSD analysis in the region that was patterned with a grid of markers afterwards.

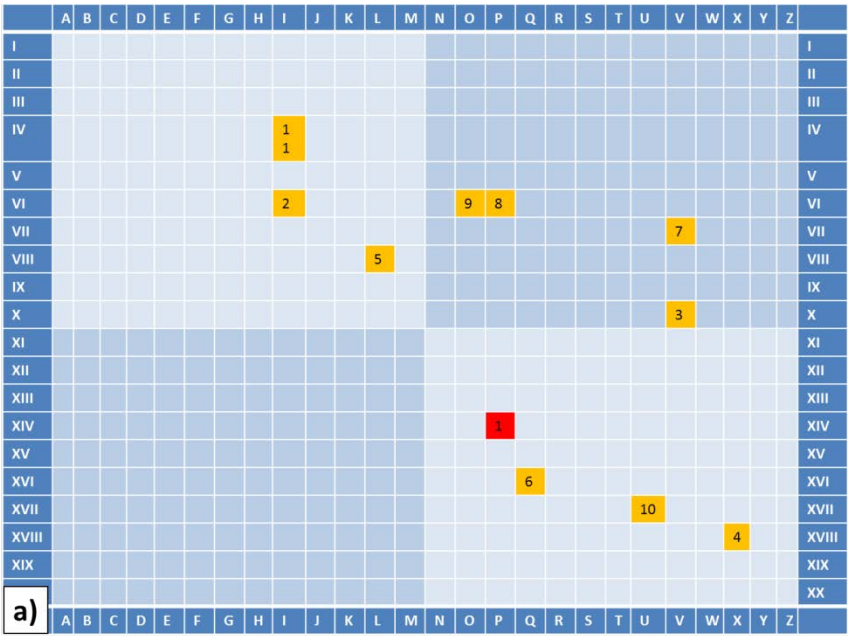

a) Theoretical design of the marker pattern.

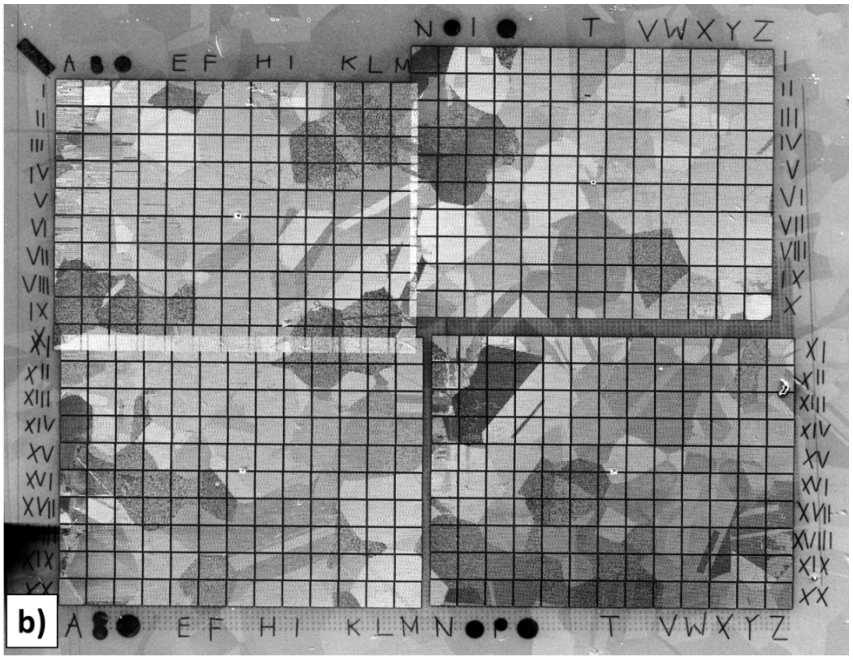

b) Actual resulting pattern overlaid over the region where EBSD analysis was performed. The marks from the EBSD analysis are still visible at the bottom of the image as dark dots in a 2µm x 2µm steps array. The red and orange coloured fields in a) represent the most promising areas for correlative microscopy study showing strong contrasting features in the SEM images numbered in the order of preference as detailed on the following pages.

Region 1 was studied and is shown in the main body of the thesis.

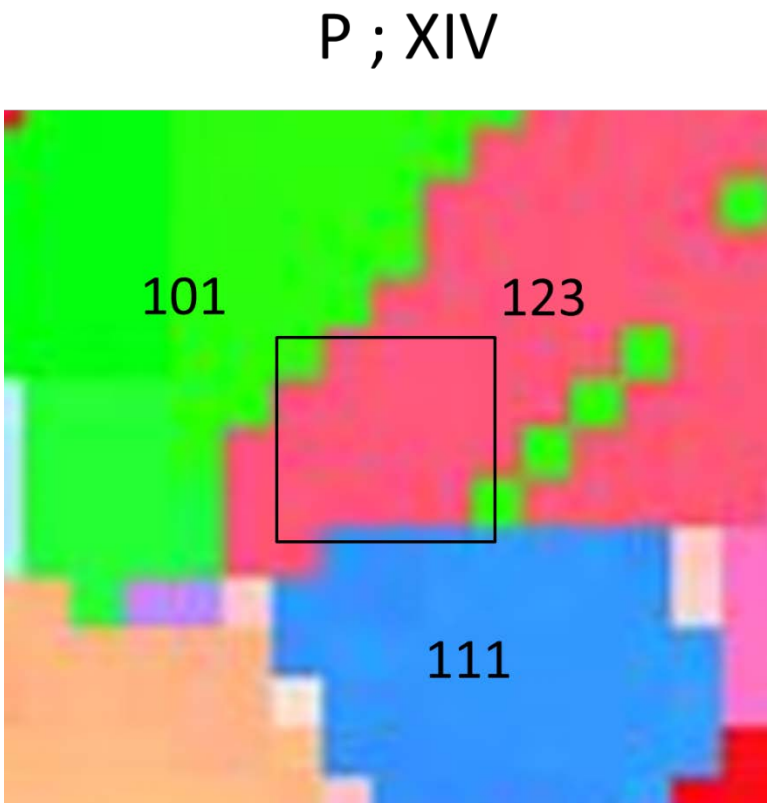

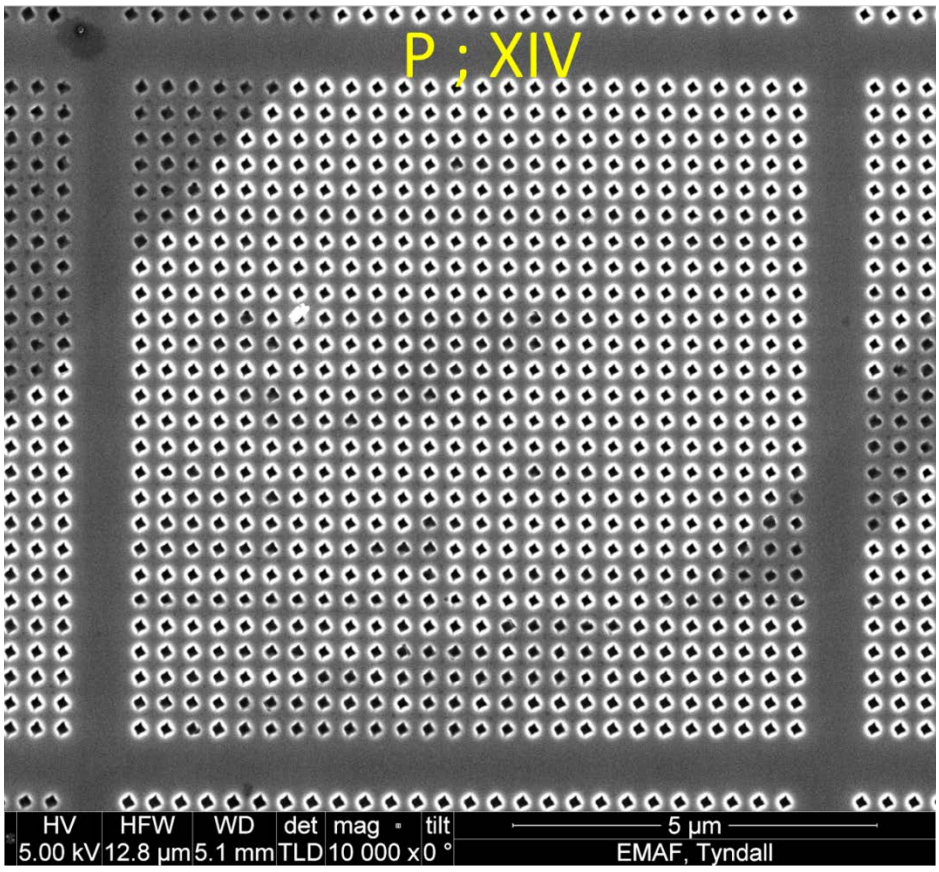

Region 2

I ; VI

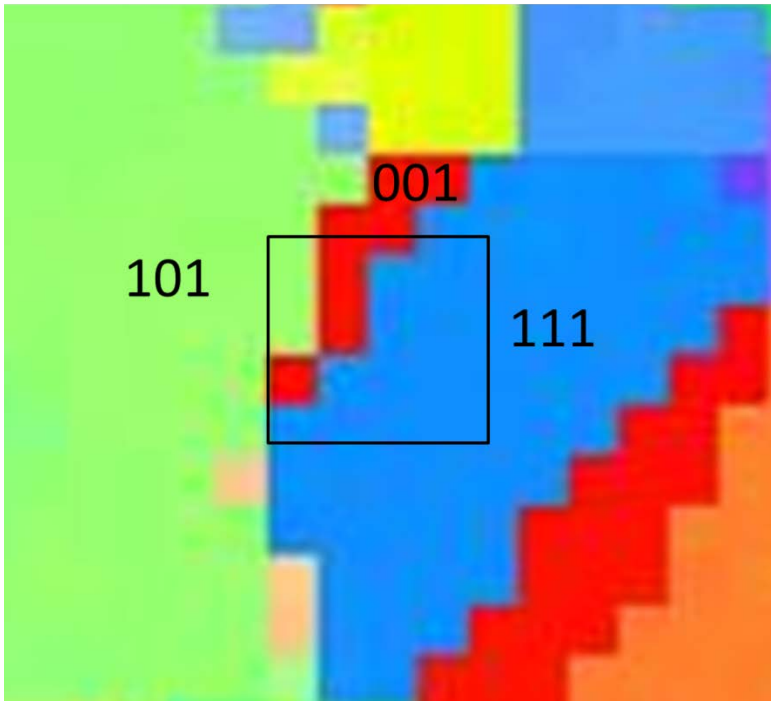
001
101
111

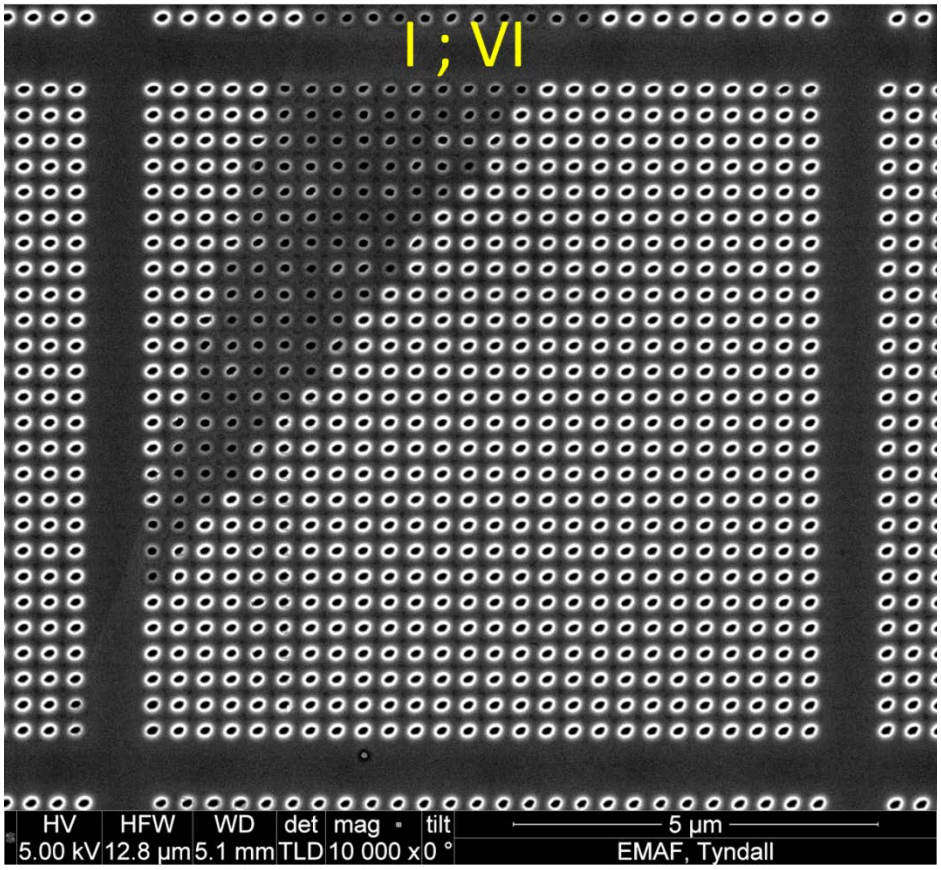
I ; VI
HV
5.00 kV
HFW
12.8 µm
WD
5.1 mm
det
TLD
mag
10 000 x
tilt
0 °
5 µm
EMAF, Tyndall

Region 3

V ; X

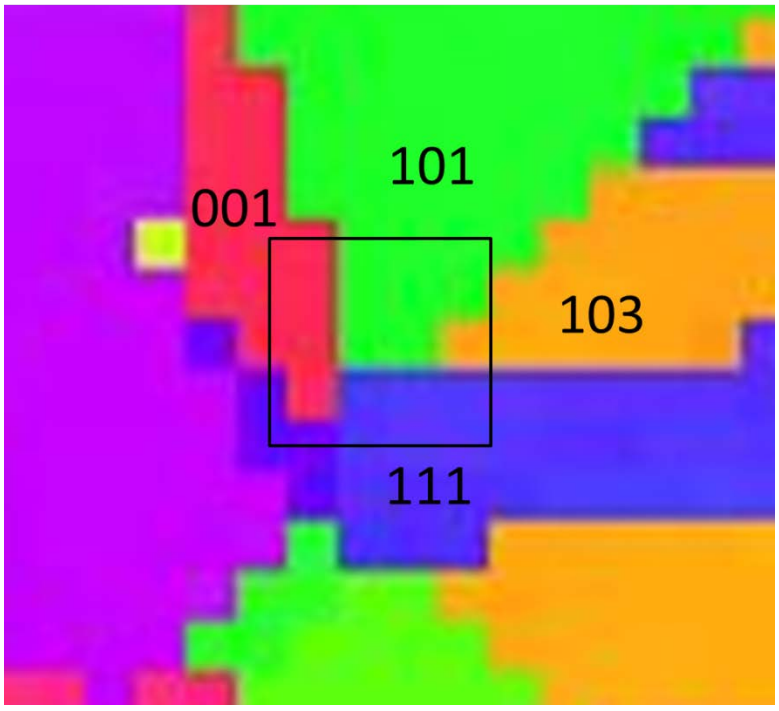
101
001
103
111

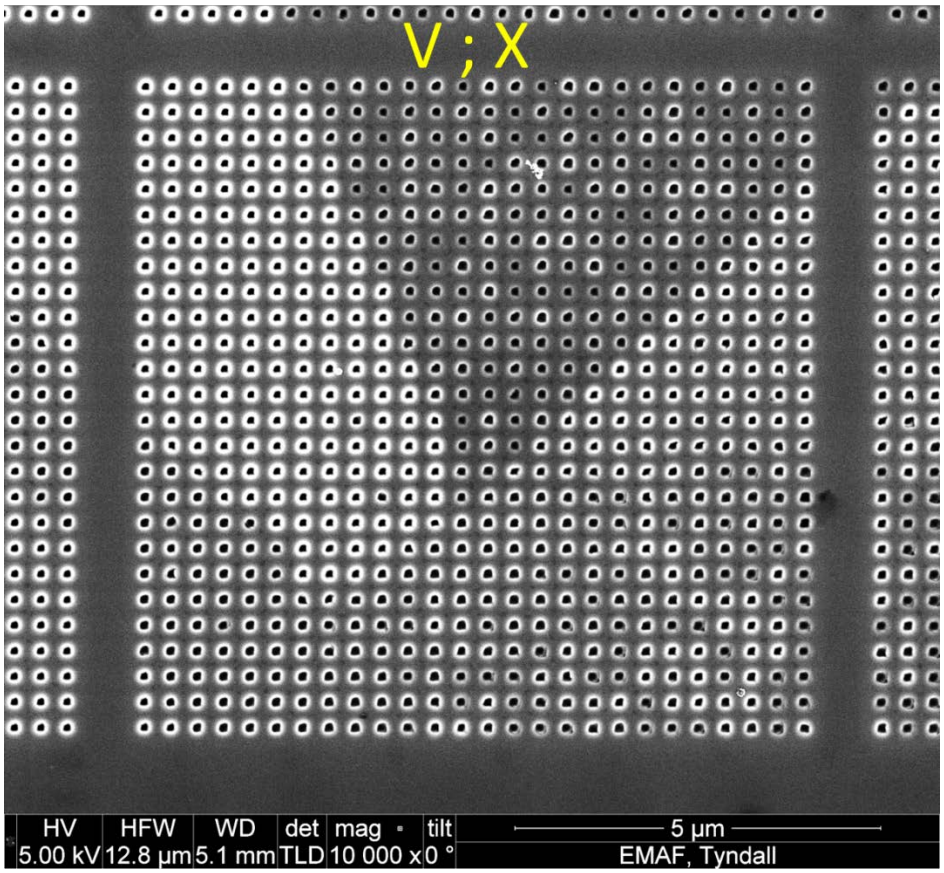
V ; X
HV
5.00 kV
HFW
12.8 µm
WD
5.1 mm
det
TLD
mag
10 000 x
tilt
0 °
5 µm
EMAF, Tyndall

Region 4

X ; XVIII

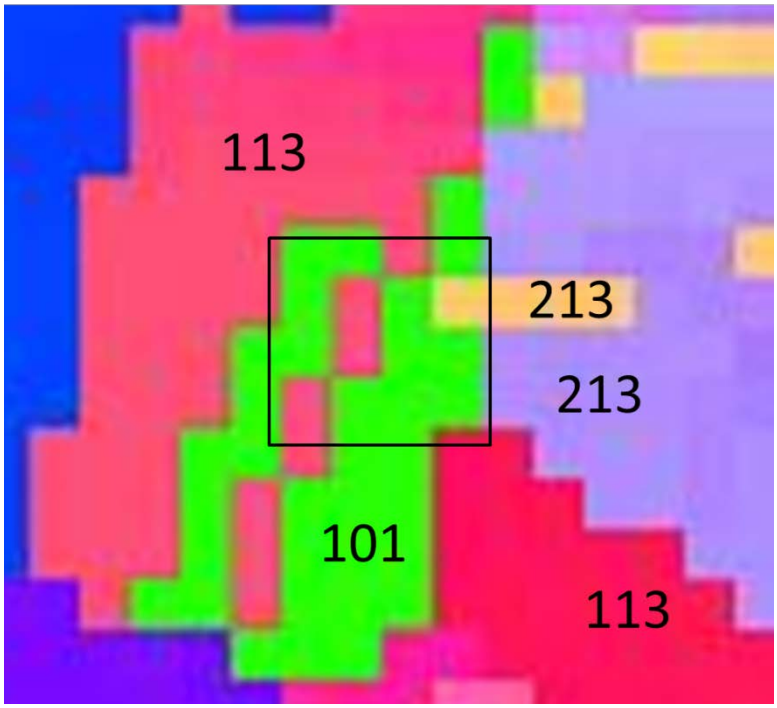

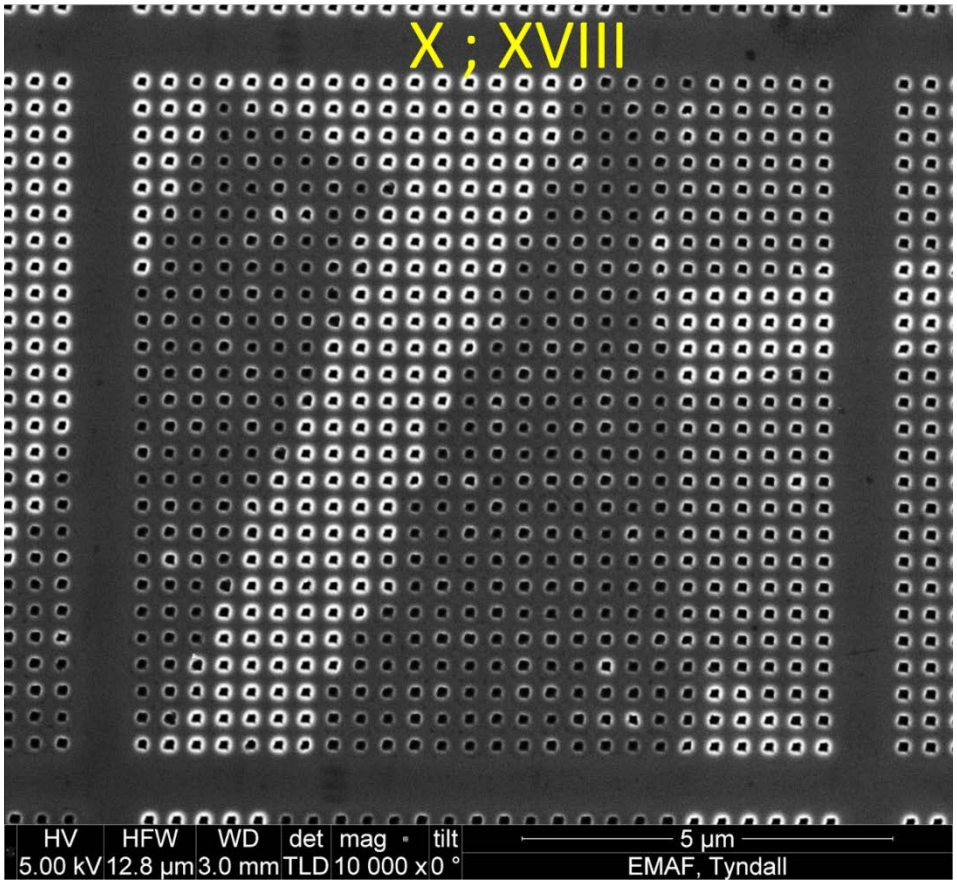

Region 5

L ; VIII

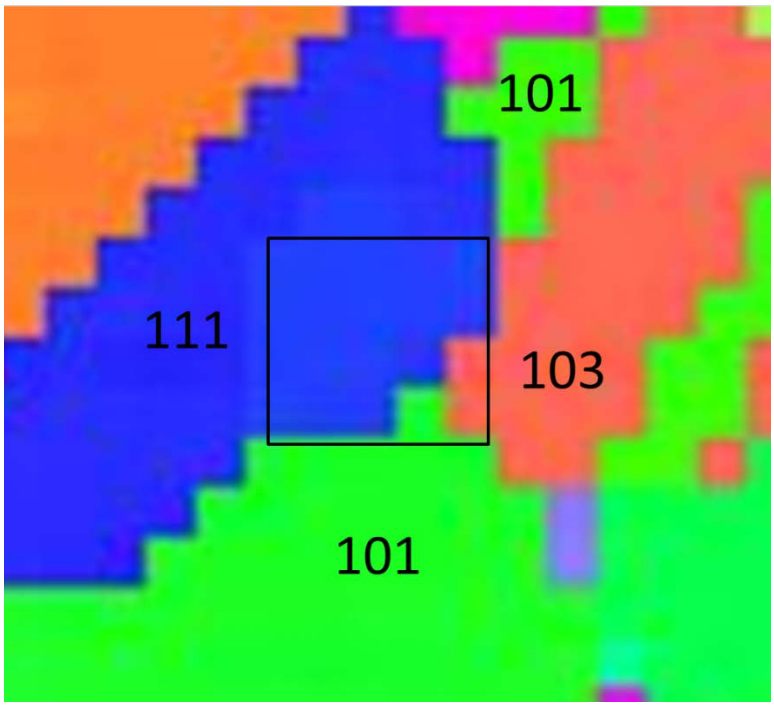

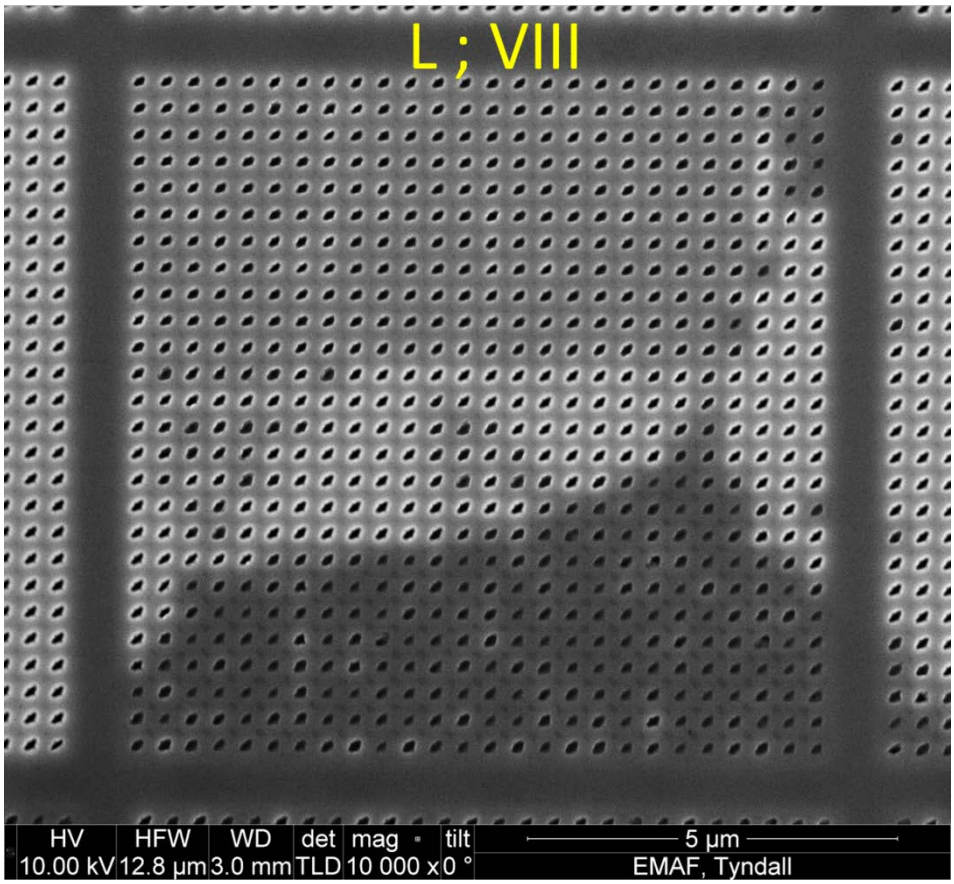

Region 6

Q ; XVI

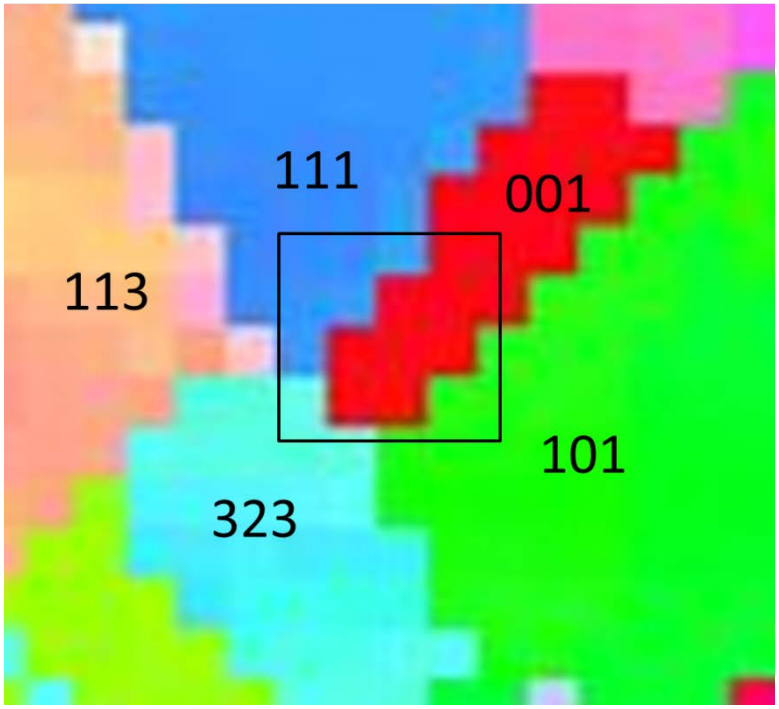

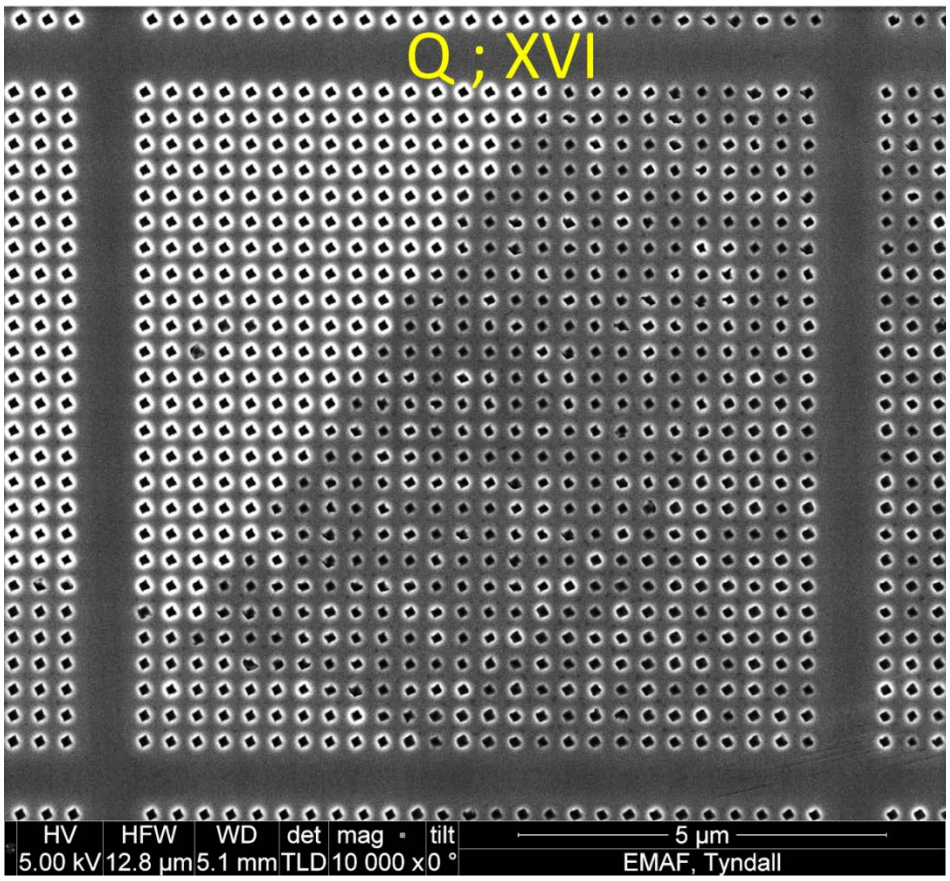

Region 7

V ; VII

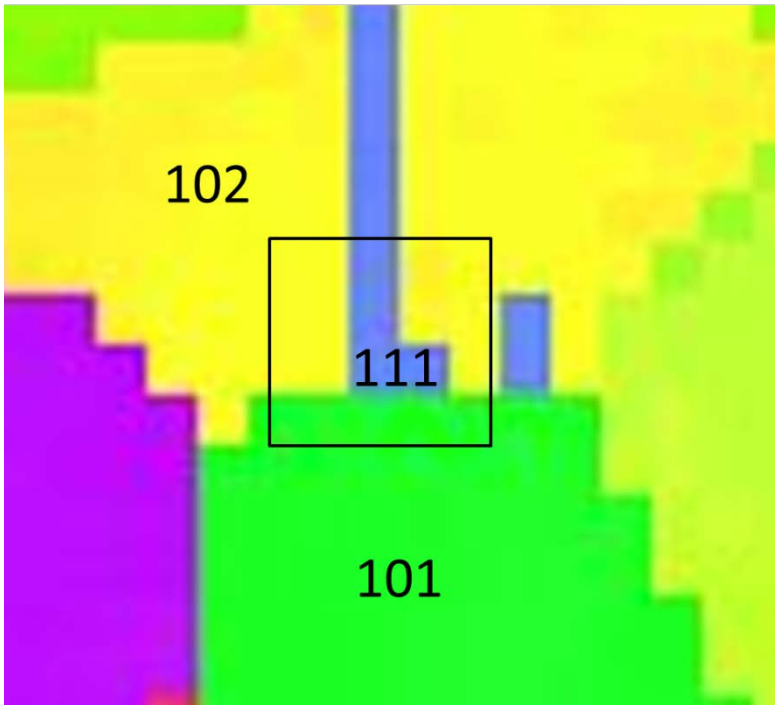

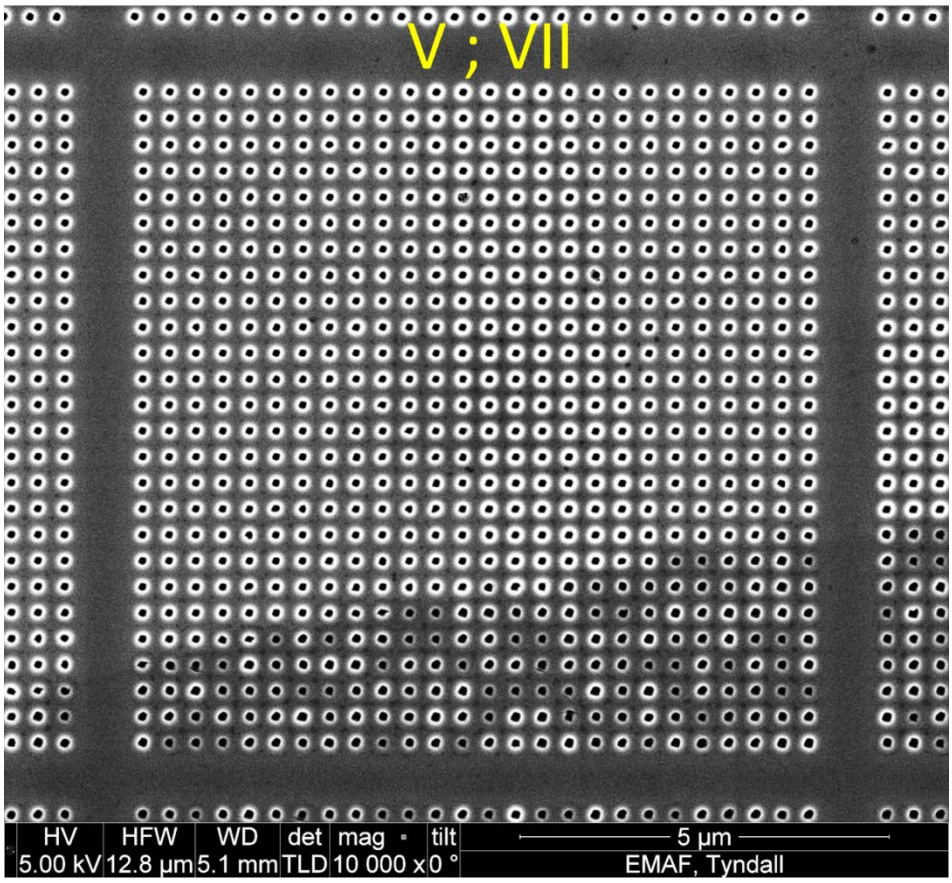

Region 8

P ; VI

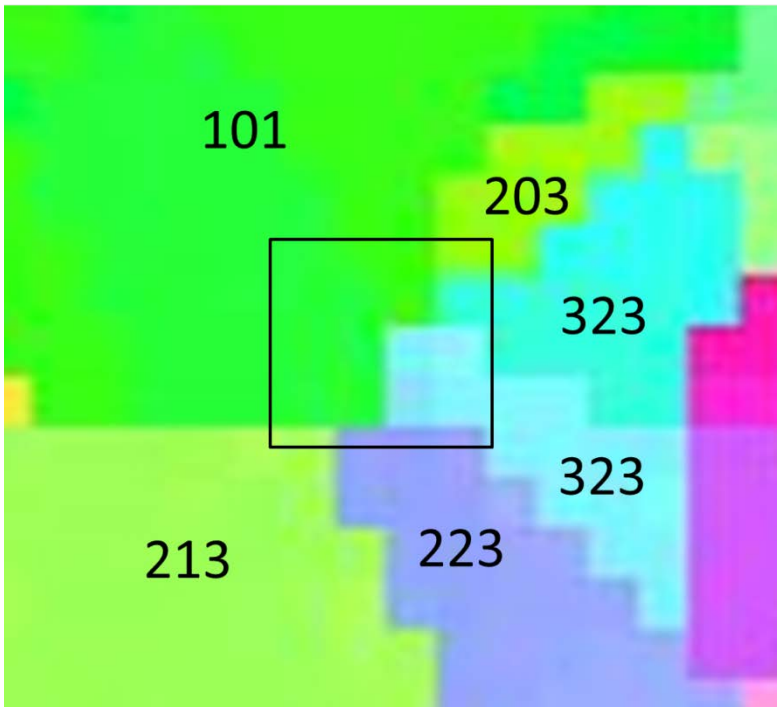
101
203
323
323
213
223

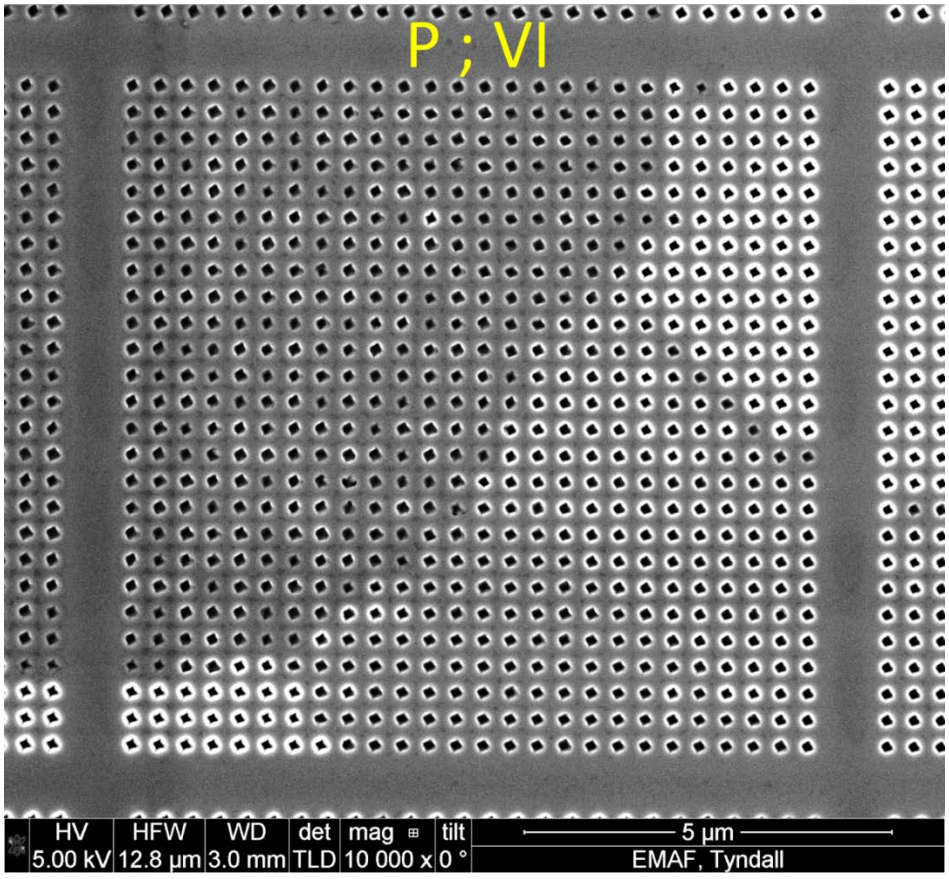
P ; VI
HV
5.00 kV
HFW
12.8 µm
WD
3.0 mm
det
TLD
mag
10 000 x
tilt
0 °
5 µm
EMAF, Tyndall

Region 9

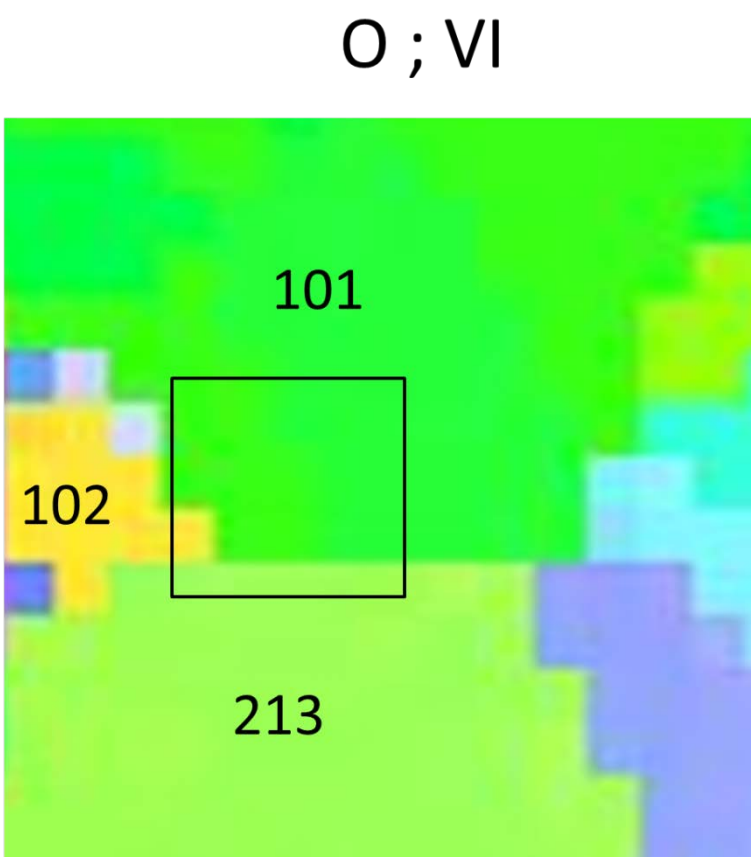
O ; VI
101
102
213

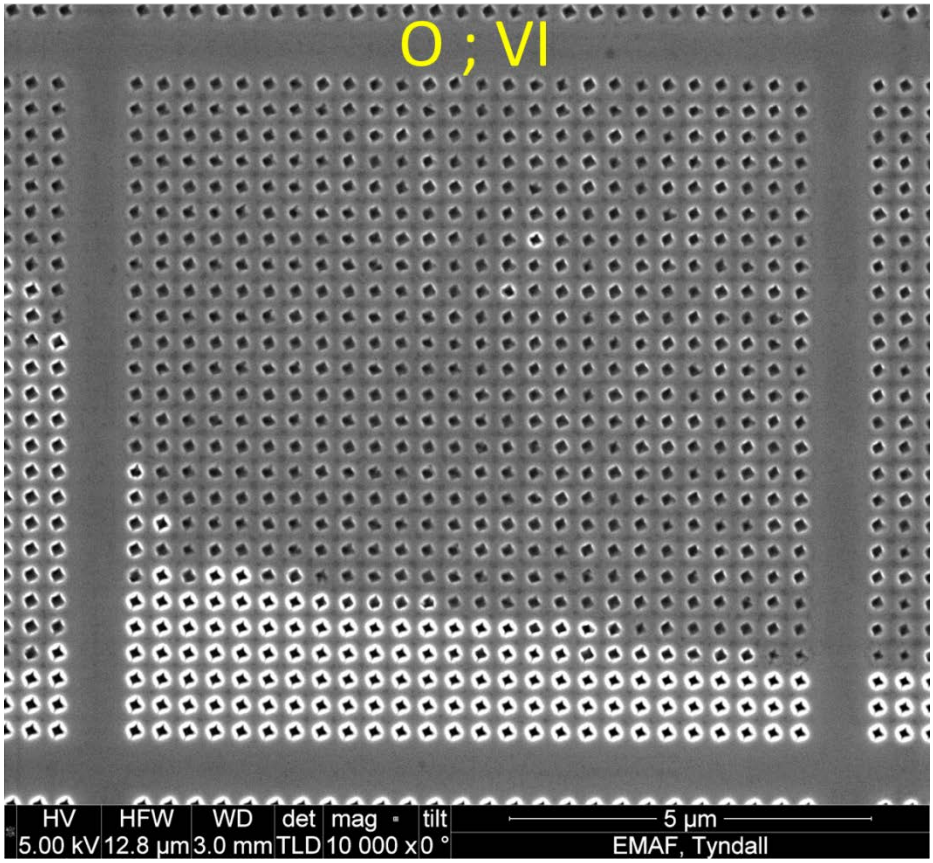
O ; VI
HV
5.00 kV
HFW
12.8 µm
WD
3.0 mm
det
TLD
mag
10 000 x
tilt
0 °
5 µm
EMAF, Tyndall

Region 10

U ; XVII

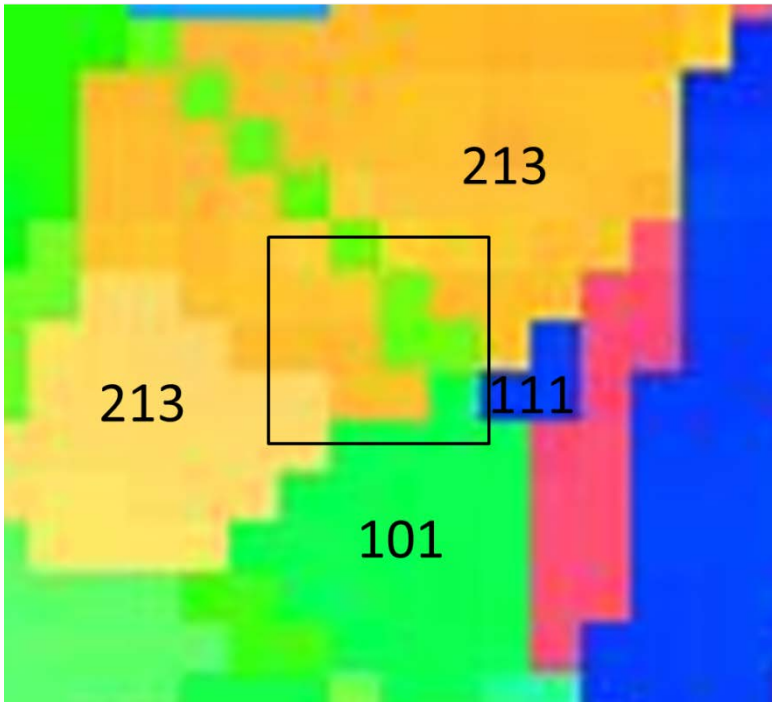

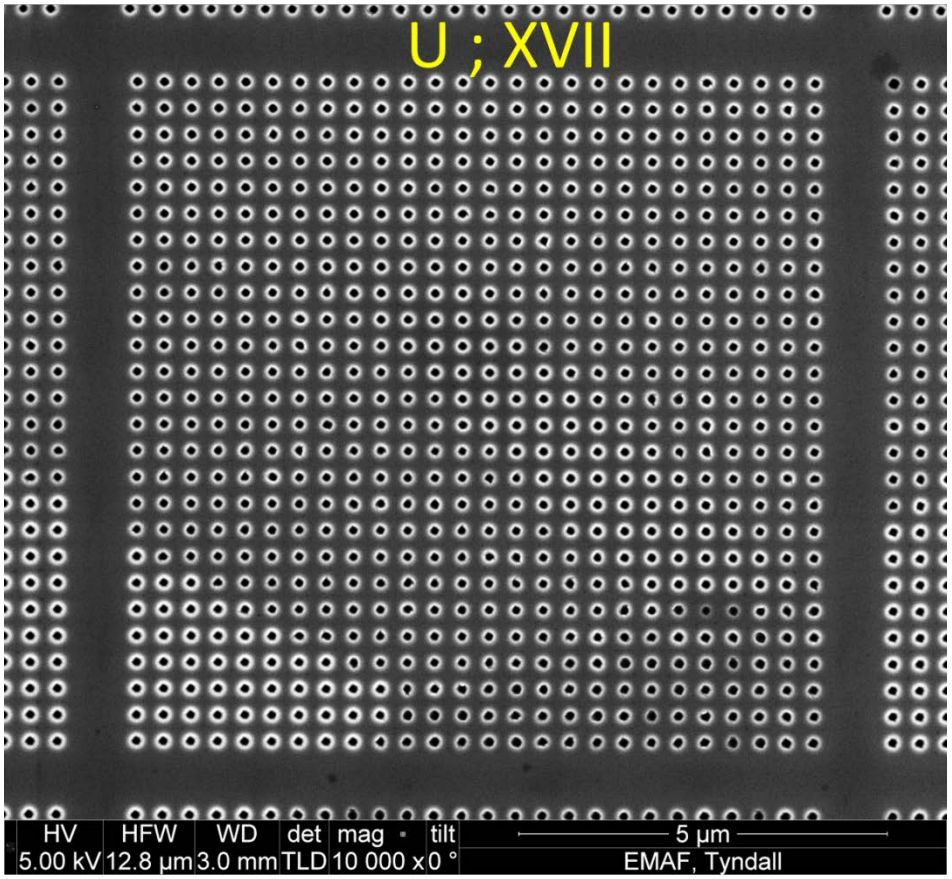

Region 11

I ; IV

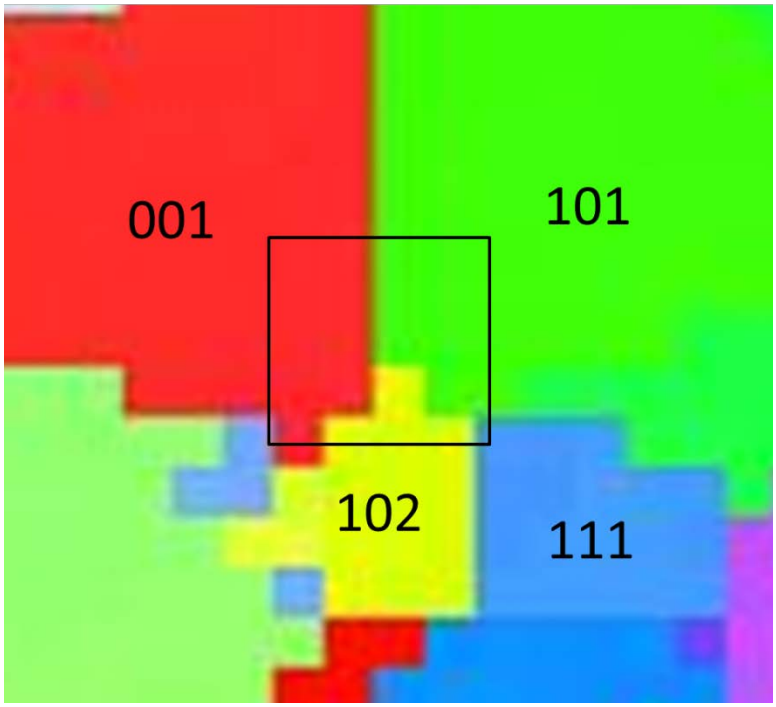

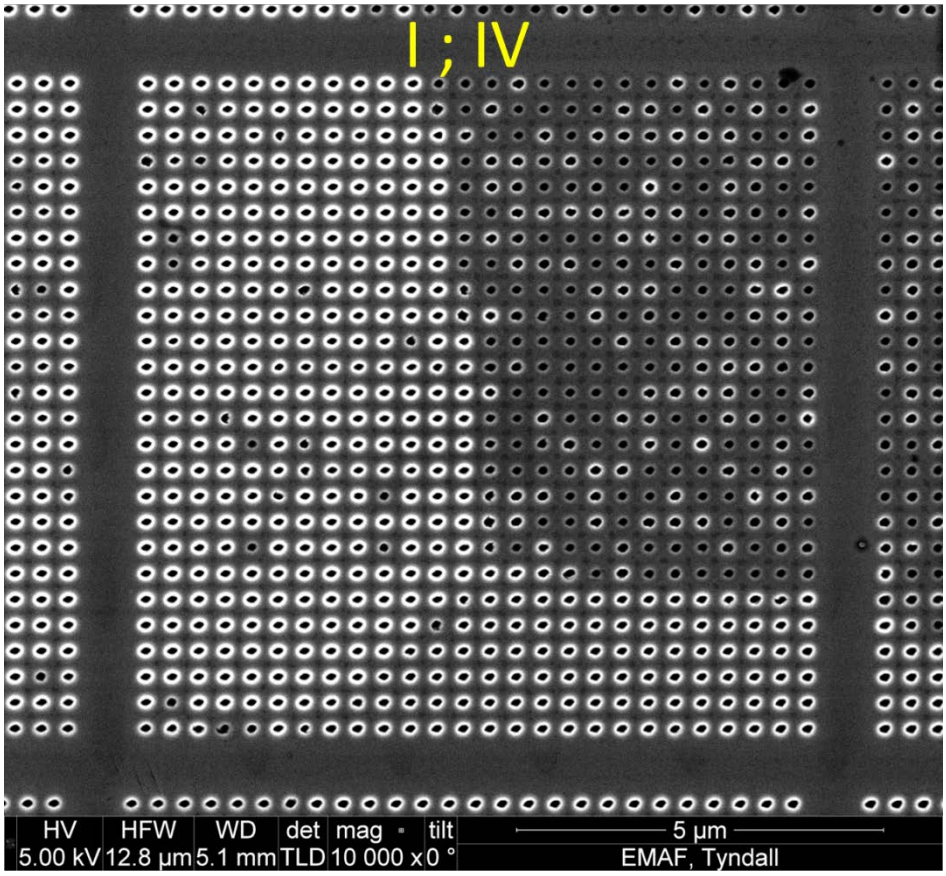

B. The synthesis of the BTFMO films on sapphire caused the appearance of a mixed phases as is shown in the following pages.

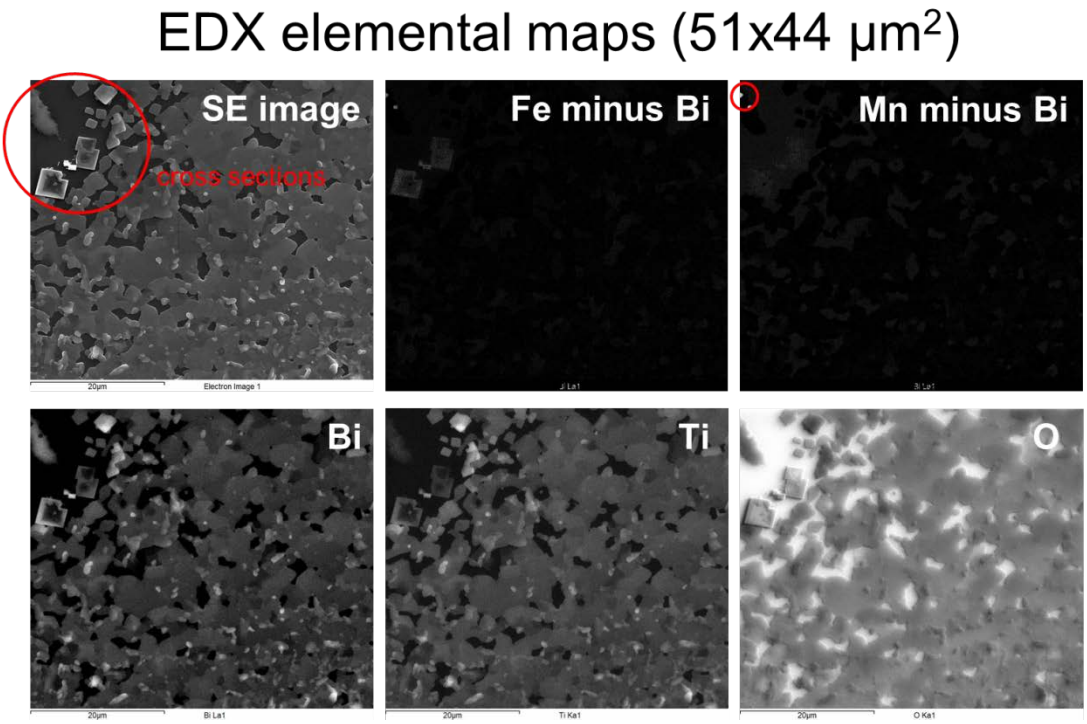

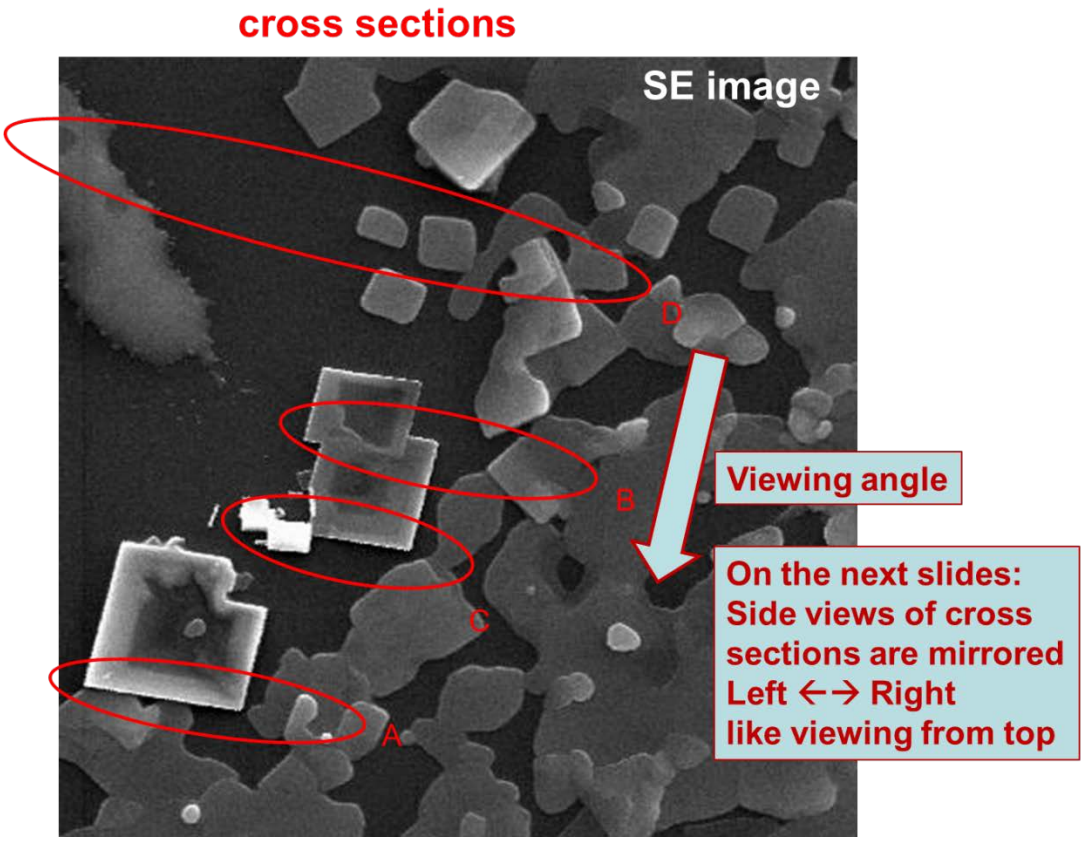

cross sections

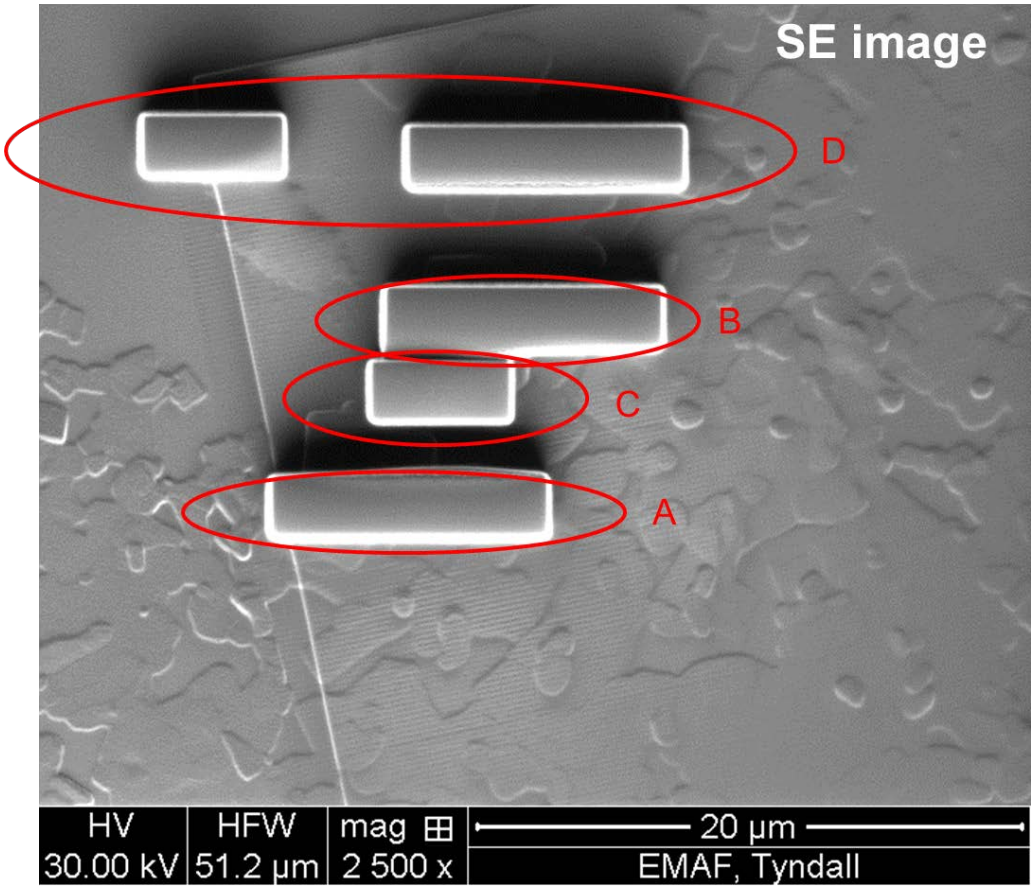

Cross section A (part 1)

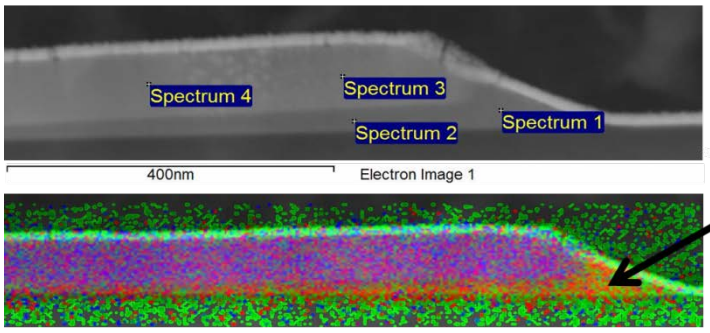

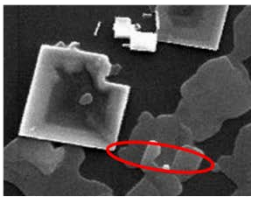

Bi rich area (Spectra 1, 2)

Bi – red
Ti – blue
Fe – green

EDX point spectra
(in weight%)

Spectrum	Ti	Mn	Fe	Bi	Total
Spectrum 1	1.53	2.81	3.83	91.83	100.00
Spectrum 2	2.24	3.50	4.69	89.56	100.00
Spectrum 3	13.70	2.10	5.99	78.22	100.00
Spectrum 4	13.72	2.24	5.52	78.53	100.00

HRTEM and SAED (Cross section A (part 1))

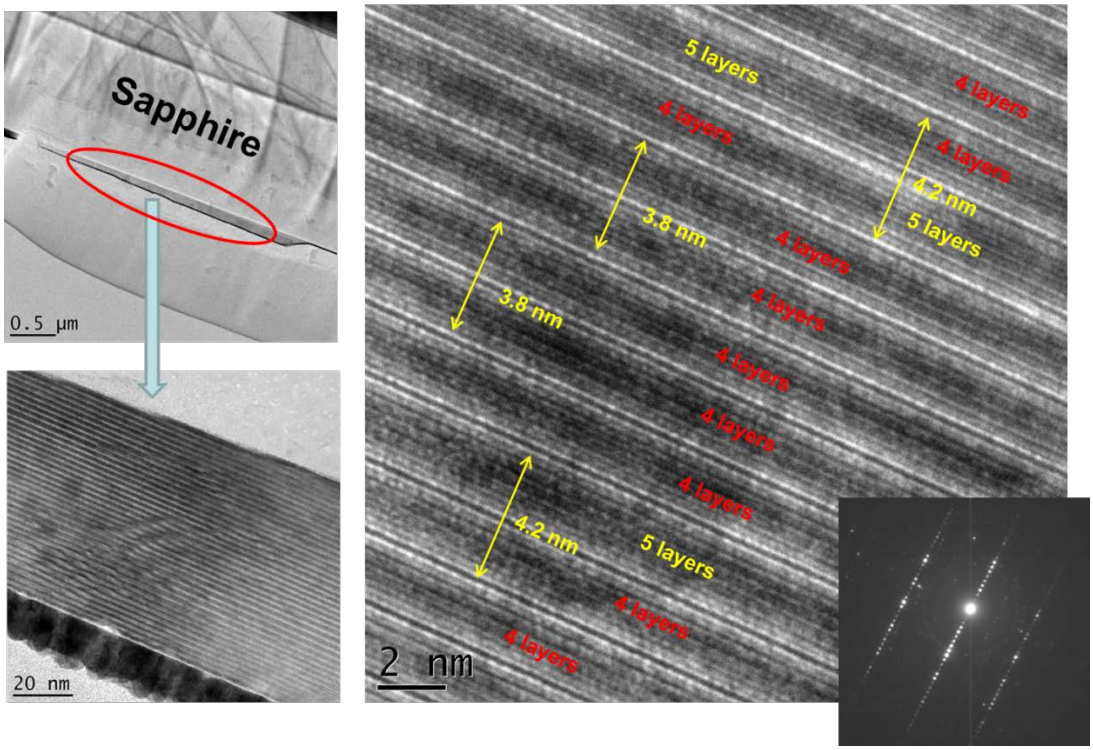

HRTEM (Cross section A (part 1))

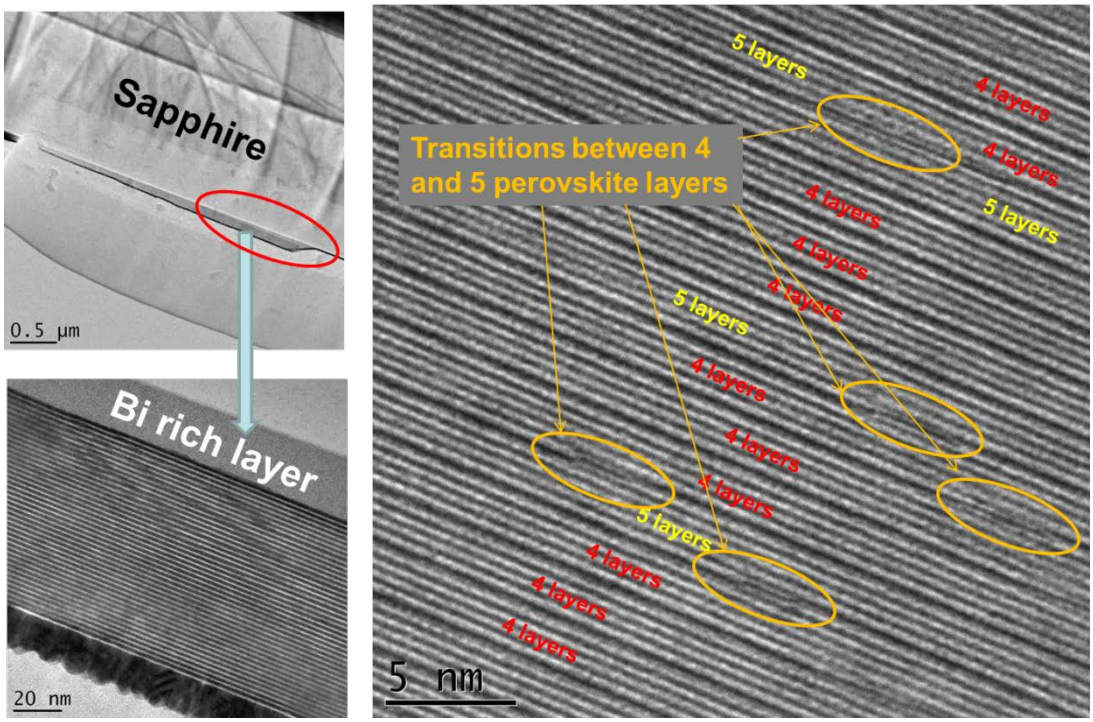

Cross section A (part 2 – Fe/Mn rich area)

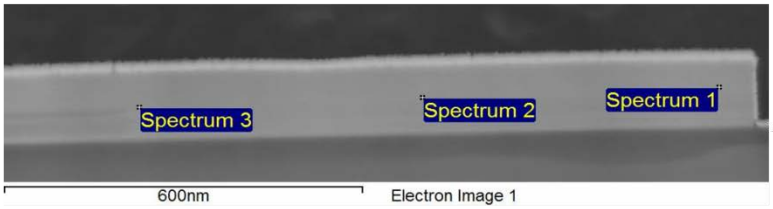

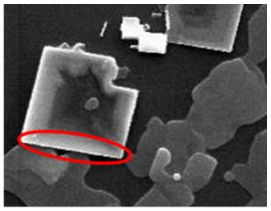

EDX point spectra
(in weight%)

Spectrum	Ti	Mn	Fe	Bi	Total
Spectrum 1	4.26	9.51	14.54	71.69	100.00
Spectrum 2	5.13	9.05	16.59	69.24	100.00
Spectrum 3	5.08	9.46	14.62	70.83	100.00

HRTEM and SAED (Cross section A (part 2 – Fe/Mn rich area))

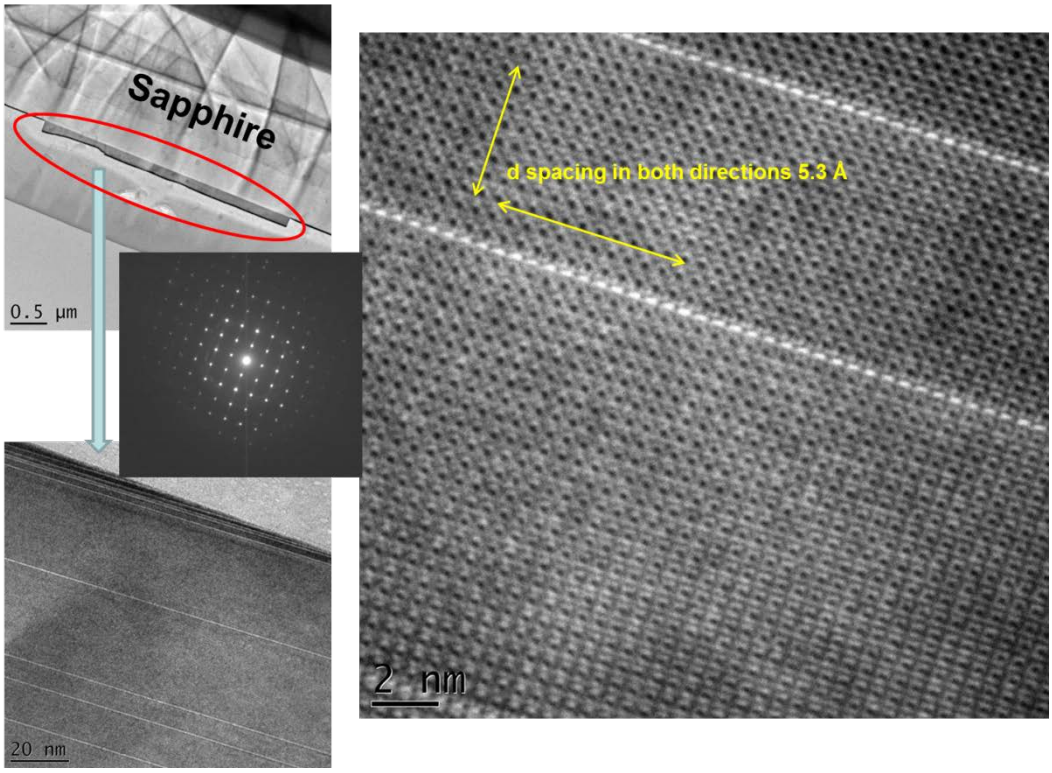

HRTEM (Cross section A (part 2 – Fe/Mn rich area continued))

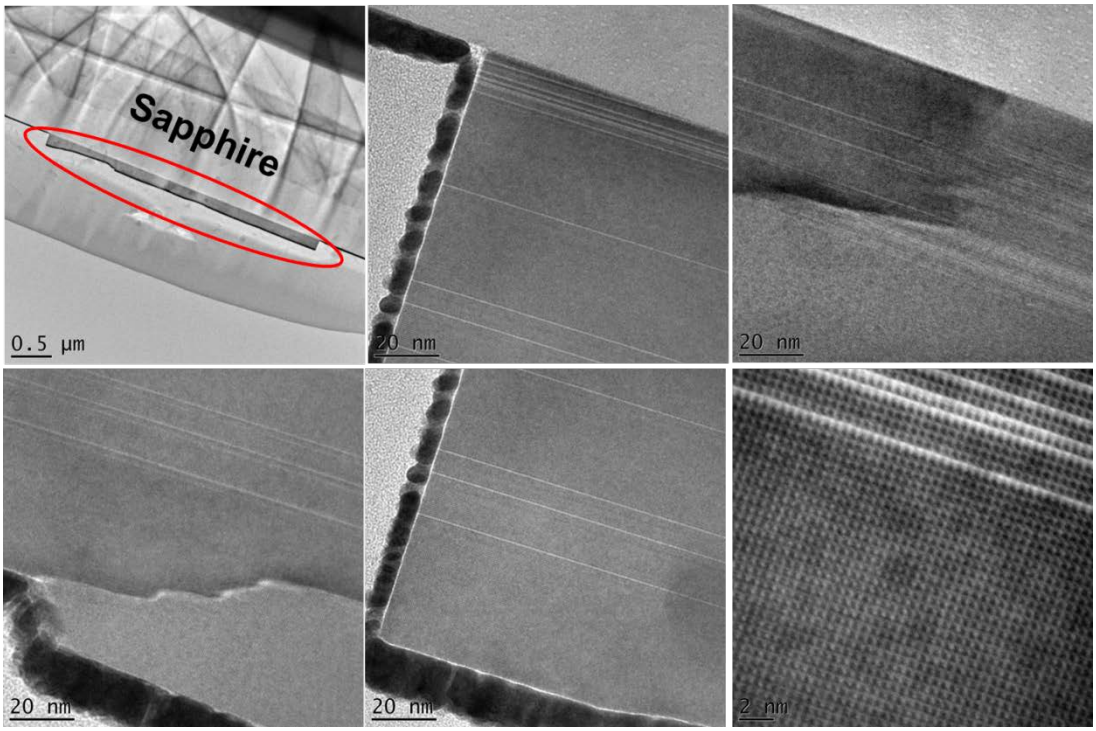

Cross section B (part 1)

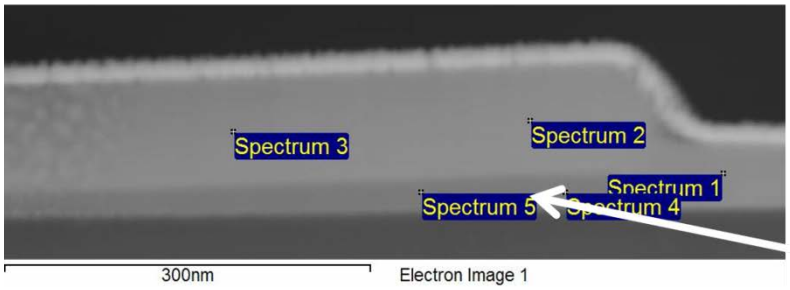

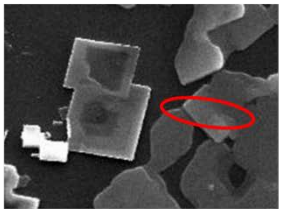

Bi rich area (Spectra 4, 5)

EDX point spectra (in weight%)

Spectrum	Ti	Mn	Fe	Bi	Total
Spectrum 1	12.74	1.92	4.14	81.20	100.00
Spectrum 2	12.43	1.69	5.16	80.73	100.00
Spectrum 3	11.86	1.58	5.40	81.16	100.00
Spectrum 4	2.74	3.27	4.30	89.70	100.00
Spectrum 5	3.22	2.26	4.01	90.51	100.00

HRTEM and SAED (Cross section B (part 1))

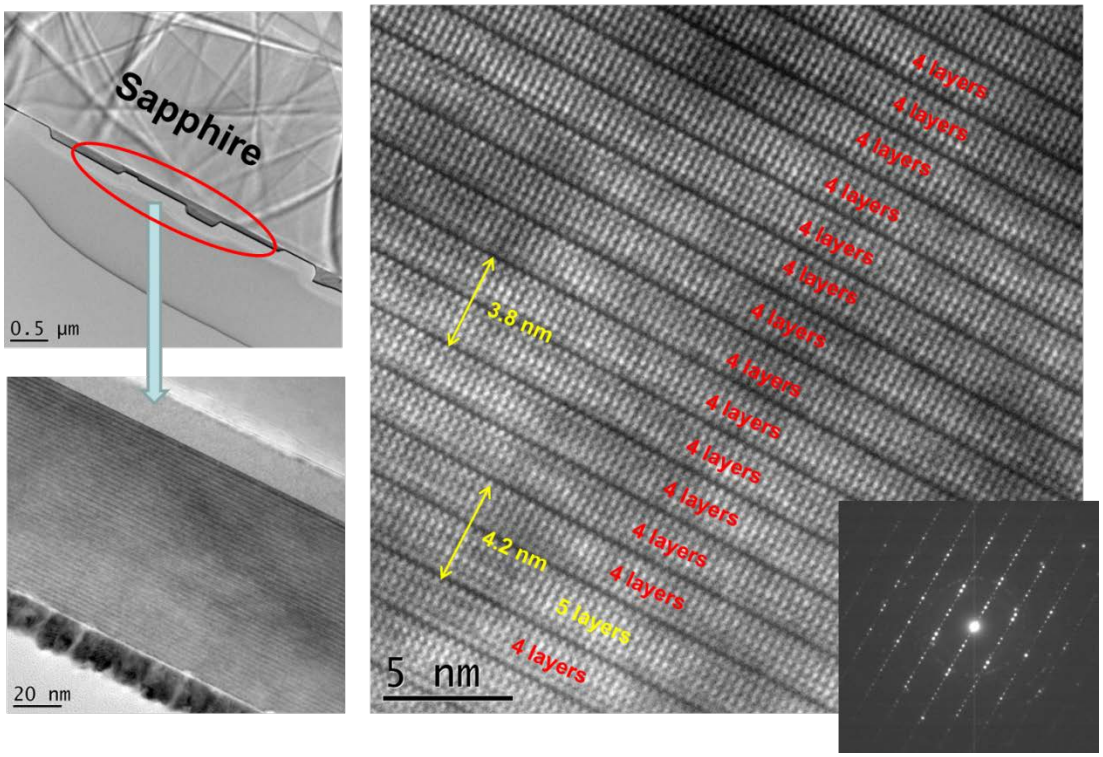

HRTEM (Cross section B (part 1 continued))

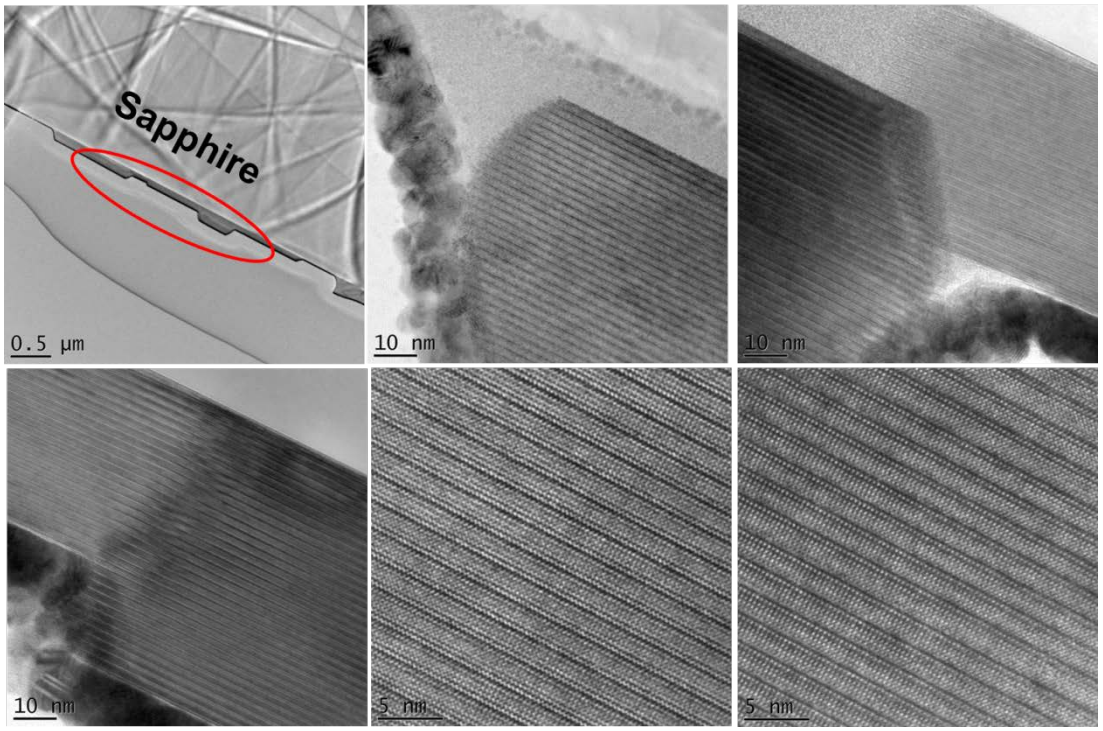

Cross section B (part 2)

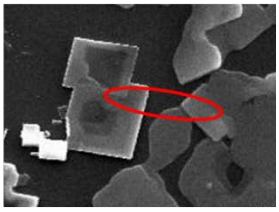

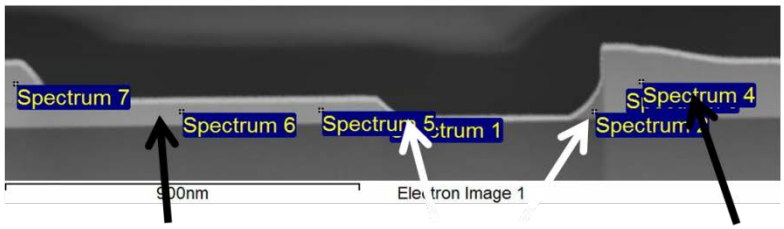

Aurivilius phase (Spectra 5 – 7)

Bi rich area (Spectra 1, 2)

Fe/Mn rich area (Spectra 3, 4)

EDX point spectra (in weight%)

Spectrum	Ti	Mn	Fe	Bi	Total
Spectrum 1	4.51	2.34	3.67	89.48	100.00
Spectrum 2	2.75	1.66	2.15	93.43	100.00
Spectrum 3	4.18	9.08	15.23	71.51	100.00
Spectrum 4	4.45	8.72	14.51	72.32	100.00
Spectrum 5	12.78	1.86	4.67	80.69	100.00
Spectrum 6	11.94	1.71	4.73	81.62	100.00
Spectrum 7	13.30	1.41	4.75	80.54	100.00

HRTEM and SAED (Cross section B (part 2 – Fe/Mn rich area))

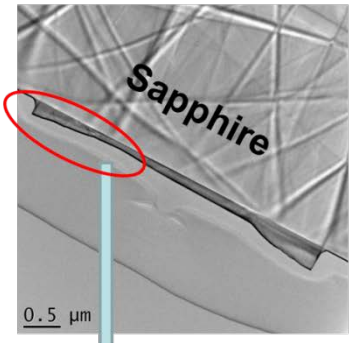

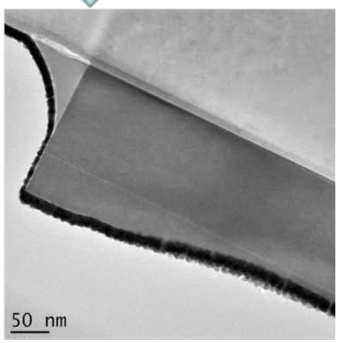

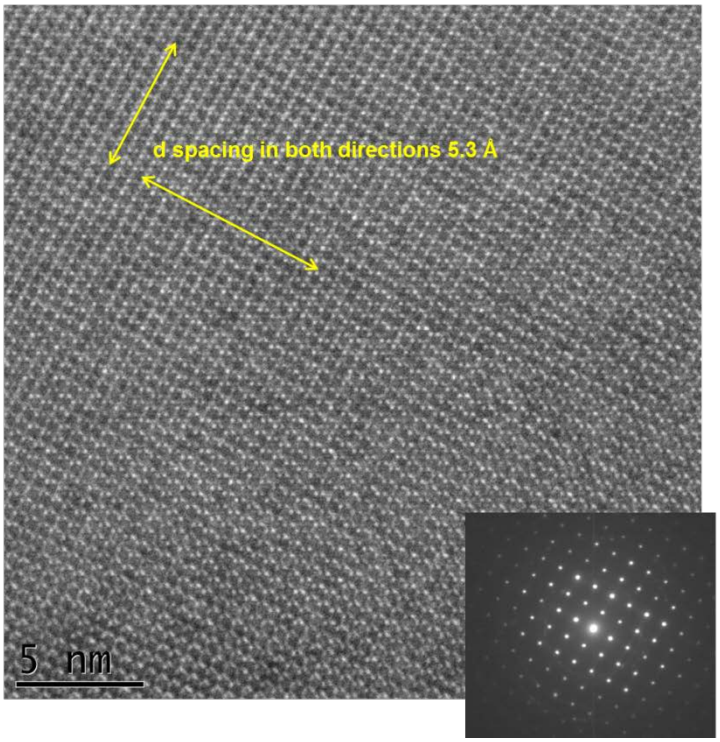

Cross section C

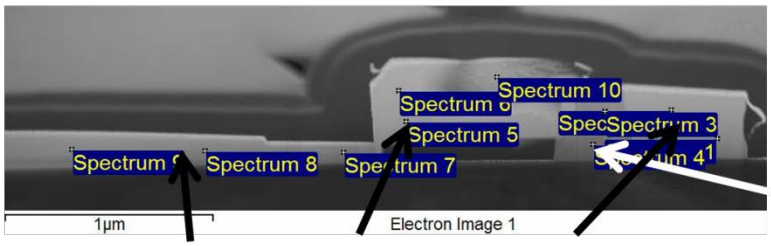

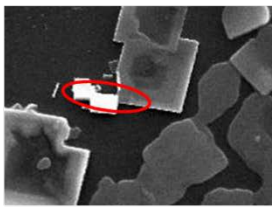

Bi rich area?? (Spectrum 4)

Fe/Mn rich areas (all spectra except #4) EDX point spectra (in weight%)

Spectrum	Ti	Mn	Fe	Bi	Total
Spectrum 1	4.30	10.17	16.33	69.19	100.00
Spectrum 2	5.94	9.85	16.78	67.44	100.00
Spectrum 3	1.48	6.19	10.00	82.33	100.00
Spectrum 4	1.66	3.47	4.60	90.27	100.00
Spectrum 5	6.58	10.64	16.13	66.65	100.00
Spectrum 6	6.56	10.19	15.25	68.00	100.00
Spectrum 7	3.96	9.57	17.03	69.44	100.00
Spectrum 8	4.66	9.68	16.19	69.47	100.00
Spectrum 9	4.50	9.54	16.18	69.78	100.00
Spectrum 10	6.23	10.69	13.39	69.69	100.00

HRTEM and SAED (Cross section C (Fe/Mn rich area))

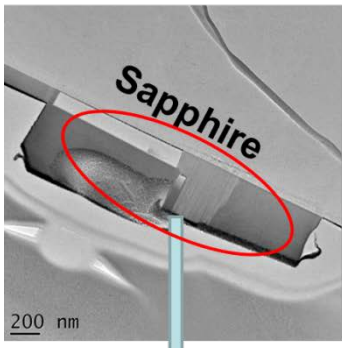

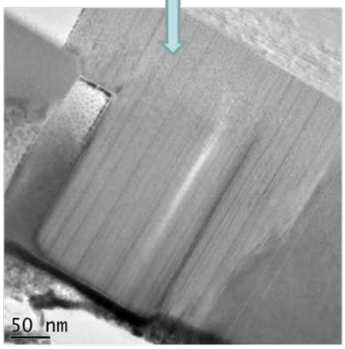

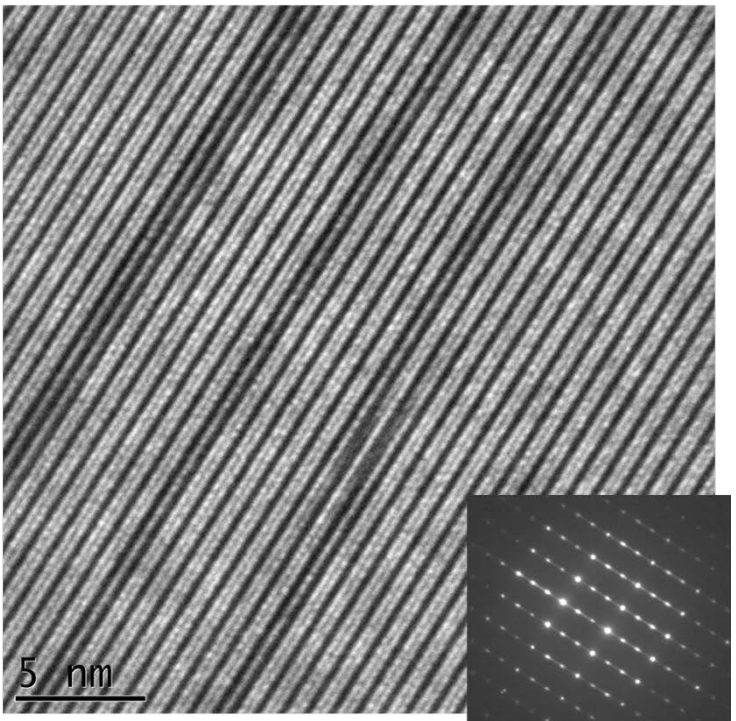

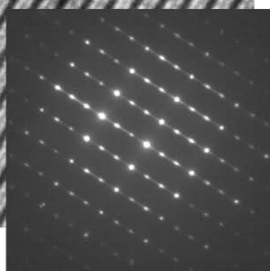

HRTEM (Cross section C (Fe/Mn rich area continued))

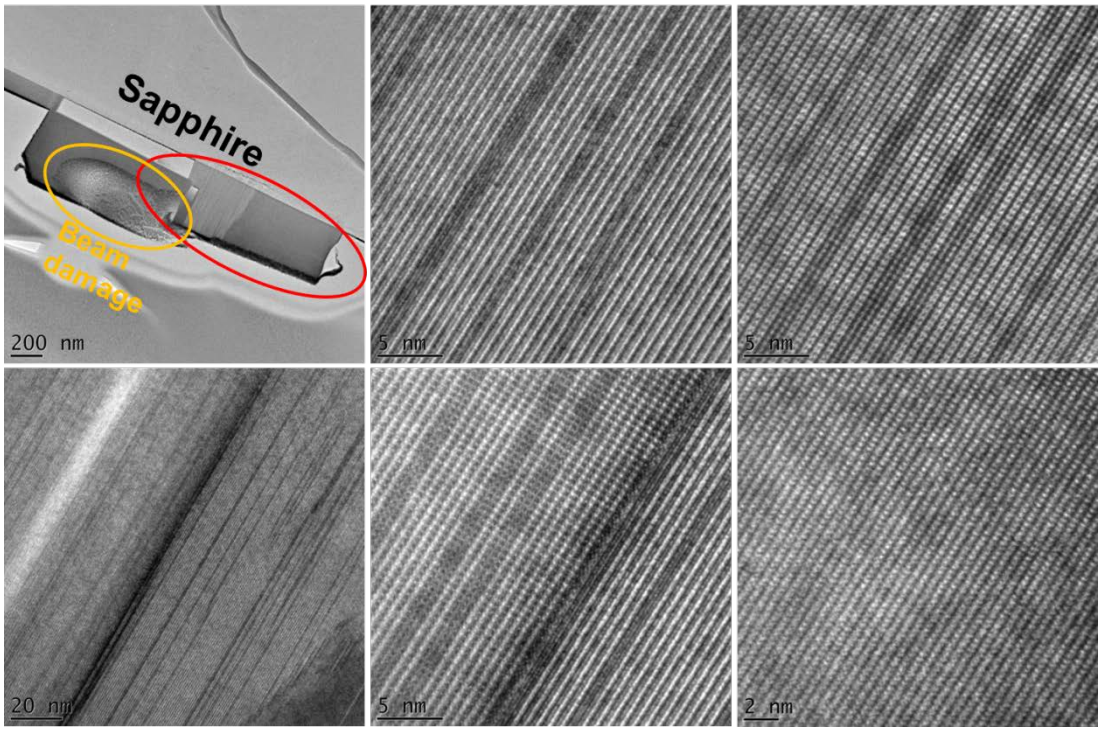

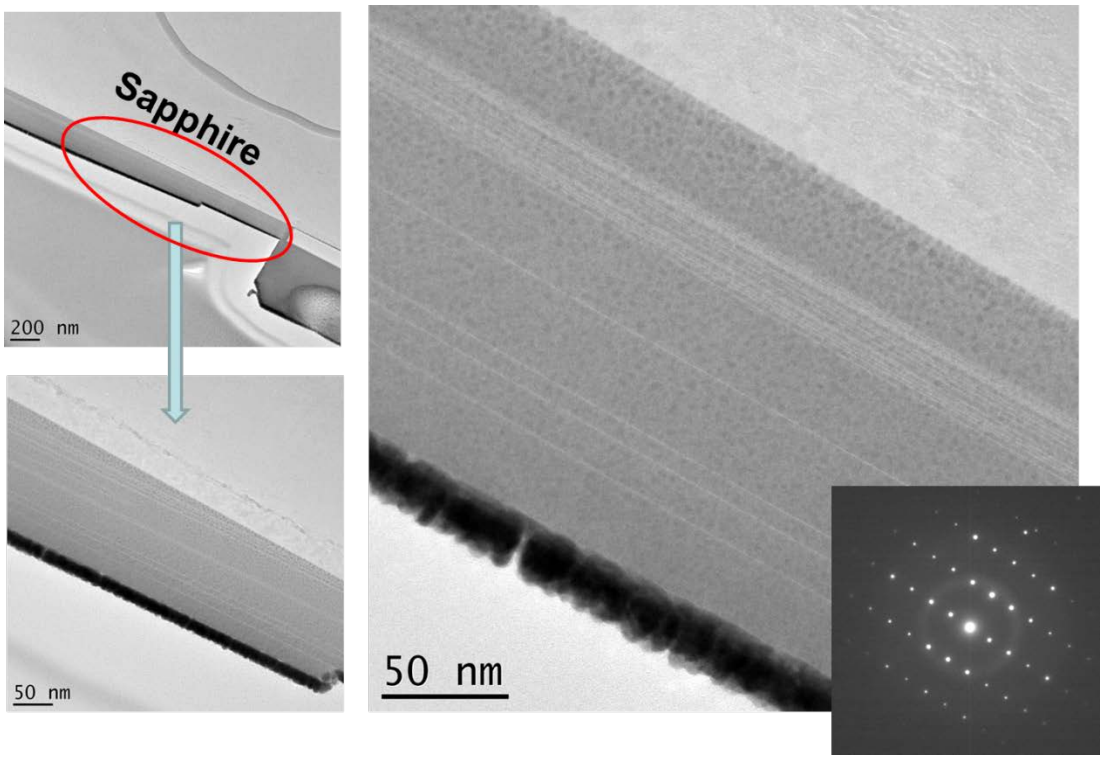

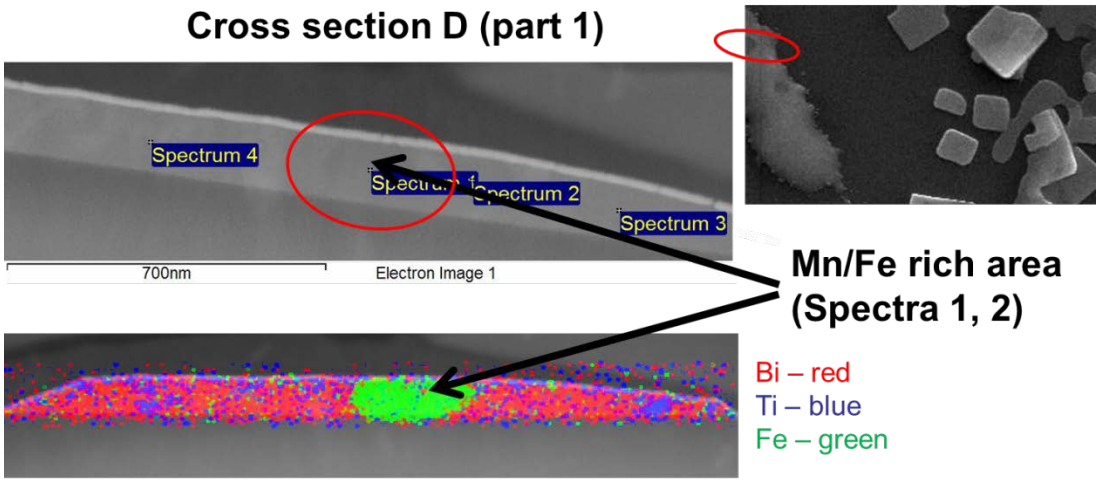

EDX point spectra (in weight%)

Spectrum	Ti	Mn	Fe	Bi	Total
Spectrum 1	0.98	51.49	25.52	22.01	100.00
Spectrum 2	1.17	52.42	26.70	19.71	100.00
Spectrum 3	2.13	1.70	4.72	91.46	100.00
Spectrum 4	3.39	1.49	6.89	88.23	100.00

HRTEM and SAED (Cross section D (part 1 – Mn/Fe rich area))

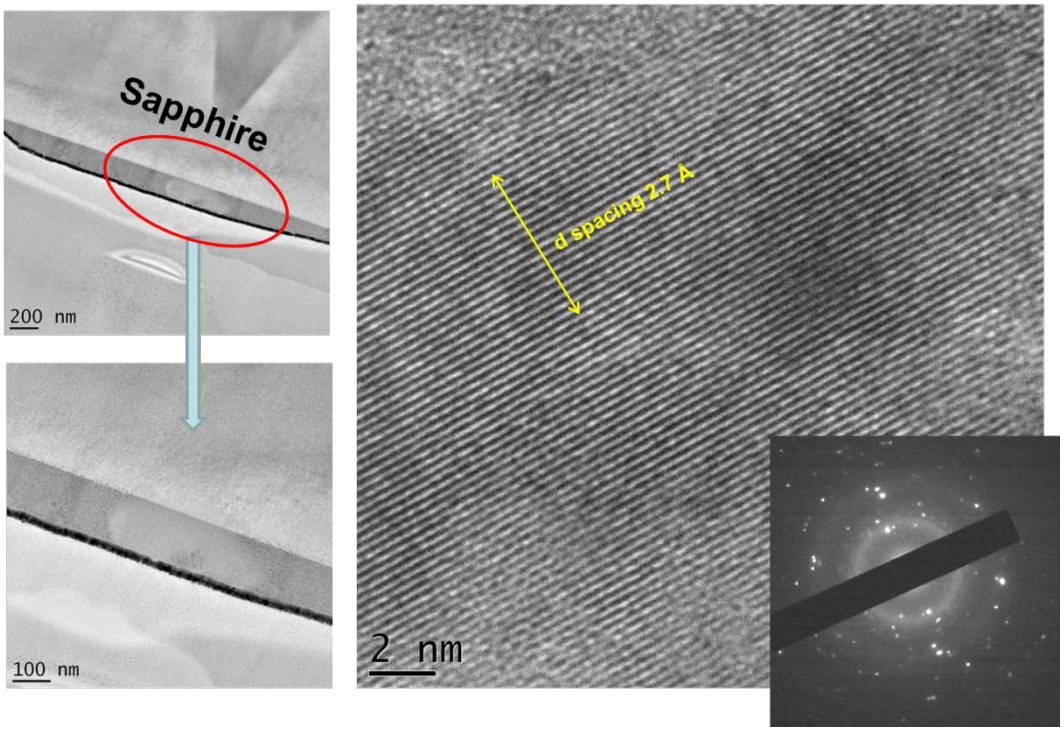

Cross section D (part 2)

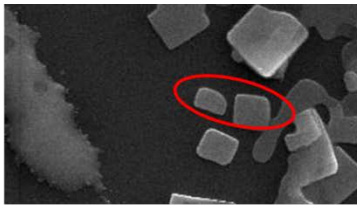

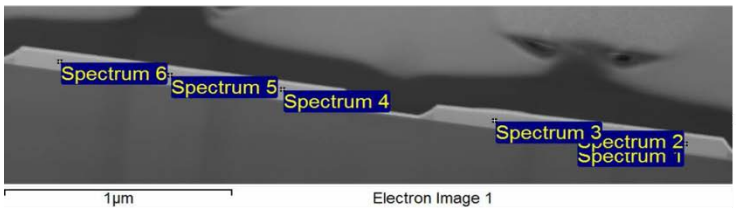

EDX point spectra (in weight%)

Spectrum	Ti	Mn	Fe	Bi	Total
Spectrum 1	14.18	1.77	5.23	78.81	100.00
Spectrum 2	13.12	2.11	5.23	79.54	100.00
Spectrum 3	12.82	1.92	4.90	80.36	100.00
Spectrum 4	13.25	1.95	5.14	79.66	100.00
Spectrum 5	12.90	2.05	5.93	79.12	100.00
Spectrum 6	13.34	1.79	5.52	79.35	100.00

Cross section D (part 3)

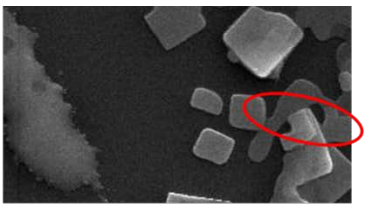

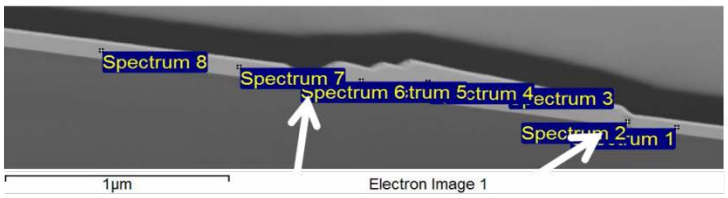

Bi rich area at the edges of Aurivilius phase (Spectra 2, 6)

EDX point spectra (in weight%)

Spectrum	Ti	Mn	Fe	Bi	Total
Spectrum 1	10.51	2.48	6.97	80.04	100.00
Spectrum 2	7.40	2.56	5.55	84.50	100.00
Spectrum 3	13.31	1.80	4.96	79.93	100.00
Spectrum 4	12.70	1.93	4.94	80.43	100.00
Spectrum 5	12.91	2.01	5.27	79.81	100.00
Spectrum 6	1.13	3.21	3.71	91.95	100.00
Spectrum 7	11.52	2.34	5.71	80.43	100.00
Spectrum 8	13.32	1.36	5.08	80.25	100.00

Cross section D (part 4)

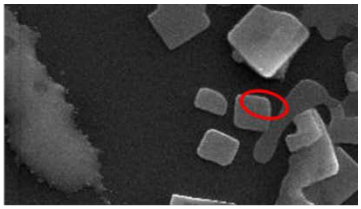

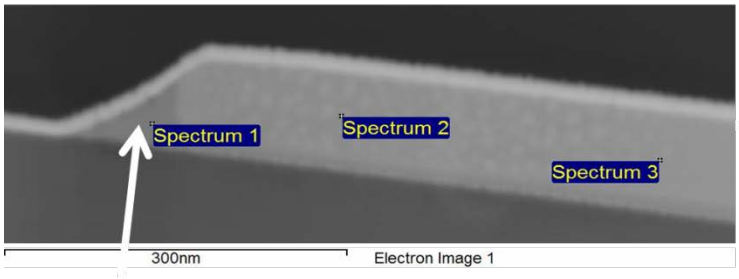

Bi rich area at the edge and underneath Aurivilius phase (Spectrum 1)

EDX point spectra (in weight%)

Spectrum	Ti	Mn	Fe	Bi	Total
Spectrum 1	1.65	2.64	3.93	91.78	100.00
Spectrum 2	12.12	1.39	5.18	81.32	100.00
Spectrum 3	12.68	1.65	5.34	80.33	100.00

HRTEM and SAED (Cross section D (part 4))

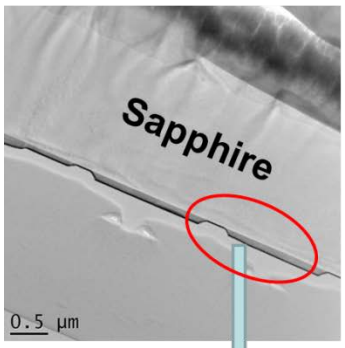

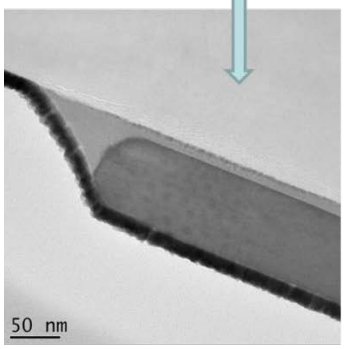

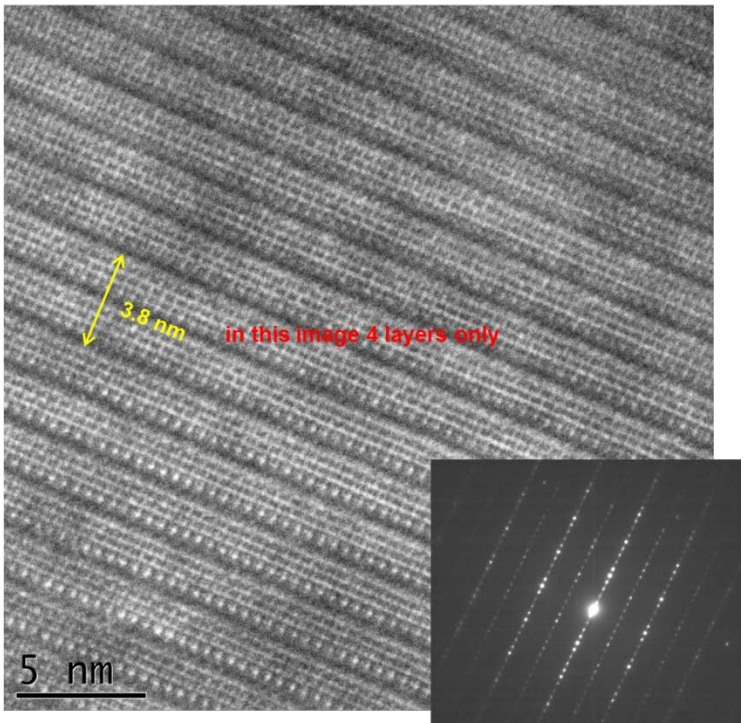

Notes and observations from the analysis shown in the previous pages:

- Aurivilius phase unit cell is mostly 3.8 nm long suggesting 4 perovskite layers per half unit cell with some areas showing 5 layers at 4.2 nm length
    - Atomic ratio Bi:Ti:Fe:Mn is approx. 20:13:5:2
- There is an amorphous substance underneath many Aurivilius crystals, also forming a meniscus at the sides of all crystals; this substance is very Bi rich and probably excess sol gel
- 72 hour EDX map across 2250 um^2 revealed different Fe and Mn rich areas
    - Bigger square shaped areas with Bi:Ti:Fe:Mn atomic ratio 1:1:3:2
    - Smaller dots with Bi:Ti:Fe:Mn atomic ratio 1:0.2:5:10
    - *(atomic ratios rounded)*
- To determine the crystal structure of the Fe/Mn areas further analysis is required

Stability, Oxidation and Shape Evolution of PVP-Capped Pd Nanocrystals

Gillian Collins[†,‡], Michael Schmidt[†,‡], Gerard P. McGlacken[†], Colm O'Dwyer[†,§] and Justin D. Holmes[†,‡,*]

[†]*Department of Chemistry and the Tyndall National Institute, University College Cork, Cork, Ireland.*

[‡]*Centre for Research on Adaptive Nanostructures and Nanodevices, Trinity College, Dublin, Ireland*

[§]*Materials and Surface Science Institute, University of Limerick, Limerick, Ireland.*

*To whom correspondence should be addressed: Tel: +353 (0)21 4903608; Fax: +353 (0)21 4274097; E-mail: j.holmes@ucc.ie

Abstract

A critical aspect in the practical application and enhanced catalytic performance of shape controlled nanocrystals is their stability and morphology retention under ambient conditions. Changes to the morphology of shape-controlled Pd nanocrystals capped by PVP are assessed by TEM and surface oxidation was evaluated by X-ray photoelectron spectroscopy (XPS), over 12 months. Surface oxidation of PVP-capped Pd nanocrystals resulted in loss of edge and corner sites and transition to spherical morphologies. The shape stability of the nanocrystals was found to follow the trend cubic < cuboctahedra < octahedral ~ concave cubes. For low index planes, {111} surfaces are more resistant to oxidation compared to {100} facets, correlating with the surface free energy of the nanocrystals. Cubic and

cuboctahedral nanocrystals transitioned to spherical particles while octahedral nanocrystals retained their morphology. The presence of high energy {110} facets were observed in the cubic nanocrystals which undergo surface reconstruction. The presence of surface defects such as stacking faults were also found to influence the rate of the structural changes. Concave cubic nanocrystals, which possess high index facets and surface energies were consistently found to display excellent morphology retention. The concave cubic nanocrystals displayed superior shape stability and reduced oxidation compared to cubic and cuboctahedral nanocrystals. XPS analysis further determined that PVP capping ligands on different Pd surface facets strongly influences the morphological consistency. The stability of the concave cubes can be attributed to stronger chemisorption of PVP capping ligands to the high index plane making them less susceptible to oxidation.

Keywords: Palladium, shape controlled nanocrystals, oxidation, stability, surface facet.

Introduction

Extensive developments in the controlled synthesis of noble metal nanocrystals (NCs), with specific morphologies, have allowed numerous shape-dependent properties to be determined.[1-3] Altering the morphology of a NC exposes surface facets which display different atomic arrangements, leading to applications in selective catalysis; several hydrogenation[4,5] and oxidation[6,7] reactions demonstrate facet dependent reactivity. Nanocrystal shape can also influence the optical properties of plasmonic nanostructures leading to enhanced sensing and biomedical applications.[8,9] While early research efforts focused on synthesizing NCs enclosed by low index surface facets, such as {111} and {100} surfaces, there has been enormous recent progress in the growth of NCs enclosed by high index faces, achieved by manipulating growth kinetics.[10,11] High-index facets are denoted by

a set of Miller indices {*hkl*} with at least one index being greater than one. The morphologies of such structures are often characterized by sharp corners giving rise to unique optical properties and improved surface enhanced Raman scattering.[11] High index surfaces have a high density of low co-ordinated atoms located at step, edge and kink sites, thus have potential for enhanced catalysis.[12] Improved catalytic and electrocatalytic performance of NCs terminated by high index facets has been demonstrated.[13-16]

Pd is an important noble metal central to heterogeneous catalysis for chemical synthesis[17], fuel cells[18] and hydrogen storage.[19] Recent developments in understanding the growth conditions and mechanisms that influence NC morphology has facilitated exceptional control over the solution synthesis of Pd NCs enclosed by well-defined facets. Shape control synthesis of Pd NCs has been reported using selective capping ligands[20-22], seeded growth[14,23-26], heteroexpitaxial growth[27-29] and electrochemical methods[16,30]. The use of shape controlled Pd NCs has been shown or has been shown in enhanced performance in catalysis[14,27] and cancer therapy.[6]

Many practical applications of NCs, such as catalysis, require a metal to be deposited on a support material. The stability of shape-defined Pd NCs on support materials over time has not been thoroughly evaluated and is of key importance in exploiting the structure dependent properties of NCs. Loss of NC shape and changes in chemical state, due to surface oxidation, can have an impact on catalytic reactivity, molecular adsorption and optical properties.

Here, we report the stability and shape evolution of faceted Pd NCs supported on activated carbon. Activated carbon is one of the most commonly used support materials due to its high surface area, inertness and low cost. In this article, the stability of shape-controlled Pd

nanostructures including cubic, octahedral and cuboctahedral NCs are assessed by TEM and XPS. In addition to low index NCs, the stability of concave cubes enclosed by high index surface facets is also investigated. The concave cubes displayed excellent stability after immobilization and superior oxidation resistance compared to cubic and cuboctahedral NCs. Structural features present in the as-synthesized NCs, such as surface faceting and defects, influence the stability of the NCs. XPS was utilized to probe the changes to the NC oxidation state and to understand the origin of the stability observed for high index surface facets. In this study, the chemisorption of PVP on the surface of Pd NCs enclosed by different surface facets was found to be important for NC stability and retention of their morphology.

Experimental

Pd NCs of different surface facets were prepared by the methods described by Xia and co-workers.[26] A variety of NC shapes and sizes were investigated including 10 nm and 20 nm Pd cubic, 28 nm cuboctahedra and octahedral NCs with an edge length of 21 nm. High index facet concave cubes were prepared from 10 nm cubic seeds, measuring ~20 nm across in length and 35 nm from corner-corner.[14] For the stability studies six batched of the each NC were prepared. Pd NCs were immobilized on activated carbon by stirring at room temperature overnight and collected by filtration. Immobilization of the NCs on carbon was evident from the color change of the solution which changed from dark brown to near-colorless. The morphological stabilities of the carbon supported NCs was carried out by preparing the samples on TEM grids. Samples for analysis were prepared in triplicate and were left in ambient conditions (air, ~20 ºC).

Materials Characterization

Microscopy. Scanning electron microscopy (SEM) images were obtained using a FEI DualBeam Helios NanoLab 600i high resolution SEM. Transmission electron microscopy (TEM) analysis was performed using a JEOL 2100 transmission electron microscope, operating at a voltage of 200 kV. Scanning transmission electron microscopy (STEM) was carried out on a FEI Titan TEM at an operating voltage of 300 kV.

X-Ray Photoelectron Spectroscopy (XPS). XPS spectra were collected on a KRATOS-AXIS-165 using a monochromatic Al Kα line (1486.6 eV) as the X-ray source. All spectra were collected at a take-off angle (Θ) of 90° to the surface normal. Spectra were referenced to the C 1s at a binding energy 284.8 eV and a Shirley background was applied. The C1s spectra were fitted to Gaussian (70 %) Lorentzian (30 %) profiles. The high resolution Pd 3d scans were fitted with asymmetric Gaussian-Lorentzian profiles. The relative ratio of the Pd 3d doublet was fixed during the fitting, while the full width at half maximum (fwhm) and peak position were allowed to vary within a reasonable range to obtain the best fit.

Results and Discussion

1. Structural Stability of Pd Nanocrystals

The as-synthesized cubic Pd cubes, shown in figure 1 (a) are largely characterized by six {100} surface facets. The cubic morphology is unaffected by the immobilization procedure onto activated carbon as shown by the STEM image in figure 1(b). Exposure of the immobilized cubes for 7 days revealed little change in the morphology of the NCs, while analysis of the same NCs after 3 months revealed that the morphology of the 10 nm cubes altered. The change in shape changes was also observed to vary within a same sample, with some NCs becoming truncated whilst others displayed more pronounced changes, such as becoming spherical (Supporting Information Figure S1). After 6 months, the cubic NCs were

almost entirely spherical in shape, as shown in figure 1(c). High resolution TEM analysis of the NCs after 6 months revealed that many of the particles were defect-free single crystalline, while others contained stacking defects such as those shown figure 1(d). In contrast, the 20 nm diameter NCs showed a greater retention of their morphology over time, with a mixture of slight and heavily truncated cubes observed as shown by comparison of the NCs 1 week and 6 months after deposition (figure 1 (e)-(f)). Cubic NCs stored under inert conditions (N_2 filled gloved box) after immobilization also exhibited rounded corners, consistent with surface atom diffusion, but no transformation from a cubic to a spherical morphology was observed indicating that interaction with O_2 influences NC stability. PVP-protected cubic NCs used in this study exhibited considerably greater stability compare to ethylene glycol protected NCs. Xiong *et. al.*[31] reported that dried 50 nm diameter Pd cubes capped with ethylene glycol formed a nanocrystalline PdO shell, readily observed by TEM after ~8 days of ambient exposure. Additionally, they reported an inverse relationship between NC size and stability with smaller (8 nm) cubes displaying superior stability (up to 90 days), compared to 50 nm cubes. This increased stability with decreasing size was not observed for the PVP-capped NCs used in this study, which clearly revealed that 10 nm cubes were less stable and lost their cubic morphology compared to the 20 nm cubes. Furthermore, TEM analysis on the aged cubes (after becoming spherical) did not show the presence of a crystalline oxide shell, suggesting a low degree of oxide formation due to a better surface passivation by bulkier PVP compared to ethylene glycol. The presence of the surrounding carbon matrix and polymeric capping ligands on the nanocrystals in this study, obstruct direct imaging of ultra-thin oxide layers by TEM.

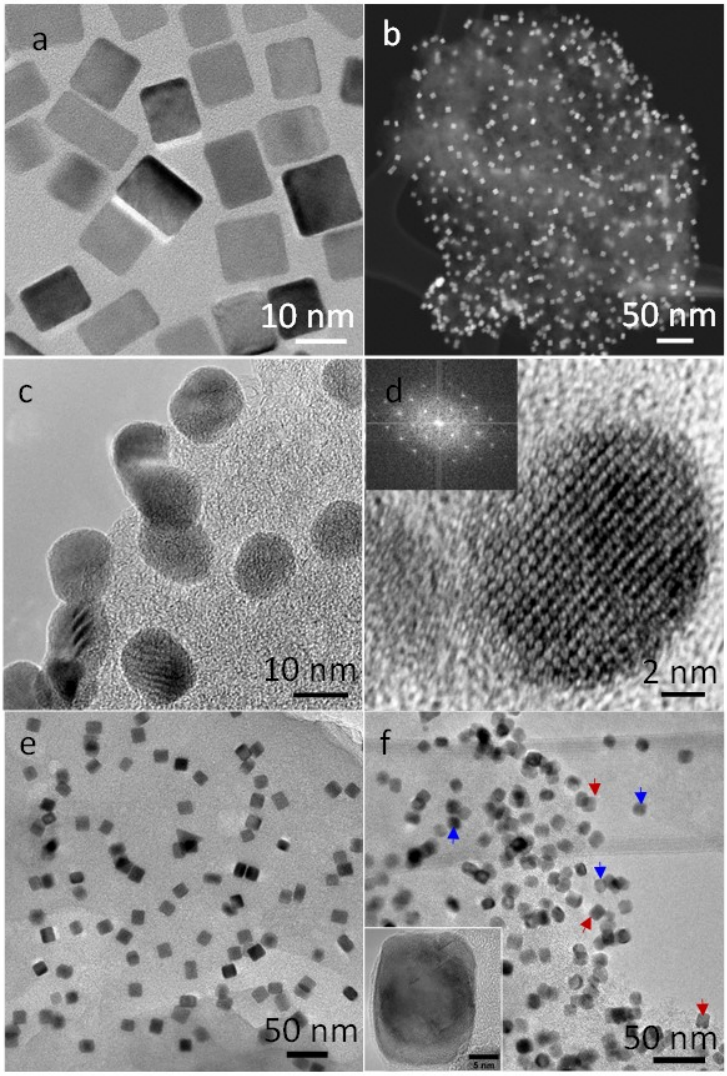

Figure 1. (a) TEM images of as-synthesized 10 nm PVP-capped cubic Pd NCs. (b) STEM image of 10 nm cubes deposited on activated carbon. (c) TEM image of 10 nm cubes 6 months after deposition onto carbon. (d) TEM image of cubic NC, aged for 12 months. (e) 20 nm cubic Pd NCs 1 week and (f) 6 months after deposition on activated carbon. The red arrows highlight NCs with well-maintained cubic morphologies and the blue arrows highlight NCs evolved to truncated NCs. Figure (f) inset shows typical 20 nm cubic Pd NC 12 month after ambient exposure (scale bar is 5 nm).

The changes in the morphology of the Pd NCs from cubic to spherical are driven by energy minimization to the most thermodynamically favourable shape. To understand the factors

contributing to the shape changes observed in the cubic NCs, high resolution TEM was used to analyze the particles at different stages of ageing. Figure 2(a) shows a TEM image of a freshly prepared cubic NC projected in the [011] direction. A significant feature shown in figure 2(a) is the presence of a {110} facet, which is not often observed on nanostructures due to its lower stability compared to {111} and {100} facets. The schematic shown in figure 2 illustrates the true structure of the cubic NCs showing the truncated corners with {111} and {110} facets in addition to the {100} cubic faces.[32] As shown in figure 2(a), these surfaces are relatively rough at the atomic scale and show missing-row reconstruction, characteristic of noble metal {110} surfaces.[33] In some regions, rows of atoms are missing along the [1-10] direction and give rise to a saw-tooth configuration, as identified by black arrows in figure 2(a). The image is magnified in the inset of figure 2(a) for clarity. Similar surface reconstruction has previously been observed on Au nanorods.[34] The presence of adatoms, shown by the white arrows in figure 2(a) is also observed. The driving force for this reconstruction is the formation of lower energy {111} micro facets on the (110) surface giving an overall lower surface energy after reconstruction, as illustrated by the inset schematic, in figure 2(a). No reconstruction was observed on the {100} facets and surface defects mainly consisted of single atom height terraces (Supporting Information Figure S2). A higher density of step sites was generally observed at the corners as shown in figure 2(b). Here, the presence of a higher index {220} and {310} facets can be seen where the {100} and {111} facets meet. This observation is in excellent agreement with DFT calculations showing high index stepped surfaces being preferential to sharp corners at the boundaries between the (100) and (111) facets.[35] Additionally, as previously described, surface reconstruction of the {110} facets is again seen in figure 2(b). As the NCs age, loss of the stepped surfaces, which are more prevalent at the corners is observed, causing rounding of the corners (figure 2(c)). The facets continue to reduce in size, eventually becoming

spherical (figure 2(d)). Such transformations are predicted by DFT calculations due to O_2 adsorption and surface oxide formation.[35] The presence of the {110} facet on the cubic NCs are influential to the stability of the NCs due to the greater reactivity and lower stability associated with the surface. Nanostructures with high surface defect densities are less stable and more susceptible to oxidation, thereby affecting the rate of structural changes.[36,37] Surface defects can also influence the co-ordination of capping ligands[38] and a more defective surface may disrupt the packing or lower the coverage of the PVP capping layer, facilitating easier oxidation of the Pd NCs.

An additional structural feature of the cubic NCs which contributes to their variable shape evolution is the presence of stacking faults, as shown in figure 2(c). Stacking faults were found to be present in some of the resulting spherical nanoparticles as shown in figure 2(f). The exact origin of the defects is unclear and was not investigated in detail in this study. The as-synthesized NCs are single crystalline with a low defect density, although stacking defects can be observed as shown in figure 2(c). Defect formation has been shown to occur as a stress relieve mechanism.[39]

The 20 nm cubic NCs display similar defect features to the 10 nm cubic NCs (figure 1(f) inset). The larger size of the particles may hinder complete transformation to spherical morphology as the effects of surface stress and interface stress, are more pronounced for smaller particles.[40]

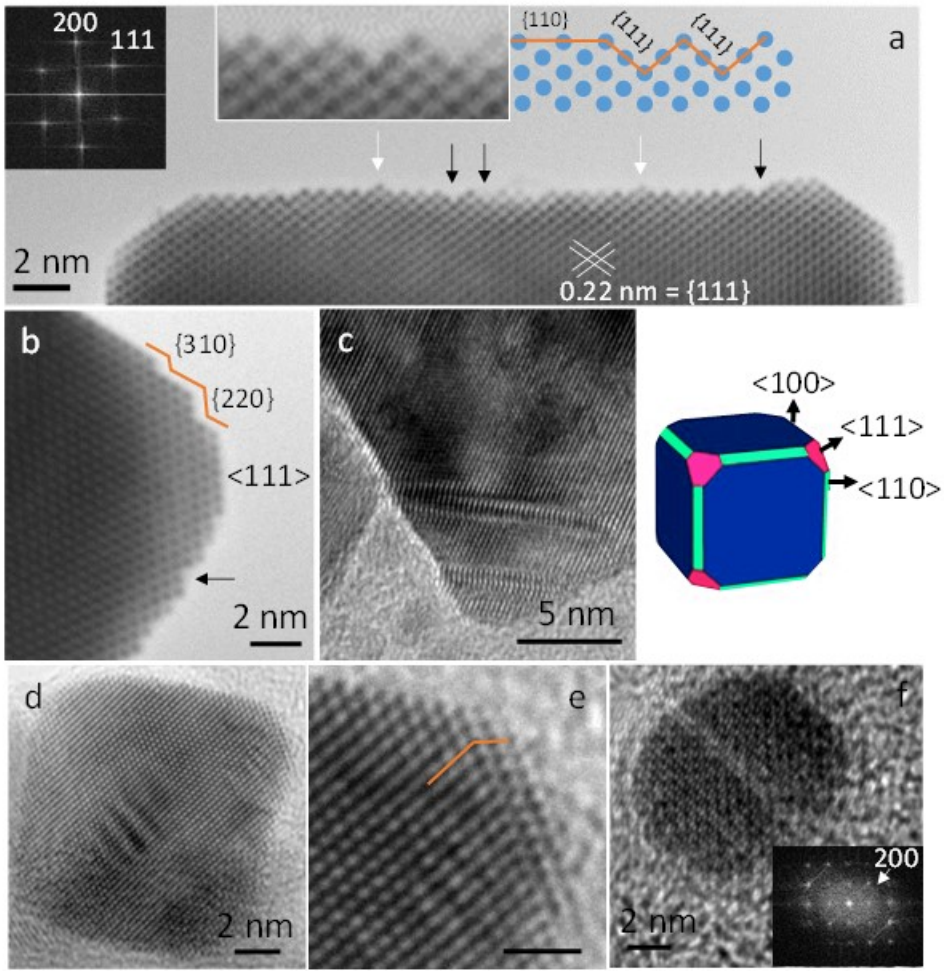

Figure 2. (a)-(b) HRTEM image of freshly synthesized cubic NC along the [110] direction. (c) Freshly prepared 20 nm cubic NC showing stacking faults. (d)-(e) 10 nm cubic NCs aged for 3 months and (f) cubic NC aged for 6 months showing stacking fault along the particle.

Pd NCs with a cuboctahedral morphology are characterized by 6 square {100} and 6 triangular {111} facets, shown in figure 3(a). Similar to the cubic NCs, aging of cuboctahedral NCs results in a morphology change to the thermodynamically lowest energy spherical shape, as illustrated in figure 3(b). TEM also reveals that many of the NCs do not experience a uniform evolution of morphology. Figure 3(c) shows an aged octahedral NC with defined facets on one side of the NC and rounding on the opposite side of the NC, which was typical of many particles. The origin of the uneven rounding of surface facets is also

attributed to the presence of surface defects as previous described for the cubic NCs. After 12 months many of the cuboctahedral NCs also became spherical (Supporting Information Figure S3).

In comparison to cubic and cuboctahedral NCs, the octahedral NCs exhibited little change to their morphology over the same time period. Ideal octahedra are characterized by eight {111} surface facets, however many of the octahedra prepared by this seeded method employed were slightly truncated, exposing vertices capped with {100} facets, as shown in the STEM image in figure 3(d). These NCs displayed excellent morphology retention as can be seen in figure 3(e), 6 months after deposition onto activated carbon. Even after 12 months the octahedral NCs displayed negligible changes to their morphology and the particles retained well-defined facets, see figure 3(f). The overall stability trend of the polyhedra was found to be cubic < cuboctahedra < octahedral, which correlates with the surface free energy of face centred cubic metals, $\gamma_{\{111\}} < \gamma_{\{100\}} < \gamma_{\{110\}}$.[41]

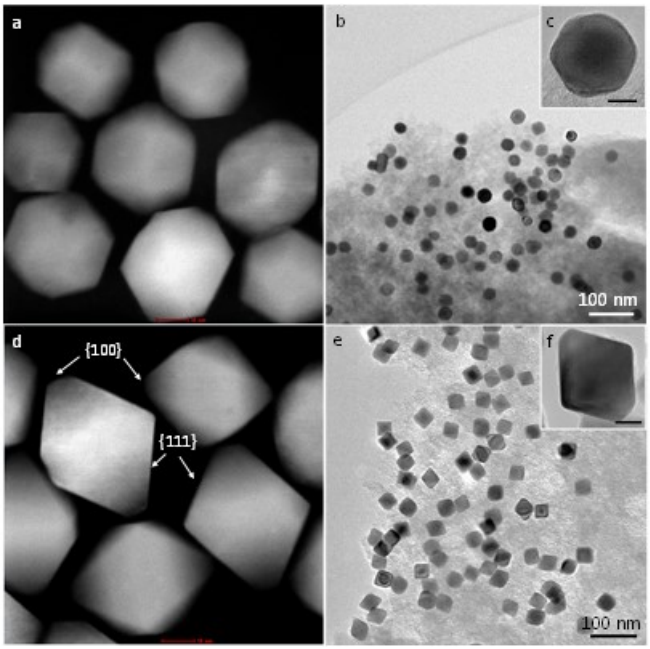

Figure 3. (a) STEM image of as-synthesized cuboctahedral NCs. (b)-(c) TEM image of cuboctahedral NCs 6 months after immobilization onto carbon. (d) STEM image of as-synthesized octahedral NCs. (e) Octahedral NCs 6 months and (f) 12 months after immobilization onto carbon. Scale bars in figures (a), (c), (d) and (f) are 10 nm.

High index surface facets are characterized by a high density of surface atoms with low coordination numbers. These open structures possess higher surface energies compared to closed pack surfaces, typically $\gamma_{\{111\}} < \gamma_{\{100\}} < \gamma_{\{hkl\}}$ for fcc Pd. Figure 4(a) shows a TEM image of as-synthesized concave Pd NCs. TEM analysis of the concave cubes 6 months after deposition on the carbon support revealed they exhibited excellent retention of morphology as shown in figure 4(b). In contrast to the cubic NCs, which loose the stepped facets on aging, HRTEM analysis of the concave cubes aged for 6 months (figure 4(c)) showed the preservation of the high index faces, with most of the exposed facets belonging to the {730} family planes, consistent with the as-synthesized NCs.[14] The NCs still retained their concave shape 12 month after deposition onto activated carbon (Supporting Information, Figure S4).

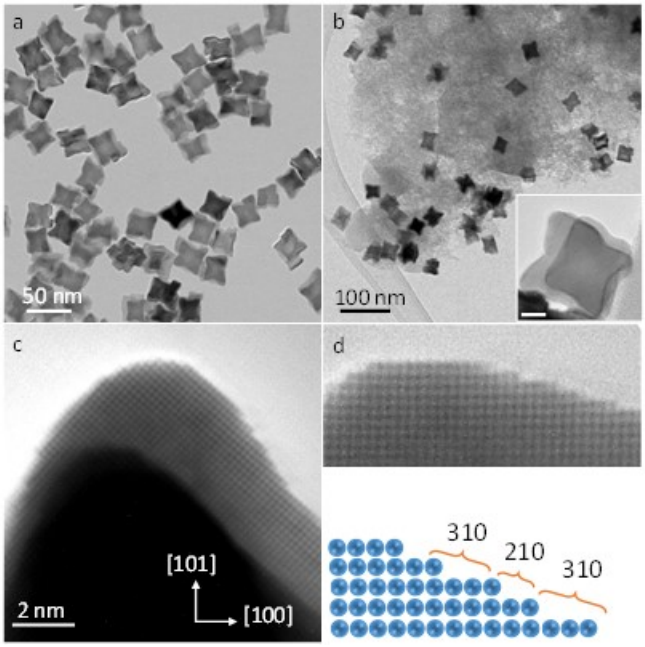

Figure 4. TEM image of (a) as synthesized concave NCs, (b) 6 months after deposited onto activated carbon. (d) HRTEM image of concave NC with incident beam along the [100] direction. The schematic illustrates the step configuration of the surface facet.

2. Oxidation and Interaction of PVP with Pd Nanocrystals

To further understand the stability of the shape-controlled NCs, XPS analysis was conducted to study the oxidation trends of the NCs as they aged and to probe the interaction of the PVP capping ligands with Pd. Figures 5(a)-(c) show the evolution of the Pd 3d core level spectra of the cubic Pd NCs over 24 h, 1 month and 6 months, respectively, after immobilization on activated carbon. The Pd 3d spectra of the cubic NCs after 24 h showed the presence of mainly metallic Pd(0) at a binding energy of 335.4 eV, in good agreement with bulk Pd (335.2 eV).[42] The slightly higher binding energy is typical of nanoparticles due to size and electronic effects.[43,44] Notably, assignment of Pd oxidation states in the 3d core level varies somewhat in literature. *In situ* XPS measurements of Pd(111) facets determined that peaks shifted to binding energies greater than +1.5 eV can be assigned to bulk oxide phases, while

smaller shifts are attributed to surface oxide and sub-surface oxide species.[42,45] Similar observations have been made for Pd(100) surfaces.[46,47] Stable surface oxides can form on (111) and (100) surfaces but not on (110) facets.[35,42] Furthermore, the structure of surface oxide species has been shown to be quite different from that of bulk PdO.[48] The second shoulder peak in figure 5(a), located at a binding energy of 337.1 eV can be assigned to bulk PdO, which is in excellent agreement with the 1.7 eV difference reported for PdO and Pd(0).[47,49] Exposure of 20 nm cubic NCs to ambient conditions for 1 month resulted in a similar Pd 3d spectra, but with increased line broadening of the peaks and a shift of 0.15 eV to higher binding energies, consistent with previous studies.[47,50] The first shoulder peak shown in figure 5(b) occurs at a binding energy of 336.5 eV, typical of PdO reported for nanoparticles.[50] The second shoulder peak centred at a binding energy of 337.6 eV, can typically be assigned to the presence of highly oxidized Pd species such as PdO_2 (reported in the range between 337.2 – 338.2 eV).[51-53] As the cubic NCs age over 6 months the PdO_x peak intensity increased, which can be seen from comparison of the Pd 3d spectra in figure 5(a)-(c). Figure 5(d) displays the Pd 3d spectra of concave cubes 4 weeks after immobilization onto activated carbon, showing the presence of predominately metallic Pd(0) at 335.2 eV and a surface PdO associated peak at 336.4 eV. Comparison of figures 5(c) and (e) clearly show that the concave cubes are considerably less oxidized than the cubic NCs after exposure to ambient conditions for 6 months, consistent with their shape retention. The total oxide signal for the concave cubes after 6 months was similar to that observed for {111} enclosed octahedral NCs, as shown in figures 5(e) and (f).

The nature of the surface facets present in the NCs is important for understanding the oxidation behaviour of faceted NCs. O_2 adsorption on Pd is spontaneous but absorption energies are facet dependent; Pd atoms on (110) surfaces have higher adsorption energies

(1.56 eV/ O atom) compared to stepped or closed packed (111) or (100) surfaces.[35] The ease of O_2 dissociation on Pd follows the trend {110} > {100} > {111}, which is the origin of the superior reactivity for oxidation-type reactions observed for Pd{110} catalysts.[6,54] Therefore, the {110} facets only observed on the cubic NCs are more reactive and susceptible to oxidation compared to the {111) and {100} facets, consistent with XPS observations.

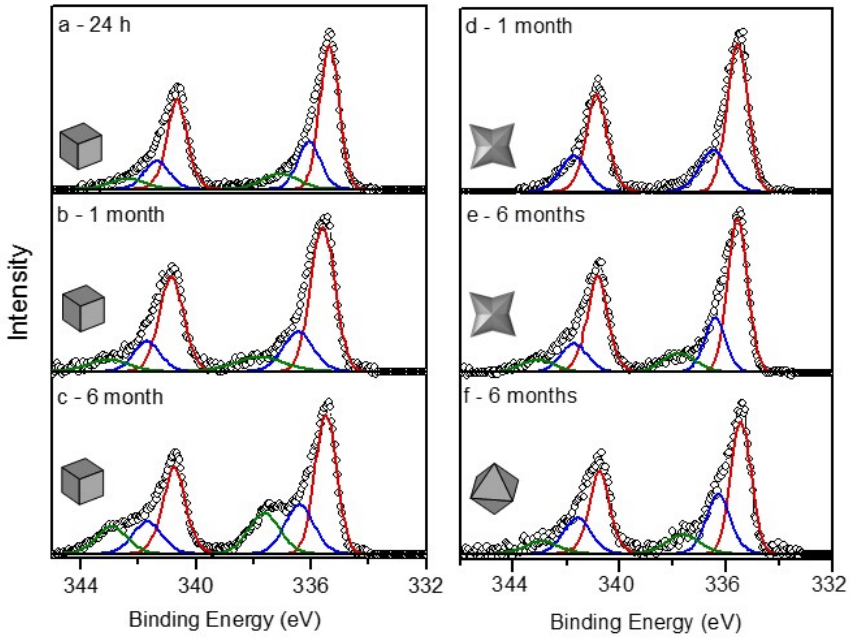

Figure 5. Background subtracted Pd 3d photoelectron emission spectra of carbon-supported Pd cubes after (a) 24 h, (b) 1 month (c) 6 months. Concave Pd cubes (d) 1 month, (e) 6 months and (f) octahedral NCs 6 months after ambient exposure.

The intriguing observation of this study is the excellent stability and oxidation resistance of concave NCs with high index facets, when the open structure of such facets is typically associated with high reactivity. Analysis of oxide phases on high index Pd surfaces is lacking in the literature. However, atomically smooth {100} and {111} surfaces have been suggested to allow oxygen diffusion into the lattice, thereby destroying the surface structure and NC

shape.[13,55] For low index surfaces, Pd(111) is more densely packed (1.53×10^{15} atoms cm^{-2}) compared to the Pd(100) surface (1.32×10^{15} atoms cm^{-2}) and Pd(110) surfaces (9.4×10^{14} atoms cm^{-2}). Consequently, oxide formation is the least favourable on Pd(111) as the higher surface atom density requires more lattice expansion to accommodate the formation of PdO_x.[56] Different factors may influence oxidation of high index surface. In contrast to low index planes, on high index faces, O_2 atoms preferentially adsorb at step sites rather than diffuse into the lattice, helping to preserve the surface structure.[13] The step structure of the high index facets may also better accommodate lattice strain induced by oxide formation, making them less susceptible to structural changes.

An important aspect in the stability of colloidal NCs is the presence of capping ligands at the particle surface. Passivating ligands can significantly alter surface free energy thereby influencing the stability and oxidation resistance of surface facets.[57] XPS analysis was used to investigate the interaction of PVP capping ligands with the Pd surface. Figure 6 shows the N 1s spectra of the different polyhedra. The cubic NCs displayed a single peak at a binding energy of 339.8 eV, characteristic of the pyrrolidone N group.[58] The N 1s binding energy is similar to that of the free PVP, indicating that the N atoms are not involved in the coordination with the Pd surface on cubic NCs, as illustrated in figure 6(b). In contrast to the cubic NCs, all other Pd polyhedra displayed the presence of a peak at 401.6 eV, in addition to the peak at 399.8 eV. Shifts to a higher binding energy are associated with decreased electron density of the N group, indicating charge transfer from the PVP to the Pd, implying that the pyrrolidone N group is involved in the coordination with the surface, as illustrated in figure 6(c). Xian *et al.*[58] showed the chemisorption of PVP to spherical Pd nanoparticles can also break the N-C bond in the N-C=O group, with following hydrolysis gave $CH_2{-}CH_2{-}NH_2^+{-}(CH_2)_3{-}COO^-$, as illustrated in figure 6(d). Their report is in excellent

agreement with the N 1s binding energy of 401.2 eV, observed here, which is generally assigned to protonated amine species.[59] The peak contribution of charged N species is larger for the concave cubes compared to the low index polyhedral, suggesting greater chemisorption of the pyrrolidone N group on the high index surface facets. The atomically stepped surface is characterized by low-coordinated number atoms which may facilitate a stronger interaction with the N groups. Bond cleavage is also considerably more favorable on stepped surfaces compared to atomically smooth surfaces which can lead to co-ordination of PVP as illustrated in figure 6(d).[60]

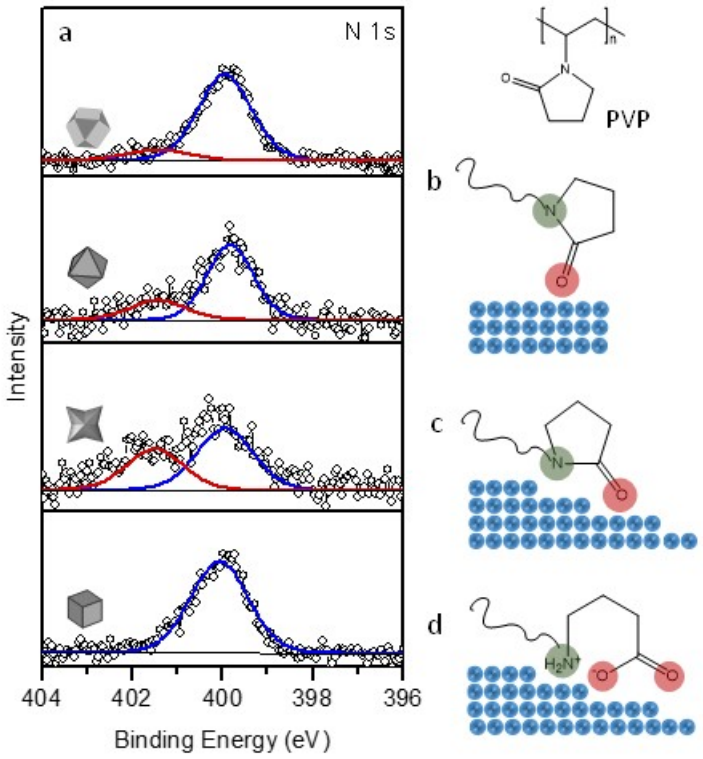

Figure 6. (a) N 1s spectra of Pd NCs immobilized on activated carbon. Schematic illustrating (b) the interaction of PVP through carbonyl O. (c) Co-ordination of PVP through both O and N groups. (d) Co-ordination of PVP with cleavage of the C-N bond.

The C 1s spectrum of the cubic Pd NCs, shown in figure 7(a) contains 3 components at binding energies of 284.8 eV (C-C, C=C), 286 eV (C-N, C-O) and 287.6 eV (C=O)[61], however adventitious hydrocarbon will also contribute to the C-C and C-O peak intensities. The C 1s spectrum of the concave cubes contains an additional peak not observed for the cubic NCs at a binding energy of 288.9 eV, typically assigned to the O-C=O group. The presence of the carboxylate group, in addition of the C=O group, indicates that a portion of the chemisorbed PVP molecules undergo cleavage of the C-N bond and subsequent hydrolysis, consistent with the N 1s spectrum. The synthesis of cubic NCs in this study uses Br^- ions as selective capping agents to promote the formation of NCs enclosed by {100} facets. Analysis of the Br 3d core level spectrum of the cubic NCs show that the Br^- species remain on the surface after immobilization onto activated carbon (Supporting Information Figure S5). The Pd(111) and high index facets were not observed to be capped with Br ions, which may facilitate stronger interactions with the PVP ligands compared to {100} facets. Furthermore, while Br ions have been shown to be chemisorbed to the surface, they can be displaced by ethylene glycol at 100 °C.[62] Removal of PVP from noble metal surfaces generally requires more forcing conditions.[63]

Several studies have shown that charge transfer and the co-ordination mode of PVP molecules with noble metal nanoparticles to be size dependent.[64-66] The XPS data in this study also indicates that the interaction mode of PVP capping ligands is also dependent on the nature of the surface facet for Pd NCs. This finding is important for both shape selective NC synthesis with high energy faceted surfaces, suggesting that the structure and electronic interaction of the ligand is important in preserving the long term stability and structure of high energy surfaces.

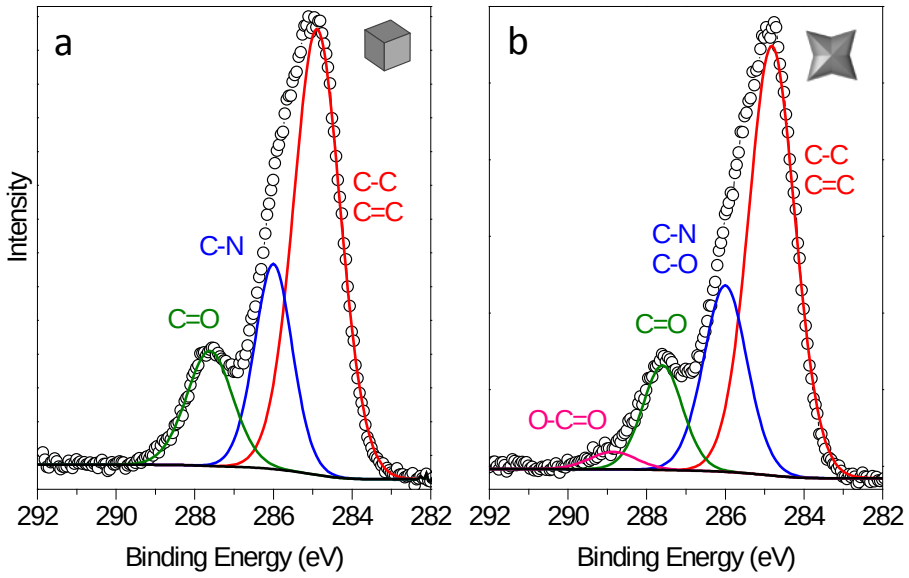

Figure 7. C 1s spectra of unsupported (deposited on glass substrate) (a) cubic Pd NCs and (b) concave cubic Pd NCs.

Conclusions

The stability, oxidation and shape evolution of well-defined Pd NCs supported on activated carbon was assessed over 12 months. For low index surfaces, the octahedral NCs with {111} facets had greater stability compared to {100} facets, due to the lower surface free energy. The presence of the relatively reactive and high energy {110} facet on the cubic NCs increases the oxidation susceptibility of the NCs making them the least stable shape studied. Surface defects influence the shape evolution of NCs resulting in non-uniform changes in their structure. Concave Pd NCs characterized by high index surface facets displayed superior stability to cubic and cuboctahedral NCs. XPS analysis identified stronger interaction between the N groups of the PVP capping ligands on the high index faces compared to the low index {100} facets. Controlling the interaction between the PVP capping ligands and the metal surface has been central in the synthesis of colloidal NCs. In particular understanding the selective chemisorption of capping ligands onto certain crystal facets has been key to controlling the growth of NCs with specific morphologies. The work

here highlights that these interactions also play a critical role in the long-term stability of NCs. Optimizing these interactions can facilitate the synthesis of NCs enclosed by well-defined surface facets with improved stability and oxidation resistance.

Structural evolution of nanoparticles is complex with several influencing factors. The stability trends observed in this study may not be general and nanoparticles prepared by alterative synthesis methods, with different capping ligands and support materials may display different stability trends. However, evaluating the stability of shape controlled nanocrystals is critical as morphological transformations due to surface defects or surface oxidation can influence the potential applications of shape-controlled such as catalysis. The excellent stability of PVP capped concaves cubes is promising as nanocrystals with high index facets have been shown to display enhanced reactivity in several catalytic applications.

Acknowledgments

We acknowledge financial support from Science Foundation Ireland (Grant 08/CE/I1432) and Enterprise Ireland (Grant IP/2011/0130). COD acknowledges the UCC Strategic Research Fund and an Irish Research Council New Foundations Award. The authors thank Dr. Fathima Laffir for assistance with XPS measurements.

Supporting Information

Additional TEM images of the cubic, cuboctahedral and concave cubic nanocrystals and the Br 3d core level XPS spectra for cubic nanocrystals can be found in the supporting information. This material is available free of charge via the Internet at http://pubs.acs.org.

References

(1) Xia, Y.; Xiong, Y.; Lim, B.; Skrabalak, S. E. Shape-Controlled Synthesis of Metal Nanocrystals: Simple Chemistry Meets Complex Physics? *Angew. Chem.-Int. Edit.,* **2009**, *48*, 60-103.

(2) Diaz Valenzuela, C.; Carriedo, G. A.; Valenzuela, M. L.; Zuniga, L.; O'Dwyer, C. Solid State Pathways to Complex Shape Evolution and Tunable Porosity during Metallic Crystal Growth. *Sci. Rep.,* **2013**, *3*.

(3) Niu, W.; Zhang, L.; Xu, G. Seed-Mediated Growth of Noble Metal Nanocrystals: Crystal Growth and Shape Control. *Nanoscale,* **2013**, *5*, 3172-3181.

(4) Bratlie, K. M.; Lee, H.; Komvopoulos, K.; Yang, P.; Somorjai, G. A. Platinum Nanoparticle Shape Effects on Benzene Hydrogenation Selectivity. *Nano Lett.,* **2007**, *7*, 3097-3101.

(5) Crespo-Quesada, M.; Yarulin, A.; Jin, M.; Xia, Y.; Kiwi-Minsker, L. Structure Sensitivity of Alkynol Hydrogenation on Shape- and Size-Controlled Palladium Nanocrystals: Which Sites Are Most Active and Selective? *J. Am. Chem. Soc.,* **2011**, *133*, 12787-12794.

(6) Long, R.; Mao, K.; Ye, X.; Yan, W.; Huang, Y.; Wang, J.; Fu, Y.; Wang, X.; Wu, X.; Xie, Y.et. al. Surface Facet of Palladium Nanocrystals: a Key Parameter to the Activation of Molecular Oxygen for Organic Catalysis and Cancer Treatment. *J. Am. Chem. Soc.,* **2013**, *135*, 3200-3207.

(7) Mostafa, S.; Behafarid, F.; Croy, J. R.; Ono, L. K.; Li, L.; Yang, J. C.; Frenkel, A. I.; Cuenya, B. R. Shape-Dependent Catalytic Properties of Pt Nanoparticles. *J. Am. Chem. Soc.,* **2010**, *132*, 15714-15719.

(8) Wiley, B. J.; Im, S. H.; Li, Z.-Y.; McLellan, J.; Siekkinen, A.; Xia, Y. Maneuvering the Surface Plasmon Resonance of Silver Nanostructures Through Shape-Controlled Synthesis. *J. Phys. Chem. B,* **2006**, *110*, 15666-15675.

(9) Zhang, J. Z. Biomedical Applications of Shape-Controlled Plasmonic Nanostructures: A Case Study of Hollow Gold Nanospheres for Photothermal Ablation Therapy of Cancer. *J. Phys. Chem. Lett.,* **2010**, *1*, 686-695.

(10) Quan, Z.; Wang, Y.; Fang, J. High-Index Faceted Noble Metal Nanocrystals. *Acc. Chem. Res.,* **2013**, *46*, 191-202.

(11) Hong, J. W.; Lee, S.-U.; Lee, Y. W.; Han, S. W. Hexoctahedral Au Nanocrystals with High-Index Facets and Their Optical and Surface-Enhanced Raman Scattering Properties. *J. Am. Chem. Soc.,* **2012**, *134*, 4565-4568.

(12) Xiong, Y.; Wiley, B. J.; Xia, Y. Nanocrystals with Unconventional Shapes - A Class of Promising Catalysts. *Angew. Chem. Int. Ed.,* **2007**, *46*, 7157-7159.

(13) Tian, N.; Zhou, Z.-Y.; Sun, S.-G.; Ding, Y.; Wang, Z. L. Synthesis of Tetrahexahedral Platinum Nanocrystals with High-Index Facets and High Electro-Oxidation Activity. *Science,* **2007**, *316*, 732-735.

(14) Jin, M.; Zhang, H.; Xie, Z.; Xia, Y. Palladium Concave Nanocubes with High-Index Facets and Their Enhanced Catalytic Properties. *Angew. Chem. Int. Ed.*

, **2011**, *50*, 7850-7854.

(15) Deng, Y.-J.; Tian, N.; Zhou, Z.-Y.; Huang, R.; Liu, Z.-L.; Xiao, J.; Sun, S.-G. Alloy Tetrahexahedral Pd-Pt Catalysts: Enhancing Significantly the Catalytic Activity by Synergy Effect of High-Index Facets and Electronic Structure. *Chem. Sci.,* **2012**, *3*, 1157-1161.

(16) Tian, N.; Zhou, Z.-Y.; Yu, N.-F.; Wang, L.-Y.; Sun, S.-G. Direct Electrodeposition of Tetrahexahedral Pd Nanocrystals with High-Index Facets and High Catalytic Activity for Ethanol Electrooxidation. *J. Am. Chem. Soc.,* **2010**, *132*, 7580-+.

(17) Blaser, H. U.; Indolese, A.; Schnyder, A.; Steiner, H.; Studer, M. Supported Palladium Catalysts for Fine Chemicals Synthesis. *J. Mol. Catal. A: Chem.,* **2001**, *173*, 3-18.

(18) Antolini, E. Palladium in Fuel Cell Catalysis. *Energy Environ. Sci.,* **2009**, *2*, 915-931.

(19) Kishore, S.; Nelson, J. A.; Adair, J. H.; Eklund, P. C. Hydrogen Storage in Spherical and Platelet Palladium Nanoparticles. *J. Alloys Compd.,* **2005**, *389*, 234-242.

(20) Xiong, Y. J.; McLellan, J. M.; Yin, Y. D.; Xia, Y. N. Synthesis of Palladium Icosahedra with Twinned Structure by Blocking Oxidative Etching with Citric Acid or Citrate Ions. *Angew. Chem. Int. Ed.,* **2007**, *46*, 790-794.

(21) Xiong, Y. J.; Xia, Y. N. Shape-Controlled Synthesis of Metal Nanostructures: The Case of Palladium. *Adv. Mater.,* **2007**, *19*, 3385-3391.

(22) Niu, Z.; Peng, Q.; Gong, M.; Rong, H.; Li, Y. Oleylamine-Mediated Shape Evolution of Palladium Nanocrystals. *Angew. Chem.-Int. Edit.,* **2011**, *50*, 6315-6319.

(23) Niu, W.; Li, Z.-Y.; Shi, L.; Liu, X.; Li, H.; Han, S.; Chen, J.; Xu, G. Seed-Mediated Growth of Nearly Monodisperse Palladium Nanocubes with Controllable Sizes. *Cryst. Growth Des.,* **2008**, *8*, 4440-4444.

(24) Zhang, Q.; Xie, J.; Yang, J.; Lee, J. Y. Monodisperse Icosahedral Ag, Au, and Pd Nanoparticles: Size Control Strategy and Superlattice Formation. *Acs Nano,* **2009**, *3*, 139-148.

(25) Niu, W.; Zhang, L.; Xu, G. Shape-Controlled Synthesis of Single-Crystalline Palladium Nanocrystals. *Acs Nano,* **2010**, *4*, 1987-1996.

(26) Jin, M.; Zhang, H.; Xie, Z.; Xia, Y. Palladium Nanocrystals Enclosed by {100} and {111} Facets in Controlled Proportions and their Catalytic Activities for Formic Acid Oxidation. *Energy Environ. Sci.,* **2012**, *5*, 6352-6357.

(27) Wang, F.; Li, C.; Sun, L.-D.; Wu, H.; Ming, T.; Wang, J.; Yu, J. C.; Yan, C.-H. Heteroepitaxial Growth of High-Index-Faceted Palladium Nanoshells and Their Catalytic Performance. *J. Am. Chem. Soc.,* **2011**, *133*, 1106-1111.

(28) Yu, Y.; Zhang, Q.; Liu, B.; Lee, J. Y. Synthesis of Nanocrystals with Variable High-Index Pd Facets through the Controlled Heteroepitaxial Growth of Trisoctahedral Au Templates. *J. Am. Chem. Soc.,* **2010**, *132*, 18258-18265.

(29) Fan, F.-R.; Liu, D.-Y.; Wu, Y.-F.; Duan, S.; Xie, Z.-X.; Jiang, Z.-Y.; Tian, Z.-Q. Epitaxial Growth of Heterogeneous Metal Nanocrystals: From Gold Nano-Octahedra to Palladium and Silver Nanocubes. *J. Am. Chem. Soc.,* **2008**, *130*, 6949-+.

(30) Tian, N.; Zhou, Z.-Y.; Sun, S.-G. Electrochemical Preparation of Pd Nanorods with High-Index Facets. *Chem. Comm.,* **2009**, 1502-1504.

(31) Xiong, Y. J.; Chen, J. Y.; Wiley, B.; Xia, Y. N.; Yin, Y. D.; Li, Z. Y. Size-Dependence of Surface Plasmon Resonance and Oxidation for Pd Nanocubes Synthesized via a Seed Etching Process. *Nano Lett.,* **2005**, *5*, 1237-1242.

(32) Xia, X.; Xie, S.; Liu, M.; Peng, H.-C.; Lu, N.; Wang, J.; Kim, M. J.; Xia, Y. On the Role of Surface Diffusion in Determining the Shape or Morphology of Noble-Metal Nanocrystals. *Proc. Natl. Acad. Sci. USA,* **2013**, *110*, 6669-6673.

(33) Bartynski, R. A.; Gustafsson, T. Experimental Study of Surface States on the (110) Faces of the Noble Metals. *Phys. Rev. B,* **1986**, *33*, 6588-6598.

(34) Wang, Z. L.; Gao, R. P.; Nikoobakht, B.; El-Sayed, M. A. Surface Reconstruction of the Unstable {110} Surface in Gold Nanorods. *J. Phys. Chem. B,* **2000**, *104*, 5417-5420.

(35) Mittendorfer, F.; Seriani, N.; Dubay, O.; Kresse, G. Morphology of Mesoscopic Rh and Pd Nanoparticles under Oxidizing Conditions. *Phys. Rev. B,* **2007**, *76*.

(36) Wang, Z. L. Transmission Electron Microscopy of Shape-Controlled Nanocrystals and their Assemblies. *J. Phys. Chem. B,* **2000**, *104*, 1153-1175.

(37) Gai, P. L.; Harmer, M. A. Surface Atomic Defect Structures and Growth of Gold Nanorods. *Nano Lett.,* **2002**, *2*, 771-774.

(38) Donkers, R. L.; Song, Y.; Murray, R. W. Substituent Effects on the Exchange Dynamics of Ligands on 1.6 nm Diameter Gold Nanoparticles. *Langmuir,* **2004**, *20*, 4703-4707.

(39) Ding, Y.; Fan, F.; Tian, Z.; L., W. W. Atomic Structure of Au-Pd Bimetallic Alloyed Nanoparticles. *J. Am. Chem. Soc.,* **2010**, *132*, 12480-12486.

(40) Jiang, Q.; Liang, L. H.; Zhao, D. S. Lattice Contraction and Surface Stress of fcc Nanocrystals. *J. Phys. Chem. B,* **2001**, *105*, 6275-6277.

(41) Barnard, A. S. Mapping the Shape and Phase of Palladium Nanocatalysts. *Catal. Sci. Technol.,* **2012**, *2*, 1485-1492.

(42) Lundgren, E.; Kresse, G.; Klein, C.; Borg, M.; Andersen, J. N.; De Santis, M.; Gauthier, Y.; Konvicka, C.; Schmid, M.; Varga, P. Two-dimensional oxide on Pd(111). *Phys. Rev. Lett.,* **2002**, *88*, 246103-246104.

(43) Smirnov, M. Y.; Vovk, E. I.; Kalinkin, A. V.; Pashis, A. V.; Bukhtiyarov, V. I. An XPS Study of the Oxidation of Noble Metal Particles Evaporated onto the Surface of an Oxide Support in Their Reaction with NOx. *Kinetics and Catalysis,* **2012**, *53*, 117-124.

(44) Paredis, K.; Ono, L. K.; Behafarid, F.; Zhang, Z.; Yang, J. C.; Frenkel, A. I.; Cuenya, B. R. Evolution of the Structure and Chemical State of Pd Nanoparticles during the in Situ Catalytic Reduction of NO with H-2. *J. Am. Chem. Soc.,* **2011**, *133*, 13455-13464.

(45) Ketteler, G.; Ogletree, D. F.; Bluhm, H.; Liu, H. J.; Hebenstreit, E. L. D.; Salmeron, M. In Situ Spectroscopic Study of the Oxidation and Reduction of Pd(111). *J. Am. Chem. Soc.,* **2005**, *127*, 18269-18273.

(46) Todorova, M.; Lundgren, E.; Blum, V.; Mikkelsen, A.; Gray, S.; Gustafson, J.; Borg, M.; Rogal, J.; Reuter, K.; Andersen, J. N.et. al. The Pd(100)-(root 5 x root 5)R27 degrees-O surface oxide revisited. *Surf. Sci.,* **2003**, *541*, 101-112.

(47) Wang, J.; Yun, Y.; Altman, E. I. The Plasma Oxidation of Pd(100). *Surf. Sci.,* **2007**, *601*, 3497-3505.

(48) Zemlyanov, D.; Aszalos-Kiss, B.; Kleimenov, E.; Teschner, D.; Zafeiratos, S.; Havecker, M.; Knop-Gericke, A.; Schlogl, R.; Gabasch, H.; Unterberger, W.et. al. In Situ XPS Study of Pd(111) Oxidation. Part 1: 2D Oxide Formation in 10^{-3} mbar O_2. *Surf. Sci.,* **2006**, *600*, 983-994.

(49) Peuckert, M. XPS Study on Surface and Bulk Pd Oxides, its Thermal Stability and a Comparison with Other Noble Metals. *J. Phys. Chem.,* **1985**, *89*, 2481-2486.

(50) Collins, G.; Blomker, M.; Osaik, M.; Holmes, J. D.; Bredol, M.; O'Dwyer, C. Three-Dimensionally Ordered Hierarchically Porous Tin Dioxide Inverse Opals and Immobilization of Palladium Nanoparticles for Catalytic Applications. *Chem. Mater.,* **2013**, *25*, 4312-4320.

(51) Kibis, L. S.; Stadnichenko, A. I.; Koscheev, S. V.; Zaikoyskii, V. I.; Boronin, A. I. Highly Oxidized Palladium Nanoparticles Comprising Pd4+ Species: Spectroscopic and Structural Aspects, Thermal Stability, and Reactivity. *J. Phys. Chem. C,* **2012**, *116*, 19342-19348.

(52) Kibis, L. S.; Titkov, A. I.; Stadnichenko, A. I.; Koscheev, S. V.; Boronin, A. I. X-Ray Photoelectron Spectroscopy Study of Pd Oxidation by RF Discharge in Oxygen. *Appl. Surf. Sci.,* **2009**, *255*, 9248-9254.

(53) Otto, K.; Haack, L. P.; Devries, J. E. Identification of Two Types of Oxidied Pd on Gamma Alumina by XPS. *Appl. Catal. B,* **1992**, *1*, 1-12.

(54) Wang, F.; Lu, Z.; Yang, L.; Zhang, Y.; Tang, Q.; Guo, Y.; Ma, X.; Yang, Z. Palladium Nanoparticles with High Energy Facets as a Key Factor in Dissociating O_2 in the Solvent-Free Selective Oxidation of Alcohols. *Chem. Commun.,* **2013**, *49*, 6626-6628.

(55) Leisenberger, F. P.; Koller, G.; Sock, M.; Surnev, S.; Ramsey, M. G.; Netzer, F. P.; Klotzer, B.; Hayek, K. Surface and Subsurface Oxygen on Pd(111). *Surf. Sci.,* **2000**, *445*, 380-393.

(56) Han, J. Kinetic and Morphological Studies of Palladium Oxidation in O_2-CH_4 Mixtures, Worcester Poltechnic Institute 2004.

(57) Collins, G.; Fleming, P.; Barth, S.; O'Dwyer, C.; Boland, J. J.; Morris, M. A.; Holmes, J. D. Alkane and Alkanethiol Passivation of Halogenated Ge Nanowires. *Chem. Mater.,* **2010**, *22*, 6370-6377.

(58) Xian, J. Y.; Hua, Q.; Jiang, Z. Q.; Ma, Y. S.; Huang, W. X. Size-Dependent Interaction of the Poly(N-vinyl-2-pyrrolidone) Capping Ligand with Pd Nanocrystals. *Langmuir,* **2012**, *28*, 6736-6741.

(59) Graf, N.; Yegen, E.; Gross, T.; Lippitz, A.; Weigel, W.; Krakert, S.; Terfort, A.; Unger, W. E. S. XPS and NEXAFS Studies of Aliphatic and Aromatic Amine Species on Functionalized Surfaces. *Surf. Sci.,* **2009**, *603*, 2849-2860.

(60) Klier, K.; Hess, J. S.; Herman, R. G. Structure Sensitivity of Methane Dissociation on Palladium Single Crystal Surfaces. *J. Chem. Phys.,* **1997**, *107*, 4033-4043.

(61) Truica-Marasescu, F.; Wertheimer, M. R. Nitrogen-Rich Plasma-Polymer Films for Biomedical Applications. *Plasma Processes Polym.,* **2008**, *5*, 44-57.

(62) Peng, H.-C.; Xie, S.; Park, J.; Xia, X.; Xia, Y. Quantitative Analysis of the Coverage Density of Br- Ions on Pd{100} Facets and Its Role in Controlling the Shape of Pd Nanocrystals. *J. Am. Chem. Soc.,* **2013**, *135*, 3780-3783.

(63) Nui, Z.; Li, Y. Removal and Utilization of Capping Agents in Nanocatalysis *Chem. Mater.,* **2014**, *26*, 72-83.

(64) Qiu, L. M.; Liu, F.; Zhao, L. Z.; Yang, W. S.; Yao, J. N. Evidence of a Unique Electron Donor-Acceptor Property for Platinum Nanoparticles as Studied by XPS. *Langmuir,* **2006**, *22*, 4480-4482.

(65) Xian, J.; Hua, Q.; Jiang, Z.; Ma, Y.; Huang, W. Size-Dependent Interaction of the Poly(N-vinyl-2-pyrrolidone) Capping Ligand with Pd Nanocrystals. *Langmuir,* **2012**, *28*, 6736-6741.

(66) Tsunoyama, H.; Ichikuni, N.; Sakurai, H.; Tsukuda, T. Effect of Electronic Structures of Au Clusters Stabilized by Poly(N-vinyl-2-pyrrolidone) on Aerobic Oxidation Catalysis. *J. Am. Chem. Soc.,* **2009**, *131*, 7086-7093.

TOC

Supporting Information

Stability, Oxidation and Shape Retention of PVP-Capped Pd Nanocrystals

Gillian Collins[†,‡], Michael Schmidt[†,‡], Gerard P. McGlacken[†], Colm O'Dwyer[†,§] and Justin D. Holmes[†,‡,*]

[†]*Department of Chemistry and the Tyndall National Institute, University College Cork, Cork, Ireland.*

[‡]*Centre for Research on Adaptive Nanostructures and Nanodevices, Trinity College, Dublin, Ireland*

[§]*Materials and Surface Science Institute, University of Limerick, Limerick, Ireland.*

*To whom correspondence should be addressed: Tel: +353 (0)21 4903608; Fax: +353 (0)21 4274097; E-mail: j.holmes@ucc.ie

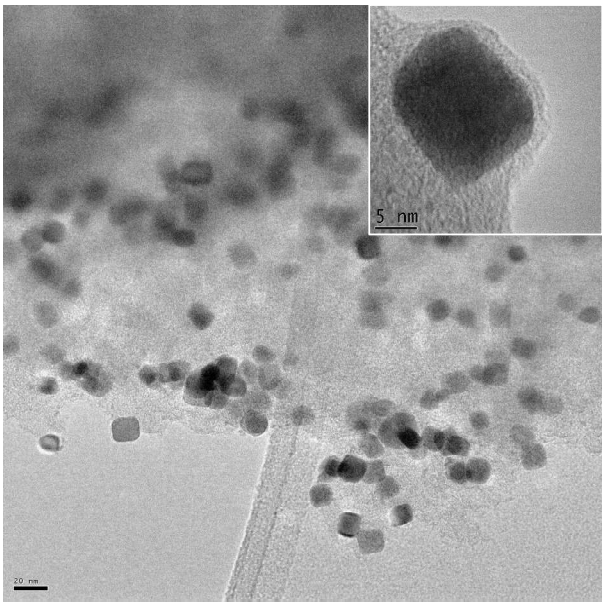

Figure S1. TEM mage of 10 nm cubic Pd NC 3 months after deposition onto activated carbon.

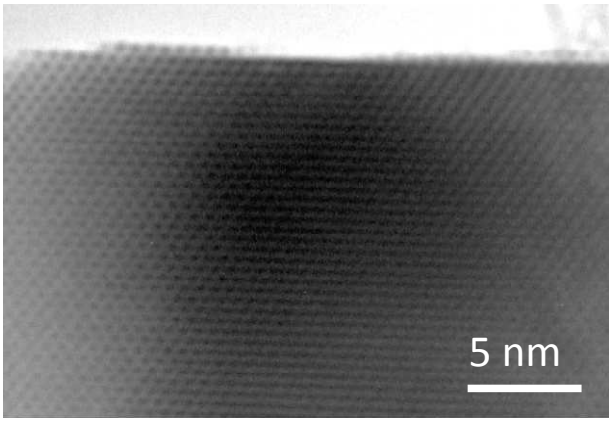

Figure S2. 10 nm cubic Pd NC showing smooth {100} surface.

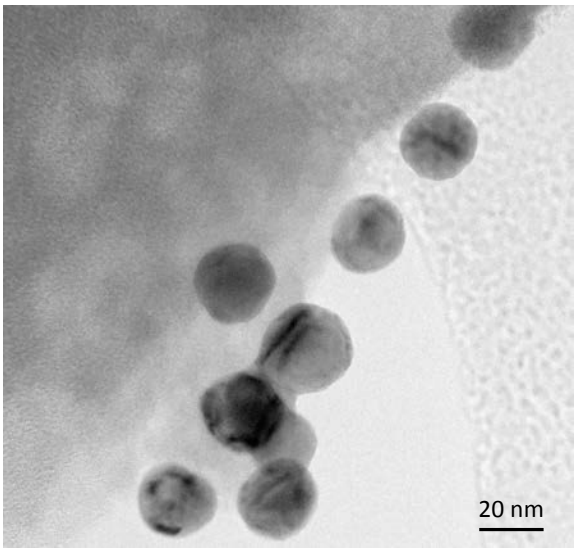

Figure S3. Cuboctahedral NCs 12 months after ambient exposure.

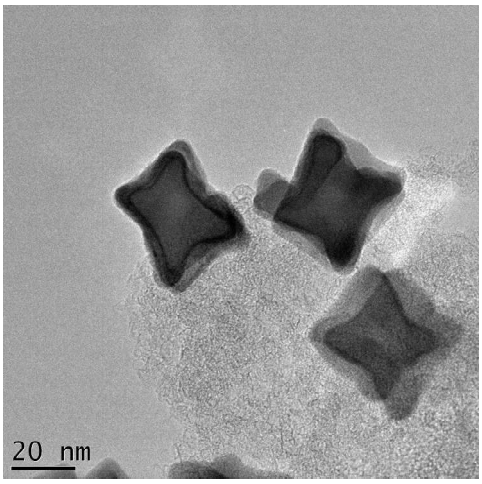

Figure S4. TEM image of concave NCs 12 months after deposition onto activated carbon

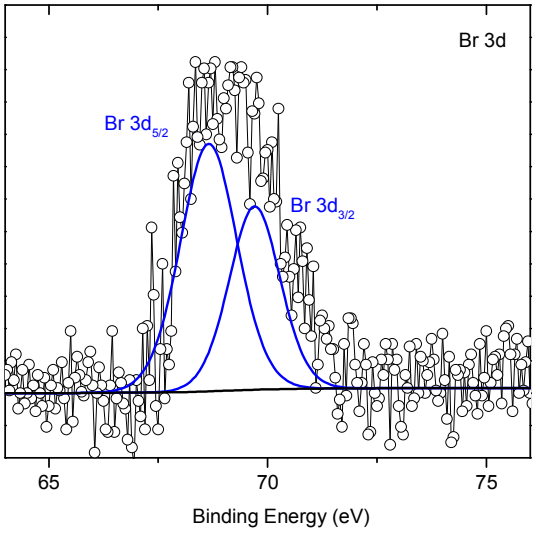

Figure S5. Br 3d core level spectrum of cubic Pd NCs after deposition onto activated carbon.

Nanoparticle Catalysis

DOI: 10.1002/anie.200((will be filled in by the editorial staff))

This is the pre-peer reviewed version that was subsequently accepted for publication in Angewandte Chemie, published in final form in Angew Chem, 53 (2014) 4142-4145

The Origin of Shape-Sensitivity in Pd Catalyzed Suzuki-Miyaura Cross Coupling Reactions

Gillian Collins, Michael Schmidt, Colm O'Dwyer, Justin D. Holmes, Gerard P. McGlacken**

Transition metal catalyzed aryl-aryl bond formation is one of the most important reactions in organic synthesis.[1] The Suzuki-Miyaura reaction is highly utilised due to its synthetic versatility[2] and its discovery was acknowledged by the Nobel Prize in Chemistry in 2010.[3] The use of heterogeneous catalysis in Suzuki-Miyaura coupling is particularly appealing as it allows for ligand-free methodologies and facilitates easy purification and metal recovery.[4] The exquisite control of size and shape dispersion now possible in solution-based colloidal synthesis has attracted much interest in studying the structure sensitivity of reactions catalyzed by noble metal nanocrystals (NCs). Understanding the structure sensitivity of a catalyst can help optimize the design of heterogeneous catalysts, and several important organic[5] and electrocatalytic[6] reactions have been shown to depend on NC shape.

The origin of shape-sensitivity in Suzuki-Miyaura coupling is controversial and is further challenged by the debate concerning the heterogeneous or homogeneous nature of the reaction mechanism. El-Sayed *et al.*[7] demonstrated that tetrahedral Pt NCs catalyzed the cross coupling of phenylboronic acid and iodobenzene, while the use of spherical Pt nanoparticles gave no conversion. They attributed the difference in reactivity to the sharp edges of the tetrahedral particles; Pd NCs with high index surface facets have displayed enhanced reactivity compared to low index facets.[8] However, NCs with high index surfaces are more susceptible to leaching and the higher activity may simply reflect greater dissolution of active molecular Pd.[9] Several studies demonstrate that NC catalyzed Suzuki coupling reactions proceed via a homogenous mechanism, where the particle serves as a source of soluble Pd that is leached from the surface.[10] Conversely, strong evidence for surface mediated catalytic processes are also reported, such as spatially controlled coupling reactions using a Pd-coated AFM probe[11] and *in-situ* X-ray absorption studies[12], which identify edge and corner atoms as the active sites. Recently, Pd supported carbon nanotubes were found to be resistant to leaching under Suzuki-Miyaura conditions but changes to the nanoparticle surface structure and chemistry were observed.[13] The existence of multiple reactions pathways in Suzuki-Miyaura coupling, implies that the role of leached Pd must also be evaluated to fully understand the effect of NC shape on catalytic reactivity.

In this report we demonstrate that the shape of the Pd catalyst influences the reactivity in Suzuki-Miyaura coupling reactions when using catalysts enclosed by defined surface facets. Superior catalytic reactivity is observed for Pd NCs enclosed by {100} surface facets compared to {111} facets. We further probe the origin of the enhanced reactivity associated with a cubic morphology, and find that the structure-sensitivity is related to the leaching susceptibility of the NCs. Molecular oxygen plays a key role in facilitating the leaching mechanism. The interaction of O_2 with Pd is itself facet dependent, which in turn gives rise to more efficient leaching from {100} facets, compared to {111} facets under the reaction conditions.

Cubic Pd NCs displaying {100} surface facets, octahedral NCs enclosed by {111} facets and cuboctahedral NCs with 6 {100} and 8 {111} surface facets were prepared as illustrated in Scheme 1.[6] The NCs were comparable in diameter ~ 20 nm and supported on activated carbon (see Supporting Information Figure. S1-S3). The catalytic properties of the polyhedra were compared in the Suzuki-Miyaura coupling of 4-bromoanisole (**1**) and phenylboronic acid (**2**) in ethanol-H_2O (3:1), with K_2CO_3 as the base at room temperature, as depicted in Scheme 1.

Scheme 1. Model Suzuki-Miyaura reaction and Pd nanocrystal catalysts used in this study.

[*] Dr. G. Collins, M. Schmidt, Dr. C. O'Dwyer, Prof. J. D. Holmes, Dr. G. P. McGlacken,
Department of Chemistry, Analytical and Biological Chemistry Research Facility and Tyndall National Institute University College Cork, Cork (Ireland).
E-mail: j.holmes@ucc.ie, g.mcglacken@ucc.ie
Dr. G. Collins, M. Schmidt, Prof. J. D. Holmes
Centre for Research on Adaptive Nanostructures and Nanodevices (CRANN), Trinity College, Dublin (Ireland)
Dr. C. O'Dwyer
Materials and Surface Science Institute (MSSI)
University of Limerick, Limerick, (Ireland).

[**] We thank Enterprise Ireland (EI2011-0139) and Eli Lilly for supporting this research.

Supporting information for this article is available on the WWW under http://www.angewandte.org

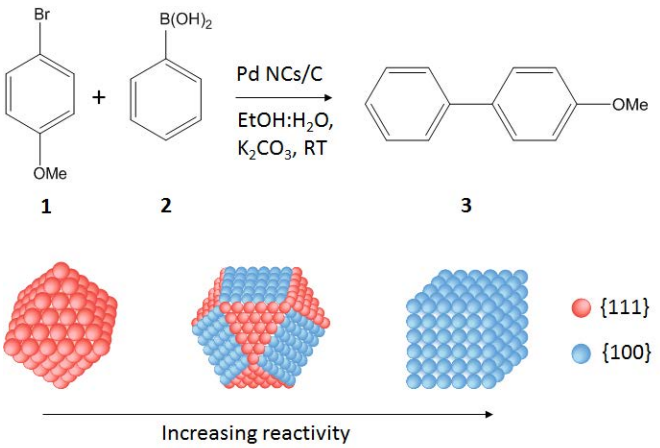

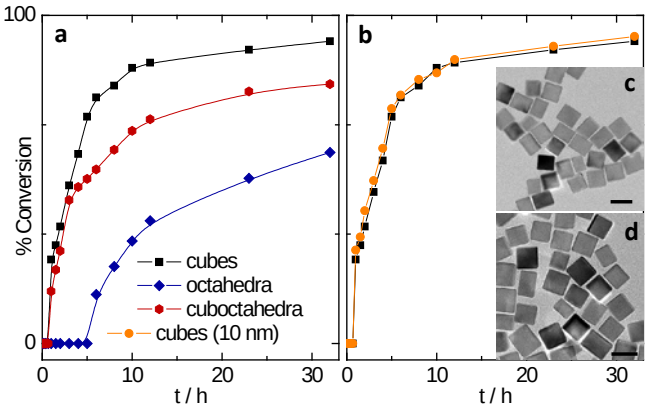

Figure 1. a) Structure sensitivity of Suzuki-Miyaura coupling of **1** and **2** over cubic, cuboctahedral and octahedral Pd NCs. b) Reaction profile of 20 nm and 10 nm cubic NCs where the total surface Pd atoms were equivalent. c) TEM image of 10 nm and d) 20 nm cubic Pd NCs. Scale bar = 20 nm.

Figure 1 illustrates the catalyzed reaction profile of 4-bromoanisole (**1**) with phenylboronic acid (**2**), showing that all of the nanoparticle polyhedra were active in generating the coupled product 4-methoxybiphenyl (**3**). A marked enhancement in the catalytic reactivity was observed for the cubic NCs. In the first 300 min, conversion with the cubic Pd NCs reached 76%, while no conversion was observed for octahedral NCs over the same time period. The final yield of the coupled product (**3**) obtained with cubic NCs was 94%, compared to 58% for octahedral NCs. Cuboctahedral NCs displayed an initial reaction profile similar to the cubic NCs, but a decrease in reactivity was observed after ~250 min, giving a final yield of 78%. Previous reports suggest that reactivity is associated with edge and corner sites, either through surface reaction[14] or by leaching of these low-coordinated atoms.[15] Cubic NCs possess the least amount of surface and edge atoms compared to cuboctahedra and octahedral NCs (Supporting Information Table S1). After normalization to either the number of surface atoms or edge atoms, the reactivity trend in our system follows cube > cuboctahedra > octahedral NCs, suggesting that the shape dependent reactivity is directly associated with the presence of the Pd{100} surface facet. To further investigate the facet effect on the coupling of **1** and **2**, we used 10 nm cubic NCs, which possess 0.4% edge and corner atoms, compared to just 0.16% for 20 nm cubes. The TEM inset in Figure 1b shows the excellent reproducibility and length control of the cubic NCs synthesized in this study. When the concentration of Pd was adjusted, such that the total number of surface Pd atoms was equivalent, the reaction profiles for both the 10 nm and 20 nm cubes were almost identical, as shown in Figure 1b. This observation suggests that the reactivity is not solely associated with the density of edge and corner site densities, but advocates a shape-dependent reactivity and a surface facet effect. Coupling of 4-iodoanisole showed the same reactivity trend with respect to the NC shape i.e. cubic > cuboctahedra > octahedra (Supporting Information, Figure S4).

TEM analysis of the catalysts after the reaction revealed that the average size of the NCs was maintained but a clear loss of the well-defined facets was observed with all polyhedra, as seen by comparison of Figure 2 (a)-(c) before the reaction, with Figure 2 (d)-(f) after reaction (also see Supporting Information Figure S5-S7). Reference samples stirred in EtOH:H_2O solvent showed no variations in morphology. Changes to NC morphology can indicate leaching, which was further assessed by inductively coupled plasma mass spectroscopy (ICP-MS). Pd was detected in the filtrate of all polyhedra after the reaction, as summarized in Table 1.

Pd concentrations in the reaction filtrate were higher for cubic NCs (1.08 ppm) compared to octahedral NCs (0.66 ppm), suggesting that the origin of the structure dependent reactivity may be due to preferential leaching from the (100) surface. The presence of O_2 in the reaction has also been shown to result in greater Pd leaching compared to reactions in inert atmosphere.[16] ICP analysis (Table 1) shows that the presence of O_2 promotes Pd leaching and is influenced by the NC shape. In the presence of O_2, leached Pd concentrations correlate directly with catalytic activity, increasing from octahedral < cuboctahedra < cubic NCs. In control experiments without dissolved O_2 (deoxygenated with Ar), the amount of Pd in the filtrates was lower and similar for all polyhedra (~80 ppb), implying Pd leaching is shape-sensitive at least under aerobic conditions. Additional ICP analysis of the NCs was undertaken to identify the primary species responsible for leaching and also to determine if a specific reagent gave rise to preferential leaching on a particular surface facet.

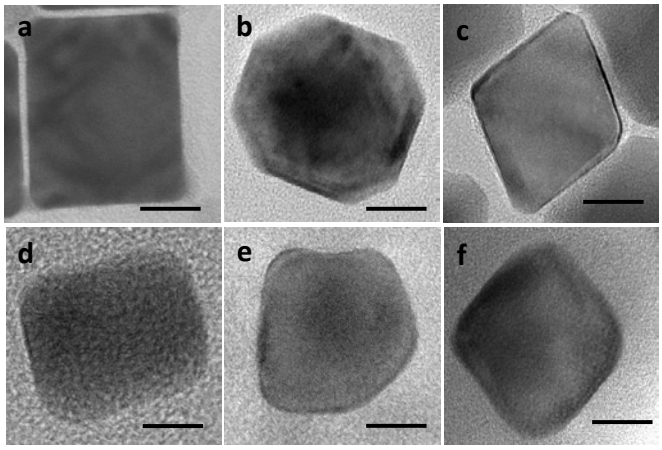

Figure 2. Pd NCs in the form of (a) cubic (b) cuboctahedral, (c) octahedral before reaction and (d) cubic, (e) cuboctahedral (f) octahedral, after reaction. Scale bar = 10 nm.

Much debate concerns the nature of the species responsible for leaching Pd. Oxidative addition of the aryl halide is often reported to be the primary mechanism for leaching,[17] while other studies demonstrate the boronic acid and base to be responsible.[10a, 18] Under our reaction system, the use of ICP analysis identified the base and boronic acid as the primary leaching reagents, however the aryl bromide also contributed to a lesser degree. Significantly, the base and boronic acid induced greater leaching from the cubic NCs compared to octahedral NCs, suggesting the {100} surface is more susceptible to leaching than {111} surfaces.

Table 1. ICP-MS analysis of reaction filtrates.

Sample[a]	[Pd]/ ppb	Sample	[Pd]/ ppb
Cubic^{Air}	1008	*Cubes:*	-
Cuboctahedra	663	K_2CO_3 + $PhB(OH)_2$	658
Octahedra	324	MeOPhBr	69
Cubic^{Ar}	96[b]	*Octahedra:*	-
Cuboctahedra^{Ar}	79[b]	K_2CO_3 + $PhB(OH)_2$	106
Octahedra^{Ar}	81[b]	MeOPhBr	51

[a] Samples normalized to 5wt % HCl. Average of 3 samples. [b] Catalyst degassed under vacuum before addition to reaction solution previously deoxygenated with Ar.

ICP analysis identified O_2 as a promoter of leaching and this observation led us to explore the impact of O_2 on the catalytic activity and to determine if the leached Pd contributed to the catalytic activity in the reaction. The influence of adsorbed O_2 and the role of dissolved O_2 during the reaction were investigated by comparing the reactivity of the NCs immobilized (Imb) and reacted (Rx) under air or Ar; the reaction profiles are compared in Figure 3b. The reaction profiles showed that the Air^{Imb}-Air^{Rx} catalysts exhibited the fastest reaction time, giving a 96% conversion after 28 h. The Air^{Imb}-Ar^{Rx} catalysts displayed similar initial profiles but the reaction become progressively slower as it progressed, resulting in a final yield of 62%. This finding confirms that dissolved O_2 promotes catalytic activity, which in turn contributes to greater leaching as determined by ICP. The Ar^{Imb}-Air^{Rx} catalytic system displayed an induction period nearly 4 times longer than that of Air^{Imb}-Air^{Rx}, with the yield decreasing to 50%, indicating that the presence of chemisorbed O_2, as well as dissolved O_2 is beneficial for catalytic activity. Finally and quite remarkably, the Ar^{Imb}-Ar^{Rx} catalytic system did not show any conversion after 28 h. Leaching concentrations also correlated with reactivity, with the filtrates under the Air^{Imb}-Air^{Rx} having the highest Pd concentrations, while

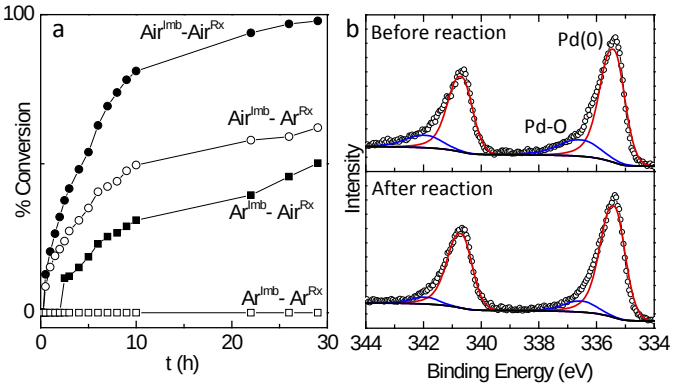

low amounts of Pd were detected in the filtered solutions of the Ar^{Imb}-Ar^{Rx} samples (Supporting Information, Table S2). Reaction profiles using 4-iodoanisole also displayed the same reactivity trend (Supporting Information, Figure S8).

Figure 3. a) Reaction profile of cubic Pd NCs immobilized and reacted under aerobic and inert conditions. b) XPS analysis of cubic NCs before and after reaction.

The beneficial effect of O_2 has been reported for Suzuki-Miyaura coupling using *in situ* generated Pd nanoparticles although it's role in the mechanism was not identified.[19] XPS analysis was used to probe changes in the surface chemistry of the catalysts. Figure 3b displays the Pd 3d core level spectra of cubic NCs before and after the reaction, showing the presence of a doublet at a binding energy (BE) of 335.4 eV (340.6 eV), which can be assigned to metallic Pd(0).[20] An additional shoulder peak at a BE of 336.4 eV was also present in the spectra for all polyhedrons. The presence of surface oxide species is typically reported at a BE ~1 eV higher than Pd(0), while bulk oxides are observed at BE >1.5 eV, thus the peak at 336.4 eV is assigned to the presence of surface Pd-O species.[21] NCs immobilized under Ar also displayed a contribution of Pd-O in the Pd 3d spectrum, as the NC synthesis is performed in air, where the presence of O_2 is important for oxidative etching and shape control of the particles.[22] The Pd 3d spectra of cubic NCs after the reaction in air displayed a decrease in the peak intensity associated with surface Pd-O (blue peak). NCs immobilized and reacted under Ar, showed negligible changes to the Pd 3d spectra (Supporting Information, Figure S9), confirming that O_2 plays a key role in the removal of surface species, as illustrated in Figure 4. O_2 adsorption on Pd surfaces is a spontaneous process but is influenced by the crystal orientation of the surface. Molecular adsorption and activation of O_2 is preferential on Pd{100} surface facets compared to {111} facets due a lower activation energy.[23] The presence of chemisorbed O_2 may facilitate the adsorption of phenyl borates which are subsequently more readily removed from the surface.[24] This scenario is also consistent with ICP analysis indicating boronic acid as a primary species responsible for Pd leaching.

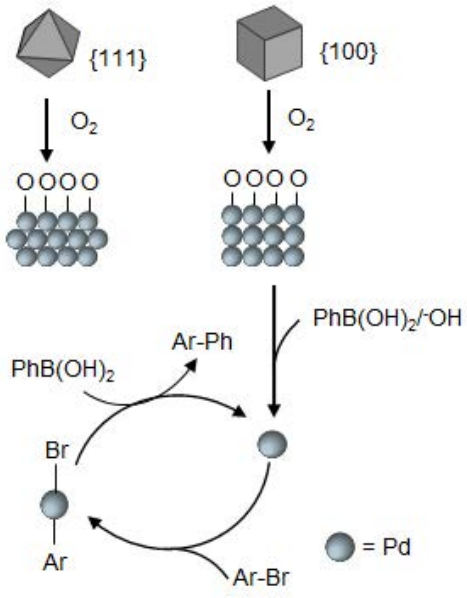

Figure 4. Schematic illustrating O_2 promoted leaching on Pd NCs.

In summary, we find that the shape sensitivity in Suzuki-Miyaura coupling originates from a homogenous reaction pathway. Leaching from the NCs is not solely attributed to the loss of low co-ordination edge and corner atoms, but to the nature of the surface facets. The catalytically active Pd species are generated by leaching of the surface oxide and this leaching mechanism is shape-sensitive. Preferential adsorption of O_2 on Pd {100} compared to Pd {111} surfaces induces greater Pd leaching and consequently enhanced reactivity when using cubic NCs compared to octahedral NCs. These insights will help in the rational design of catalysts and reaction conditions for cross-couplings and other important transformations.

Received:
Published online on:

Keywords: palladium · heterogeneous catalysis · Suzuki-Miyaura coupling · surface facet

[1] J. Hassan, M. Sevignon, C. Gozzi, E. Schulz, M. Lemaire, *Chem. Rev.* **2002**, *102*, 1359-1469.

[2] a) N. Miyaura, A. Suzuki, *Chem. Rev.* **1995**, *95*, 2457-2483; b) G. A. Molander, N. Ellis, *Acc. Chem. Res.* **2007**, *40*, 275-286; c) G. C. Fu, *Acc. Chem. Res.* **2008**, *41*, 1555-1564.

[3] C. C. C. J. Seechurn, M. O. Kitching, T. J. Colacot, V. Snieckus, *Angew. Chem.* **2012**, 124, 5150-5174, *Angew. Chem. Int. Ed.* **2012**, *51*, 5062-5085.

[4] a) L. Yin, J. Liebscher, *Chem. Rev.* **2007**, *107*, 133-173; b) M. Lamblin, L. Nassar-Hardy, J.-C. Hierso, E. Fouquet, F.-X. Felpin, *Adv. Synth. Catal.* **2010**, *352*, 33-79; c) Y. Xiong, B. J. Wiley, Y. Xia, *Angew. Chem.* **2007**, 119, 7291, *Angew. Chem. Int. Ed.* **2007**, *46*, 7157-7159; d) H. Zhang, M. S. Jin, Y. J. Xiong, B. Lim, Y. N. Xia, *Acc. Chem. Res.* **2013**, *46*, 1783-1794.

[5] a) M. Crespo-Quesada, A. Yarulin, M. Jin, Y. Xia, L. Kiwi-Minsker, *J. Am. Chem. Soc.* **2011**, *133*, 12787-12794; b) K. M. Bratlie, H. Lee, K. Komvopoulos, P. Yang, G. A. Somorjai, *Nano Lett.* **2007**, *7*, 3097-3101.

[6] M. Jin, H. Zhang, Z. Xie, Y. Xia, *Energy Environ. Sci.* **2012**, *5*, 6352-6357.

[7] a) R. Narayanan, M. A. El-Sayed, *Langmuir* **2005**, *21*, 2027-2033; b) R. Narayanan, M. A. El-Sayed, *J. Phys. Chem. B* **2005**, *109*, 12663-12676.

[8] a) F. Wang, C. Li, L.-D. Sun, H. Wu, T. Ming, J. Wang, J. C. Yu, C.-H. Yan, *J. Am. Chem. Soc.* **2011**, *133*, 1106-1111; b) *Angew. Chem.* **2013**, *125*, 2580-2584, X. Huang, Y. Li, Y. Chen, E. Zhou, Y. Xu, H. Zhou, X. Duan, Y. Huang, *Angew. Chem. Int. Ed.* **2013**, *52*, 2520-2524; c) *Angew. Chem.* **2010**, *122*, 5082-5086, A. Mohanty, N. Garg, R. Jin, *Angew. Chem. Int. Ed.* **2010**, *49*, 4962-4966.

[9] J. Xu, A. R. Wilson, A. R. Rathmell, J. Howe, M. Chi, B. J. Wiley, *ACS Nano* **2011**, *5*, 6119-6127.

[10] a) P.-P. Fang, A. Jutand, Z.-Q. Tian, C. Amatore, *Angew. Chem.* **2011**, *123*, 12392-12396, *Angew. Chem. Int. Ed.* **2011**, *50*, 12184-12188; b) M. B. Thathagar, J. E. ten Elshof, G. Rothenberg, *Angew. Chem.* **2006**, *118*, 2952-2956, *Angew. Chem. Int. Ed.* **2006**, *45*, 2886-2890.

[11] a) J. J. Davis, K. S. Coleman, K. L. Busuttil, C. B. Bagshaw, *J. Am. Chem. Soc.* **2005**, *127*, 13082-13083; b) J. J. Davis, C. B. Bagshaw, K. L. Busuttil, Y. Hanyu, K. S. Coleman, *J. Am. Chem. Soc.* **2006**, *128*, 14135-14141.

[12] a) P. J. Ellis, I. J. S. Fairlamb, S. F. J. Hackett, K. Wilson, A. F. Lee, *Angew. Chem.* **2010**, *122*, 1864-1868, *Angew. Chem. Int. Ed.* **2010**, *49*, 1820-1824.

[13] L. Shao, B. Zhang, W. Zhang, S. Y. Hong, R. Schlçgl, D. S. Su, *Angew. Chem.* **2013**, 125, 2168-2171, *Angew. Chem. Int. Ed.* **2013**, *52*, 2114-2117.

[14] a) J. Le Bars, U. Specht, J. S. Bradley, D. G. Blackmond, *Langmuir* **1999**, *15*, 7621-7625; b) Y. Li, E. Boone, M. A. El-Sayed, *Langmuir* **2002**, *18*, 4921-4925.

[15] H. Ramezani-Dakhel, P. A. Mirau, R. R. Naik, M. R. Knecht, H. Heinz, *Phys. Chem. Chem. Phys.* **2013**, *15*, 5488-5492.

[16] R. G. Heidenreich, E. G. E. Krauter, J. Pietsch, K. Kohler, *J. Mol. Catal. A* **2002**, *182*, 499-509.

[17] a) Y. Y. Ji, S. Jain, R. J. Davis, *J. Phys. Chem. B* **2005**, *109*, 17232-17238; b) Z. Niu, Q. Peng, Z. Zhuang, W. He, Y. Li, *Chem. Eur. J.* **2012**, *18*, 9813-9817; c) A. K. Diallo, C. Ornelas, L. Salmon, J. R. Aranzaes, D. Astruc, *Angew. Chem.* **2007**, *119*, 8798-8802, *Angew. Chem. Int. Ed.* **2007**, *46*, 8644-8648.

[18] S. S. Soomro, F. L. Ansari, K. Chatziapostolou, K. Koehler, *J. Catal.* **2010**, *273*, 138-146.

[19] W. Han, C. Liu, Z. Jin, *Adv. Synth. Catal.* **2008**, *350*, 501-508.

[20] G. Collins, M. Blomker, M. Osaik, J. D. Holmes, M. Bredol, C. O'Dwyer, *Chem. Mater.* **2013**, *25*, 4312-4320.

[21] a) G. Ketteler, D. F. Ogletree, H. Bluhm, H. J. Liu, E. L. D. Hebenstreit, M. Salmeron, *J. Am. Chem. Soc.* **2005**, *127*, 18269-18273; b) E. Lundgren, G. Kresse, C. Klein, M. Borg, J. N. Andersen, M. De Santis, Y. Gauthier, C. Konvicka, M. Schmid, P. Varga, *Phys. Rev. Lett.* **2002**, *88*, 246103.

[22] a) Y. J. Xiong, J. M. McLellan, Y. D. Yin, Y. N. Xia, *Angew. Chem.* **2007**, *119*, 804-808, *Angew. Chem. Int. Ed.* **2007**, *46*, 790-794; b) Y. J. Xiong, J. Y. Chen, B. Wiley, Y. N. Xia, S. Aloni, Y. D. Yin, *J. Am. Chem. Soc.* **2005**, *127*, 7332-7333; c) M. C. Liu, Y. Q. Zheng, L. Zhang, L. J. Guo, Y. N. Xia, *J. Am. Chem. Soc.* **2013**, *135*, 11752-11755.

[23] R. Long, K. Mao, X. Ye, W. Yan, Y. Huang, J. Wang, Y. Fu, X. Wang, X. Wu, Y. Xie, Y. Xiong, *J. Am. Chem. Soc.* **2013**, *135*, 3200-3207.

[24] H. Tsunoyama, H. Sakurai, N. Ichikuni, Y. Negishi, T. Tsukuda, *Langmuir* **2004**, *20*, 11293-11296.

Entry for the Table of Contents (Please choose one layout)

Layout 2:

Nanoparticle Catalysis

Gillian Collins, Michael Schmidt, Colm O'Dwyer, Justin D. Holmes*, Gerard P. McGlacken*

The Origin of Shape-Sensitivity in Pd Catalyzed Suzuki-Miyaura Cross Coupling Reactions

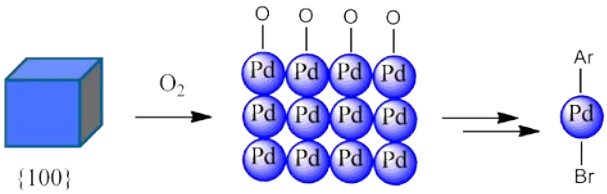

The Origin of Shape-Sensitivity in Pd Catalyzed Suzuki-Miyura Cross Coupling

Gillian Collins, Michael Schmidt, Colm O'Dwyer, Justin D. Holmes and Gerard P. McGlacken**

Supporting Information

Nanocrystal Synthesis and Immobilization

Shape controlled nanocrystals used in this study were prepared according to literature several procedures.[1] Synthesis of Pd nanocubes: 105 mg of PVP (Mw ~ 55,000), 60 mg of ascorbic acid and 300 mg of KBr were dissolved in 8 ml of water. The mixture was heated for 10 min at 80 °C, under stirring followed by addition of 57 mg Na_2PdCl_4 in 3 ml of water. The solution was heated to 80 °C and aged for 3 h after which the product was collected by centrifugation, washed with water and briefly sonicated. This purification procedure was repeated 3 times. Finally, the nanocubes were re-dispersed in 11 ml of water. Synthesis of 20 nm cubes followed the same procedure with the addition of 600 mg of KBr. Octahedra and cuboctahedra were prepared from cubic Pd seeds. 105 mg of PVP, 100 μl of formaldehyde and 0.3 ml of seed solution were added to 8 ml of water and heated to 60 °C. Varying amounts of Na_2PdCl_4 dissolved in 3 ml of water were added to obtain cuboctahedra (8.7 mg) or octahedral (29 mg). The reaction was kept at 60 °C for 3 h and the products were collected and purified by the procedure previously described. The nanocrystals were immobilized on carbon by stirring the solution in the presence of activated carbon at room temperature, which has been previously dried in a vacuum oven at 120 °C. The product was collected by filtration and dried under vacuum. Similar Pd loadings, as determined by ICP, were used in the reaction. The average Pd loading was 3.6 wt%, with not more the 0.2 wt% difference between each catalyst sample.

Suzuki-Miyaura Cross Coupling Reactions

In a typical experiment 0.268 g of phenylboronic acid (2.2 mmol). 0.468 g of 4-methoxyiodobenzene or 0.25 ml of 4-methoxybromobenezene (2 mmol), 0.553 g (4 mmol) of K_2CO_3 were added to 30 ml of

ethanol/water (3:1). The reactions were initiated by addition of the catalyst (0.5 mol %). Reactions were conducted at room temperature and sampled at regular intervals for GC analysis. Samples were analyzed using an Agilent 7890A GC system, equip with a flame ionisation detector (FID). Products were identified against authenticated standards and quantified by calibration to obtain response factors (RF) against the known internal standard (dodecane).

Materials Characterization:

Electron Microscopy.

Scanning electron microscopy (SEM) images were obtained using a FEI DualBeam Helios NanoLab 600i high resolution SEM. Transmission electron microscopy (TEM) analysis was performed using a Jeol 2100 transmission electron microscope at an operating voltage of 200 kV.

X-ray Photoelectron Spectroscopy.

XPS data was acquired using a KRATOS AXIS 165 monochromatized (Al Kα = 1486.6 eV) x-ray photoelectron spectrometer. Spectral fitting was carried out on using CASA software. All spectra were referenced to the C 1s spectrum at a binding energy (BE) of 284.6 eV. The photoemission data was processed using a Shirley background correction. The high resolution Pd 3d core level spectra were fit to asymmetric Gaussian-Lorentzian profiles. The Pd(0) peak was fixed at a binding energy of 335.4 eV with a FWHM of 0.9.

Table S1. Statistics of surface atoms and surface sites on cubic, cuboctahedral and octahedral Pd NCs.

Nanocrystal	**N_{tot} [a]**	**N_{surf} [b]**	**N_{e+c} [c]**	**% surf**	**% e+c**	**yield [d] %**	**TOF_{tot} [e]**	**TOF_{surf} [f]**
cubes	515151	30002	596	5.82	0.16	94	6.2	106
octahedra	316394	23718	918	7.5	0.29	58	3.8	52
cuboctahedra	702219	42012	1404	6.0	0.2	79	5.3	88

Calculations for cubic and octahedral nanocrystals are based on equations derived by Hartog and van Hardeveld assuming a perfect face centred cubic lattice.[2] Calculations for the cuboctahedra nanocrystals were based on the work of Benfield for a cuboctahedron consisting of 6 square and 8 triangular faces.[3] [a] m is the number of atoms lying on an equivalent edge including the corner atoms. [b] N_{tot} is the total number of atoms in each nanocrystal (cubic: $N_{tot} = 4m^3 - 6m^2 + 3m$; octahedral, $N_{tot} = 1/3m(2m^2 + 1)$ and cuboctahedral $N_{tot} = 1/3(2m - 1)(5m^2 - 5m + 3)$. [c] N_{surf} is the number of surface atoms (cubic $N_{surf} = 12m^2 - 24m + 14$; octahedral $N_{surf} = 4m^2 - 8m + 6$ and cuboctahedral $N_{surf} = 10m^2 - 20m + 12$). N_{e+c} is the number of edge and corner atoms. Cubic: $N_{e+c} = 12(m - 2) + 8$; octahedral $N_{e+c} = 12(m - 2) + 6$; cuboctahedral $N_{e+c} = 24(m - 2) + 12$. [d] Percentage yield after 30 h (determined by GC). [e] TOF_{tot} is the turnover frequency calculated from molar equivalents of Pd (0.5 mol%). [f] TOF_{surf} are the turnover frequencies normalized to the total number of surface atoms on each polyhedron.

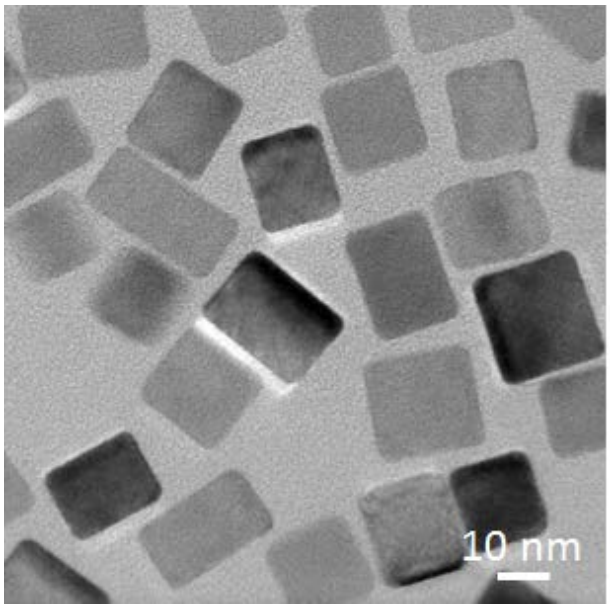

Fig. S1 TEM of (a) as-synthesized unsupported Pd cubic NCs.

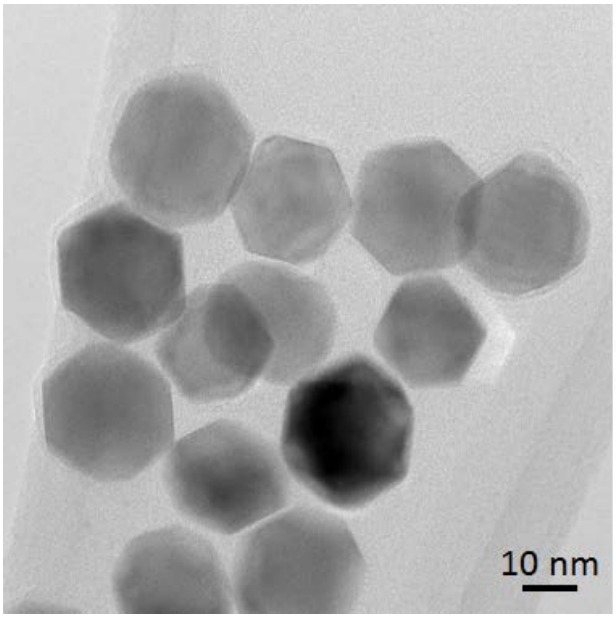

Fig. S2. TEM of (a) as-synthesized unsupported Pd cuboctahedra NCs.

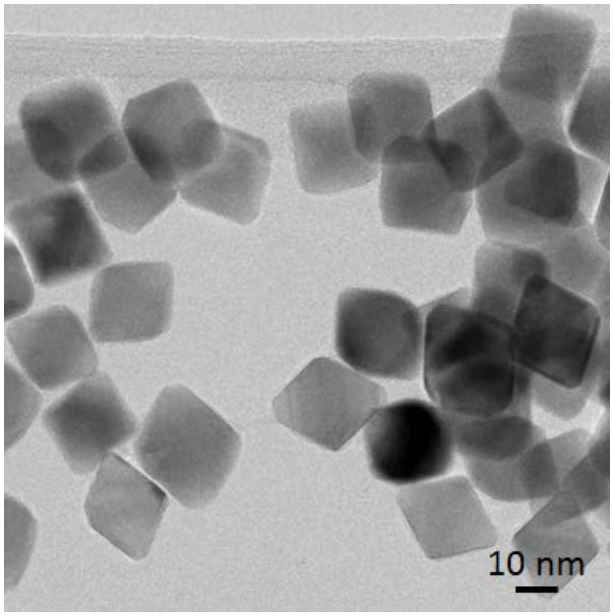

Fig. S3. TEM of (a) as-synthesized unsupported Pd octahedral NCs

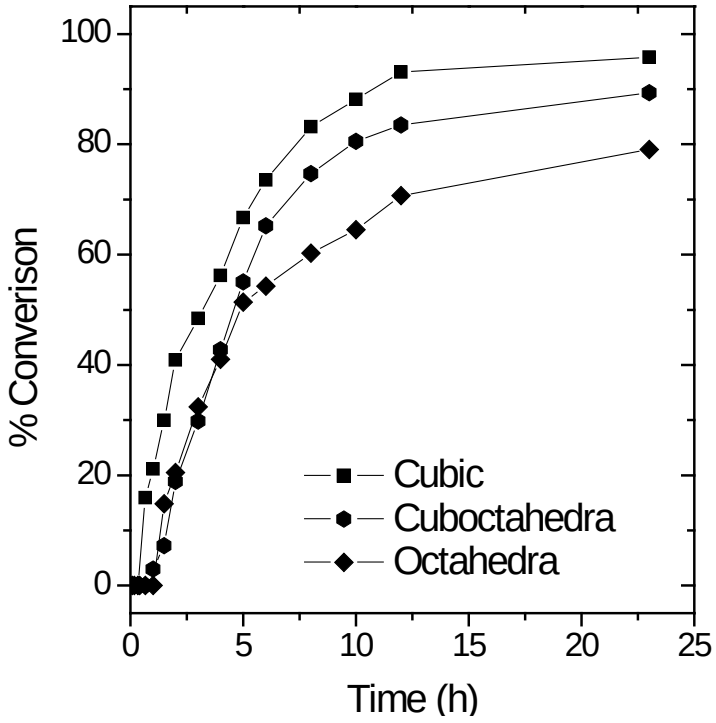

Figure S4. Reaction profile of Suzuki coupling of 4-iodoanisole and phenyl boronic acid catalysed by cubic, cuboctahedral and octahedral Pd NCs.

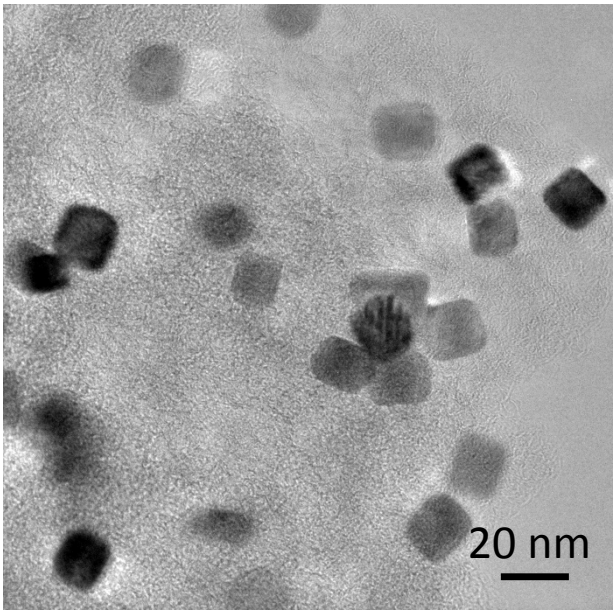

Figure S5. Cubic Pd NCs after Suzuki coupling reaction.

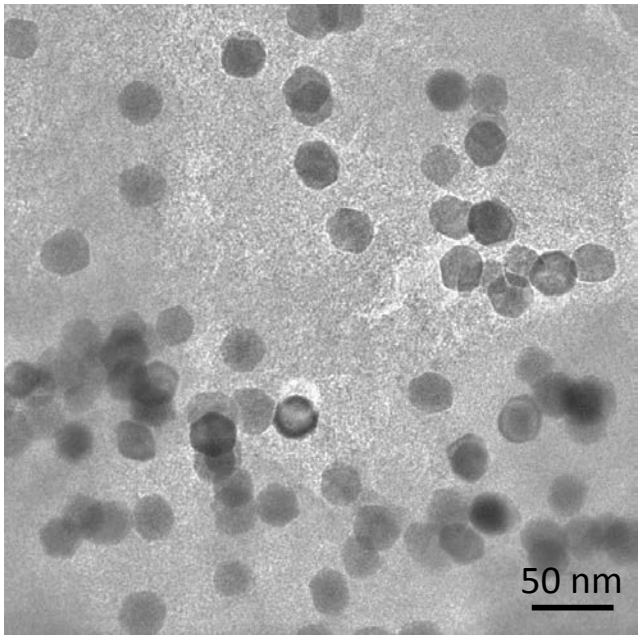

Figure S6. Cuboctahedral Pd NCs after Suzuki coupling reaction.

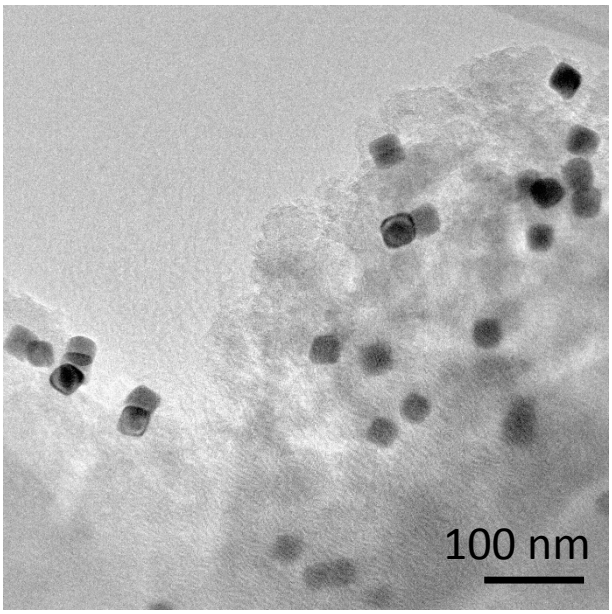

Figure S7. Octahedral Pd NCs after Suzuki coupling reaction.

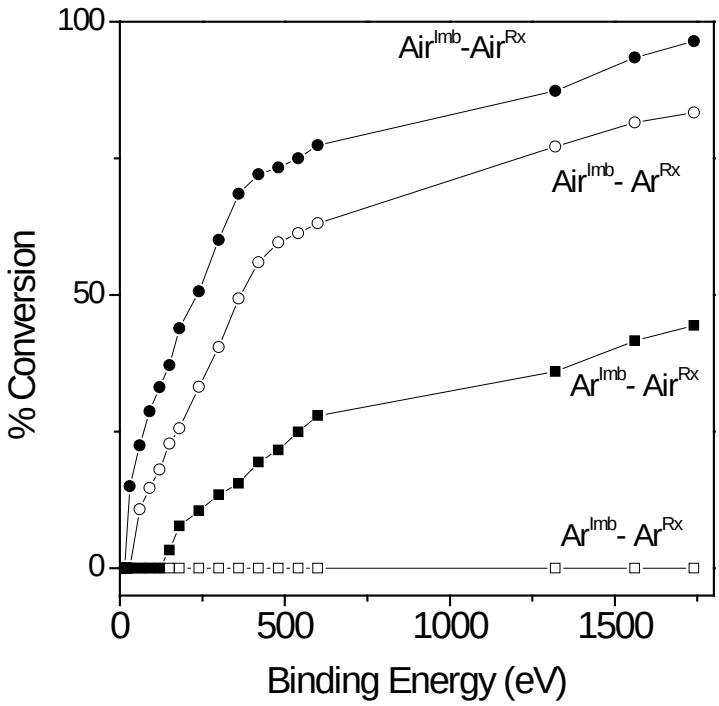

Figure S8. Reaction profile of 4-iodoanisole and phenylboronic acid using cubic Pd NCs.

Table S2. ICP analysis of reaction filtrates using cubic Pd NCs immobilized and reacted under air or Ar.

Reaction	**[Pd]/ ppm**
Air^{Imb}-Air^{Rx}	1.22
Air^{Imb}-Ar^{Rx}	0.63
Ar^{Imb}-Air^{Rx}	0.61
Ar^{Imb}-Ar^{Rx}	0.12

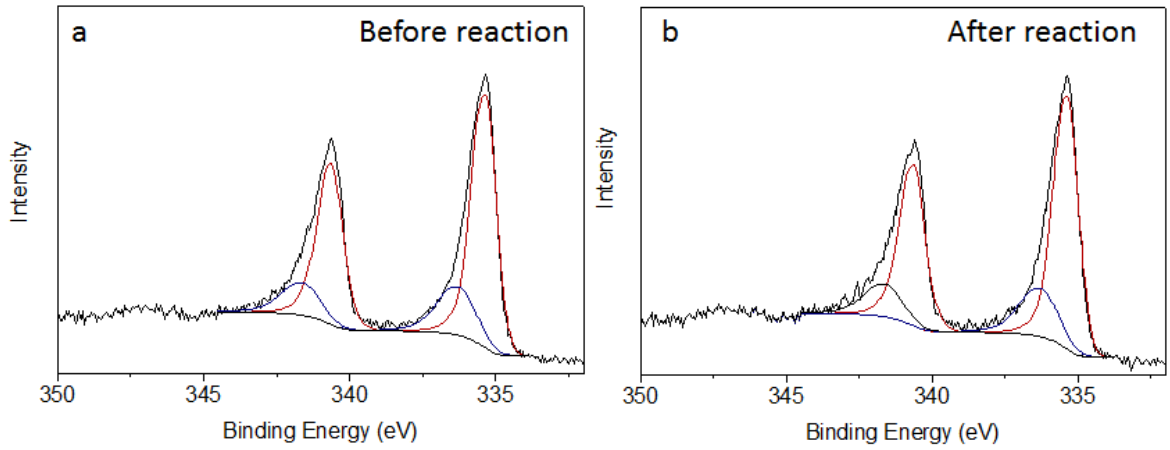

Figure S9. Pd 3d core level spectra of Pd NCs immobilized under Ar (a) before reaction and (b) after reaction under Ar.

[1] a)M. Jin, H. Zhang, Z. Xie, Y. Xia, *Energy Environ. Sci.* **2012**, *5*, 6352-6357; b)M. Jin, H. Zhang, Z. Xie, Y. Xia, *Angew. Chem. Int. Ed.* **2011**, *50*, 7850-7854.

[2] Vanharde.R, F. Hartog, *Surf. Sci.* **1969**, *15*, 189-230.

[3] R. E. Benfield, *J. Chem. Soc., Faraday Trans.* **1992**, *88*, 1107-1110.

Enhanced Catalytic Activity of High Index Faceted Palladium Nanoparticles in Suzuki-Miyaura Coupling due to Efficient Leaching Mechanism

Gillian Collins[†, ϕ *], *Michael Schmidt* [†, ϕ], *Colm O'Dwyer*[†,§,] *Gerard McGlacken*[† *], *and Justin D. Holmes*[†,ϕ]

[†]*Department of Chemistry Department and the Tyndall National Institute, University College Cork, Cork, Ireland.*

[ϕ]*Centre for Research on Adaptive Nanostructures and Nanodevices, Trinity College, Dublin, Ireland.*

[§]*Materials and Surface Science Institute, University of Limerick, Limerick, Ireland.*

*To whom correspondence should be addressed: Tel: +353 (0)21 4205143; Fax: +353 (0)21 4205143; E-mail: g.collins@ucc.ie

Abstract

The structure-property relationship of palladium (Pd) catalysts in Suzuki-Miyaura cross coupling reactions was investigated using Pd nanocrystals of uniform size and shape. Superior catalytic reactivity was observed for Pd nanoparticles with high index {730} surface facets compared to low index {100} facets. While the nanocrystal morphologies were

maintained during the reaction, the presence of leached Pd clusters, identified by high resolution transmission electron microscopy (TEM), indicate a leaching mechanism. The nature of the surface facets on the nanoparticles were observed to influence the rate of Pd leaching during the Suzuki coupling reaction. The enhanced reactivity observed for the high index facet catalysts stems from the greater number of leachable atoms of low abstraction energy available on high index planes.

Key words: Palladium nanocrystals, shape control nanoparticles, Suzuki coupling, leaching.

Introduction

Noble metal nanocrystals (NCs) with high index surface facets have attracted much interest due to their potential for enhanced catalytic performance.[1] High index facets are denoted by a set of Miller indices {*hkl*}, where one index is greater than one. Unlike low index planes characterized by such as {111} and {100} facets, which are relatively smooth, the surface atomic structure of high index facets are characterized by a high density of step, terrace and kink sites.[2] Such surfaces are well known to improve catalytic rates for many reactions.[3] The physical origins of structure sensitivity are complex and generally ascribed to electronic and geometrical effects that influence adsorption energies and reaction pathways.[4] Chemisorption of reaction species can be preferential on step and kink sites due to their low co-ordination numbers (6-7) or allow more energetically favorable transition states compared to close-packed surfaces.[5]

Pd is an important noble metal as a heterogeneous catalyst for chemical synthesis, automotive and fuel cell applications.[6-7] Pd is the principle catalyst metal for carbon-carbon cross coupling reactions which are central to a variety of chemical processes for pharmaceutical

and fine chemicals industries.[8] The versatile nature of these reactions has also lead to many other applications such as the surface modification of semiconductors[9], the preparation of inorganic-organic nanocomposites[10] and sensors.[11] Coupling reactions conventionally use homogenous catalysts but heterogeneous nanoparticle-based catalysts are attractive as they offer convenient removal of the catalyst post reaction. The possibility of recovery and recyclability of the catalyst also makes them more economically attractive, especially for expensive noble metals. A variety of coupling reactions including Suzuki-Miyaura, Heck, Ullman, Stille and Sonogashira, all proceed under heterogeneous conditions.[6, 12-15] Suzuki coupling reactions are one of the most widely utilized methods for the construction of carbon-carbon bonds and are very effective under heterogeneous conditions.[12] Suzuki coupling of aryl chlorides, even deactivated ones, can be achieved under heterogeneous conditions, which are desirable for industrial synthesis due to the low cost of chloride starting materials.[14, 16-17]

A wide variety of heterogeneous catalysts have been studied for Suzuki coupling including dispersed nanoparticles,[18-19] powder-supported nanoparticles[20-22] and catalytic thin films.[23 24] Several studies have demonstrated considerably enhanced catalytic performance of Suzuki reactions when using NCs enclosed by high index surface facets.[25-29] A variety of preparation methods have been reported for Pd NCs with high index surface facets such as seeded growth[27], epitaxial growth[26, 30] and electrochemically[31-33] and solid state methods.[34] The origin of the enhanced reactivity observed is generally attributed the high density of low-coordinate atoms present at the surface of the catalyst.[2] Early reports of heterogeneously catalyzed Suzuki coupling suggest a surface driven reaction occurring at the edge and corner sites of nanoparticles[35-36] and this hypothesis is supported by a number of studies providing evidence of a surface mediated process.[37-39] If a reaction occurs preferentially at edge sites then enhanced reactivity reported for high index planes compared to low index planes would be reasonable due to the stepped nature of the high index facets. A considerable number of

mechanistic studies have identified that leaching processes occur in many nanoparticle catalyzed reactions.[40-42] Although debate still surrounds the leaching mechanism, dissolved Pd from the nanoparticle surface has been shown to play a central role in the catalytic cycle of Suzuki reactions. [43-44]

Herein, we investigate the structure-property relationship of catalysts in Suzuki cross coupling reactions using Pd catalysts of uniform size and shapes. The catalytic reactivity of Pd nanoparticles with low index {100} facets and high index {730} facets are compared. A considerably improved catalytic performance was observed from high index NCs. Catalytic studies, high resolution electron microscopy and XPS analysis was used to elucidate the mechanism of the enhanced reactivity associated with the high index surface planes. We identify that the superior activity observed for the high index faceted catalysts stems from the greater leaching of Pd atoms from the surface rather than a true surface-mediated process.

Experimental

Pd NC Synthesis: Cubic NCs with edge lengths of 10 and 20 nm were synthesized as previously described and used for the seeded growth of the concave NCs.[27] The mean edge length was determined to be 10.6 nm (standard deviation, σ = 1.3) and 19.4 nm (σ =1.9) for the cubic NC and 35.1 nm (σ = 3.2) for the concave cubic NCs (Supporting Information Figure S1). These nanoparticles are capped with PVP and Br capping ligands. To avoid the influence of support materials on the catalytic activity of the NCs, unsupported nanoparticles were used.

Materials Characterization: Scanning electron microscopy (SEM) images were obtained using a FEI DualBeam Helios NanoLab 600i high resolution SEM. Transmission electron microscopy (TEM) analysis was performed using a Jeol 2100 electron microscope at an

operating voltage of 200 kV. X-ray Photoelectron Spectroscopy (XPS) was acquired using a KRATOS AXIS 165 monochromatized X-ray photoelectron spectrometer equipped with an Al Kα (hv = 1486.6 eV) X-ray source. Spectra were collected at a take-off angle of 90° and all spectra were reference to the C 1s peak at 284.6 eV.

Catalytic studies: In a typical reaction, 0.268 g of phenylboronic acid (2.2 mmol). 0.468 g of 4-methoxyiodobenzene or 0.25 ml of 4- methoxybromobenezene (2 mmol), 0.553 g (4 mmol) of K_2CO_3 were added to 30 ml of ethanol/water (3:1). The reactions were initiated by addition of the catalyst. Reactions were conducted at room temperature and sampled at regular intervals for GC analysis. Samples were analyzed using an Agilent 7890A GC system, equipped with a flame ionization detector (FID). Products were identified against authenticated standards and quantified by calibration to obtain response factors (RF) against the known internal standard (dodecane). The turnover number (TON) and turn over frequency (TOF) were calculated based on the amount of biaryl product formed. The TON^{surf} and TOF^{surf} are the TON and TOF normalized to the number of surface Pd atoms. The number of surface atoms on cubic and concave cubic NCs was calculated based geometrical considerations assuming a face centred cubic (fcc) Pd lattice. The total number of Pd atoms per NC was estimated by the volume of a cube or concave cube/volume of the unit cell ($3\sqrt{a}$) × number of atoms per unit cell (4), where a is the lattice constant for fcc Pd, taken to be 0.389 nm. The total number of surface atoms was estimated by: surface area of the cube/surface area of the 2 dimensional lattice × 2. For concave cubes, this relationship was multiplied by 3/7 assuming the atomic density of the {730} surface facets is three-sevenths that of the {100} facets. The volume of a concave cube was approximated by taking the volume of a cube minus the volume of the square pyramids occupying the 6 sides of a cube.

Results and Discussion

Figures 1 (a) and (c) show TEM images of cubic NCs enclosed by 6 {100} surface facets, with closed packed atoms and a surface atom co-ordination number of 8. Figure 1(b) shows a TEM image of concave cubic Pd NCs that measure 20 nm across and 35 nm from corner to corner. Based on the projection of angle along the direction[27], the faces can be indexed to the {730} surface facet, as shown in figure 1 (d).[2] A {730} facet consists of a periodic series of two (210) facets and one (310) facet, as illustrated in the TEM in figure 1(e) and the schematic in figure 1(f). The density of step surface atoms is ~5 × 10^{14} cm^{-2}, which implies that about 40 % of surface atoms are located at step sites. The catalytic performance of the low and high index surface planes was compared in the cross coupling of 4-methoxyiodobenzene (1) acid and phenylboronic (2) in EtOH/H_2O, as illustrated in scheme 1.

c

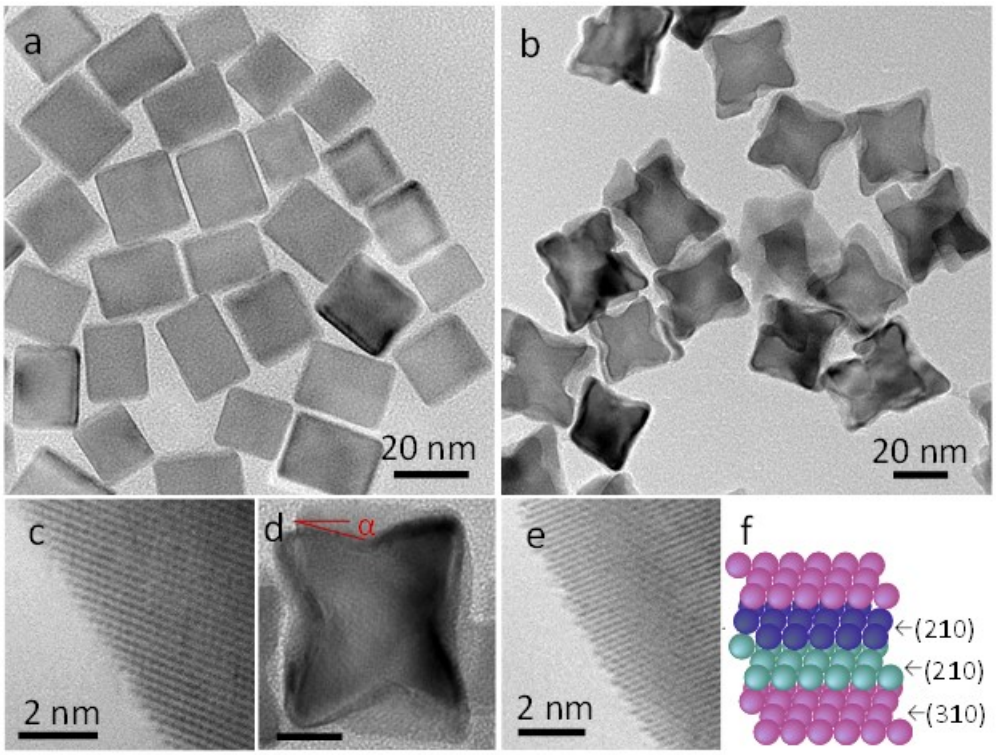

Figure 1. TEM image of as-synthesized (a) 20 nm cubic Pd NCs, (b) concave cubic Pd NCs. (c) Surface of cubic NCs, (d) concave cubes, (e) surface of concave cubic NCs and (f) schematic illustrating the {730} facet. Scale bar figure (d) is 10 nm.

Scheme 1. Model Suzuki-Miyaura reaction used in this study.

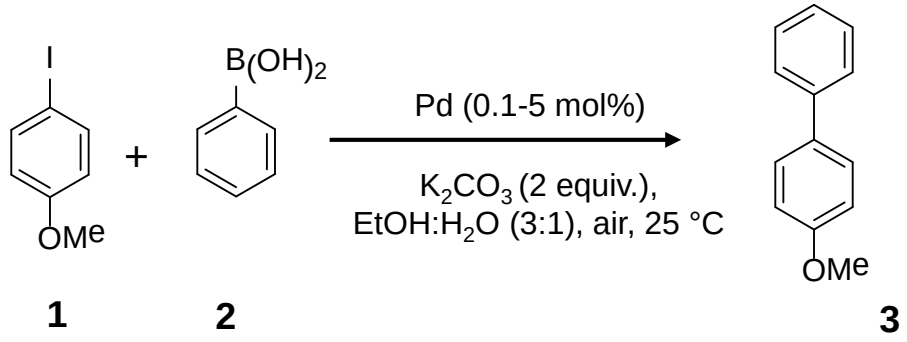

1 **2** **3**

Figure 2 shows the reaction profiles for cubic (10 nm and 20 nm) and concave cubic NCs and reveals significant differences in the catalytic behavior with both size and shape effects observed in the catalytic activity. The concave cubes and 10 nm cubic catalysts were found to be active for the coupling reaction while the 20 nm cubic NCs showed no reactivity, at a Pd concentration of 0.5 mol%. The enhanced catalytic activity of the high index surface facets is apparent, with the yield of biphenyl product increasing from 54 % for cubic catalysts to 92 % for concave cubic catalyst, after 30 h. This reactivity represents a 7-fold increase in the TON for the high index surfaces (TON = 7077) compared to low index planes (TON = 1073), after normalization to the number of surface atoms for each NC. Both the 10 nm and 20 nm cubic catalysts were found to be inactive for the coupling of 4-methoxybromobenzene and phenylboronic acid, while concave cubes displayed similar reactivity as the aryl iodides

achieving an 89 % yield. No induction period was observed for the concave cubes, whereas the reaction catalyzed by the cubic catalysts displayed a considerable lag time of 300 min.

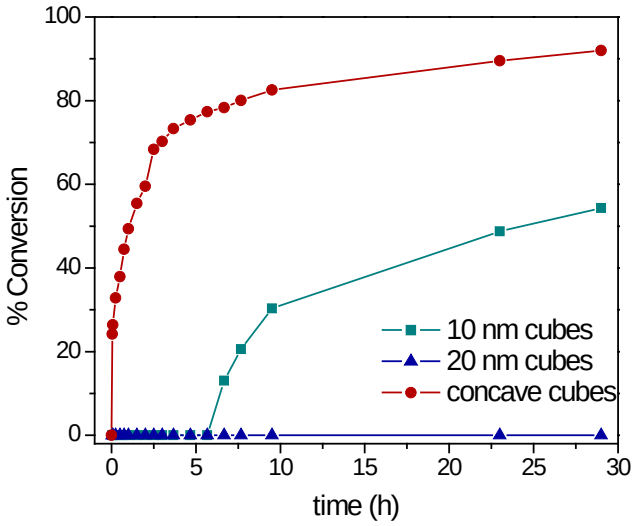

Figure 2. Reaction profile of Suzuki coupling reactions using Pd NCs with high and low index facets.

Figures 3 (a) and (b) show SEM images of the cubic and concave cubic catalysts collected after the reaction, respectively. The catalysts showed negligible change to their morphology and the well-defined surface facets were intact, as shown by the inset TEM images. While the NCs showed little change to their overall shape, a slight reduction in the mean edge length and a boarding in the size distribution was observed. The mean edge length for the 10 nm cubic NCs decreased to 10.6 nm (σ=1.3) and 9.6 nm (σ =1.9), while the edge length for the concave cubic NCs decreased from 35.1 nm (σ = 3.2) to 31.6 nm (σ = 3.9), (Supporting Information Figure S1 and S2). Negligible changes to the edge length of the 20 nm cubic NCs was observed; 19.5 nm (σ =1.9) before and 18.9 nm (σ =2.1) post reaction. Detailed TEM analysis revealed the presence of small nanoparticles about 1-2 nm in diameter, in the Pd residue collected after the reaction, as shown in figures 3 (c) and (d). High resolution

imaging of these particles, shown in figures 3 (c) and (d) insets, indicates a d spacing of 0.23 nm, which can be attributed to Pd(111) lattice fringes.[23] Pd clusters are observed in the TEM grids of both low index and high index particles. These particles were not present in the as-synthesized solution of the catalyst NCs and so can attributed to leached Pd during the reaction.[45] Notably, Pd clusters of 1-2 nm in diameter only comprise ~200-300 atoms, which accounts for about 0.4 % of the total atoms in a 10 nm cubic NC. Significant changes to the NC morphology were not readily apparent at high catalyst concentrations (0.5 mol%), consistent with previous reports.[27] When the Pd catalyst concentration is decreased to 0.1 mol%, after reaction at room temperature, dissolution of the concave cubic structures was clearly observed as shown in figure 3 (d). Figure 2 also demonstrates the lower activity of the 20 nm compared to 10 cubic NCs, which fail to catalyze the reaction at a Pd concentration of 0.5 mol%. If the surface of the cubic NCs were solely the active sites, then the surface normalized TONs should be similar for both the 10 and 20 nm cubic NCs, which is not the case. The lower activity of the 20 nm cubic NCs is attributed to the lower leaching susceptibility, which may be correlated to the greater stability of the 20 nm cubic NCs compared to the 10 nm NCs.[46] The superior stability of the larger cubic NCs leads to less leaching and therefore reduced catalytic performance in the coupling reaction.

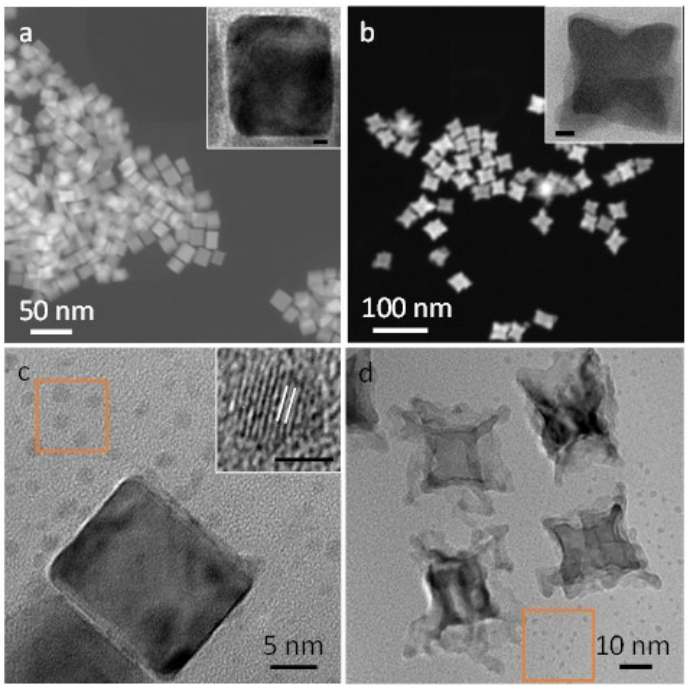

Figure 3. SEM image of cubic Pd NCs and (b) concave cubic Pd NCs cubes after a Suzuki coupling reaction (0.5 mol%) The insets in (a) and (b) show TEM images of the individual NCs. Scale bars in insets are 2 nm. (c) TEM image of cubic NCs and (d) concave NCs Pd 0.1 mol% after the reaction showing dissolution and the presence of small diameter Pd nanoparticles. The scale bar insets of (c) and (d) are 2 nm.

The effect of catalyst concentration was assessed and figure 4 shows the reaction profiles of cubic and concave cubic NCs with a Pd concentration of 0.1, 0.5, 1 and 5 mol%. The TONs and TOFs for the different catalyst concentrations are shown in table 1. Cubic NCs (figure 4 (a)) displayed an increased conversion rate with increasing Pd concentration. No conversion was observed with a Pd concentration of 0.1 mol%. Similarly, while the 20 nm cubic NCs (figure 4 (b)) gave no conversion at 0.5 mol%, yields of 32% and 48% could be achieved with 1 and 5 mol% Pd, respectively. Interestingly, the concave cubic catalysts did not exhibit the same reactivity trend, with varying catalyst concentration. As shown in figure 4(c), a Pd concentration of 1 mol% was faster than a higher catalyst concentration of 5 mol%. Figure

4(d) shows a magnification of the first 180 min of the reaction, illustrating that initially the 5 mol% displayed the fastest conversion, but the reaction slowed as it progressed. This inverse relationship between the Pd concentration and rate has been associated with a homogenous mechanism.[47] Deactivation of this so-called *homeopathic* Pd occurs as the solubilized Pd nucleates to form Pd clusters that continue to grow.[48-49] Quenching of the catalytically active Pd species in solution becomes more efficient as the Pd concentration increases due to greater leaching.[15] TEM analysis also provided evidence for this deactivation mechanism at higher Pd concentrations, which showed the presence of Pd aggregates compared to discreet nanoparticles observed at lower Pd concentrations (Supporting Information Figure S3). It is worth noting that although leaching is identified as an important step in the catalytic activity of the NCs, it does not identify the nature of the catalytic species *i.e.* if the reaction is catalyzed by molecular Pd or the small diameter clusters observed by TEM. The leached Pd species exist as solubilized Pd in equilibrium with the Pd clusters and it is not possible to distinguish if the catalytically active species is homogeneous or heterogeneous in nature.

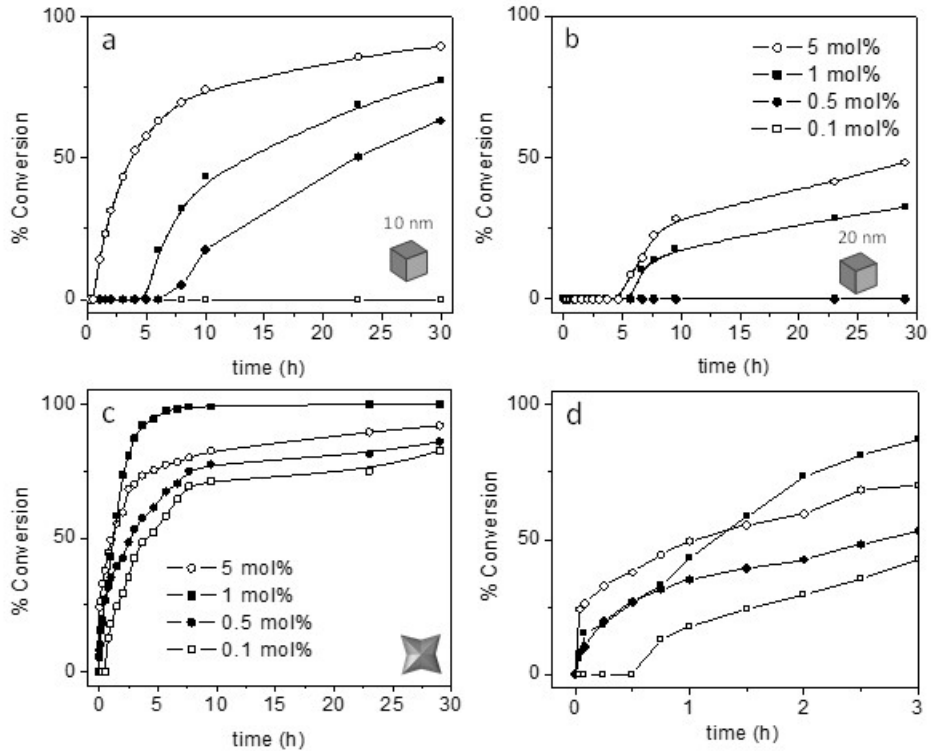

Figure 4. Reaction profile with varying Pd concentrations for (a) 10 nm cubic NCs, (b) 20 nm cubic NCs and (c) and (d) concave cubic NCs.

Table 1. Effect of catalyst concentration for cubic and concave cubic NCs in Suzuki coupling.

Catalyst	Yield	Time	TON^{tot}	TON^{surf}	TOF^{surf}
mol%	**%**	**h**			
Cube (10 nm)					
0.1	0	30	0	0	0
0.5	59	30	118	1073	38
1	77	30	77	700	23
5	89	30	17.8	161	5
Cube (20 nm)					

0.1	0	30	0	0	0
0.5	0	30	0	0	0
1	32	30	32	533	18
5	48	30	9.6	160	5.3
Concave cube					
0.1	72	9.5	720	28000	3032
0.5	89	9.5	178	6846	721
1	100	9.5	100	4000	133
5	83	9.5	16.6	638	67

*See Experimental section for calculation of TOFs.

A significant difference in the catalytic behavior is the absence of an induction period for the high index NCs and a very long induction time for the cubic NCs. Lag periods have been attributed to the time required to leach sufficient Pd into solution for catalytic turnover. Based on the TEM analysis indicating a homogeneous mechanism, the absence of an induction period for the concave cubic NCs suggests rapid leaching from the NC surfaces. To investigate if the induction time was associated with Pd leaching the reaction catalyzed by the cubic NCs was stopped after 60 min, by which time no biphenyl product was formed, the presence of Pd clusters was not observed by TEM analysis. In comparison, when the reaction catalyzed by the concave cubic NCs was stopped after 60 min, when conversion is at 38%, the presence of the leached Pd clusters were observed by TEM (Supporting Information Figure S4). While TEM cannot quantify the leached Pd, it qualitatively shows that the presence of leached Pd, in the form of molecular or clusters, play a central role in the catalytic activity.

To further investigate the reaction regents that contribute to leaching, the cubic NCs (0.5 mol %), which have a long induction period, were pre-stirred separately in solutions of the aryl iodide, boronic acid + K_2CO_3, K_2CO_3 and EtOH:H_2O for 3 hours, after which time the remaining reagents were added. The reaction profiles were monitored to determine if the conversion rates improved due to leaching. Figure 5 compares the reaction profiles of the pre-stirred solutions and a control reaction where no pre-stir was conducted. All of the pre-stirred solutions except the EtOH:H_2O solvent exhibited faster reactions, with the base and boronic acid having the most influence, increasing the yield to 90% from 59% without the pre-stir. The faster conversion was observed for the pre-stir samples suggesting leaching of Pd occurs and that all the agents can promote leaching to some degree. Much debate surrounds the leaching mechanism, with oxidative addition of the aryl halide being common for organic solvents[41], while the base and boronic acid promote leaching under aqueous conditions.[43]

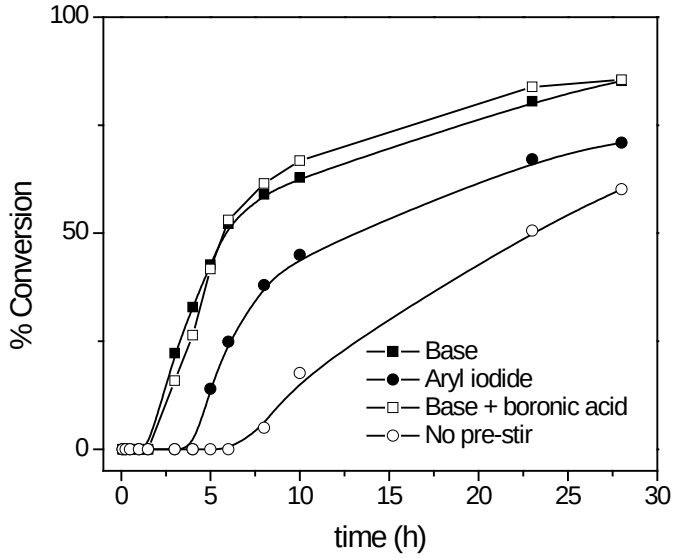

Figure 5. The influence of pre-stirring cubic catalysts in solutions of K_2CO_3, 4-methoxyiodobenzene, K_2CO_3 + phenylboronic acid. NCs pre-stirred in EtOH:H_2O showed no difference to the control and is omitted for clarify.

The effect of the individual reagents on the morphology of the cubic catalysts, stirred separately in EtOH:H_2O solutions of 4-methoxyiodobenzene, phenylboronic acid + K_2CO_3, K_2CO_3 and phenylboronic acid, was also assessed by TEM. After 24 h, the nanoparticles were collected and analyzed by TEM as shown in figure 6. Stirring the aryl halide left the cubic morphology excellently preserved (figure 6 (a)) and the presence of Pd clusters was not readily apparent. A mixture of boronic and base also left the cubic shape intact but the presence of small diameter (1-2 nm) Pd nanoparticles were readily identified, similar to that observed in the post reaction mixture. Finally, stirring the catalysts in the presence of the base alone caused no significant change in morphology and no Pd clusters were observed by TEM (Supporting Information figure S5). Interestingly, the boronic acid alone has the most significant influence on the morphology of the NCs; the concave cubic NCs lost their defined edges becoming more spherical as shown in figure 6(c). Many of the cubic NCs dissolved and the catalysts became spherical. The diameter of these particles was larger (5-10 nm) than those observed when the NCs are stirred in boronic acid + K_2CO_3. Unlike the base or aryl halide, the boronic acid can act as both a reducing agent for the leached Pd and a capping ligand that facilitates the formation of Pd nanoparticles.[50] Note that the overlayers surrounding the NCs in the TEM images arise from contamination during the reaction.

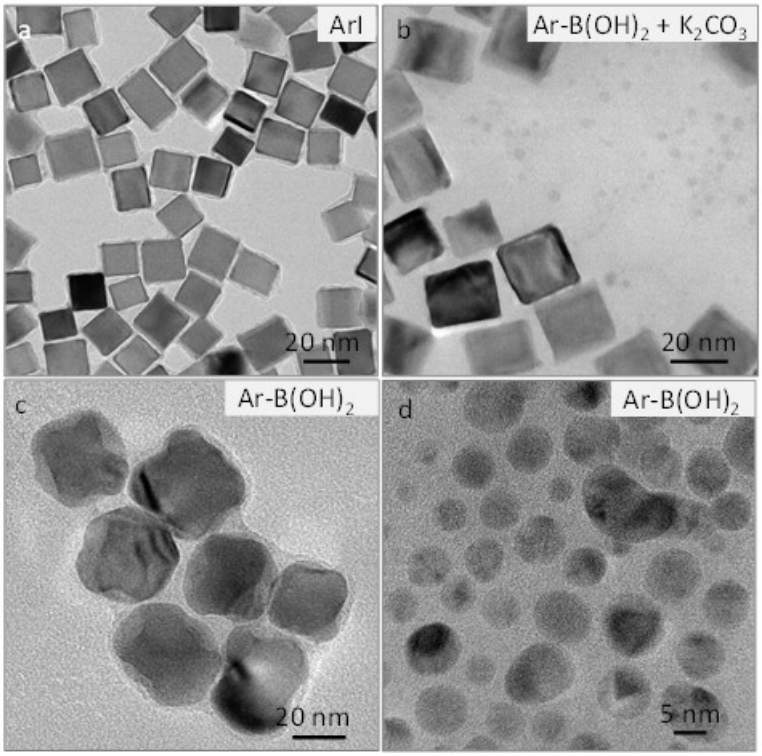

Figure 6. TEM images of cubic NCs after stirring in (a) MeO-Ph-I, (b) phenylboronic acid and K_2CO_3 (c) concave NCs and (d) cubic NCs stirred in phenylboronic acid.

Filtration tests are commonly used to assess the homogeneity of heterogeneity of the reaction mechanism, although it has been noted that redisposition of the leached Pd make them unreliable.[51] Figure 7 (a) shows the reaction profile catalyzed by concave cubes when the reaction mixture was filtered through activated carbon and washed with EtOH:H_2O, 90 min after the reaction was initiated. Comparison with the non-filtrated reaction clearly show that formation of the biaryl product stops after filtration. This loss of catalytic activity can be attributed to the removal of both the parent NC and the Pd clusters formed due to leaching. TEM analysis of the activated carbon confirmed the capture of Pd clusters in addition to the concave cubes by filtration as shown in figure 7 (b) and (c). TEM analysis of the centrifuged filtrates did not contain Pd clusters which were present in the non-filtered samples.

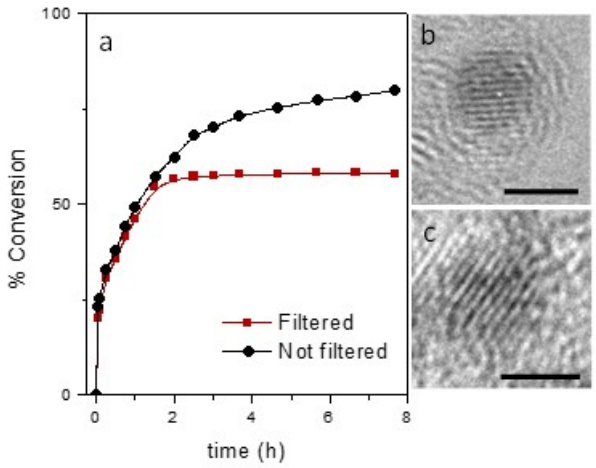

Figure 7. (a) Reaction profile of Suzuki coupling reactions catalyzed by concave Pd NCs showing the effect of filtration 90 min into the reaction. (b)-(c) TEM image of Pd clusters captured on activated carbon after reaction filtration. Scale bar = 2 nm.

XPS analysis was used to determine if leaching gave rise to changes in the NC surface chemistry. Figure 8 shows the Pd 3d core level of the cubic NCs before and after the reaction. Before the reaction, the NCs primarily consisted of metallic Pd, as indicated by the Pd(0) peak at a binding energy of 335.0 eV. The small shoulder peak located at a binding energy of 336.1 eV is typically assigned to surface PdO and a very small peak at 337.1 eV assigned to bulk PdO_x.[46] Figure 8 (b) shows the Pd spectrum after the reaction, with an increased intensity of the bulk PdO_x peak. The formation of oxide is consistent with the presence of Pd clusters, which undergo surface oxidation in the absence of stabilizing ligands. The survey spectra shows the presence of the N 1s peak at 400 eV, indicating that the retention of the PVP capping layer (Supporting Information Figure S6). A small reduction in the Pd:N ratio for the catalysts was observed after the reaction; Pd:N of 4 to 3.8 for the 10 nm cubic NCs and Pd:N of 2.7 to 2.3 for the concave cubic NCs. A more

significant decrease in the Pd:Br ratio was observed, decreasing by 25% for the cubic NCs and 51% for the concave cubic NCs. Supporting Information Table S1).

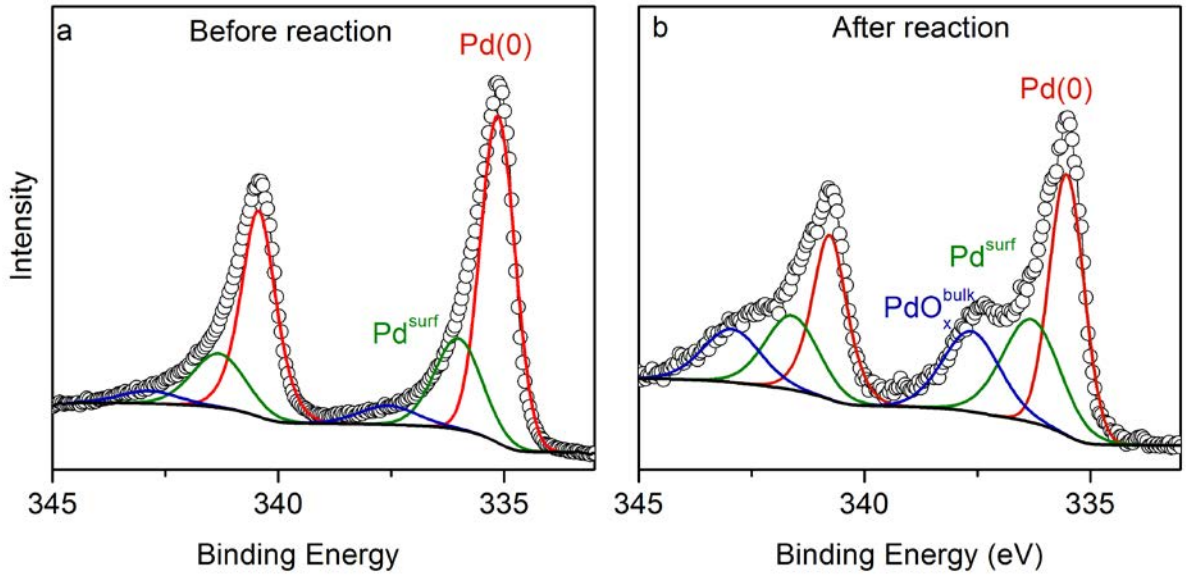

Figure 8. Pd 3d core level spectra of cubic NCs (a) before the reaction and (b) after the reaction. Spectrum (b) was collected using Pd catalysts from several reactions.

The data obtained from the present study correlate well with the catalytic leaching mechanism, although the contribution of a heterogeneous mechanism cannot be completely ruled out. While the parent NCs serve as reservoirs for more active Pd species it is not possible to differentiate between the catalytic activity of solubilized Pd complexes and the Pd clusters observed by TEM. The significant difference in catalytic activity between the high and low index facet NCs suggests that leaching is the rate determining step in this study. Atom abstraction energies for a 3 nm spherical Pd nanoparticles were calculated to be 45 kcal mol^{-1}.[52] Atoms with lower co-ordination numbers, such as vertex and edge atoms, have lower abstraction energies compared to face atoms. Computational modelling of nanoparticle catalyzed Suzuki coupling reactions are lacking, however density functional theory (DFT)

calculations based on homogenous catalysts determine the typical activation energies for oxidative addition of aryl iodides and transmetalation to be 20-25 kcal mol^{-1}.[53-54] The relatively high activation energies for Pd leaching support the consensus that leaching is the rate-determining step. The surface atomic structure influences the stability and leaching susceptibility of Pd atoms and consequently catalytic activity. There are formally no step sites on {100} surfaces, while 42% of the atoms on a {730} surface are step sites, therefore the concave cubes have a high number of leachable atoms with lower abstraction energy compared to the cubic NCs. In the Suzuki reaction the higher surface step atom density of the concave cubic catalysts facilitates more efficient leaching leading to the superior catalytic performance. The rapid leaching resulted in no measureable induction period for reactions involving concave cubic Pd NC catalysts. In contrast, a long lag time was observed with cubic NCs reflecting the slower leaching from closed packed surfaces.

Conclusions

Pd NCs with high index surface facets display superior catalytic performance in Suzuki coupling reactions compared to low index faces. The origin of enhanced catalytic activity associated with catalysts enclosed by high index surfaces was investigated. Both cubic and concave cubic NCs show increasing TOFs with decreasing concentrations, often indicative of a leaching process. TEM analysis identified the presence of small diameter Pd clusters in solution after the reaction, indicating a homogenous leaching mechanism. These Pd clusters were only observed after the formation of biphenyl *i.e.* not observed during the induction period. The high number of surface atoms located at step sites on the concave cubic NCs make it more energetically favorable to leach atoms from high index surface facets compared to closed packed surfaces on cubic NCs.

This works shows that understanding leaching processes is central to the design of heterogeneous catalysts for Suzuki coupling and similar reaction systems. The shape of catalyst NC can considerably influence the leaching properties and therefore catalytic activity of the NCs. Furthermore, the study illustrates that the use of relatively large NCs (> 10 nm) serve as reservoirs for more active Pd species, which is consistent with previous reports. It is important to highlight that while homogeneous Pd, generated through leaching is an important step in the catalytic cycle, it does not imply that the overall reaction mechanism is homogeneous. The exact nature of the active species remains unclear as the leached solubilized Pd is in equilibrium with the small diameter Pd clusters. If these clusters are active in the reaction then further elucidation of this equilibrium and use of smaller diameter Pd nanoparticles (< 3 nm) has the potential to further optimize activity in Suzuki coupling reactions.

Acknowledgments

We thank Enterprise Ireland (grant EI2011-0139) and Eli Lilly for supporting this research. We also acknowledge financial support from Science Foundation Ireland under award 08/CE/I1432.

Supporting Information Available

TEM images of leached Pd nanoparticles in the reaction solution and the XPS survey spectra and quantification of concave and cubic catalysts after reaction can be found in the Supporting Information. This information is available free of charge via the internet at http://pubs.acs.org/.

References

1. Tian, N.; Zhou, Z.-Y.; Sun, S.-G.; Ding, Y.; Wang, Z. L., *Science* **2007,** *316*, 732-735.
2. Quan, Z.; Wang, Y.; Fang, J., *Acc. Chem. Res.* **2013,** *46*, 191-202.
3. Ford, L. P.; Nigg, H. L.; Blowers, P.; Masel, R. I., *J. Catal.* **1998,** *179*, 163-170.
4. Liu, Z. P.; Hu, P., *J. Am. Chem. Soc.* **2003,** *125*, 1958-1967.
5. Baker, T. A.; Xu, B.; Jensen, S. C.; Friend, C. M.; Kaxiras, E., *Catal. Sci. Technol.* **2011,** *1*, 1166-1174.
6. Yin, L.; Liebscher, J., *Chem. Rev.* **2007,** *107*, 133-173.
7. Antolini, E., *Energy Environ. Sci.* **2009,** *2*, 915-931.
8. Torborg, C.; Beller, M., *Adv. Synth. Catal.* **2009,** *351*, 3027-3043.
9. Collins, G.; O'Dwyer, C.; Morris, M.; Holmes, J. D., *Langmuir* **2013,** *29*, 11950-11958.
10. Zhang, Q.; Russell, T. P.; Emrick, T., *Chem. Mater.* **2007,** *19*, 3712-3716.
11. Xu, S.-Y.; Ruan, Y.-B.; Luo, X.-X.; Gao, Y.-F.; Zhao, J.-S.; Shen, J.-S.; Jiang, Y.-B., *Chem. Commun.* **2010,** *46*, 5864-5866.
12. Lamblin, M.; Nassar-Hardy, L.; Hierso, J.-C.; Fouquet, E.; Felpin, F.-X., *Adv. Synth. Catal.* **2010,** *352*, 33-79.
13. Choudary, B. M.; Madhi, S.; Chowdari, N. S.; Kantam, M. L.; Sreedhar, B., *J. Am. Chem. Soc.* **2002,** *124*, 14127-14136.
14. Yuan, B.; Pan, Y.; Li, Y.; Yin, B.; Jiang, H., *Angew. Chem. Int. Ed.* **2010,** *49*, 4054-4058.
15. Deraedt, C.; Astruc, D., *Acc. Chem. Res.* **2014,** *47*, 494-503.
16. LeBlond, C. R.; Andrews, A. T.; Sun, Y. K.; Sowa, J. R., *Org. Lett.* **2001,** *3*, 1555-1557.
17. Han, W.; Liu, C.; Jin, Z., *Adv. Synth. Catal.* **2008,** *350*, 501-508.
18. Kim, S. W.; Kim, M.; Lee, W. Y.; Hyeon, T., *J. Am. Chem. Soc.* **2002,** *124*, 7642-7643.
19. Lu, F.; Ruiz, J.; Astruc, D., *Tetrahedron Lett.* **2004,** *45*, 9443-9445.
20. Collins, G.; Schmidt, M.; O'Dwyer, C.; Holmes, J. D.; McGlacken, G. P., *Angew. Chem. Int. Ed.* **2014,** *53*, 4142-4145.
21. Crudden, C. M.; Sateesh, M.; Lewis, R., *J. Am. Chem. Soc.* **2005,** *127*, 10045-10050.
22. Taladriz-Blanco, P.; Herves, P.; Perez-Juste, J., *Top. Catal.* **2013,** *56*, 1154-1170.
23. Collins, G.; Blomker, M.; Osaik, M.; Holmes, J. D.; Bredol, M.; O'Dwyer, C., *Chem. Mater.* **2013,** *25*, 4312-4320.
24. Hariprasad, E.; Radhakrishnan, T. P., *ACS Catalysis* **2012,** *2*, 1179-1186.
25. Mohanty, A.; Garg, N.; Jin, R., *Angew. Chem. Int. Ed.* **2010,** *49*, 4962-4966.
26. Wang, F.; Li, C.; Sun, L.-D.; Wu, H.; Ming, T.; Wang, J.; Yu, J. C.; Yan, C.-H., *J. Am. Chem. Soc.* **2011,** *133*, 1106-1111.
27. Jin, M.; Zhang, H.; Xie, Z.; Xia, Y., *Angew. Chem. Int. Ed.* **2011,** *50*, 7850-7854.
28. Hong, J. W.; Kim, M.; Kim, Y.; Han, S. W., *Chem. Eur. J.* **2012,** *18*, 16626-16630.
29. Chen, Y.-H.; Hung, H.-H.; Huang, M. H., *J. Am. Chem. Soc.* **2009,** *131*, 9114-9121.
30. Yu, Y.; Zhang, Q.; Liu, B.; Lee, J. Y., *J. Am. Chem. Soc.* **2010,** *132*, 18258-18265.
31. Tian, N.; Zhou, Z.-Y.; Sun, S.-G., *Chem. Comm.* **2009,** 1502-1504.

32. Chen, Y.-X.; Lavacchi, A.; Chen, S.-P.; di Benedetto, F.; Bevilacqua, M.; Bianchini, C.; Fornasiero, P.; Innocenti, M.; Marelli, M.; Oberhauser, W.; Sun, S.-G.; Vizza, F., *Angew. Chem.-Int. Edit.* **2012,** *51*, 8500-8504.
33. Tian, N.; Zhou, Z.-Y.; Yu, N.-F.; Wang, L.-Y.; Sun, S.-G., *J. Am. Chem. Soc.* **2010,** *132*, 7580-+.
34. Diaz Valenzuela, C.; Carriedo, G. A.; Valenzuela, M. L.; Zuniga, L.; O'Dwyer, C., *Sci. Rep.* **2013,** *3*, 2642.
35. Le Bars, J.; Specht, U.; Bradley, J. S.; Blackmond, D. G., *Langmuir* **1999,** *15*, 7621-7625.
36. Li, Y.; Hong, X. M.; Collard, D. M.; El-Sayed, M. A., *Org. Lett.* **2000,** *2*, 2385-2388.
37. Davis, J. J.; Bagshaw, C. B.; Busuttil, K. L.; Hanyu, Y.; Coleman, K. S., *J. Am. Chem. Soc.* **2006,** *128*, 14135-14141.
38. Davis, J. J.; Coleman, K. S.; Busuttil, K. L.; Bagshaw, C. B., *J. Am. Chem. Soc.* **2005,** *127*, 13082-13083.
39. Ellis, P. J.; Fairlamb, I. J. S.; Hackett, S. F. J.; Wilson, K.; Lee, A. F., *Angew. Chem. Int. Ed.* **2010,** *49*, 1820-1824.
40. Pachon, L. D.; Rothenberg, G., *Appl. Organometal. Chem.* **2008,** *22*, 288-299.
41. Niu, Z.; Peng, Q.; Zhuang, Z.; He, W.; Li, Y., *Chem. Eur. J.* **2012,** *18*, 9813-9817.
42. Gaikwad, A. V.; Holuigue, A.; Thathagar, M. B.; ten Elshof, J. E.; Rothenberg, G., *Chem. Eur. J.* **2007,** *13*, 6908-6913.
43. Fang, P.-P.; Jutand, A.; Tian, Z.-Q.; Amatore, C., *Angew. Chem. Int. Ed.* **2011,** *50*, 12184-12188.
44. Diallo, A. K.; Ornelas, C.; Salmon, L.; Aranzaes, J. R.; Astruc, D., *Angew. Chem. Int. Ed.* **2007,** *46*, 8644-8648.
45. Thathagar, M. B.; ten Elshof, J. E.; Rothenberg, G., *Angew. Chem. Int. Ed.* **2006,** *45*, 2886-2890.
46. Collins, G.; Schmidt, M.; McGlacken, G. P.; O'Dwyer, C.; Holmes, J. D., *J. Phys. Chem. C* **2014,** *118*, 6522-6530.
47. Adrio, L. A.; Nguyen, B. N.; Guilera, G.; Livingston, A. G.; Hii, K. K., *Catal. Sci. Technol.* **2012,** *2*, 316-323.
48. de Vries, A. H. M.; Mulders, J.; Mommers, J. H. M.; Henderickx, H. J. W.; de Vries, J. G., *Org. Lett.* **2003,** *5*, 3285-3288.
49. Gaikwad, A. V.; Rothenberg, G., *Phys. Chem. Chem. Phys.* **2006,** *8*, 3669-3675.
50. Narayanan, R.; El-Sayed, M. A., *J. Phys. Chem. B* **2005,** *109*, 4357-4360.
51. Widegren, J. A.; Finke, R. G., *J. Mol. Catal. A* **2003,** *198*, 317-341.
52. Ramezani-Dakhel, H.; Mirau, P. A.; Naik, R. R.; Knecht, M. R.; Heinz, H., *Phys. Chem. Chem. Phys.* **2013,** *15*, 5488-5492.
53. Xue, L.; Lin, Z., *Chem. Soc. Rev.* **2010,** *39*, 1692-1705.
54. Braga, A. A. C.; Ujaque, G.; Maseras, F., *Organometallics* **2006,** *25*, 3647-3658.

Supporting Information

Enhanced Catalytic Activity of High Index Faceted Palladium Nanoparticles in Suzuki-Miyaura Coupling due to Efficient Leaching Mechanism

Gillian Collins[*,†,ϕ], *Michael Schmidt, Colm O'Dwyer*[†,§], *Gerard McGlacken*[*,†], *and Justin Holmes*[†,ϕ]

[†]*Chemistry Department, and Tyndall National Institute, University College Cork, Cork, Ireland.*

[ϕ]*Centre for Research on Adaptive Nanostructures and Nanodevices, Trinity College, Dublin, Ireland*

[§]*Materials and Surface Science Institute, University of Limerick, Limerick, Ireland.*

*To whom correspondence should be addressed: Tel: +353 (0)21 4205143; Fax: +353 (0)21 4274097; E-mail: g.collins@ucc.ie

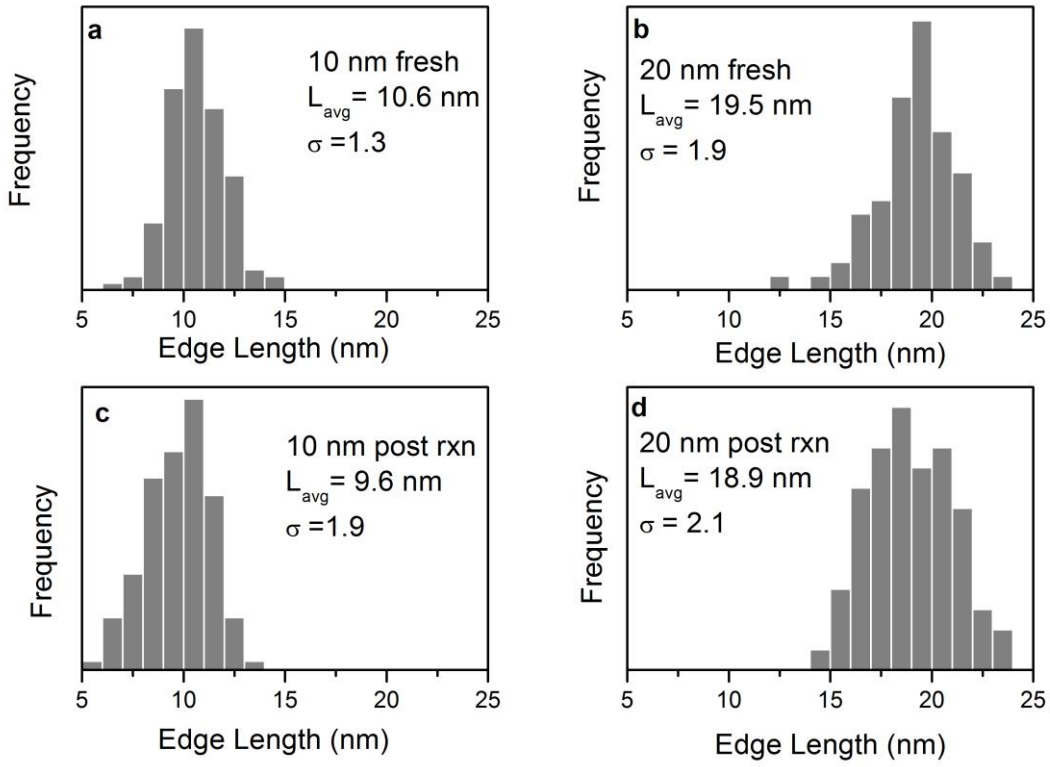

Figure S1. Size distribution histogram of 10 and 20 nm cubic NCs (a)-(b) before reaction and (c)-(d) after reaction.

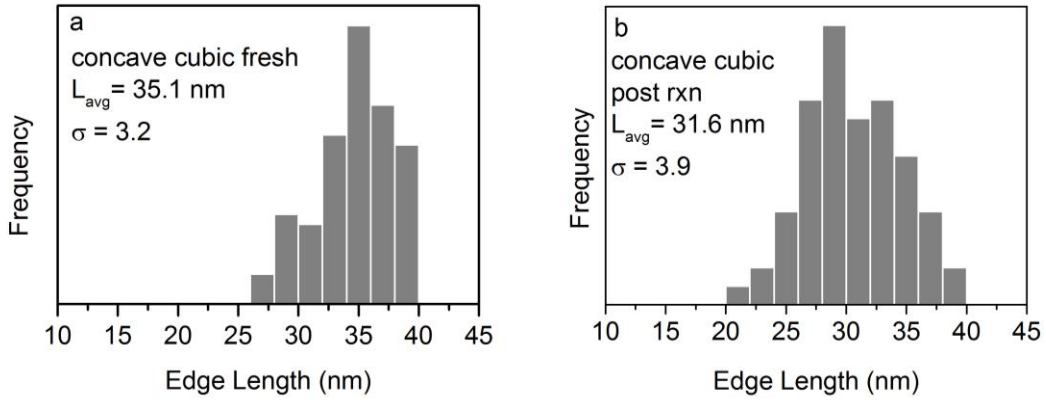

Figure S2: Size distribution histogram of concave cubic NCs (a) before and (b) after the reaction.

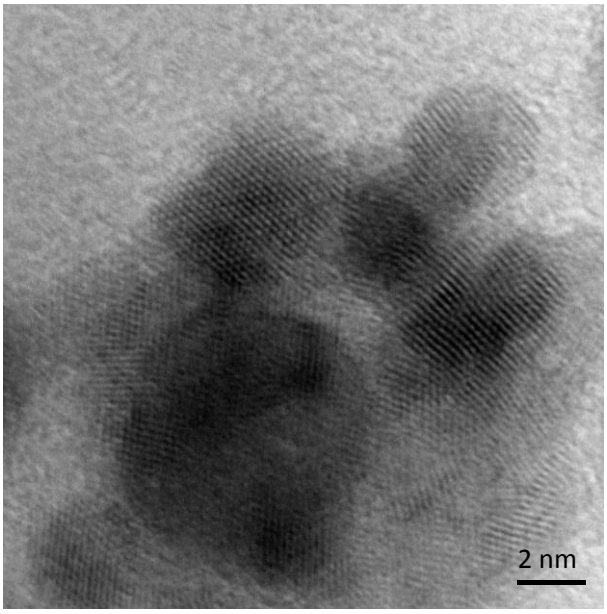

Figure S3. Formation of Pd clusters observed in reaction when using concave cubic nanocrystals at 5 mol %.

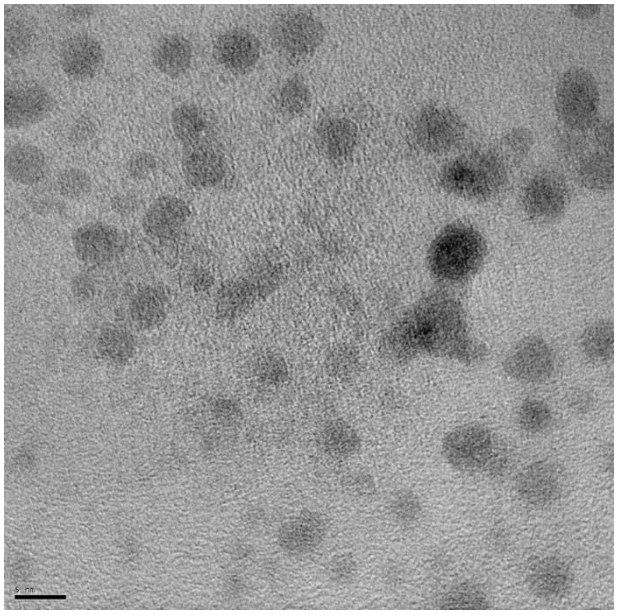

Figure S4. Pd nanoparticles leached from concave cubic nanocrystals 60 min after the reaction. Scale bar is 5 nm.

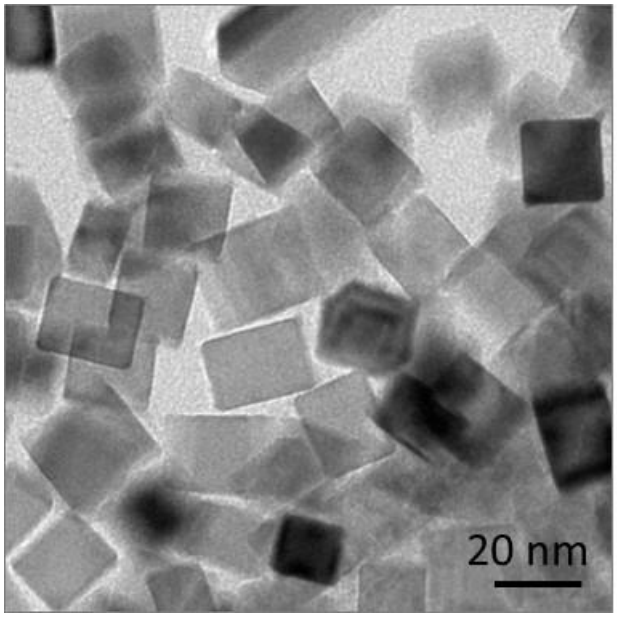

Figure S5. Cubic Pd nanocrystals stirred in presence of K_2CO_3.

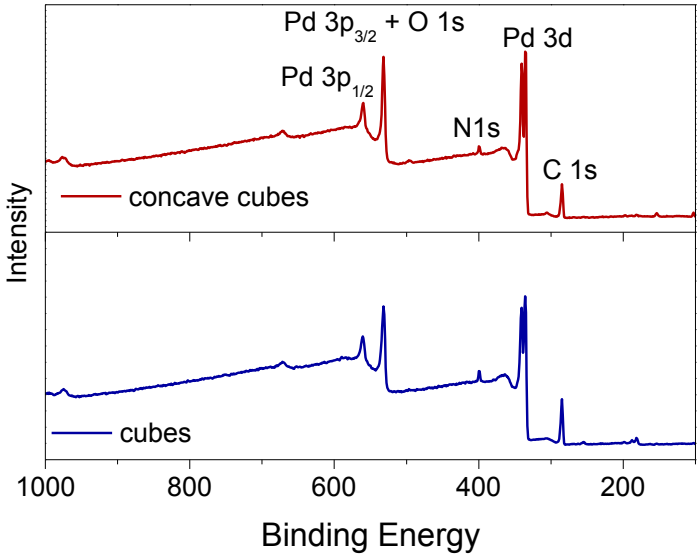

Figure S6. Survey spectra of concave cubes and concave cubic Pd nanocrystals after Suzuki coupling reaction.

Table S1. Quantitative XPS analysis of (a) cubic and (b) concave cubic NCs before and after reaction.

(a) Cubic NCs before and after reaction

Before Reaction				Post Reaction		
core level	**Position (eV)**	**% Concentration**		**core level**	**Position (eV)**	**% Concentration**
O 1s	532.3	48.3		O 1s	532.3	44.4
N 1s	399.7	4.0		N 1s	399.7	2.7
Pd 3d	335.0	15.8		Pd 3d	335.0	10.4
C 1s	284.8	31.4		C 1s	284.8	42.3
Br 3d	68.8	0.4		Br 3d	68.8	0.2

(b) Concave NCs before and after reaction

Before reaction				Post Reaction		
core level	**Position (eV)**	**% Concentration**		**core level**	**Position (eV)**	**% Concentration**
O1s	531.4	39.6		O 1s	531.4	35.5
N 1s	400.0	5.2		N 1s	400.0	4.2
Pd 3d	335.0	14.1		Pd 3d	335.0	13.7
C 1s	284.8	39.4		C 1s	284.8	45.8
Br 3d	68.3	1.7		Br 3d	68.3	0.8